HafenCity Universität Hamburg
Department Geomatik

Backscatter Analysis of Multibeam Sonar Data in the Area of the Valdivia Fracture Zone using Geocoder in CARIS HIPS&SIPS and IVS3D Fledermaus

Master Thesis
by
Tanja Dufek

In partial fulfillment of the requirements
for the degree of
Master of Science in Geomatics

1st Examiner: Prof. Dr.-Ing. D. Egge
2nd Examiner: Prof. Dr.-Ing. H. W. Schenke

July 2012

Declaration §23(4) PSO

I declare, that this Master Thesis – in the case of group work the respective marked parts of the work – has been completed independently without outside help and only the defined sources and study aids were used.

Literally or copied passages or passages analogous in sense from different text sources are marked by referencing the respective sources.

Hamburg, July 27, 2012

(Tanja Dufek)

Contents

List of Figures

VI

List of Tables

Abstract

This thesis deals with a backscatter analysis of multibeam echosounder data acquired during RV Sonne cruise SO213 leg 1 in the area of the Valdivia Fracture Zone in the South-East Pacific. An area of 53 x 25 km^2 was systematically mapped with profiles in diverse directions using a Simrad EM 120 of Kongsberg (12 kHz). For ground-truthing three sediment samples were recovered.

The raw backscatter data was processed with Geocoder in *CARIS HIPS and SIPS* and *FMGeocoder Toolbox (Fledermaus)*. Geocoder was originally developed by Dr. Luciano Fonseca and is licensed by the University of New Hampshire. It was implemented in both commercial software packages recently.

At first, radiometric and geometric corrections for image restoration, enhancement, and geometric rectification were applied to the dataset. Both software packages returned similar results, but it could be observed that the computation of the actual slope for a removal of topographic effects did not work to full extent in either software.

Following initial processing, mosaicing of individual data files into one large seabed image was accomplished using a weighted interpolation method to reduce nadir and seam-effects. This method assigns lower weights to backscatter measurements of the very inner and towards the outer beams. An examination of the results revealed that the mosaic obtained by *FMGeocoder Toolbox* showed less artifacts and therefore a more homogeneous image.

Geocoder provides the possibility of an automatic sediment classification employing an Angular Range Analysis (ARA). This was tested for both software products with diverse settings (with and without ground-truthing) for an evaluation of the results. The estimations of sediment type distribution in both Geocoder implementations differed significantly from one another. Even though the removal of topographic effects did not work properly, the sediment classification yielded acceptable estimations for some of the tested settings.

Although the seafloor topography influenced the appearance of backscatter strengths in the mosaic, a conclusion on the sediment type distribution of the investigation area was possible based on the angle-invariant backscatter information, the recovered sediment samples, and echograms of a sub-bottom profiler.

Chapter 1

Introduction

The attempt to map the surroundings of one's environment dates back millennia. The first known map was painted on a tablet of clay around 2300 BC. It displays the town Nuzi (southwest of Kirkuk in Iraq) with surrounding mountains, rivers, and settlements of northern Mesopotamia (Clark, 2005). The early maps were largely influenced by the view and knowledge of the world of that time and lack spatial correctness. The geographical cognizance improved during the last millennium as global trade (and especially maritime trade) emerged. The first world chart was published around 1500, even though several parts of the continents were not yet discovered. Over time cartographic techniques improved, which resulted in more and more geographically correct depictions of the landmasses.

A large improvement of mapping the Earth's surface was made when remote sensing techniques emerged. The term "remote sensing" comprises the examination or gathering of a place from a distance (Briney, 2008). The first airborne photographs were taken in 1858 from a captive balloon over Paris, which heralds the begin of modern remote sensing. Its techniques became more common in the following wars like the American Civil War (1861 - 1865) when messenger pigeons, kites and balloons were equipped with cameras to gather pictures of enemy territory. Today a large variety of sensors (cameras, infra-red cameras, Radar[1], Lidar[2]) are used as well as a variety of manned or unmanned platforms (e.g., airplanes or spacecrafts). Since satellite emerged in the late 20th century, information on the Earth's surface and even the surfaces of other planets can be obtained on a global scale. Reflecting the large variety of sensors, the types of collected data and the applications of remote sensing are multifacated. Today remote sensing is used, among other things, for air traffic monitoring, observation of meteorological processes, weapon ranging, terrain analysis, or generation of digital terrain and elevation models for example (Albertz, 2007; Briney, 2008).

The seafloor is covered by water and therefore not directly observable like the Earth's surface. Nowadays, satellite altimetry is indirectly used to generate a geomorphological overview of the ocean floor. Satellites measure the height of the ocean surface and its waviness. These measurements can be transformed into depth information by using a model (Sandwell and Smith, 1997) that relates variations in sea surface height to gravity and finally to seafloor features.

---

[1]Radio detection and ranging
[2]Light detection and ranging

Different global bathymetric datasets are available like GEBCO (resolution of 30 arc-seconds) and ETOPO (resolution of 1 arc-minute). Beside satellite altimetry measurements they include ship soundings and regional datasets (GECBCO, 2012; NOAA, 2012) for improvement of accuracy. However, the resulting resolution and the lack of accuracy in some areas make these datasets not sufficient for most applications.

Conventional remote sensing techniques that collect surficial data use electromagnetic signals. These signals are strongly absorbed by water and cannot be directly used for seafloor investigation. Thus, seafloor investigating systems employ acoustic impulses as these are less absorbed by water and therefore reach a larger range in the propagation medium.

Before acoustic systems were invented for water depth measurements, mechanical techniques were used. The first evidence for water depth measurements dates back to 1800 BC according to depictions of Egyptians using sounding poles. Later on, ropes with attached weights (sounding lines, lead lines) were used, which were lowered into the water down to the seabed. The length of the rope could be measured and therefore the water depth could be determined. These mechanical sounding systems were not easily applicable for systematic deep-sea depth measurements (Theberge, 1989).

After the sinking of the RMS Titanic in 1912, engineers tried to develop systems for iceberg detection using sound waves, not knowing that ice is not a good acoustic reflector. It was however accidentally discovered that the emitted sound waves were effectively reflected by the seafloor. The first echosounder was patented by Alexander Behm, a German physician, in 1913 (Beuck, 2006). An echosounder is an active sonar that transmits an acoustic signal vertically into the water. The acoustic impulse travels through the water column to the seafloor, where it is reflected. The echo is received by the sonar system, which measures the propagation time of the signal between transmission and reception. When the water sound velocity is known, the water depth can be calculated.

The first mapping sonars were single-beam echosounders (SBES), which transmit one vertical (downwards directed) acoustic impulse into the water for measuring the depth underneath the vessel. Between the two world wars the technology of underwater acoustic developed strongly and came into wide use for diverse applications as for depth measurements, fish or submarine detection (Lurton, 2010).

In the early 1960s sidescan sonars (SSS) were invented and became popular. They emit two impulses – one impulse per side – in a large angle in across-track direction towards the seafloor. They collect "acoustic images" of the seabed by recording the backscattered intensity and the run-time of the signal. As the direction of the reflections is unknown, they cannot be used for creation of terrain models but their advantage over SBES is their large seafloor coverage (Lurton, 2010).

In the 1970s multibeam echosounder (MBES) emerged. MBES transmit a fan of a large number of acoustic impulses (beams) into the water. Therefore a wide stripe of seabed perpendicular to the ship track can be scanned by multiple simultaneous soundings. This way, larger seafloor coverage of depth soundings is achieved than with the employment of SBES (Lurton, 2010).

The development of sonar technology made the investigation of the seafloor with high accuracy possible, which is important for the improvement of the general knowledge of this environment. Considering that over two third of the Earth's surface is covered with water and that even planet Mars is better mapped, the general lack of knowledge about the ocean becomes obvious. This knowledge gap is mainly related to deep-sea areas, as they are harder to investigate. Shallow-water environments close to the shore and waterways are usually very well known due to their importance for shipping and its safety.

Seafloor scattering information has been the subject of research of the last decades. The aim is to use this information for obtaining sediment properties (e.g., grain size) by analyzing the backscattered response. For conventional sampling methods an instrument (i.e., sediment sampling corer or camera) needs to be lowered from a vessel to the seafloor, which is very time consuming. The approach of remote seafloor classification has the advantage over conventional sediment investigation methods of being much more efficient as it covers a large continuous area. Sediment samples or photographs only depict a local situation, which cannot be extrapolated easily over larger areas.

Different approaches evolved for remote determination of seafloor properties. Special seafloor classification systems were developed like for example "RoxAnn", which is connected to an existing echosounder (usually SBES) (IHO, 2005). Since the 1980s the combination of MBES and SSS technology has emerged: MBES do not only measure the seafloor topography but also record backscattered intensities. This combined acquisition of seafloor topography and its reflectivity is a large advantage over conventional SSS due to its geometric accuracy. Therefore, the investigation of MBES backscatter for remote seafloor classification came into focus of research recently.

As computer technologies have advanced rapidly in accord with remote sensing technologies, techniques for more accurate and faster processing and analysis of backscatter data have emerged. Different methods for seafloor classification based on the MBES backscatter data have been developed (Masetti et al., 2011). One broadly adopted approach investigates the backscatter strength in correspondence to the grazing angle. It is often referred to as "Angular Range Analysis" (ARA) and utilizes the fact that different sediment types cause diverse angular backscatter responses (De Moustier et al., 1991). The ARA applies an inverse model to estimate sediment properties based on the backscatter angular responses. Different models of the acoustic behavior of sediments (Jackson et al., 1986; Stockhausen, 1963) can be used for an ARA. As the seabed can consist of a various composition of sediments and different surficial characteristics, the behavior of an acoustic wave at the water-sediment boundary is complex. Different sediment wave theories were developed, which describe the behavior of the seabed in diverse

ways, for example as fluid, elastic, or poroelastic medium (Jackson et al., 2007). While research on improvements of MBES backscatter processing and modeling of acoustic behavior in sediments is ongoing, MBES backscatter data is used in various fields today, including fishery habitat analysis, oilfield development, and target detection in shallow water (Hewitt et al., 2010).

One of the most promising MBES backscatter processing and analysis software tool is called "Geocoder", which was developed by Dr. Luciano Fonseca and is licensed by the University of New Hampshire (Fonseca et al., 2005, 2007a). It processes backscatter data, creates mosaics, and performs an ARA for a remote estimation of seafloor properties. It is a stand-alone software but was implemented recently in software of different companies: IVS (QPS), CARIS, Reson, Triton, Fugro, Hypack, Chesapeake Technology (CCOM/JHC, 2012). It shows good processing, mosaicing, and analysis results for shallow-water environments (Fonseca et al., 2007a; Amolo, 2010).

One aim of this thesis is to test and evaluate the implemented Geocoder in *CARIS HIPS and SIPS* and *Fledermaus*[3] by using it for processing, mosaicing and analysis of MBES deep-sea data (about 2,100 m to 4,800 m water depth). The investigated dataset was acquired during a RV Sonne cruise in 2011 with a Kongsberg Simrad EM 120 echosounder (12 kHz) in the South-East Pacific in the area of the Valdivia Fracture Zone. For ground-truthing three sediment surface samples were recovered. The second aim of this thesis is to draw a conclusion on the sediment type distribution throughout the survey area based on the obtained angle-invariant backscatter data in conjunction with the recovered sediment samples and dub-bottom profiler echograms.

Chapter 2 of this thesis deals with the basic principles behind the acquired data. It is divided into two parts: First, the principles of geoscience, where an insight is given into the evolution of morphological seafloor structures as well as into marine sediments and their distribution. And second, the principles of underwater acoustics, where the basics of sonar system and the theory of backscatter is outlined. Chapter 3 elaborates on the hydrographical data acquisition and sediment sampling for the dataset of this thesis. The different systems and instruments are presented. Chapter 4 describes the used method Geocoder, its implementation in *CARIS HIPS and SIPS* and *Fledermaus*, as well as the used software settings for the investigated dataset. In Chapter 5 the results of the backscatter processing and analysis are discussed and both software products are compared. Chapter 6 deals with the analysis of the geotectonic formation of the study area and the examination of the angle-invariant backscatter data. The changes in intensity values are investigated for their possible causes and an assumption is made regarding the sediment distribution based on the backscatter data. In the end an overall conclusion is drawn.

---

[3]The software toolset *Fledermaus* was originally developed by the company Interactive Visualization System (IVS3D), but was inherited by Quality Positioning Service (QPS) during the completion of this thesis.

Chapter 2

Basic principles

2.1 Principles of geoscience

2.1.1 The morphological structure of the ocean floor

More than two third of the Earth's surface is covered by water and only less than one third is higher than sea level. Fig. 2.1 shows the distribution of heights above (topography) and below (bathymetry) the sea-surface. The hypsometric curve shows a bimodal distribution with two maxima: one reflects the distribution of submarine elevations and one of the subaerial elevations. The mean depth of the ocean basins is 3.8 km and the mean continental elevation is 840 m. The deep-sea area has the largest share of 78 % of the water covered area (Anderson et al., 2010).
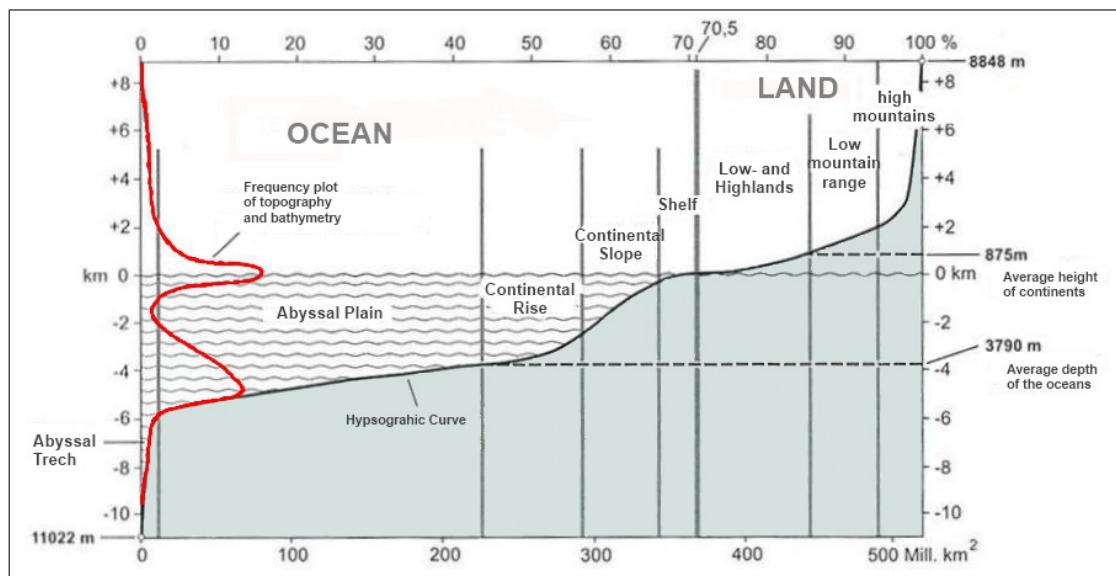
Figure 2.1: Hypsometric curve of the Earth's surface (red) and depth provinces of the ocean floor. (Kelletat, 1999)

The ocean floor can be divided into different provinces of depth: the continental shelf, continental slope, continental rise, and abyssal plain (Fig. 2.1). The continental shelf is connected with the continents. It has a low gradient of approximately 0.5° and a mean water depth of 150 m. Its average width is 60 km

ranging from a few kilometers (at the Pacific coast of North and South America) to more than 300 km (in the Arctic Ocean). The continental shelf ends seawards at the continental break, where the seafloor steepens and the continental slope begins. Typically, the continental slope has a gradient of 3° to 6° and a width of 20 km to 150 km. Here, the lighter continental crust collides with the heavier oceanic crust. The continental slope thus represents the actual crossing between land and ocean. It extends from the shallow depths of the continental shelves to water depths of 2 km to 3 km, where the seafloor slope decreases to a mean value of 1°. This area is the continental rise. It extends seaward for a few hundred kilometers into water depths of up to 4 km, where it turns into the deep ocean basin or abyssal plain. "Continental margin" comprises the continental shelf, slope and rise (Pinet, 2006; Bahlburg et al., 2012).

2.1.2 Influence of plate tectonics on marine geomorphology

The theory of plate tectonics deals with the movement of the lithosphere, comprised of several continental plates, and the forces acting upon them. The lithosphere is the Earth's upper rigid crust. Due to its movement on the less rigid asthenosphere, it is broken into 13 larger and some smaller plates (Fig. 2.2). The continental land masses are situated on the different plates and are changing their position relative to each other. Some of the plates are named after the continents they are carrying (Fig. 2.2) (Press et al., 2008).
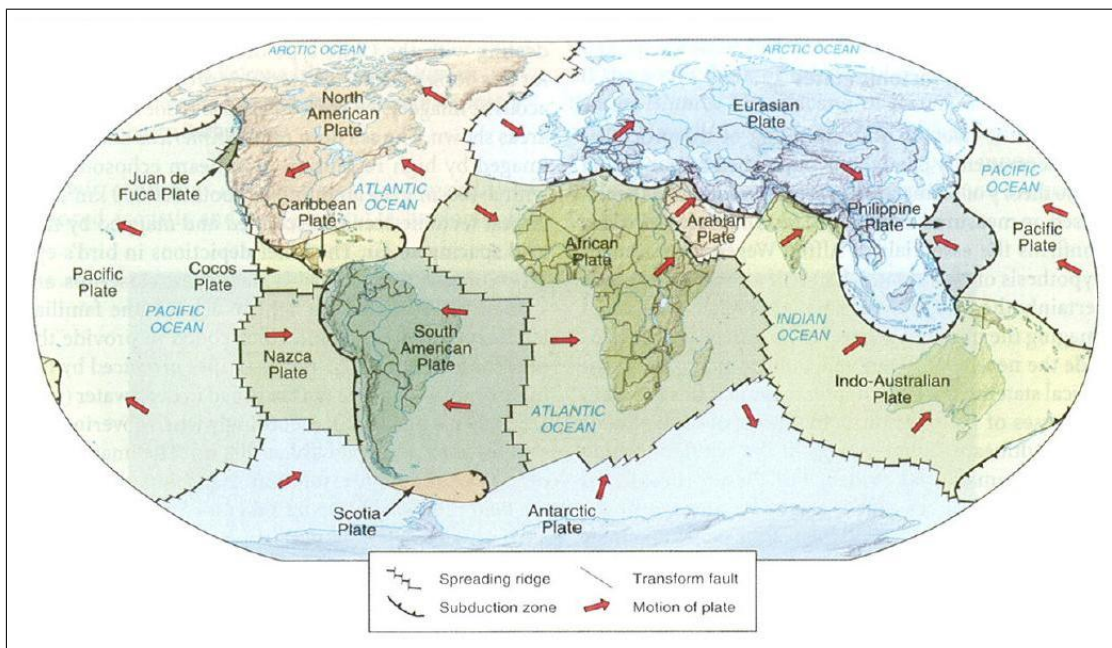
Figure 2.2: Diagram of the tectonic plates and their margins. (Wille, 2005)

Tectonic structures of the ocean

Large seafloor structures originate from the tectonic movement of the continental plates. When continental plates interact with each other, strong forces are active. These forces can be released in earthquakes, volcanism, formation of rift structures, and faulting on the ocean floor. The boundaries between plates are visible as large features on the seafloor. In the following, the main undersea structures and their tectonic origins are described acoording to Tarnuck et al. (2009); Press et al. (2008); Pinet (2006); Blondel et al. (1997).

Ocean ridges: Ocean ridges are submarine mountain ranges. They arise from the abyssal plain in 5,000 m depth up to 2,500 m depth. They are often called mid-ocean ridges because they are often found in the middle of oceans like in the Atlantic or Indic. In the Pacific, the largest ocean ridge is found in the east and therefore called East-Pacific Ridge or East-Pacific Rise. Ridges are usually oriented in north-south direction and have a combined length of 60,000 km – occupying one third of the seafloor. Mid-ocean ridges result from divergent (constructive) plate boundaries, where the plates separate and move away from each other. As they move apart, mantle material ascends in the rift valley of the ridge and welds as new crust to the edges of the older crust. As a result, new seafloor – new lithosphere – is created. The older crust moves eastwards and westwards (Fig. 2.3, top). This process is known as seafloor-spreading.

Abyssal trenches: Abyssal trenches are relatively steep, long and narrow depressions or basins. They can reach depths of 3,000 m to 5,000 m relative to the surrounding ocean floor. They are the deepest regions on Earth and are mostly found close to land at continental margins. Abyssal trenches are formed at convergent (destructive) plate boundaries. Plates collide and one of the plates is pressed below the other, a process called subduction. The lithosphere of the subductive plate is dragged down into the asthenosphere where it melts (Fig. 2.3, top). The deepest known point of the ocean is found in the Mariana Trench in 11,034 m depth.

Transform faults and fracture zones: The axis of mid-ocean ridges is not continuous but segmented by geologically active transform faults. Transform faults originate at conservative plate boundaries, where adjacent plates slide horizontally in different directions and vertical displacement takes place. Fracture zones are the inactive elongation of transform faults extending up to a few thousand kilometers into the deep ocean basin. The plates move in the same direction at fracture zones, and only slow vertical motion occurs (Fig. 2.3, bottom).

The velocity of the seafloor spreading at ocean ridges varies strongly. The East-Pacific-Rise is a fast-spreading ridge with a mean spreading velocity of 150 mm/year. The Mid-Atlantic Ridge is a slow-spreading ridge with a mean spreading velocity of 25 mm/year (Press et al., 2008). As the plates spread apart, the age of the seafloor is positively correlated with the distance from the seafloor spreading center. The farther away from the spreading center, the older the crust (Pinet, 2006).
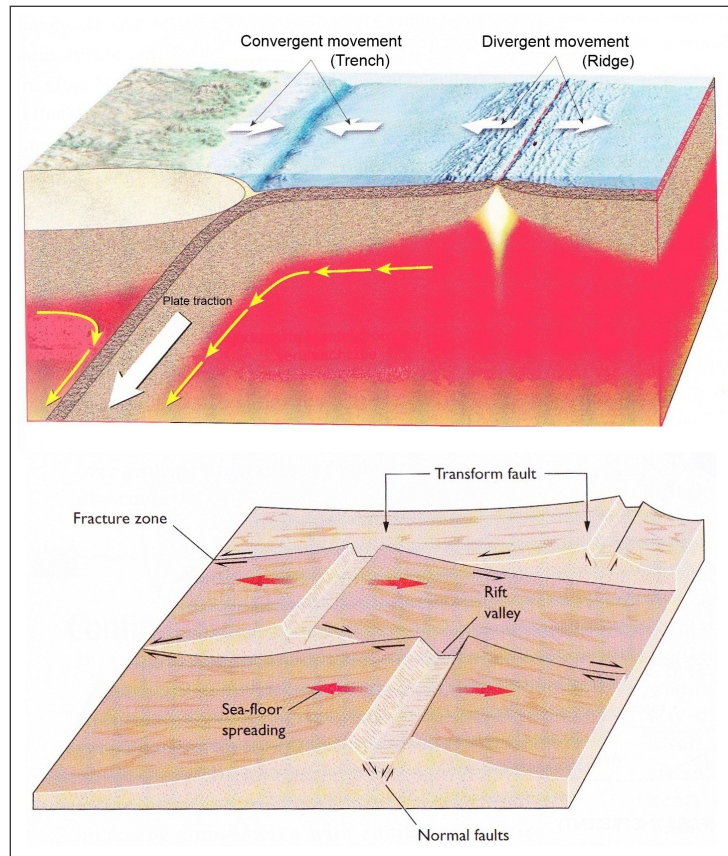
Figure 2.3: Diagram of the origin of abyssal trenches and ridges (top) (Tarnuck et al., 2009) and diagram of transform faults and fracture zones (bottom) (Pinet, 2006).

2.1.3 Marine sedimentation

Sediments are "layered deposits of loose material" (Spektrum, 2002). They play an important role in the rock-cycle which consists of various sedimentary stages in different intersecting processes. At first physical or chemical weathering on land takes place. Small particles are loosened from bedrock and removed by erosion from their origin. Erosional forces are for example rain, ice, wind or gravity (e.g., landslides). The downhill transporting energy decreases with time and the particles are deposited either on land or in the ocean. This continuous process is called sedimentation and creates different layers of sediments in the accumulation space. Younger sediment covers older sediment layers, which are therefore compressed. As time is passing by, diagenesis occurs where the compressed sediments turn into sedimentary rock by increasing pressure, temperature, and the rate of chemical reactions (Press et al., 2008).

2.1.3.1 Classification of marine sediments

The ocean is the largest accumulation space since nearly the entire ocean floor is covered by sediments. These sediments play an important role in geosciences as records of Earth history because they store the chemical and mineralogical environment that existed during their creation. Thus, the scientific investigation of sediments leads to a better understanding of past climate changes, tectonic plate motion, fossil extinction, and the the age of the seafloor.

Sediments can be classified in two different ways: by origin or by grain size. Both classifications are described in the following.

Classification of sediments by origin:

When classifying sediments by origin, five types can be distinguished. To be precise, marine sediments are actually a mixture of these five types, but usually one is dominant.

Terrigenous sediments comprise of approximately 45% of marine sediments. They originate on land where they are eroded from bedrock and swept into the sea. They are found throughout the ocean but are concentrated along the continental margins, which are close to the source (land) and the transportation forces like rivers or wind. Within the ocean the terrigenous sediments are distributed by bottom currents. The grain size of deposited sediments depends on the velocity of the bottom currents. In high energetic environments (high speed of current), larger material is precipitated. The speed of the current decreases the farther it moves and finer material is deposited. This process results in a correlation between distance to the continent, water depth and grain size: The farther away from the continent, the larger the water depth and the smaller the grain size (Press et al., 2008).

Biogenous sediments account for around 54 % of marine sediments and originate from organic sources. The term "biogenous ooze" is used when the material consists of at least 30 % biogenic material by weight. The main sources of biogenous sediments are marine organisms living in the upper hundred meters of the ocean. After death their skeletons or shells sink down to the ocean floor. There are two main groups of biogenous sediments: Calcareous ooze consists of calcium carbonate ($CaCO_3$) and emanates from zooplankton (e.g., foraminifera) and phytoplankton (such as coccolithophores), whereas Siliceous ooze consists of Silicia (SiO_2) and is produced by Diatoms or Radiolaria (single-celled animals). The deposition of terrigenous and biogenous sediments occurs simultaneously in regionally different concentrations. Fig. 2.4 depicts microscopic pictures of biogenic sediments (Pinet, 2006).
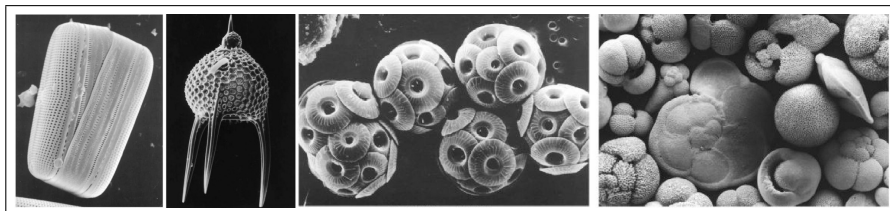
Figure 2.4: Microscope images of biogenous sediments. From left to right: Diatoms, Radiolaria, Coccolithosphores, Foraminifera. (Bellevue College, 2012)

Hydrogeneous sediments are produced by chemical processes when ions are dissolved by seawater and precipitate to the ocean floor. Hydrogeneous sediments are created at or close to their accumulation space. Examples of this sediment type are manganese nodules (Bellevue College, 2012).

Volcaneous sediments consist of ashes from former volcano eruptions. They can be found in areas with high tectonic activity (Pinet, 2006).

Cosmogenous sediments consist of extraterrestrial fragments originating from meteors and cosmic dust. They are very rare and tend to be found in the deep ocean where other sediments accumulate very slowly (Bellevue College, 2012).

Classification of clastic sediments by grain size:

Clastic sediments are terrigenous sediments and are fragments of bedrock. They can be classified by their grain size that ranges from large boulders to very small grains of microscopic clay. Usually, the following types are differentiated (from largest to smallest): gravel, sand, silt, and clay. Numerous classification scales have been developed, but most often the scale proposed by Wentworth (1922) is used (Tab. 2.1), which was also utilized as foundation for the German DIN 4022.

Sediment	Type	Diameter (μm)	Diameter (mm)	ϕ
Gravel	Boulder		> 256	
	Cobble		$65 - 256$	$< $ -6
	Pebble		$4 - 64$	-2 $-$ -6
	Granule		$2 - 4$	-1 $-$ -2
Sand	very coarse	$1{,}000 - 2{,}000$	$1 - 2$	$0 - $ -1
	coarse	$500 - 1{,}000$	$0.5 - 1$	$0 - 1$
	medium	$250 - 500$	$0.25 - 0.5$	$1 - 2$
	fine	$125 - 250$	$0.125 - 0.25$	$2 - 3$
	very fine	$62.5 - 125$	$0.0625 - 0.125$	$3 - 4$
Silt	coarse	$31 - 62.5$	$0.031 - 0.0625$	$4 - 5$
	medium	$15.6 - 31$	$0.0156 - 0.031$	$5 - 6$
	fine	$7.8 - 15.6$	$0.0078 - 0.0156$	$6 - 7$
	very fine	$3.9 - 7.8$	$0.0039 - 0.0078$	$7 - 8$
Clay		< 3.9	< 0.0039	> 8

Table 2.1: Classification of clastic sediments as proposed by Wentworth (1922).

The grain size can be expressed directly as grain diameter (in millimeters or microns) or by the value phi (ϕ). This value is dimensionless and was introduced by Krumbein (1934). It is the negative logarithm to the base of 2 of the grains' diameter in millimeters:

$$\phi = -\log_2 \ d[mm] \tag{2.1}$$

The classification scale developed by Wentworth (1922) was originally created for clastic sediments but can also be used for biogenous sediments. In Tab. 2.2 different organisms, which are sources of sediments in the deep ocean, and their average sizes (diameter) are listed. The strong variation in size results from the fact that one type of organisms has different species that vary in size. The listed values are average dimensions.

Type	Composition	Size [micron]	Size Class
Foraminefera	$CaCO_3$	> 50 - 400	sand
Coccolithophores	$CaCO_3$	3	fine silt
Diatoms	SiO_2	50 (10 - 100)	silt - very fine sand
Radiolaria	SiO_2	50 - 400	sand

Table 2.2: Sizes and distribution of biogenous sediments. (Kennett, 1982)

2.1.3.2 Pelagic sediments

The sediments found in deep-sea areas are called pelagic sediments. Tab. 2.3 shows the distribution of sediments in the ocean. Continental margins occupy a relatively small share (21 %) of the oceanic extent compared to the deep ocean floor (78 %). Nevertheless, they comprise 87 % of all marine sediments due to their vicinity to the continents (sources of terrigenous sediments) and their shallow water depths. This leads to high biogenetic production and therefore high accumulation of biogenous sediments. As deep-sea areas are far away from the continents, the accumulation of terrigenous material is relatively low compared to the continental margins (Bellevue College, 2012).

Region	Percent of ocean area	Percent of total marine sediments	Volume of average thickness
Continental shelf	9	15	2.5 km
Continental slope	6	41	9 km
Continental rise	6	31	8 km
Deep ocean floor	78	13	0.6 km

Table 2.3: Distribution of marine sediments. (Bellevue College, 2012)

Different sedimentation processes occur in the deep-sea (Fig. 2.5). Terrigenous sediments are mainly deposited on the shallow continental shelves by rivers and wind. These sediment layers can become instable and lead to bulk emplacements induced by gravity, which are downslope transportations of terrigenous material from the continental shelf or upper continental slope (typically debris flows or turbidity currents). They can transport the sedimentary material very far into the deep-sea area. Terrigenous sediments can also be transported in the deep ocean directly by wind. These sediments are called "pelagic clay" or "brown clay" due to its red color resulting from high iron concentration (Pinet, 2006).

Another important source of pelagic sediments are microorganisms (biogenous sediments). These organisms are widely spread throughout the world's ocean. After their deaths, their remains settle to the ocean floor or are dissolved. The potential dissolution depends on the chemical composition of the biogenous material. Cold bottom water is slightly acidic for calcium carbonate, therefore carbonate material is dissolved when sinking below a certain depth. This depth is called the "carbonate compensation depth" (CCD). The CCD depends on the supply of carbonate, the acidity, temperature and pressure of the water. It varies between different locations of the ocean. Most often it lies between 4,200 m and 4,500 m in the Pacific Ocean and at approximately 5,000 m below the water surface in
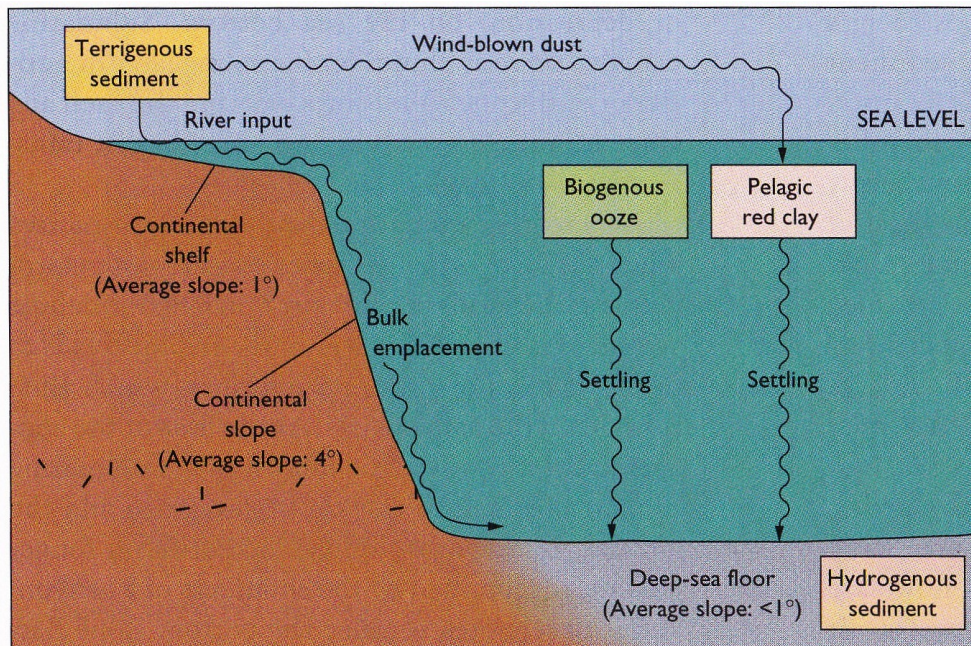
Figure 2.5: Sedimentation processes in the deep-sea. (Pinet, 2006)

the Atlantic Ocean. It is an important chemical zone controlling the distribution of calcareous ooze (Press et al., 2008; Bahlburg et al., 2012).

Hydrogenous sediments in the deep water are mainly manganese nodules. They are created by a chemical reaction of the ocean water with the sediments of the ocean floor. They are mainly found in the Pacific Ocean that is covered by 20 to 50 % with manganese nodules (Pinet, 2006).

Fig. 2.6 shows the distribution of pelagic sediments throughout the ocean. Terrigenous material is mainly found on continental margins. In the Northern Atlantic, Northern Pacific and close to India, terrigenous material is also found in the deep-sea where it is brought by debris flows or turbidity currents. Areas with high biological productivity have a large population of planktonic organisms that contribute large quantities of calcareous and siliceous shells to the ocean floor. The equator and the polar regions are fertile areas and thus exhibit a large concentration of siliceous ooze. Due to the carbonate compensation depth, calcareous ooze cannot be found in deep abyssal plains. It is found on the crests of ocean ridges, seamounts or plateaus, where the water depth does not exceeds the CCD. Pelagic clay is mostly located in the deep abyssal plains where the influence of bulk emplacements and biogenous production is negligible. Tab. 2.4 shows the composition of pelagic sediments of the oceans. The Pacific has a relatively small amount of calcareous ooze and a large amount of pelagic clay compared to the global average (Pinet, 2006; Tarnuck et al., 2009).

The thickness of the sediment layer covering the ocean floor depends on the age of the basement and the sedimentation rate. Close to the ocean ridges where new oceanic crust is created, the sediment cover is very low. It increases with distance to the spreading ridges where the crust is older and the sediment consequently has had a longer time to accumulate. The sedimentation rate in the deep ocean
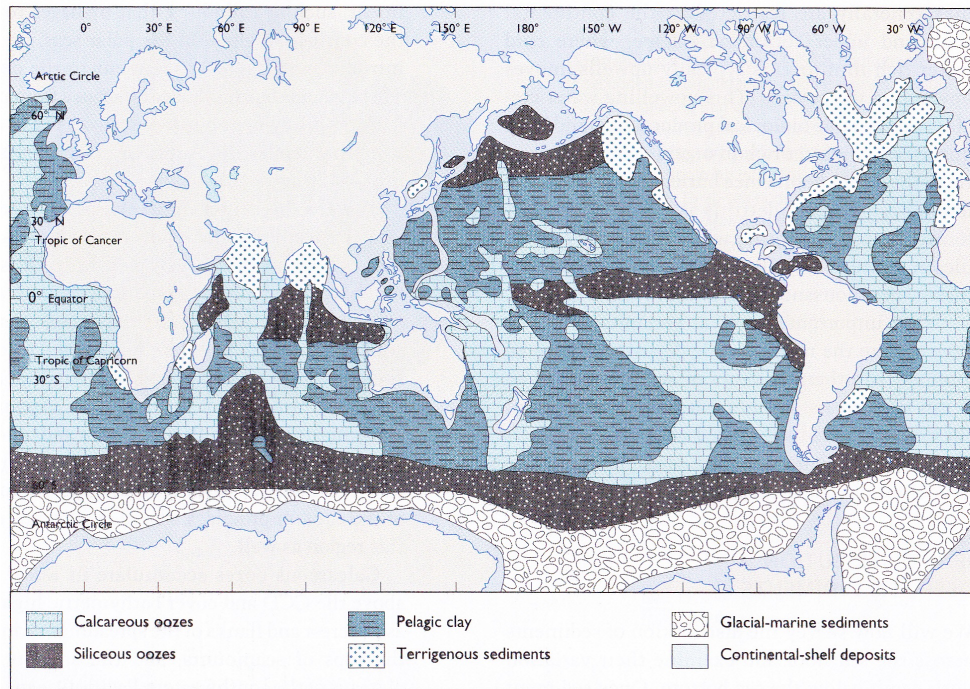
Figure 2.6: Sediment distribution of the deep-sea. (Pinet, 2006)

depends on the composition of the sediment. Terrigenous sediments on the continental margins have the largest sedimentation rate with more than 5 cm per 1,000 years. Biogenic oozes accumulate at a rate of 1 to 3 cm per 1,000 years and pelagic clay at less than 1 cm per 1,000 years (Pinet, 2006; Bahlburg et al., 2012).

Type	Atlantic [%]	Pacific [%]	Indic [%]	Global [%]
Foraminefera ooze ($CaCO_3$)	65	36	54	47
Pteropod ooze ($CaCO_3$)	2	0.1	-	0.5
Diatoms ooze (SiO_2)	7	10	20	12
Radiolarian ooze (SiO_2)	-	5	0.5	3
Pelagic clay	26	49	25	38

Table 2.4: Composition of pelagic sediments of the oceans. (Pinet, 2006)

2.2 Principles of underwater acoustics

Detailed maps of the seafloor morphology and its features are very important as they provide significant help for the understanding of local geophysical and geological processes of the ocean. Hydroacoustic systems like echsounders are used for highly accurate water depth determination. This section describes the principles of multibeam echosounders and backscatter theory.

2.2.1 Principles of multibeam echosounders

Multibeam echosounders (MBES) are an extension of single-beam echosounders (SBES) that only transmit one single vertical beam towards the seafloor for determining the water depth. A MBES transmits a fan of up to a several hundred beams to the seabed. This way a large number of simultaneous depth measurements in a wide stripe along the ship track can be recorded. The width of the individual beams is commonly around 1° to 2° (along-track and across-track aperture). The aperture angle of the fan varies according to the different systems between approximately 120° and 210°. An opening angle of 150° results in a width of the ensonified stripe of 7.5 times the water depth. Compared to a SBES the coverage is much improved and thus increases the efficiency (Lurton, 2010). In Fig. 2.7 the acquisition geometry of a MBES is illustrated.
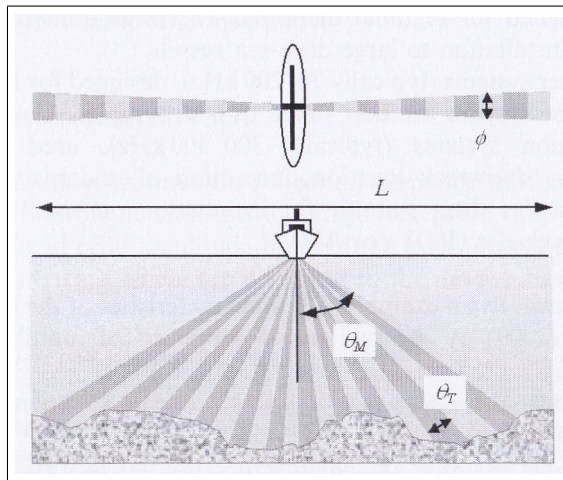
Figure 2.7: Multibeam echosounder geometry: swath width L, along-track aperture ϕ, across-track aperture θ_T and maximum beam tilt angle (fan aperture angle) θ_M. (Lurton, 2010)

The frequency of MBES is usually low for deep-sea systems (12 kHz to 30 kHz) and high for shallow-water systems (240 kHz to 500 kHz). At low frequencies the attenuation in the water column is lower, so that a greater water depth can be reached. Generally, the transducer of deep-water systems consists of two arrays: one transmission array for transmitting the acoustic signal and one reception array for receiving it. Due to their size and weight, they are mounted in the hull of the ship. The transmitting unit is oriented along the ship axis and is responsible for the along-track resolution, whereas the receiving unit is oriented across the ship axis and imposes the across-track resolution. The resulting product determines the final resolution (Lurton, 2010).
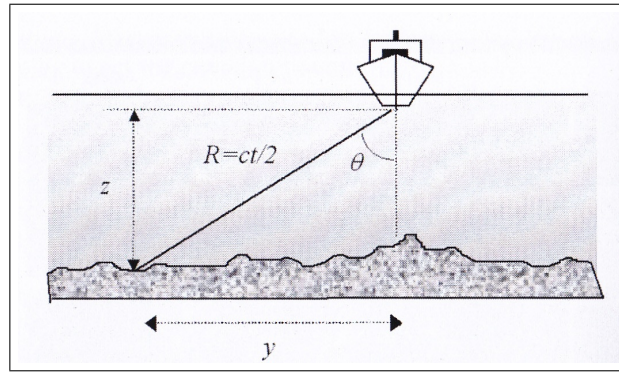
Figure 2.8: Depth measurement by time and angle measurements. (Lurton, 2010)

Most transmitters employ the piezoelectric effect to transform an electronic signal into a mechanical one and radiate it as an acoustic impulse into the water column. After being reflected by the seafloor, the acoustic impulse is received by the reception unit and transformed back into an electronic signal. The echosounder system measures the time between transmission and reception. Using this measurement of the two-way travel time t, the water sound velocity c, and the incident angle θ, the water depth at a certain location from the transducer (y, z) can be calculated by following formulas (Lurton, 2010):

$$y = R \sin \theta = \frac{ct}{2} \sin \theta \tag{2.2}$$

$$z = R \cos \theta = \frac{ct}{2} \cos \theta \tag{2.3}$$

These formulas are simplifications as they assume a constant water sound velocity throughout the water column. Usually this is not the case. The acoustic path is therefore not a straight line but tilted due to refraction effects. If this is taken into account, the formulas become more complicated (Lurton, 2010).

The MBES has to import and process data of other ancillary systems to ensure high quality depth measurements. The geodetic position of the ship is determined by a positioning system, commonly Global Positioning System (GPS). By using the formulas Eq. 2.2 and Eq. 2.3 the time measurement and resulting depth measurement can be transformed from the local ship coordinate system into a global geographical coordinate system. The accuracy of positioning depends on the mode: GPS, Differential GPS (DGPS), or high accuracy Real Time Kinematic (RTK) with real time corrections. For deep-water applications the accuracies of GPS (5 to 10 m) or DGPS (2 m) are sufficient. For further reading on satellite navigation refer to Bauer (2002) or (Leick, 2004).

Another important sensor is the motion sensor for detecting the movements (heading, roll, and pitch) of the platform. This information is forwarded to the echosounder. By slightly changing the transmission times and accounting for different reception times for the individual sections of the array, the ship motion can be compensated in real-time.

A further important factor influencing the recording of high-quality data is the knowledge of the accurate sound velocity in water. Sound velocity profiles should be carried out in regular intervals in dependence of the water mass changes in the investigation area to ensure a correct calculation of the acoustic paths between the echosounder and the seafloor and therefore the determination of the water depth. Considering all these factors, the vertical accuracy of multibeam sounders is in practice better than 1 % of the water depth (Lurton, 2010).

MBES do not only measure water depth but also acquire the seabed reflectivity similar to sidescan sonars. This information of the backscattered intensity can be used for various applications (e.g., seabed image creation, object detection, or derivation of physical seafloor properties). The acquired seafloor response is sampled in time. As the topography of the seafloor is known from the conducted depth measurements, the position of the intensity values can be estimated. First, the center point of a beam is positioned on the swath before the adjacent intensity values are placed around it until reaching the boundary of the neighboring beam (Fig. 2.9). The depths at the center points are known, and for the intermediate points the depth values are interpolated. This recombining of the time signal is done image line by image line, which have a width equivalent to the swath. The geometrical distortion is smaller than in sidescan images (Lurton, 2010).
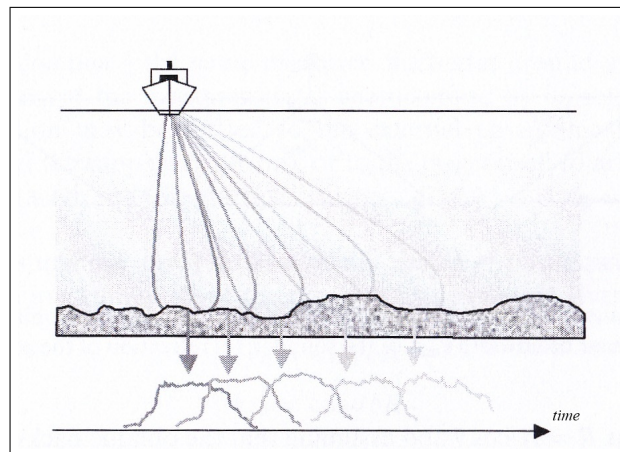
Figure 2.9: Formation of a sonar image. (Lurton, 2010)

2.2.2 Principles of backscatter theory

Multibeam echosounders transmit a large number of beams in different grazing angles. In Fig. 2.10 (top) the terms of grazing and incident angle are depicted. A transmitted sound wave travels through water by displacement of water particles. Water has a low acoustic impedance (product of density and sound velocity), which results in a low resistance to the propagation of the acoustic wave. The seafloor in comparison has a high impedance and does not permit the undisturbed propagation of the sound wave as the particles are more densely packed and therefore do not move easily. Since the total energy needs to be maintained, the obstructed energy is radiated back into the water. In Fig. 2.10 (bottom) the three different processes that can occur when a slanted beam reaches the seafloor

are depicted: A part of the incident wave is reflected in symmetrical direction (specular reflection), a part is scattered in all directions, and another part penetrates the seabed, where it travels in another direction due to refraction. The scattering of the acoustic energy back towards the sonar is called backscatter. This backscattered energy is received by the echosounder and used for depth and intensity measurements (Lurton, 2010).
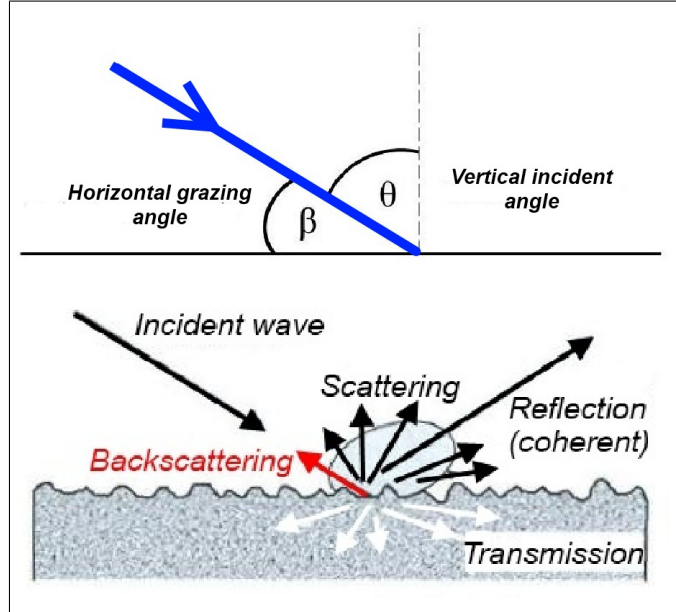
Figure 2.10: Horizontal grazing angle and incident angle (top) and reflection, transmission, and scattering of an incident wave by the seafloor (bottom) (Lurton, 2010).

The intensity of the received echo (echo level EL) depends on the transmitted source level SL, the transmission loss TL and the target strength TS. Their relation to each other is given by the sonar equation:

$$EL = SL - 2TL + TS \tag{2.4}$$

The transmission loss is applied twice due to the two-way travel distance from the transducer to the target and back again. It is caused by spherical spreading of the signal and its attenuation in the water column:

$$2TL = 2\alpha R + 40 \log R \tag{2.5}$$

where R is the slant-range and α the absorption coefficient. The target strength (in dB) is defined as the ratio between the backscattered intensity I_{bs} and the incident intensity I_i:

$$TS = 10 \log \frac{I_{bs}}{I_i} \tag{2.6}$$

The target behaves as a secondary source when re-transmitting the signal. In the context of MBES, target is the seafloor. The target strength is the logarithmic expression for the backscattering cross-section and can be decomposed into two

parts: the backscattering strength for a unit of surface BS in dB/m^2 and the actual ensonified area at the seafloor (backscattering area) BA:

$$TS = BS + 10\log(BA) \tag{2.7}$$

At a vertical incidence of $\theta = 0°$, the backscattering area depends on the along-track aperture ψ_x, the across-track aperture ψ_y at vertical incidence and the slant-range R. In other directions than $\theta = 0°$ the backscattering area depends on the transmit pulse length τ, the along-track resolution ψ_x, the sound velocity c, and the slant-range R (Hammerstad, 2000):

$$BA = \psi_x \psi_y R^2 \qquad \text{for } \theta = 0° \tag{2.8}$$

$$BA = \frac{c\tau}{2\sin\theta}\psi_x R \qquad \text{for } \theta > 0° \tag{2.9}$$

The backscatter strength for a unit of surface represents the bottom reflectivity. It is often referred to as backscatter coefficient, scattering cross section per unit solid angle per unit area of scattering surface, or scattering cross section. It can be expressed as (Jackson et al., 1986):

$$BS = \frac{R^2 I_S}{I_O A} \tag{2.10}$$

where R is the slant-range, I_S is the scattered intensity, I_O the incident intensity, and A the ensonified area. BS is dimensionless and therefore independent of the employed unit system. The backscatter strength is the quantity most often used in literature and is defined as the dB-value of the backscatter strength for a unit of surface and does not reference to a unit of length (Jackson et al., 1986):

$$\text{Backscatter strength} = 10\log BS \tag{2.11}$$

The backscatter strength varies in dependence of the seafloor characteristics and the incidence angle. The returned energy is inversely proportional to the incidence angle: The returned energy will be high at small and low at large incident angles. Lambert's law is a widely used approximation for the backscatter coefficients in practice (Lurton, 2010):

$$BS = BS_0 + 10\log\cos\theta \tag{2.12}$$

BS_0 is the mean backscatter coefficient (mean unit backscatter strength). The upper limit can be defined as around -5 dB/m^2 (Lurton, 2010). Practical observed values for BS$_0$ range between -10 and -40 dB/m^2.

The backscatter strength of the seafloor does not only depend on the characteristics of the incident signal (angle, frequency), but also on the physical nature of the seafloor (e.g., structure, roughness) and its intrinsic structure (Lurton, 2010). These three factors and their influence on the scattering field are shown in Fig. 2.11.

The upper example in Fig. 2.11 illustrates the dependence of the local geometry on the backscatter strength. A slope facing towards the acoustic source, or a large grazing angle, will produce a stronger backscatter signal than a slope facing
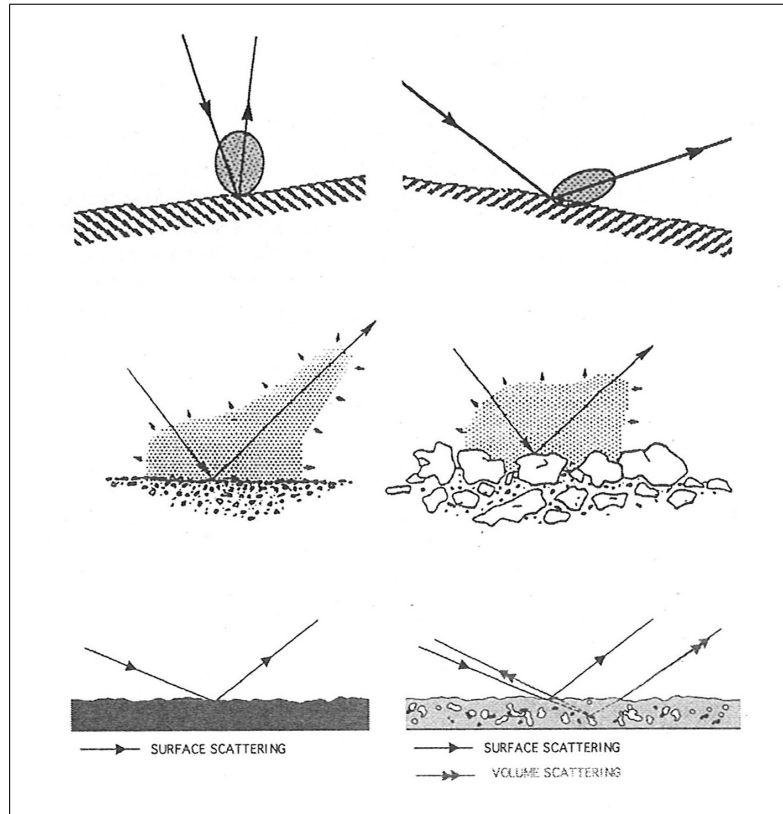
Figure 2.11: Backscattering from the seafloor is influenced by three factors (from top to bottom): local geometry of ensonification, roughness of the seafloor at scales comparable to the sonar's wavelength, intrinsic properties of the seafloor (e.g., rocks vs. sediments) (Blondel et al., 1997)

away of the source, or a small grazing angle. The example in the middle shows the effect of the seafloor roughness. A smooth surface will mostly scatter along the specular direction, which results in a very low backscatter. At a perfectly flat and homogeneous seafloor, no scattering but only reflection would occur. In comparison, a rough surface scatters more strongly in direction of the source. The bottom example shows the impact of heterogeneities in the sediment on the backscatter strength.

Two sources for scattering at the seafloor are distinguished according to Ivakin (1998): surface (or interface) scattering and volume scattering.

Surface scattering results from the microscale roughness of the seafloor. The term "microscale roughness" applies to seafloor irregularities that are comparable in size with acoustic wavelengths. The effect of roughness depends on the signal's frequency, the incident angle, and the local characteristics of roughness. Close to the vertical incident direction, the acoustic wave is reflected in specular direction. This is possible due to facets, which are oriented in a way, that they allow for signal reflection in specular direction. When the incident angle increases, the number of right oriented facets decreases and therefore the level of facet backscattering. At grazing incidences, backscattering by microscale roughness (Bragg regime) dominates. The backscattering field in direction of the incoming signal is created by a continuum of contributions of points along the seabed whose

returned signals are in phase. In Fig. 2.12 (left) a graph of the backscattering strength in dependence of the incident angle is plotted. It shows that in the nadir area the facet regime is dominant, whereas the Bragg regime dominates when the incident angle is more oblique. The backscatter strength does not only depend on the angle but also on the surface roughness, which is shown in Fig. 2.12 (right). With increasing roughness, the level of the Bragg regime increases and the level of the facets regime decreases. Furthermore, the angular extent of the facets regime increases (Lurton, 2010).

The impedance is the product of sound velocity and density of the medium. The larger the impedance contrast between water and seabed, the more energy is reflected or scattered and the less energy penetrates into the seafloor. The impedance of a seabed depends on the sediment grain size and can be correlated to the roughness. If the grain size of the seabed increases, the impedance and therefore its roughness increases as well. This results in a lower level of the facet regime with a larger angular extent in the angular response (Masetti et al., 2011).
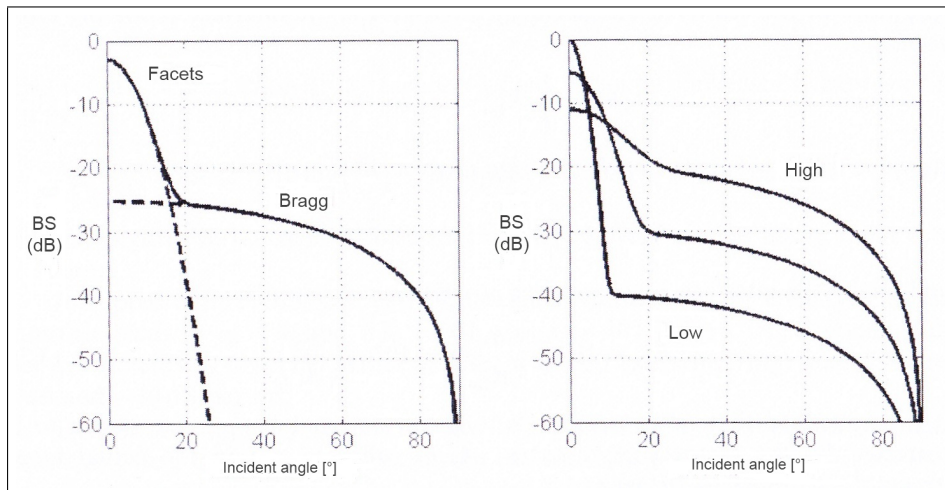
Figure 2.12: Idealized backscattering strength as a function of the incident angle. Facets and Bragg regime (left) and influence of roughness (right). (Lurton, 2010)

The *volume scattering* depends on the heterogeneities in the sediments. It affects the part of the signal that penetrates the seabed. The strength of seafloor penetration depends on the frequency (lower frequency results in deeper penetration) and on the impedance contrast (lower impedance contrast results in deeper penetration) of the seabed. When the signal penetrates the seafloor, refraction, absorption, and scattering processes occur in dependence of the sediment composition. Volume scattering becomes dominant at increasing incident angles (Lurton, 2010).

Chapter 3

Data acquisition and processing

3.1 Overview of the investigation area

The data for this thesis was collected on the RV Sonne cruise SO213 leg 1 (SO213-1). The expedition started from Valparaiso (Chile) on December 27, 2010 and ended in Valparaiso on January 12, 2011. The profiles used for backscatter analysis were recorded on January 7-8, 2011.
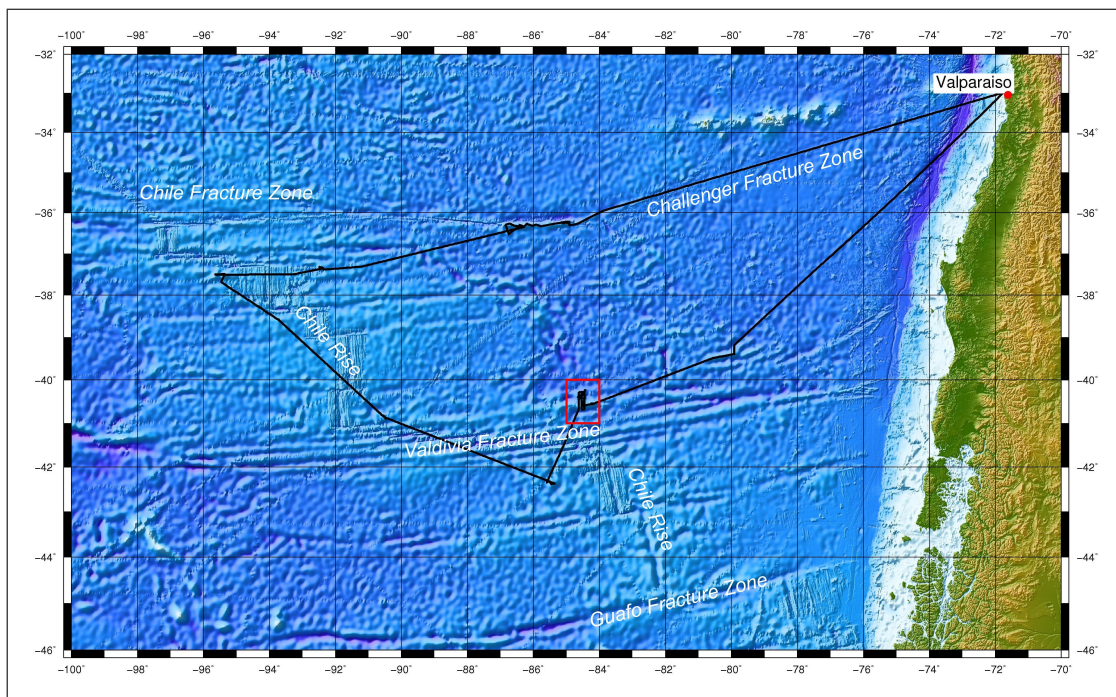
Figure 3.1: Ship track of RV Sonne cruise SO213-1. The investigation area is highlighted in red. [Mercator projection, standard parallel: 39°S, global dataset: GEBCO 2008 (30 arc-seconds)].

The cruise was organized by the Alfred Wegener Institute for Polar and Marine Research (Bremerhaven) and the IFM-Geomar (Kiel) and was the first of two associated expeditions for geological and geophysical research in the South Pacific. The chief scientist was Prof. Dr. Ralf Tiedemann. The cruise was part of the project SOPATRA (South Pacific Transects), which was funded by the German Federal Ministry of Education and Research. The aim of the cruise was to collect

geological and geophysical datasets to reconstruct atmospheric-oceanographic circulation patterns of the South Pacific and thus improve of the understanding of climate processes and their causes and effects (Tiedemann, 2011).
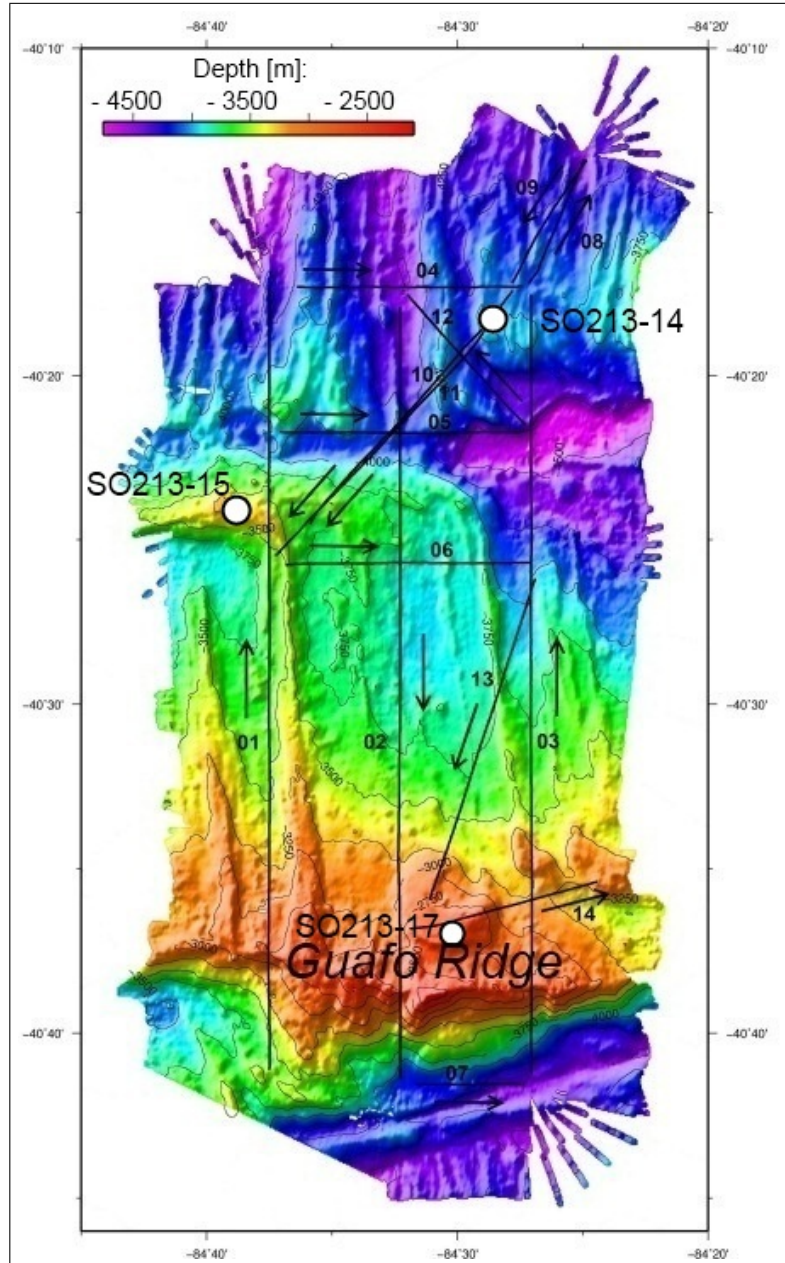
Figure 3.2: Multibeam (MBES) data and locations of surface sediment samples (white dots). The profiles used for backscatter analysis (black lines) are depicted as well as their direction of recording and their numeration. (Mercator projection, standard parallel: 40° 28' S) [App. A, Fig. A.1]

During SO213-1, the multibeam echosounder (MBES) Simrad EM 120 from Kongsberg was continuously acquiring depth measurements outside the Chilean exclusive economic zone. A systematic recording of a 1,325 km² (53 x 25 km²) large area was conducted and was analyzed for backscatter in this thesis. The area of investigation lies roughly 950 km west of the Chilean coast and 750 km south of Valparaiso. The water depths range from 2,091 m to 4,778 m. The

acquisition time of the analyzed data was around 14 hours and 45 minutes. Fig. 3.2 shows a bathymetric chart of the investigation area generated with GMT (Generic Mapping Tool). To view this chart in a larger scale, refer to Fig. A.1 in the Appendix A. The ridge in the south of the surveyed area was named "Guafo Ridge" after the Guafo Island off Chile based on the conducted depth soundings during SO213-1. The locations of recovered sediment samples are marked by white dots in the figure. They are used in this thesis for grain size measurements (Section 3.5.1) and for ground-truthing in the backscatter analysis. This area was chosen for backscatter analysis due to the variation in depth and therefore its probable variation of sediment grain sizes.

The survey area can be divided into three major parts by bathymetry. The northern part is the deepest area (approximately from 4,700 m to 3,000 m water depth) and shows linear structures (lobes/folds) oriented in north-south direction. The southern margin of this part is defined by an east-west oriented fault that has an average width of 2 to 3 km. Its depth ranges compared to the surrounding terrain between nearly 500 m in the east to 200 m in the west. The following part in southern direction is the intermediate bathymetric part. It has a medium water depth (around 3,600 m) which becomes shallower farther south. Lobes of 200 m to 300 m average height cross this intermediate area in north-south direction. These lobes originate at the peak of the Guafo Ridge and decrease in height and width into northern direction. The southern part is dominated by the Guafo Ridge. Its northern slope is relatively gentle when developing from the bathymetric rise of the intermediate survey area. The southern slope of the Guafo Ridge is very steep: the water depth increases from 2,200 m to 4,500 m over a distance of about 6,000 m.

The track planning for data acquisition was done using the global dataset of GEBCO 2008[4] with a resolution of 30 arc-seconds. The aim was to collect the MBES data in parallel profiles with the adjacent ones in the opposite direction. Additionally, some cross profiles were recorded. Due to the search for coring locations and ship time limitation, the final profiles differ slightly from the planned ones: Profiles 4 to 6 could only be recorded in the same direction and not as planned in reverse direction. But additionally diagonal profiles (10 and 11) could be added. Fig. 3.2 shows the final profiles as well as their direction of recording and their numeration. The corresponding acquisition times and length of survey profiles are listed in App. B, Tab. B.1. The fan aperture angle had to be adjusted during data acquisition due to strong changes in bathymetry. The ship speed was approximately 10 knots.

---

[4]GEBCO Digital Atlas. Reference: IOC, IHO, and BODC, 1994, 'Supporting Volume to the GEBCO Digital Atlas', published on behalf of the Intergovernmental Oceanographic Commission (of UNESCO) and the International Hydrographic Organization as part to the General Bathymetric Chart of the Oceans (GEBCO); British Oceanographic Data Centre, Birkenhead.

3.2 Hydrographic data acquisition

3.2.1 Research Vessel Sonne

The German research vessel Sonne was built in 1969 at the Rickmers shipyard in Bremerhaven. It was first used by the *Hochseefischerei Nordsee* for fishery. In 1977 Sonne was purchased by the *RF Forschungsschifffahrt GmbH* and rebuild to a research vessel. A second large modification took place in 1991 when the vessel was lengthened by 10.8 m and received an additional deck and new machinery. Today, RV Sonne has a length of 97.61 m and a width of 14.2 m. It has room for 25 scientists and 25 crew members for up to 50 days on sea. Expeditions are coordinated by the *German Federal Institute for Geoscience and Natural Resources (Bundesanstalt für Geowissenschaften und Rohstoffe - BGR)* in Hannover (BGR, 2012).

Figure 3.3: Research Vessel Sonne. (www.marum.de)

3.2.2 Multibeam echosounder Kongsberg Simrad EM 120

The multibeam echosounder Simrad EM 120 of Kongsberg was installed on RV Sonne in 2001. It is a deep-sea system which allows measurements up to a water depth of 12,000 m with a nominal sonar frequency of 12 kHz for bathymetric mapping. Two linear transducer arrays for transmitting and receiving the acoustic signal are the basic components of the system. They are mounted in the ship's hull and have dimensions of 4.02 m x 0.78 m and 3.60 m x 0.42 m. The transducer arrays are split in sectors with independent active steering to allow compensation for ship motion. A frequency range from 11.25 to 12.75 kHz is used to code the different transmit sectors. The fan consists of 191 beams with a width of 2° x 2°. The fan aperture angle can be set up to 150° allowing a theoretical seafloor coverage of up to 7.5 times the water depth. A swath width of around 20 km is generally achievable in deep water areas, depending on bottom conditions (Kongsberg, 1999). In Fig. 3.4 (left) the reachable swath width according to the seafloor type is shown.

In deep waters, a pulse length of 15 ms is used. The ping rate depends on the water depth and and amounts to 5 Hz (Kongsberg, 1999) in deep areas. The beam spacing can be set to "equidistant" or "equiangle". For the acquisition of multibeam during SO213-1 the mode was set to "equidistant" to ensure an uniform sampling of the seafloor in across-track direction. In Tab. 3.1 the technical specifications of the EM 120 are listed.
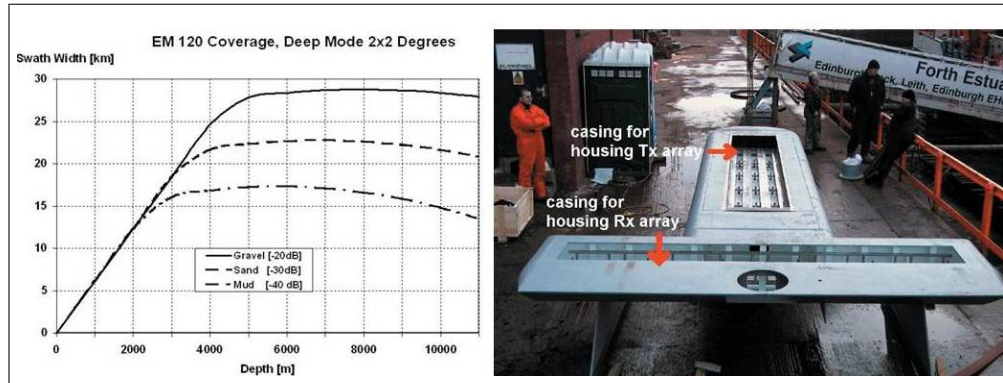
Figure 3.4: Achievable swath width as a function of the seafloor type (left) (Kongsberg, 1999) and picture of the casing for EM 120 transducer arrays (Kongsberg, 2005) (right).

Frequency	12 kHz
Maximum Ping Rate	5 Hz
Number of Beams per Ping	191
Beam Width	2°x2°
Beam Spacing	Equidistant and Equiangle
Coverage sector	Up to 150°
Depth Range	20 to 11,000 m
Pulse length	2.5 to 15 ms
Range Sampling Rate	2 kHz (37 cm)

Table 3.1: Technical specifications of Simrad EM 120. (Kongsberg, 1999)

For data acquisition on RV Sonne, the software SIS (Seafloor Information System) developed by Kongsberg was used. SIS allows a screen layout with up to seven simultaneous display windows for monitoring the acquired data in real time.

The recorded data was stored in the Kongsberg *.all format. Every 30 minutes a new file was automatically generated by the system. A Kongsberg *.all format file consists of different datagrams (e.g., depth datagram, attitude datagram, SVP datagram, image datagram).

Backscatter values are stored in two different ways: First, the average of the sample amplitude values for each individual beam is saved in the depth datagram with a resolution of 0.5 dB, and second, the backscatter information is stored in the image datagram as time series of image reflectivity. This time series format is similar to the sidescan intensity format. One time series of backscatter strength is recorded around the detection point of each received beam (Hammerstad, 2000). In the investigation area the number of pixels in the image datagram varies roughly between 3,800 and 4,500 pixels per ping. The resolution of the time series format is therefore much higher compared to the resolution of the beam average format. An extract of a raw file with the datagrams is shown in App. B, Fig. B.1.

3.2.3 Sub-bottom profiler Parasound P70

Sub-bottom profilers (or sediment profilers) are used for the investigation of the upper sediment layers of the seafloor. Different sediment types have different acoustic reflectivity. Sediments with larger grain size depict strong reflections in comparison to finer sediments or sediments with larger water content. Layers with diverse acoustic properties can therefore be displayed in echograms, which are used to obtain information about the composition of the upper seafloor sediment layers (Fig. 3.5). Sub-bottom profilers are single-beam echosouders and employ a lower frequency than echosounders for a higher seafloor penetration.
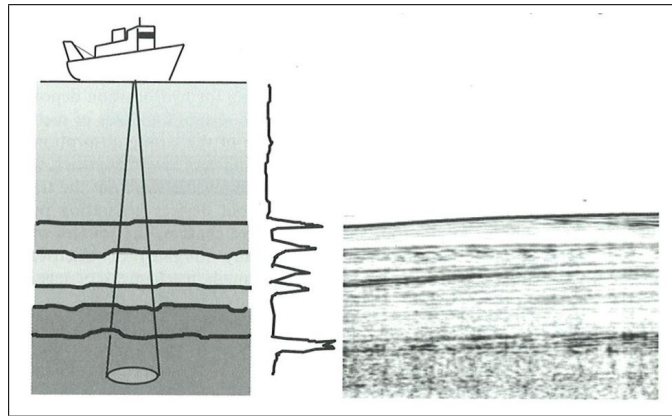
Figure 3.5: Schematic depiction of the functionality of a sub-bottom profiler. The signal penetrates into the seafloor and ensonifies the sediment layers (left). The returned time-domain signal for the echo (middle) is depicted as cross-section of the seafloor in the echogram (right). (Lurton, 2010)

On RV Sonne the sub-bottom profiler Parasound P70 of Atlas Hydrographic GmbH is mounted. This echosouder system utilizes the parametric effect to generate a low-frequency signal and therefore combines the advantages of a high- and low-frequency domain. As the signal is modulated of two high-frequency signals, a smaller aperture angle (about 4° instead of 20°) and therefore a better horizontal resolution is achieved. One of the two primary frequencies is fixed to 18 kHz whereas the second one can be adjusted between 20.5 kHz and 23.5 kHz. Thus, the resulting frequency can vary between 2.5 kHz and 5.5 kHz. Usually a signal of 4 kHz is used, which achieves a seafloor penetration of up to 200 m with a vertical resolution of 30 cm in ideal conditions (Atlas Hydrographic GmbH, 2012). In Tab. 3.2 the technical specifications of Parasound P70 are listed.

Frequency	$0.5 - 6$ kHz
Depth Range	10 to 11,000 m
Max. Depth Penetration	200 m
Aperture Angle	4.5° x 5° (depending on frequency)

Table 3.2: Technical specifications of Parasound P70. (Atlas Hydrographic GmbH, 2012)

3.2.4 Positioning and motion compensation

RV Sonne operates a number of GPS navigation receivers, including an Ashtech GG24, an Ashtech Z-Sensor, and a Trimble 4000DS. The data from each GPS receiver is logged independently in the ship's database. One receiver (usually Ashtech GG24) is manually selected as *system GPS* that provides the scientific equipment onboard (including the EM 120) with navigational input. The positioning accuracy is around 5 m (BGR, 2009). Differential GPS is also available on RV Sonne, but needs to be specifically requested in the planning phase of the cruise and is only available at large expenses. It was not used during SO213-1.

For motion compensation a Kongsberg Seatex MRU 5 is used. It contains three axis angular rate sensors and three axis acceleration sensors to detect the roll, pitch and heave movements of the vessel. The motion reference unit (MRU) imports speed and heading data from other ship-mounted sensors to improve quality. By taking external measurements of a speed log and a gyro compass into account, the roll, pitch and heave measurement drift caused by turning and acceleration of the ship can be eliminated. The accuracy of the MRU is 0.03° root mean square at a ±5° amplitude (Kongsberg, 2006).

3.2.5 Sound velocity profile

Water sound velocity profiles were acquired through CTD (Conductivity, Temperature, Depth) measurements during SO213-1. The probe is lowered to the seafloor and measures the temperature, conductivity (salinity), and pressure at regular depth intervals. Additionally, open tubes are mounted around the sensors. When the instrument is lifted back up through the water column, the tubes can be closed at different water depths to obtain water samples. These samples can be used for further chemical or biological analysis.
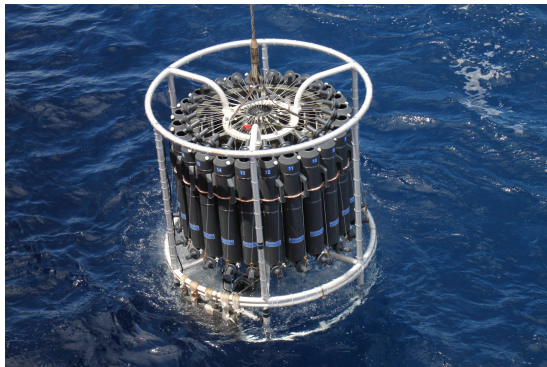
Figure 3.6: CTD probe with mounted tubes for water sampling. (Picture by T. Ronge, AWI)

Sound velocity profiles were generated (in *.asvp format) from CDT measurement using Kongsberg software. This information was employed by the echosounder to ensure high quality depth measurements.

The CTD profile that was used during the data acquisition for this thesis was SO213-12-3. It was conducted on January 6, 2011 around 5 pm UTC at a distance of 100 nm from the investigation area.

In the upper meters of the water column, measurements of water properties are disturbed due to the closeness to the ship and mixture of water layers resulting from veering and heaving of the probe during its deployment. Therefore a velocity probe is installed on RV Sonne close to the transducer arrays. This probe measures the sound velocity of the upper water layer in real time and forwards it to the system to improve beam forming.

3.3 Hydrographic data processing

Multibeam echosounder data is subject to diverse errors, which can be either random or systematical. To exclude systematical errors and to ensure high data quality, a calibration of the system, the measurement of the water sound velocity profile in regular intervals, and the monitoring of the data acquisition are important. In Schenke (1992) possible error sources are listed:

- Roll and pitch compensation error

- Gyro or bearing error

- Positioning error

- Height error

- Omega effect

  – The side echo of a beam is received before the actual echo reaches the receiver, therefore the actual depth is assumed to be shallower. The omega effect can occur at slanted flanks.

- Tunnel effect

  – The echo of an inner beam is received earlier than the actual outer beam and therefore processed instead. This leads to an underestimation of depth at the outer beams position.

- Interferences with ship noise or other hydroacoustic systems

- Backscatter characteristics of the seafloor

- Error of the refraction correction through usage of a wrong water sound velocity profile

Not all of these error sources can be eliminated completely. Therefore the data needs to be examined carefully and corrected if necessary before further processing can take place. This accounts especially for random errors as they cannot be influenced during the data acquisition.

The bathymetric data post processing was done in *CARIS HIPS and SIPS 7.1*. After importing the raw data format and converting it into the *CARIS HDCS* structure, the navigation data was examined for errors. *CARIS* provides a *Navigation Editor* (Fig. 3.7, top) for this purpose, where each recorded position, speed, distance and "course made good" are displayed. Depending on the detected error, the wrong value can be deleted with interpolation of the adjacent measurements or deleted without interpolation. Errors in navigation were only found occasionally in the data of this thesis. Outliers were deleted with interpolation as the data was recorded in straight profiles and thus an interpolation did not change the track geometry.
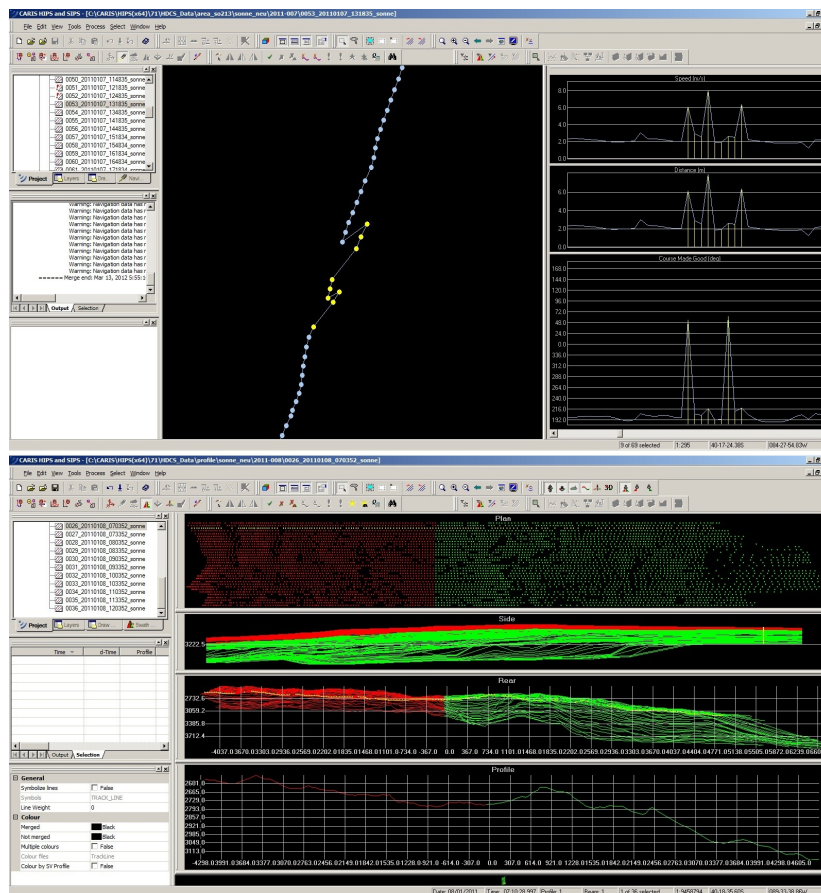
Figure 3.7: Navigation Editor (top) and Swath Editor (right) of *CARIS HIPS and SIPS*.

The depth measurements where examined in the *Swath Editor* (Fig. 3.7, bottom). It allows different viewing angles of the data for error detection: plan, rear, profile and side view. This way, gross errors could be eliminated. After examining the data for errors, a BASE ((Bathymetry Associated with Statistical Error)) surface was created (App. A, Fig. A.2) to check the processing result for missed blunders.

3.4 Digital modeling of bathymetric data

A digital terrain model (DTM) is "[...] a statistical representation of the continuous surface of the ground by a large number of selected points with known X, Y and Z coordinates in an arbitrary coordinate field." (Miller et al., 1958). The sources of DTMs are measurement points. By using perspective views and shadings of a DTM, geomorphological structures in the dataset can be interpreted more easily.

There are different methods for DTM creation like triangulation or raster (irregular or regular) by interpolation or statistical computation (De Smith et al., 2009). In this thesis the irregular distributed soundings were interpolated in a regular raster grid for representation of the survey area.

Raster data consists of regular arranged rows and columns of grid cells. Each grid cell stores one value, which represents the height of the terrain (i.e., water depth). The value of each cell is calculated from a number of measurement points. Not all relevant soundings contribute equally as their influence on the computed raster cell value is usually weighted. With the *Inverse Distance Weighted* approach, the weights decrease with increasing distance to the grid node. This method is used by the software *Fledermaus* and *CARIS*. *CARIS* also uses an additional approach based on the swath angle: The weight depends on the angle of incidence on the seafloor. Sounding collected with a large grazing angle have a higher weight than soundings from a low grazing angle (CARIS, 2012a). The open source software GMT, which was also used for visualization of the bathymetry in this thesis, uses continuous curvature splines with a tension parameter for modeling the terrain.

When modeling a surface as a regular grid, the cell size is an important parameter. It depends on the density of data points and the morphology of the terrain. The smaller the cell size, the higher the resolution of the resulting grid. If the resolution is chosen too small, aliasing[5] can distort the resulting image. When the cell size is chosen too large, small structures can be lost. To determine a cell size suitable for the DTM of the investigation area, the spatial resolution of the measured data on the seafloor should be examined carefully.

3.4.1 Quality considerations related to spatial resolution

The area of ensonification of a beam (footprint) depends on the water depth, the beam opening angle, and the incident angle. Regarding the recorded soundings during SO213-1, the diameter of an ensonified area of a nadir beam is around 120 m in average (87 m in a water depth of 2,500 m and 157 m in a water depth of 4,500 m). The footprint of outer beams is about 450 m and therefore larger due to the measurement geometry.

The spatial resolution of the data points can be calculated by using the echosouder characteristics, the water depth, and the ship's speed. In this context one has

---

[5]step-like offset of linear features

to differentiate between the spatial resolution in travel direction and the spatial resolution perpendicular to the direction of travel.

3.4.1.1 Spatial resolution of data points in along-track direction

The density of data points in along-track direction depends on the duration between two measurements (ping rate) and the speed of the vessel. The ping rate depends on the water depth. The Simrad EM 120 has a maximum ping rate of 5 Hz. When examining the recorded data a ping was received by the sonar every 14 seconds. The speed of the vessel during data acquisition was 10 knots or 5.14 m/s. When using the formula

$$P_a = v \cdot t \tag{3.1}$$

with the speed v and the time t between two measurements, the distance of data points in direction of travel P_a can be calculated. Using the above derived mean values for the speed and data rate, the distance between depth measurements in along-track direction is 72 m. The average footprint in the investigation area is 120 m for nadir beams. The footprints on the seafloor therefore overlap by approximately > 40 %.

3.4.1.2 Spatial resolution of data points in across-track direction

Each beam has an beam angle of 2° x 2°, yet the angle of radiation depends on the fan aperture angle and the water depth. During data acquisition, the opening angle had to be adjusted according to seafloor topography. It varies between 110° in depths of $\geq$ 3,500 m and 130° in water depths $<$ 3,000 m.

Assuming a water depth of 4,500 m and an average aperture angle of 110°, the width of the swath would be 12,853 m. At a depth of 2,500 m and a swath angle of 130°, the ensonified area in across-track direction would be 10,723 m. The mean swath width on the seafloor is therefore 11,800 m. This calculated mean value for the swath width coincides very well with observations made during monitoring the data acquisition. When dividing the average swath width by 191 beams, a rough estimate for the distance between the measurement points (between the midpoints of their footprint) in across–track direction yields 62 m (overlap of around 50 %). This is similar to the value of data point resolution in along-track direction.

3.4.2 Visualization in GMT

The overview maps of the acquired multibeam data were created using GMT (Generic Mapping Tools). GMT is an open source collection of tools for processing and visualizing geographical data. The tools include options for filtering, gridding, rastering, or displaying the dataset. The used programs in GMT are listed in the following with descriptions according to Wessel et al. (2012). The order of description is inherited by their succession in execution.

- gmtconvert: converts the xyz ascii-format into binary format.

- blockmean: filters the data to avoid aliasing.

- surface: grids the filtered data by using a curvature surface (spline) algorithm (resolution: 74 m, tension parameter: 0.35).

- grdmask: a mask-grid file is created, where the grid values outside the dataset are set to NaN (Not a Number) and all other to 0.

- grdmath: the mask-grid file is added to the original grid file. The result is a new grid with values only in the area of the dataset.

- grdgradient: computes a directional derivative in a given direction (315°).

- grd2cpt: the boundaries of a chosen color palette (rainbow) are fitted to the grid file.

- grdimage: creates a colored map of the grid file.

- psbasemap: creates a chart of the data in postscript format (with frame, defined projection, scale bar, etc.).

These commands can be extended by commands for contouring (grdcontour) and for plotting the tracklines (psxy) for example. These command lines were brought together in a script for simplification of execution. The script is shown in App. B., Fig. B.2.

3.5 Sediment samples

3.5.1 Multicorer

The surface sediment samples, which were used in this thesis for ground-truthing of the backscatter data, were collected with a multicorer (MUC). With a MUC samples of the upper sediment layers and the sediment-water boundary can be recovered. It consists of a metal frame and an internal part of 12 vertical mounted tubes of a length of 30 cm (Fig. 3.8, a). It is lowered from the ship to the seafloor by a winch. When reaching the seafloor the outer frame is set on the floor and the inner part with the tubes is pushed into the upper sediments by a mounted weight. When the multicorer is lifted, the tubes are closed by shutters. Back on deck, the tubes filled with sediment and water can be taken off the instrument and into the laboratory for sampling (Fig. 3.8, b).

During SO213-1 each sediment sample was split into centimeter intervals and filled in labeled bags for further analysis back in the institute and archival storage. The multicorer samples were quick-frozen due to the particular analysis to be done by the geologists. The three samples used for ground-truthing in this thesis were taken from the uppermost centimeter representing the seabed surface. The locations of the samples are depicted in Fig. 3.2.
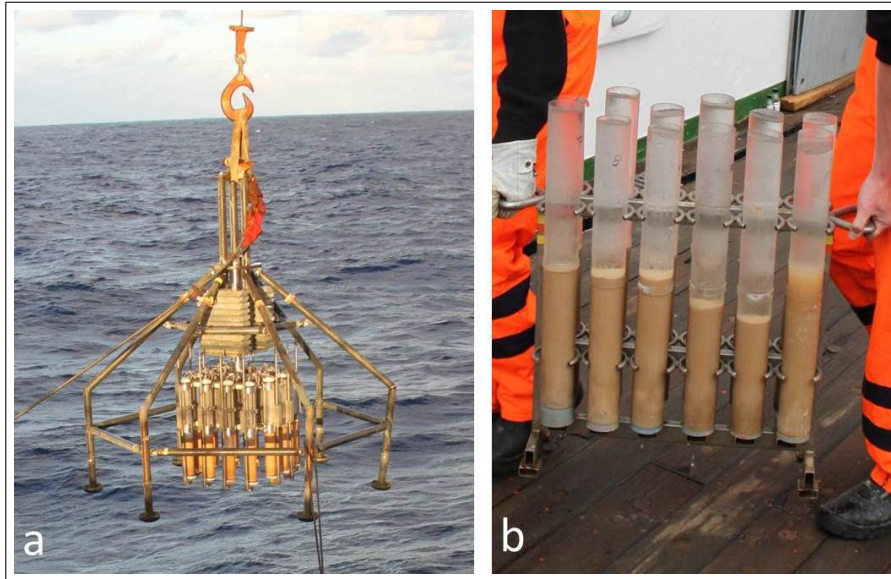
Figure 3.8: Multicorer is lifted back on deck (a) and filled tubes of the multi-corer (b). (Pictures by T. Ronge, AWI)

3.5.2 Grain size determination using a Laser Particle Sizer

3.5.2.1 Beckman Coulter LS 200

The Beckman Coulter Particle Sizer LS 200 from the MARUM (University of Bremen) was used for grain size measurement of the three sediment samples in the area of investigation. Fig. 3.9 shows a schematic view of the LS 200. The light source creates a monochromatic laser beam of 750 nm. The laser passes two different lenses to focus the beam and keep it at a constant intensity before it reaches the sample cell. In the sample cell the sediment solution is continuously pumped through the laser beam. The particles in the sediment solution scatter the laser light and generate unique angular scattering patterns. A Fourier lense focuses the beam, which is dispersed by particles in the sediment solution before it reaches a detector array. The results are given in volume percentage of 92 size classes ranging from 0.4 to 2,000 μm (MARUM, 2011).
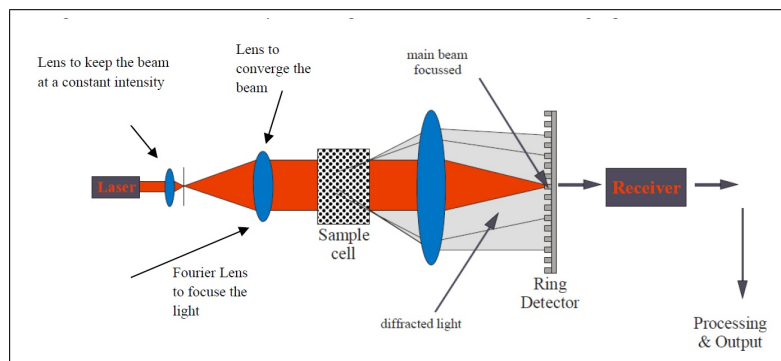
Figure 3.9: Schematic representation of a Beckman Coulter Particle Sizer LS 200. (MARUM, 2011)

3.5.2.2   Results of grain size determination

The sediment samples were dissolved in approximately 50 ml demi-water (mineral and gas-free water) to gain a 8 to 12 % solution. Salt sodium diphosphate was added to the solution to dissolve the flocculation caused by the quick-freezing. Each measurement was repeated four times to check for possible changes in the results. The results are presented in Tab. 3.3 and in Fig. 3.10. The horizontal axis of the graph shows the grain size in μm in logarithmic scale like commonly done in grain size distribution graphs.

	SO213-14	SO213-15	SO213-17
Water depth [m]:	4,050	3,246	2,561
Mean [μm]:	3.38	58.0	81.5
Median [μm]:	3.58	98.13	130.7
Grain size volume percent:	sand: 0	sand: 61.5	sand: 71.2
	silt: 46.6	silt: 27.4	silt: 21.2
	clay: 53.4	clay: 11.2	clay: 7.6

Table 3.3: Measured grain sizes for surface sediment samples.
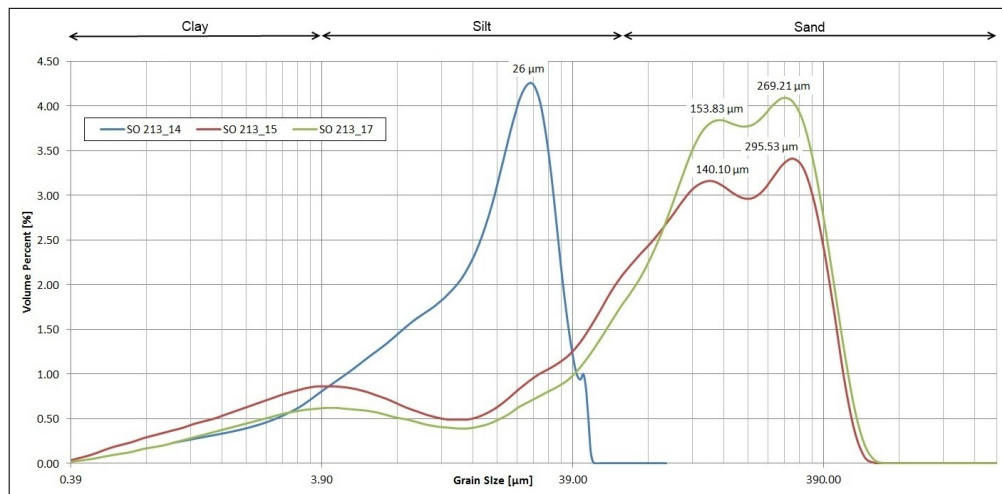
Figure 3.10: Grain size distribution of the recovered sediment samples measured with a Beckman Coulter LS 200.

3.5.3   Manganese nodules in MUC SO213-14

Manganese nodules consist mainly of manganese but also of metals like copper, cobalt and nickel. Especially the components copper and nickel are interesting from an economic point of view. The largest nodule field between the Clipperton and Clarion Fracture Zone in the North-East Pacific has a double average concentration of copper and nickel than the land based resources. Manganese nodules are mainly found in the Pacific and Indian Ocean in areas of water depths between 4,000 m and 6,000 m, where the sedimentation rate is very low (around 2 mm/1,000 years) or bottom currents prevent sedimentation. Their internal structure is very complex and their physical and chemical characteristics differ in

dependence of the location. Nodules found in areas of siliceous ooze for example show a particular large concentration of copper and nickel. Their growth rate lies around a few mm in 10^6 years. The average size of manganese nodules varies between 1 cm to 10 cm. Different processes are involved in the origin of manganese nodules: Metals are precipitated from the seawater, sediment or dissolved from submarine volcanoes (Halbach et al., 1988; Kennett, 1982).

In the retrieved sediment samples of multicorer station SO213-14 manganese nodules were found. Fig. 3.11 shows a photograph of a pattern representing the sampled area of the multicorer tubes and the manganese nodules lying on it. This demonstrates the density of the manganese nodules on the seafloor, which is estimated to be around 70%. The average size of the nodules is 2 x 3 cm^2 with a diameter ranging from 1 cm to 4 cm.

Figure 3.11: Picture of the manganese nodules obtained at SO213-14.

Chapter 4

Method

The implemented Geocoder in *CARIS HIPS and SIPS 7.1* and *Fledermaus 7.3* is used for backscatter processing and analysis in this thesis. This software includes possibilities for backscatter correction, mosaicing, and estimation of seafloor properties (e.g., grain size).

In the beginning of this chapter, the analogy to airborne remote sensing techniques is shortly elaborated. Afterwards, a description of the Simrad model, which is automatically applied by the EM 120 during data acquisition to the measured amplitudes, is given. Then the processing steps for multibeam backscatter data in Geocoder are explained. Section 4.4 deals with the implementation of Geocoder in *CARIS HIPS and SIPS* and the chosen parameter settings for the analysis of the collected dataset. Afterwards, in Section 4.5, the implementation of Geocoder in *Fledermaus* is pointed out as well as the applied parameter settings.

4.1 Analogy of backscatter processing to airborne remote sensing techniques

The remote acquisition of seafloor images by sidescan sonars or multibeam echosounders is similar to airborne remote sensing techniques for mapping the Earth's surface. Usually airplanes or satellites are used as platforms for the acquiring systems. A large variety of different sensors is employed in remote sensing, for example cameras, Lidar or Radar systems. Sidelooking Airborne Radar (SLAR) systems for example have a similar acquisition geometry to sonars. They are active sensors, transmitting electromagnetic radiation and receiving the backscattered signal in a very narrow but long angle perpendicular to the flight direction.

All remotely acquired digital data - whether of the Earth's surface or of the seafloor - needs to be processed to remove various distortions before it can be used for spatial interpretation or analysis. Generally, the digital imagery processing in remote sensing includes following corrections (Albertz, 2007):

Geometric rectification: Hardware and differences in the topographic heights are sources of geometric distortions. Images of linear-scanning sensors like Radars show a parallel projection in travel direction. The system measures the run time of the signal and therefore refers to slant-ranges. This results in distortions perpendicular to the flight direction in areas of height variations. Higher objects are shifted towards the nadir direction, because they are hit earlier by the wavefront. Geometric rectification includes the mapping of a two-dimensional image coordinate system into a global geodetic coordinate system by transformation and resampling. This process is also called georeferencing or geocoding.

Radiometric corrections / Image restoration: Radiometric corrections are applied to reduce the effects of perturbations during data acquisition and data transfer. Perturbations are caused for instance by the propagation medium (i.e., atmosphere or water). Problems in data transfer are often visible as white lines or false pixels in the data. Radiometric corrections concern only the pixel values of the image and do not change the geometry. Effects which are not object-specific are eliminated so that only the object information is visible in the resulting image.

Image enhancement: Image enhancement techniques increase the quality of an image for the human eye and thus improve it for a visual analysis. These techniques include contrast enhancement and filtering. The visual detail recognition in images can be improved by different filters. The most common are highpass filters and lowpass filters. Highpass filters emphasize sharp features like edges and therefore enhance the sharpness of images. Lowpass filter reduce the noise and have a smoothing effect.

Mosaicing: To obtain a map of a larger area than covered by one image, the individual images can be assembled to one large picture. This process is called mosaicing. The single components are linked together by distinctive points in overlapping areas. Afterwards a radiometric alignment of the different images can be applied to obtain a homogeneous mosaic.

Even though these airborne remote sensing methods differ from seafloor mapping systems in terms of signal's wavelength or acquisition geometry, the steps of digital image processing are very similar. For further information on remote sensing techniques and processing of aerial images refer to Albertz (2007), Luhmann (2003) or Jähne (2005).

4.2 Kongsberg TVG correction

The backscatter strength depends on seafloor characteristics and the incidence angle (Section 2.2.2): Coarser sediments return higher backscatter values than finer-grained sediments and when ensonifying a homogeneous seabed, the reflected energy will be high at small and low at large incidence angles (Fig. 4.1, left). The Simrad EM 120 of Kongsberg applies a model to eliminate this angular response signature during data acquisition automatically by employing a time varying gain (TVG). The result is a homogeneous intensity image of the seafloor in real time.

Depending on the incidence angle, a linear correction (nadir) or a correction after Lambert's Law (off nadir) is applied under the assumption of a flat seafloor (Fig. 4.1, middle). The crossover angle with the mean backscatter coefficient (BS_0) is set by Kongsberg to 25° by default. The values for backscatter coefficients at nadir (BS_N) and at oblique incidences (BS_0) are estimated based on previous pings and applied in real-time (Hammerstad, 2000). The result is an angular independent image (Fig. 4.1, right).
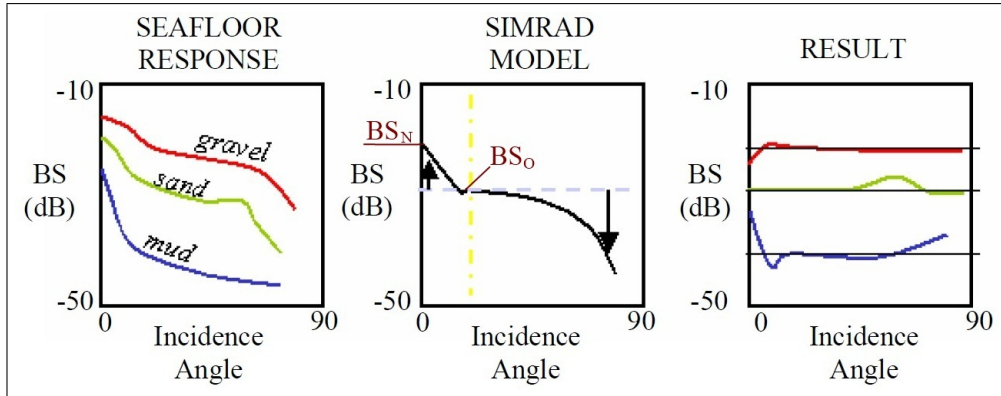
Figure 4.1: Simrad backscatter corrections for seafloor angular response. Angular response of three different seafloor types (left), the Simrad model (middle), and the result of the applied model (right) are depicted. (Llewellyn, 2006)

The time varying gain is logged by the system, so that the original amplitudes can be reconstructed. This is necessary in postprocessing as the Kongsberg model assumes a flat seafloor, which usually does not coincide with the reality. Therefore, the changes of the applied model need to be re-calculated to retrieve the raw intensity values before the actual bathymetry can be taken into account (Hammerstad, 2000).

4.3 Geocoder

Geocoder is a software toolset developed by Dr. Luciano Fonseca and licensed by the University of New Hampshire. It processes raw backscatter data, creates backscatter mosaics and performs an Angular Range Analysis (ARA) for a remote estimation of seafloor properties. Geocoder can process sidescan and multibeam backscatter (average and time series) data. This section describes the processing steps applied to the backscatter data in Geocoder. The order of description is the same as their usage in processing.

4.3.1 Radiometric and geometric corrections

Radiometric corrections are applied to the recorded intensity values to obtain the best estimate of the backscatter strength returned from the seafloor by removing perturbations of the water column effecting the signal. The recorded values are first corrected for TVG, transmit powers and receiver gains, which are applied by the system during data acquisition (Section 4.2). The sonar equation (Eq. 2.4)

expresses the mathematical relation of the received intensity value (echo level) to the backscatter strength per unit (backscatter coefficient). The latter is the value, which one wants to obtain. Therefore the raw intensity values need to be corrected for the elements of the sonar equation, which are the source level, spherical spreading, attenuation in the water column, correction for actual seafloor slope (calculation of effective incident angle), and the computation of the actual area of ensonification. Furthermore, a beam pattern correction is applied to remove hardware and sediment artifacts in along-track direction. Speckle noise is removed by combining stacking and a morphological median filter with a percentile threshold (Fonseca et al., 2005, 2007a).

Geometric distortions occur because the data is sampled in time (time series format). These distortions are corrected in Geocoder by a slant-range correction, which is based on the bathymetric measurements. It transforms the slant-range time samples into horizontal distances to the acoustic source. Geometric distortions also occur due to the movement of the platform, therefore the information of auxiliary sensors is very important. Recorded values of navigation, heading and attitude are interpolated in time for each ping transmit time to determine the position of a data sample on the seafloor in reference to the ship. Hence it is possible to map each slant-range corrected backscatter sample to a mosaic cell in the projected coordinate system using straightforward geometric mapping during mosaicing (Fonseca et al., 2005). Fig. 4.2 shows an angular response before and after radiometric and geometric corrections were applied.
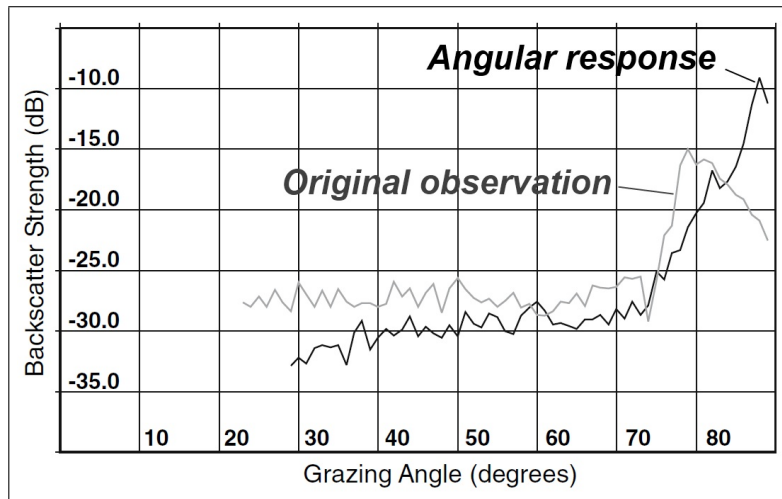
Figure 4.2: Backscatter angular response of a seafloor patch acquired by a Simrad EM 3000. The gray line shows the original observation and the black line the angular response after radiometric and geometric corrections were applied. The maximum backscatter from the original observation is not situated in the nadir area but at a grazing angle of 80° because of a slope. (Fonseca et al., 2007a)

4.3.2 Mosaic blending

The results of the applied corrections listed above are the corrected backscatter angular responses. As these angular responses depend on the incidence angle, they cannot be mapped directly into a mosaic. The values close to nadir are higher than at larger angles and would lead to artifacts in the mosaic. The angular dependence is removed from the data before mosaicing to obtain angle-invariant data and therefore a homogeneous image of the backscatter strength of the surveyed area. For the normalization of backscatter strength across the swath, an angular varying gain (AVG) correction is applied. Geocoder preserves the angular response for the Angular Range Analysis (ARA) as the angular response is an intrinsic property of the seafloor and is used by the ARA for estimation of seabed properties (Fonseca et al., 2007a, 2009).

Generally, there are different methods for the calculation of the AVG correction for the normalization of the backscatter strength along a swath: Lambertian corrections (Hammerstad et al., 1991), Chebychev filters (Cervenka et al., 1993) or moving average (Chaves, 1986; Fonseca et al., 2005). Geocoder uses a moving average window to calculate the mean intensity of a number of angular responses, the size of which is user-specified. Three different methods are available in Geocoder for normalization of the resulting AVG array: flat, trend, and adaptive. The flat method calculates the average intensity value of the AVG array and the other values are normalized to this value. "Flat" therefore refers to the mean intensity line that would be plotted with respect to the grazing angle. The trend technique employs a linear least-squares approach, where a straight line is fitted to the total backscatter curve for the data between 30° and 60° on starboard and port side. The AVG array therefore is normalized to a flat line, but to the best fitting curve. The adaptive method uses the best of the flat and trend approaches. If the slope of the best fitting line is less than 15° then the flat approach is used. Otherwise the trend technique is employed (according to *CARIS* internal document received from Corey Collins, *CARIS* Product Manager).

After the angular response has been removed, the backscatter data can be mapped to mosaic cells by homography mapping. One data sample is mapped simultaneously with its adjacent sample and two samples of the neighboring ping like indicated in Fig. 4.3. The backscatter values of the vertices in the projected coordinate system are assigned to the values of the original data. The pixels inside the polygon within the four vertices are calculated by interpolation of the vertices values. This method is an average weighted by the inverse-square distance interpolation (Malinverno et al., 1990; Fonseca et al., 2005).

Aliasing effects in the data can be observed when the resolution of the mosaic is much lower than of the original data. Geocoder corrects aliasing effects by inverse mapping with pre-filtering. The corners of the cells in the mosaic are inverse mapped in the acquisition coordinate frame. When one cell corresponds to a number of pixels, a Gaussian filter is applied to average their contribution. This technique allows to generate a mosaic at lower resolution, where the general seafloor features are preserved and the aliasing artifacts are reduced (Fonseca et al., 2005).
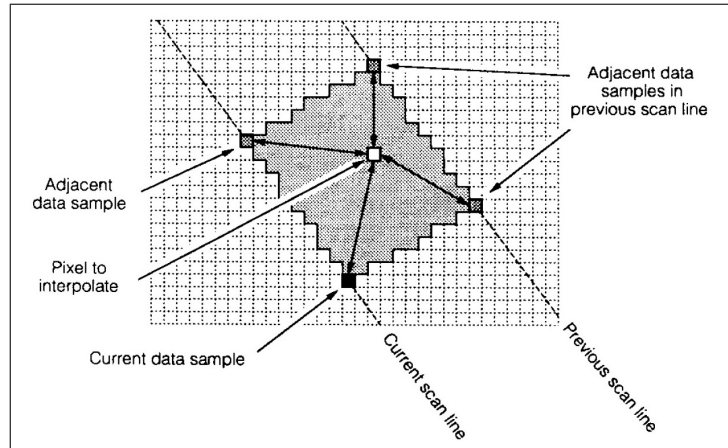
Figure 4.3: Mapping method of data samples into the projected coordinate system. The value of a pixel (white) is interpolated by a weighted average (inverse-square distance) of the vertices (original data values). (Malinverno et al., 1990)

Additionally, a quality factor is stored for each mosaic cell. Its value is set in accordance to the incident angle. Values close to nadir and far off nadir are assigned with lower quality factors than samples in the mid-range. When overlapping data is mosaicked, the quality factor determines the strength of the contributing values for the mapped value. To reduce seam-effects, a feathering technique (Rzhanov et al., 2002) is implemented. This blending technique checks the quality factors of overlapping samples. If their difference is larger than a threshold, the value with the larger factor is mapped. If the difference of the factor is smaller than the threshold, the resulting pixel value will be an average of the contributors (Fonseca et al., 2005).

4.3.3 Angular Range Analysis

The Angular Range Analysis (ARA) employs the fact that each sediment type has a unique angular response (Fig. 4.4). The backscatter variation with respect to the grazing angle is a function of the seafloor properties. To estimate seafloor characteristics by using the corrected backscatter strength, an inversion of an acoustic backscatter model is used. Geocoder uses the effective density fluid model after Williams (2001). It is a simplification of the Biot theory which regards sediment as poroelastic medium (mixture of particles and water) (Biot, 1956, 1962). It accounts better for the parameter porosity, tortuosity and permeability. The effective density fluid model was modified for the calculation of the volume scattering contribution (Fonseca et al., 2002). This model was implemented into *CARIS* and *FMGeocoder Toolbox*. In *CARIS* it is also possible to choose the Biot theory for the ARA as required. In the following the regular Geocoder approach is described.

The three main parameters that control the model are the acoustic impedance contrast (which controls the strength of seafloor penetration), the seafloor roughness, and the sediment heterogeneities. They can be described by the following model parameters (Fonseca et al., 2007a):
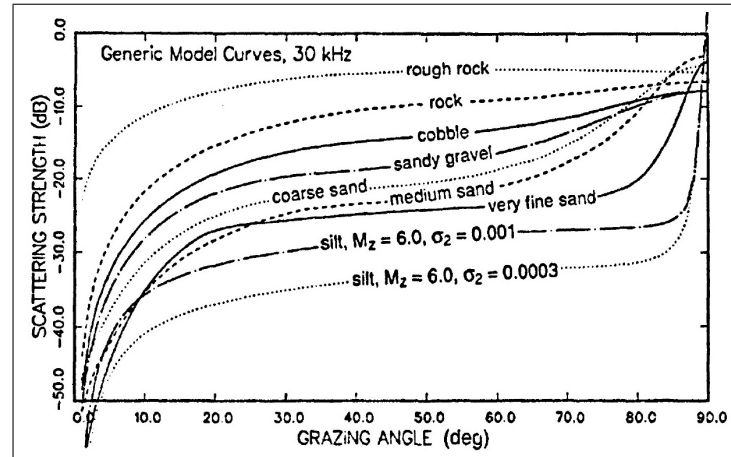
Figure 4.4: Model curves (Jackson model) for backscatter strength of different sediment types. M_z indicates the grain size in phi units and σ_2 the volume parameter. (University of Washington - Applied Physics Laboratory, 1994)

- Sound speed ratio (ratio of sediment sound speed to water sound speed)

- Density ratio (ratio of sediment density to water density)

- Loss parameter (ratio of imaginary wave number to real wave number for the sediment)

- Porosity

- Permeability

- Tortuosity

- Spectral exponent (exponent of bottom relief spectrum)

- Spectral strength (strength of bottom relief spectrum)

- Volume scattering parameter

In order to isolate the influence of the impedance, the roughness, and the sediment heterogeneities, the angular response of each seafloor patch (20 to 30 consecutive pings and half a swath) is divided into three ranges (or angular regimes) according to the grazing angle: the near (90°–65°), the far (65°–35°) and the outer range (35°–5°) (Fonseca et al., 2007a). This process is also called partial stacking technique (Fig. 4.5).

Following ARA-parameters are calculated for the near and far range: mean backscatter, angle, slope, and intercept. For the outer range only the mean is determined. The slope is strongly influenced by the seafloor roughness and the intercept is influenced by the impedance. The relationship is complex and described by mathematical models for acoustic backscatter. Geocoder uses the Jackson model (Jackson et al., 1998). The total-slope and the total-intercept for each seafloor patch are determined. They are defined as the slope and the intercept of the line connecting the near-intercept and the far-intercept (Fig. 4.5). The total-slope and the total-intercept of each patch of the survey area are plotted in a Cartesian graph. A trend line for the survey is defined as the linear regression of
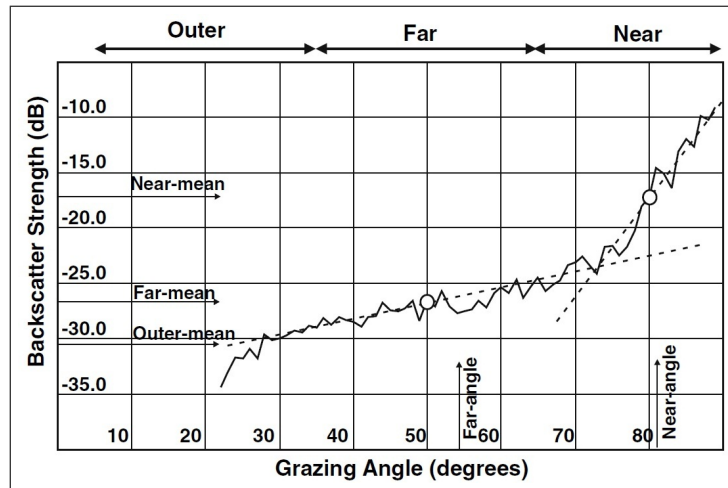
Figure 4.5: Stacked backscatter angular response of a Simrad EM 3000. The dashed line at the near range defines the near-slope and the near intercept (white circle). The dashed line at the far range defines the far-slope and the white circle the far-intercept. The arrows at the left side indicate the calculated dB levels for the near-mean, far-mean and outer-mean. The arrows at the bottom show the near-angle and the far-angle. (Fonseca et al., 2007a)

all values. The orthogonal distance is the last ARA-parameter to be determined. It is defined as the geometrical orthogonal distance of each coordinate pair (total-slope, total-intercept) to the trend line (Fig. 4.6). According to the backscatter model this parameter has a strong correlation with the volume heterogeneities (Fonseca et al., 2007a, 2009).
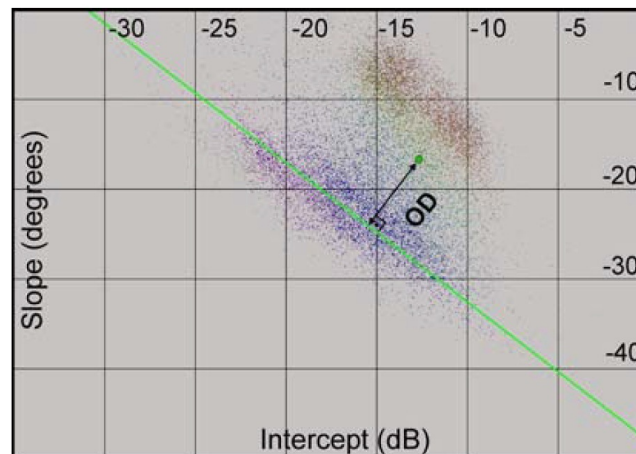
Figure 4.6: Intercept-slope graph with trend line (green). The orthogonal distance (OD) of one particular seafloor patch is indicated in the graph. The points are color-coded in accordance to the acoustic impedance from the final model inversion. This data was collected with a Simrad EM 3000. (Fonseca et al., 2007a)

After determination of the ARA-parameters, a constrained iterative inversion of the model is applied. The model implements constraints based on inter-relations for sediment physical properties according to Hamilton (1974). As a result of using the constraint inversion, the input parameters cannot vary independently

but are constrained by physical property inter-relationships (Fonseca et al., 2007a; Mayer et al., 2007).

The iteration of the model concerns only the ARA-parameters. Therefore, ARA-parameters are also calculated for a modeled backscatter response (model-ARA-parameters) of a seafloor patch. The model parameters (i.e., density ratio, sound speed ratio, loss parameter) are iteratively changed until the model-ARA-parameters are adjusted to the observations by following the constraining equations. When the constrained iterative inversion approaches a set of model-ARA-parameters, it is assumed that the model is a good representation of the seafloor patch and accordingly the model parameters can be used to describe the corresponding seafloor patch (Fonseca et al., 2007a).

4.4 Geocoder in *CARIS HIPS & SIPS 7.1*

CARIS HIPS and SIPS is a hydrographic processing software for single beam, multibeam, sidescan, and Lidar data. Geocoder has been implemented in *CARIS HIPS & SIPS* since version 7.0 released in August 2009. Beforehand, only sidescan data could by processed using the Sidescan Editor. Geocoder is implemented in the new Mosaic Editor, which is designed for processing sidescan and multibeam backscatter data (CARIS, 2012a).

In the first part of this section the workflow is described after CARIS (2012a) and CARIS (2012b) if not stated differently. Afterwards the corrections and their chosen parameter settings are clarified before the results of the mosaicing and the sediment analysis are presented for the data of SO213-1.

4.4.1 Workflow

Before the backscatter data can be processed, the bathymetric data needs to be processed. After importing the raw data files into *CARIS* format using the Conversion Wizard, a possible tidal correction is followed by the removal of blunders in navigation (Navigation Editor), attitude (Attitude Editor), and depth measurements (Swath Editor and/or Subset Editor). Subsequently a BASE surface can be generated to visualize the survey area.

The processing and analysis steps of backscatter data (backscatter correction, mosaicing, and sediment analysis) are all accomplished in the Mosaic Editor. The Mosaic Editor has two processing engines: The SIPS engine and the Geocoder engine. The SIPS engine is designed for processing sidescan data and has therefore optimized sidescan routines built in. The Geocoder engine on the contrary has routines implemented for multibeam imagery data. This includes automatic gain corrections, normalization of data from different sonar systems with varying acquisition settings or automatic slope correction based on the bathymetric measurements. It can process three different data formats: sidescan data, multibeam time series, and beam average data. Fig. 4.7 depicts the workflow of backscatter

processing in the Mosaic Editor. The different processing steps of the Geocoder engine are explained in the following.
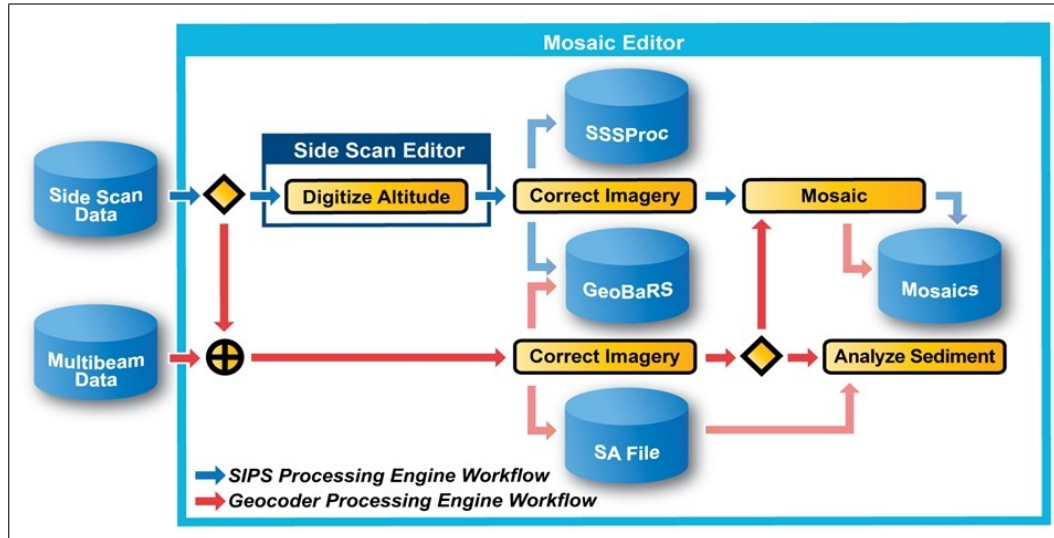
Figure 4.7: Workflow of backscatter processing in the Mosaic Editor for sidescan and multibeam data. When multibeam backscatter data is processed, GeoBaRs and sediment analysis files are generated for a further mosaic generation and sediment analysis. (MacDonald et al., 2009)

4.4.1.1 Corrections and creation of GeoBaRs

The first step of multibeam backscatter processing is the generation of GeoBaRs (Georeferenced Backscatter Raster). The file size defines the GeoBaR extent as one GeoBaR is always created from one raw data file. During their creation different corrections are applied to the recorded backscatter data. Tab. 4.1 lists the corrections multibeam time series data and their default settings, which can be switched on and off by the user. Further hidden corrections are applied which can not be interfered with (e.g., slant-range correction).

Correction	Default
Auto gain correction	on
Auto TVG correction	on
Anti-Aliasing	on
Beam-pattern correction	off
AVG correction / AVG window size	off / 300
Despeckle	on

Table 4.1: Available corrections for backscatter data in *CARIS* and their default specifications.

The first three correction, which are switched on by default, are called "general corrections". According to CARIS (2012a) one should create at least one Geo-BaR with default settings at first. Afterwards, the produced GeoBaR is should be examined and recomputed with adjusted parameters. The chosen parameters can then be applied to the whole dataset. The resolution of a GeoBaR can be set

manually or be computed by the software automatically. GeoBaRs have three layers: intensity (current intensity after corrections), original intensity, and weights (based on sonar geometry, used for mosaic generation). Different GeoBaRs can be created for one file.

Beam pattern correction
The beam pattern correction is applied to remove artifacts produced by hardware or sediments. A beam pattern file (*.bpt) needs to be created by the user before this correction can be accomplished. It is suggested to create such file over a homogeneous surface with no depth variation (CARIS, 2012a). The user selects a part of the track of a suited area and the angular response of this area is compared to a modeled response. The model can optionally be improved by specifying the dominant sediment type (ground-truthing). The beam pattern correction is computed and saved in the beam pattern file, which can then be applied to the whole dataset. In CARIS (2012a) it is recommended to choose an area of around 250 pings for beam pattern file generation.

AVG
To remove the angular dependence from the angular response to obtain angle-invariant data and therefore a homogeneous mosaic, three different methods are available: flat, trend, and adaptive. Furthermore, the AVG window size can be set by the user to define the number of pings over which the chosen filter should be applied. The default method is flat and the default value for the AVG window size is 300.

Despeckle
The speckle correction removes pixel intensity values that are inconsistent with their neighboring pixel values to generate a more homogeneous image. If an intensity level is out of range, this pixel value is replaced by a calculated intensity based on the adjacent pixels. Four different strengths are provided in the Geocoder engine: weak, moderate, strong, and very strong.

4.4.1.2 Mosaicing

One GeoBaR of each file is taken for mosaicing. In case of more than one available GeoBaR, a "Resolve Conflict" dialog box opens. The user can choose which GeoBaR should be taken: the most recent, the one with the finest resolution or manually by name. In case of overlapping GeoBaRs, five methods are available for solving this conflict:

- Auto-seam (the pixel with the larger weight is chosen)

- Full blend (adopted from Geocoder, uses a weighted average of the conflicting values)

- Overwrite (uses the draw order to define which pixel is mapped)

- Shine through (the highest intensity value is used)

- Underlay (opposite of overwrite - the first pixel value is mapped)

The auto-seam and full blend techniques assign a weighting function to the pixel values. Samples at the edge of the swath or in the nadir region receive lower weights than values in the mid-range.

Each mosaic has four attribute layers: intensity, original intensity, weight and contributors. Like GeoBaRs, mosaics can be edited for brightness and contrast. It is also possible to add, remove or modify component GeoBaRs of an existing mosaic. Little gaps in the mosaic can be closed by interpolation.

4.4.1.3 Sediment Analysis Tool

The ARA of Geocoder is implemented in *CARIS HIPS & SIPS* as Sediment Analysis Tool (SAT). A binary sediment analysis file is generated when a Geo-BaR is created. The patch size can be set by the user. Its default value is 30 pings.
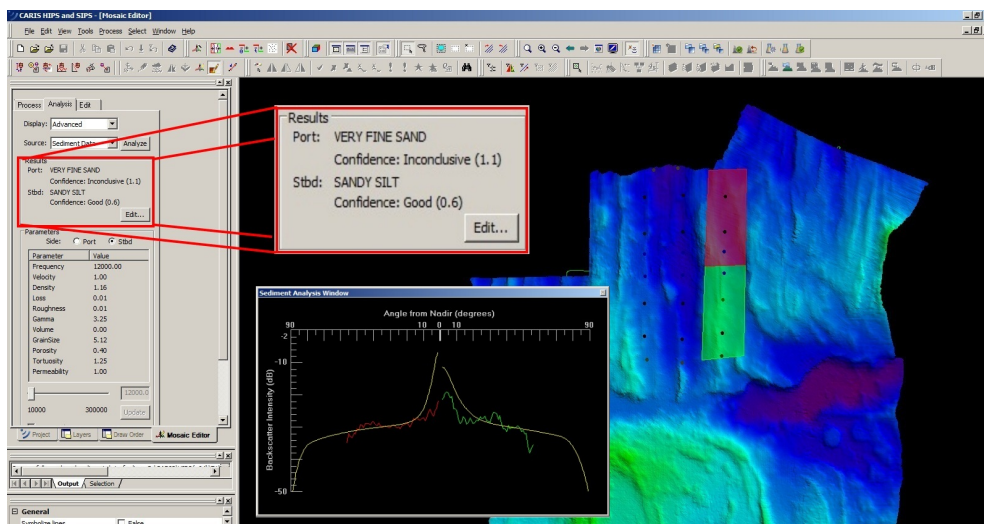
Figure 4.8: ARA result representation in *CARIS*. The activated patches are highlighted in green (starboard) and red (portside). The results of sediment classification are given in the analysis tab on the left with the corresponding confidence level. Below the model parameters are listed. The sediment analysis window shows the observed angular response (green, red) and the modeled curve (yellow).

The results of the sediment analysis are shown in the analysis tab for a selected part of the track, separately for portside and starboard side. A confidence level is assigned to the result (Fig. 4.8), which indicates the magnitude of deviation of the modeled angular response from the observed angular response. It is related to the orthogonal distance parameter of the ARA. When the advanced mode is activated, the model parameters (frequency, velocity, density, loss, roughness, gamma, volume, grain size, porosity, tortuosity, and permeability) and their values are shown below the estimated sediment type. Their values can be adjusted and the resulting changes are observable in the sediment analysis window, which depicts the corrected angular response and the modeled response for the selected data. The results are also shown as colored dots on the mosaic. Different colors indicate different values. For each patch four dots are displayed. They represent

(from nadir) grain size, roughness, volume and impedance. The ARA results can be exported in ascii format.

4.4.2 SO213-1 backscatter processing in *CARIS HIPS & SIPS 7.1*

The Geocoder engine of *CARIS HIPS and SIPS 7.1.1* is used for processing the multibeam backscatter data of SO213-1. In this section the chosen corrections, mosaicing, and ARA parameters and their settings are described. To investigate the influence of the settings on the output, different parameter options are chosen and the results are compared.

4.4.2.1 Generation of GeoBaRs

The Simrad EM 120 records backscatter information in two formats: as average beam intensity and as beam time series. Geocoder can process both formats (Section 3.2.2). GeoBaRs are created with both formats for comparison (Fig. 4.9). The resolution was determined automatically and yields around 27 m for beam time series data and 55 m for beam average data. This difference in resolution is not surprising as the beam average format stores one average backscatter value per beam whereas the time series format records a large number of amplitude (over 2,000) per ping. Therefore the time series data format is chosen for further processing.
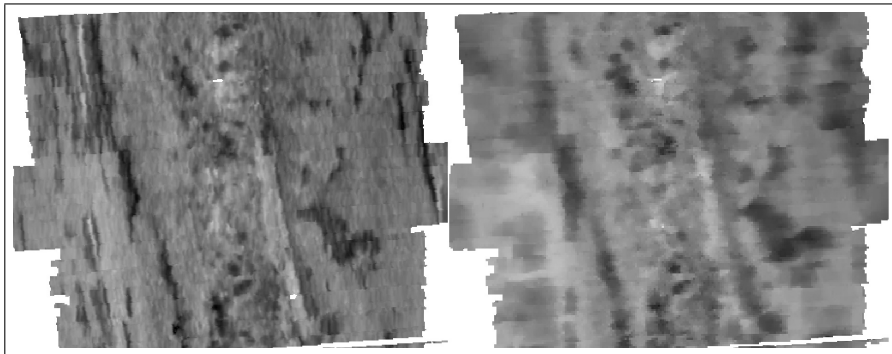
Figure 4.9: Comparison of GeoBaRs generated with time series (left) and beam average data (right) in *CARIS*.

In CARIS (2012a) it is suggested to first apply the general corrections (auto gain, TVG, and anti-aliasing) for GeoBaR creation and then test the effect of the other correction before applying them to the whole dataset. Fig. 4.10 depicts sections of four GeoBaRs generated with different combinations of general corrections. Bright colors indicate high and dark colors low backscatter values. The first mosaic (Fig. 4.10, top left) shows TVG corrected data. GeoBaRs cannot be created without applying a TVG correction. The next mosaic (Fig. 4.10, top right) shows data after applying TVG and auto gain correction. The visual comparison of both datasets fails to find a difference. The data example on the bottom left (Fig. 4.10) is corrected for TVG and anti-aliasing. It does not differ from the

data next to it (Fig. 4.10, bottom right) where the auto gain correction is applied additionally. A difference in the images on the top compared to the images on the bottom is clearly visible. The upper images show linear artifacts in the data, which are not visible on the bottom images where anti-aliasing correction is applied. The influence of the auto gain correction is not noticeable and the influence of the TVG correction cannot be assessed as no image can be generated without switching this correction on. In the further processing steps, all three general corrections are applied.
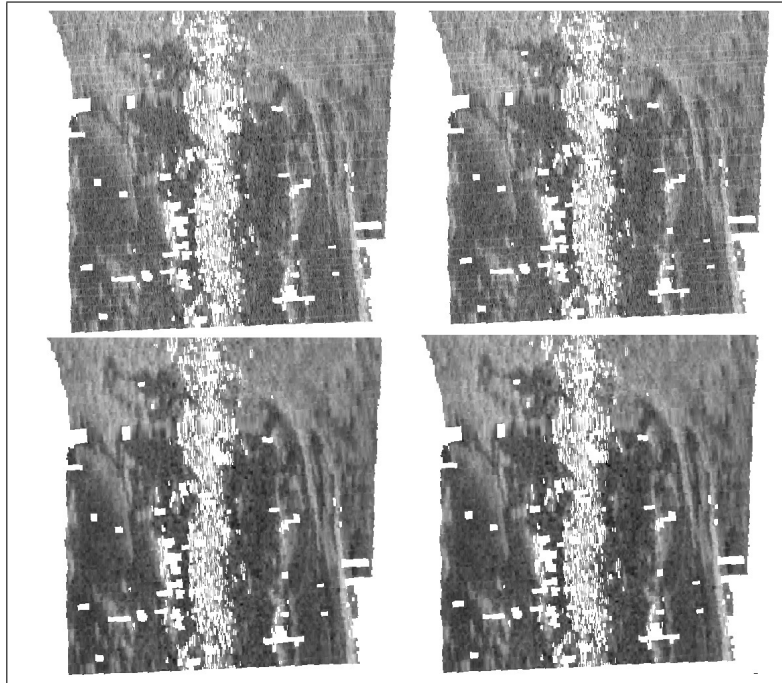
Figure 4.10: GeoBaRs generated with different general corrections in *CARIS*. From top left to bottom right: Backscatter data corrected for TVG / auto gain and TVG / TVG and anti-aliasing / auto gain, TVG, and anti-aliasing.

CARIS offers three different methods for AVG corrections to remove the angular response. It normalized backscatter values across the swath and minimize the seam-effects between overlapping profiles for a homogeneous mosaic. A comparison of the results does not show any significant difference. An adaptive AVG correction is applied to the data of SO213-1 as this method seems the most suitable and is recommended for terrains with strong bathymetric variations (CARIS, 2012a).

In Fig. 4.11 the effect of the AVG correction is depicted. The left example shows the overlapping area of two profiles with general corrections, but no AVG correction. Seam-effects are visible in the middle of the image. The subsequent datasets are processed using the adaptive AVG correction and window sizes of 10, 30, and 300. The window size sets the number of pings over which the correction is computed. For processing the SO213-1 data, an AVG window size of 30 is chosen. A lower number than the default value of 300 seems reasonable as the data was acquired in the deep-sea which results in a low ping rate. Furthermore, the investigated data shows large topographic variation between the pings, which makes an averaging over a large window size inappropriate.
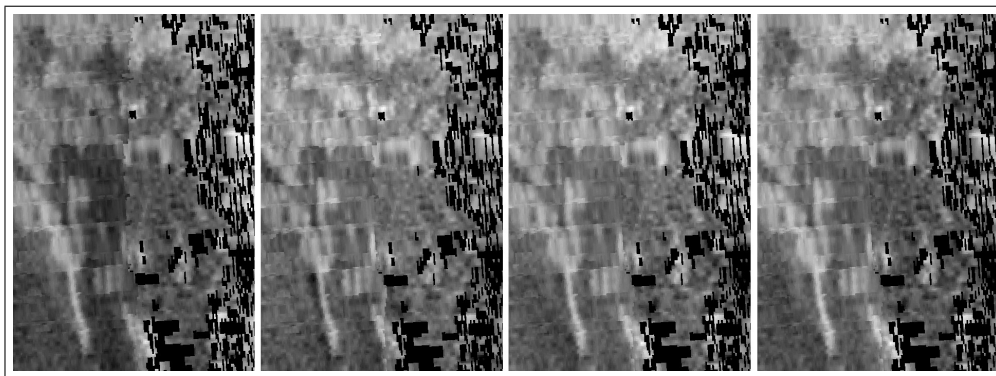
Figure 4.11: GeoBaRs generated with different AVG correction settings in *CARIS*. From left to right: no AVG, AVG window size 10 (adaptive), AVG window size30 (adaptive), AVG window size 300 (adaptive).

Different settings for the speckle removal are tested (Fig. 4.12). The image on the left is created with no despeckle, the middle one with weak despeckle, and the one on the right with moderate despeckle. When applying the despeckling function, data gaps in the middle of the swaths were closed by interpolation. These gaps are also obvious in areas, where no editing of the bathymetric data in the nadir region was necessary. They are probably caused by the choice of raster resolution which is slightly to high for the nadir region, due to the relatively small footprint. The weak despeckle method shows some noise whereas this is removed when using the moderate technique. No differences can be observed between the moderate, strong or very strong option. Therefore moderate speckle correction is applied to the data of SO213-1.
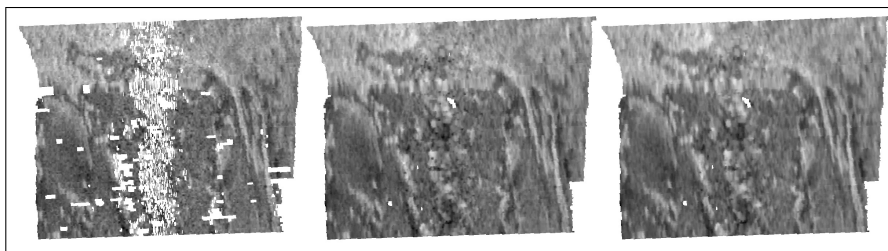
Figure 4.12: GeoBaRs generated with different correction settings in *CARIS*. All datasets were corrected for auto gain, TVG, anti-aliasing, and AVG. From left to right: no despeckle, weak despeckle, moderate despeckle.

To test the beam pattern correction, a beam pattern file is created. As suggested in CARIS (2012a), it is generated in a flat and homogeneous region. As the cruise SO213-1 was conducted in the area of the Chile Rise and the adjacent Fracture Zones, no perfectly suited region can be found throughout the entire dataset. The most appropriate data for the generation of a beam pattern file is shown in Fig. 4.13 (left). This data was collected on the 10th of July, lies about 600 km to the north-east of the investigation area, and has a depth variation of about 60 m. Only an area of 65 pings can be selected for the beam pattern file generation due to topographic variations, which is far less than the recommended 250 lines, as *CARIS* only allows to create a beam pattern file of one data file. The chosen pings are indicated with red lines in the middle of Fig. 4.13. The mosaic on

the right of Fig. 4.13 depicts the backscatter data after beam pattern correction, AVG correction (adaptive - 30), and speckle removal (moderate). When visually comparing mosaics assembled of data with and without beam pattern correction, the visual difference is very small and hardly recognizable.
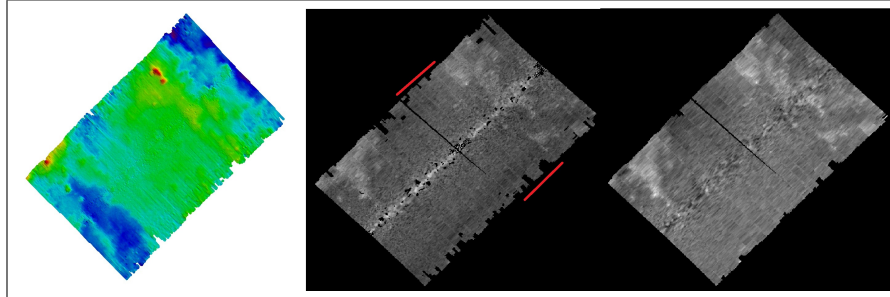
Figure 4.13: Overview of the area for beam pattern file generation. From left to right: BASE surface of relative homogeneous area (resolution: 30 m), mosaic of the same area with default setting (auto gain correction, TVG correction, anti-aliasing) with red lines indicating the pings used for the generation of the beam pattern file, and mosaic after applying corrections for beam pattern, AVG, and speckle noise. (CARIS, 2012a)

The resulting beam pattern, which is applied to the dataset of the investigation area, is displayed in Fig. 4.14. The yellow curve shows the measured backscatter response. The blue curve represents the modeled backscatter and the green and red graph depict the corrected beam pattern.
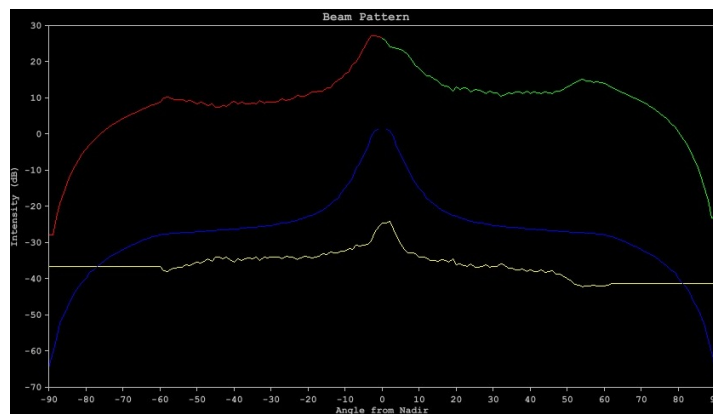
Figure 4.14: Beam pattern file used for beam pattern correction. It shows the uncorrected beam pattern trace (yellow), the modeled backscatter (blue) and the true beam pattern trace for the selected area (green and red).

4.4.2.2 Mosaicing

All five methods for mosaicing are tested (Fig. 4.15). The methods overwrite, shine-through, and underlay showed strong seam-artifacts. Especially the methods overlay and underlay do not seem suited as they only concern the order of import. A totally different mosaic would be produced if the loading order would be changed. The most homogeneous mosaics are created with the full blend and

auto-seam method. In both mosaics some artifacts are still visible where overlapping profiles in diverse directions were recorded. Images of the whole mosaics can be found in App. A, Fig. A.4 and A.5. The charts of the mosaics were generated by importing them as geotiff into *ArcGIS 10* and adding a coordinate grid.
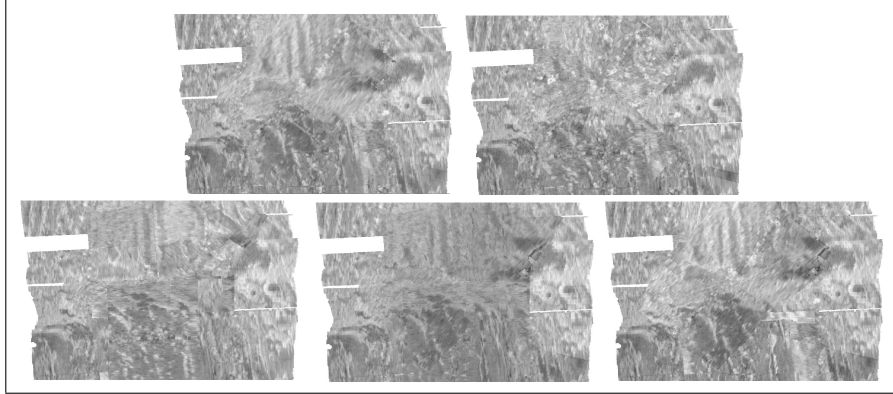
Figure 4.15: Details of mosaics produced with different mosaicing methods in *CARIS*. From top left to bottom right: full blend, auto-seam, overwrite, shine-through, underlay.

In Tab. 4.2 the settings of the corrections are listed, which were applied during multibeam backscatter processing in *CARIS HIPS and SIPS*.

Parameter	Setting
Processing engine	Geocoder
Source data type	Time Series
Auto gain correction	on
Auto TVG correction	on
Anti-Aliasing	on
Beam-pattern correction	on
AVG correction	adaptive/30
Despeckle	2 (moderate)
Mosaic	full blend & auto-seam

Table 4.2: Correction settings for backscatter processing in *CARIS*.

4.4.2.3 Sediment analysis

Each sampling location is at least covered by two profiles. The sediment classifications of the corresponding patches are compared to the measured grain size measurements by the Beackman Coulter LS 200. Different ARA settings are chosen for comparison of their results for sediment classification.

The patch size for the ARA can be defined by the user in along-track direction. The default value is 30 pings. Different patch sizes are specified and the results compared (App. B, Tab. B.2). Furthermore, the sediment classification when applying the Jackson model and the Biot theory are compared (App. B, Tab. B.4). Afterwards, the influence of the beam pattern correction is investigated by testing the ARA sediment classification with and without beam pattern corrected

data (App. B, Tab. B.4). All three sediment sampling locations are separately employed for ground-truthing. In App. B, Tab. B.6 the obtained sediment types by the Jackson model with different ground-truthing locations are presented. The analysis is repeated with the appliance of the Biot theory (App. B, Tab. B.7) with ground-truthing. At each ground-truthing location the profile with the lowest topographic variation is chosen. The results are discussed in Section 5.3.3 for the differences in sediment classification at the sediment sampling locations. In Section 5.3.4 the areal results are compared.

4.5 Geocoder in *FMGeocoder Toolbox (Fledermaus)*

Fledermaus is a package of software tools for processing and visualizing bathymetric data. It was developed by IVS3D[6] and is owned by QPS[7] since 2012. The *FMGeocoder Toolbox (FMGT)* is implemented in *Fledermaus* since version 7.0 (2009) for multibeam backscatter processing and analysis.

In this section the processing workflow is described before the applied settings for the backscatter processing of the investigation area are explained. All information was taken from IVS3D Fledermaus (2011) if not stated differently.

4.5.1 Workflow
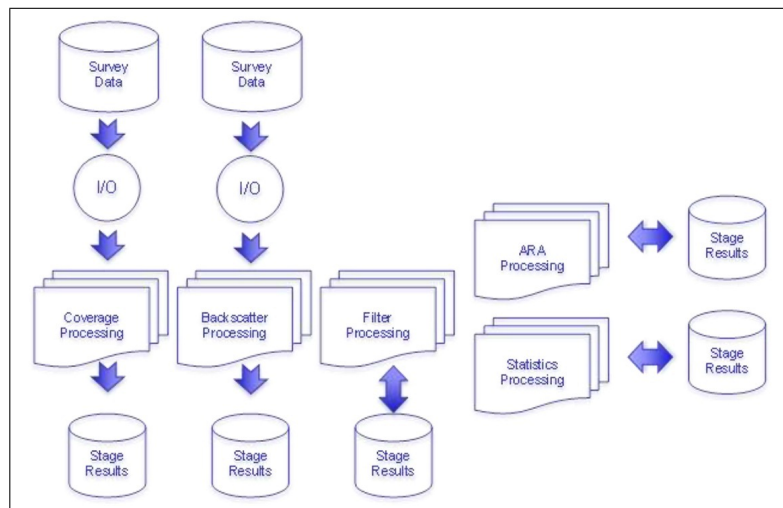
Figure 4.16: Processing stages of *FMGT*. (IVS3D Fledermaus, 2011)

When the raw data files (beam average or beam time series) are loaded in *FMGeocoder Toolbox*, some preliminary processing takes place. It includes indexing of the files for faster processing, extracting of metadata, and computation of the coverage, where the navigation is extracted and the extend of the swath is calculated. After the files are loaded the data can be processed. There are three

---

[6]Interactive Visualization System
[7]Quality Positioning Services

different outputs: mosaic, statistics, and ARA. After the generation of a mosaic, the statistics and/or the sediment analysis can be computed. These five primary processing stages are shown in Fig. 4.16. The first three stages depend on the output of the previous stage, whereas the last two stages (statistics and ARA) depend on the first three, but are independent from each other.

4.5.1.1 Corrections and mosaicing

During mosaic generation, backscatter and filter processing take place. They include radiometric and geometric corrections followed by mosaic blending. The mosaic resolution is calculated automatically during coverage processing when the data is loaded, but it can be changed manually. Tab. 4.3 lists the corrections which can be applied to the backscatter data and their default settings. They are the same corrections as in *CARIS*, but include a larger number of hidden corrections which cannot be changed by the user.

Correction	Default
Tx/Rx power gain correction	on
Beam-pattern correction	on
AVG correction / AVG window size	on (flat) / 30
(Anti-Aliasing	on)
(Despeckle	on)

Table 4.3: Available corrections for backscatter data in *FMGT* and their default specifications. The corrections in brackets are applied automatically. (IVS3D Fledermaus, 2011)

The beam pattern correction is switched on by default. If no beam-pattern file (*.bpt) is loaded to the project, a default file with all zeros will be applied instead. For generating the beam pattern file, a part of the track needs to be highlighted, before the measured angular response of that segment is compared to a modeled response curve. The delta values are stored in the beam pattern file and applied to the whole data set. The user can specify the sediment type for a better modeling of the angular response (ground-truthing) like in *CARIS*.

The AVG correction methods are the same as in *CARIS*: flat, moderate, and adaptive. The flat technique is used as default with a window size of 30.

When two or more samples overlap during mosaicing, the blending algorithm is used. The user can set the percentage indicating the contribution of each cell, which has a default value of 50 % (i.e., equal contribution from two cells). Three options for blending in overlapping areas near nadir are available: blend (default option, blending of nadir pixels and other), and two methods which are called "no nadir if possible". These two options give higher preference to not-nadir pixel values to reduce artifacts of nadir samples. Further information about the difference between these two algorithms could not be found in the manual, but they are most likely interpolation algorithms that are similarly weighted to the ones in Geocoder.

The appearance of a mosaic can be improved by the user by histogram stretching. It is also possible to remove segments of the data or change the order of the mosaiced data files.

4.5.1.2 Statistics

After mosaic generation, the statistics can be calculated. They are presented as parameter layers, with a resolution of 20 times the mosaic resolution. This default value can be changed by the user. Different layers are generated: mean, median, minimum, maximum, mode, skewness, kurtosis, variance, m3, m4, quadrile range, num. indep. samples, num. Samples, grazing angle, 10th percentile, 25th percentile, 75 percentile, and 90th percentile. They are independent surfaces. When they are made slightly transparent and are displayed on top of the backscatter mosaic, both information layers can be made visible simultaneously. Each individual layer can be exported as geotiff, surface, and in ArcGIS format.

4.5.1.3 Angular Range Analysis

The Angular Range Analysis in *FMGeocoder Toolbox* applies the Jackson model. The patch size is fixed and cannot be changed by the user. The patch size is defined as 30 consecutive pings and half a swath width (starboard side/portside).
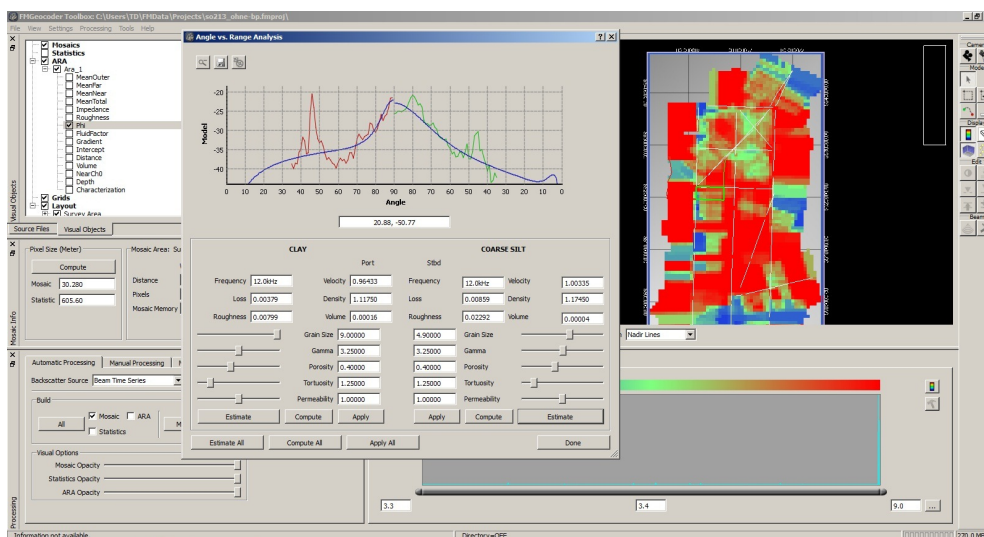
Figure 4.17: ARA result presentation in *FMGT*. The attribute layer "phi" is shown on the right. The "angle vs. range analysis" display shows the observed angular response (green, red) and the modeled curve (blue) as well as the model parameters for the selected patch.

The results are visible in different attribute layers (Fig. 4.17), which are presented as surfaces. The pixel values of the attribute layers result from interpolation of the patch results. The attribute layers are: mean outer, mean far, mean near, mean total, impedance, roughness, phi, fluid factor, gradient, intercept, distance, volume, nearCh0, depth, and characterization. Each individual layer can be exported as geotiff, surface, in ArcGIS format, and as SD file.

The original patch results of the ARA can also be exported as "ASCII ARA" (text file with projected Easting and Northing of each patch with values for all ARA layers) or as "Point ARA Object" which creates a point SD Fledermaus file, where each patch result is displayed by a colored sphere. This presentation is similar to the colored dots overlay in *CARIS*.

4.5.2 SO213-1 backscatter processing in *FMGeocoder Toolbox*

For the backscatter processing of SO213-1 *Fledermaus* Version 7.3.1a (October 2011) is used. Later versions (7.3.2 & 7.3.2a) were available, but crashed when loading the raw *.all data files. The data files were split before importing so that the data where the ship changed course was not taken into account.

4.5.2.1 Corrections and mosaicing

Different tests with various correction settings are done in *FMGT* to investigate their influence on the data. In Fig. 4.18 the differences in the data when applying no corrections (left), auto gain correction (middle), and an additional adaptive AVG correction are depicted. There are no differences visible between the first two results. The AVG correction shows good results in removing the strong backscatter response in the near nadir region, whereas the track of the ship is clearly visible in the first two data examples.
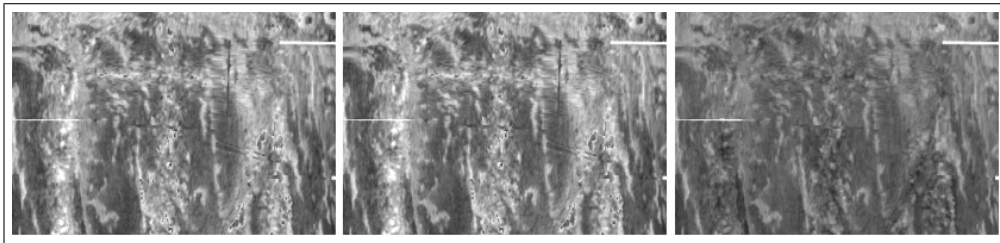
Figure 4.18: Comparison of different correction settings in *FMGT*. From left to right: no corrections, auto-gain correction, auto-gain correction and AVG correction (adaptive - 30).

The three different AVG methods are tested. The results of the trend and adaptive method are the same, and the differences between flat and adaptive are not very large, which indicates that due to the strong bathymetric variations of the seafloor only the trend technique is used by the software. Fig. 4.19 shows the difference of the resulting mosaics generated with the flat (left) and adaptive (right) method. The adaptive method is chosen for processing of the dataset as it shows slightly better compensation of the terrain. A variation of the AVG window size does not yield visible differences in the results. The window size is set to 30 for processing.

To test the effect of the beam pattern correction on the data, a beam pattern file of the same area as in *CARIS* is created. It is depicted in Fig. 4.20 with the observed values (green), the modeled angular response (blue), and the resulting
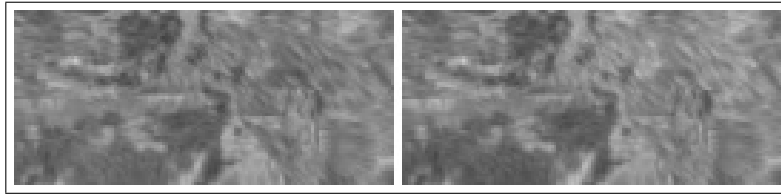
Figure 4.19: Comparison of mosaics created with different AVG settings in *FMGT*. Left: flat AVG correction; Right: trend/adaptive AVG correction.

correction in red. As it is possible in *FMGT* to create a beam pattern file over different data files, about 100 pings are chosen.
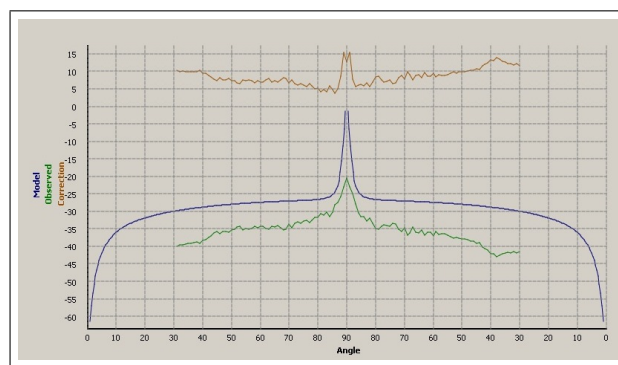
Figure 4.20: Beam pattern correction display in *FMGT*. The green curve shows the measured values, the blue one the modeled curve, and the red one the correction applied to the dataset.

Three mosaics are generated using different methods: full blend, "no nadir if possible 1", and "no nadir if possible 2" (Fig. 4.21). For the full mosaics refer to App. B, Fig. A.6 to A.8. The mosaic resulting from full blend method shows nadir artifacts as it does not apply a lower weight to the nadir values. The "no nadir if possible 2" algorithm creates a mosaic, which shows the most homogeneous image for the southern part of the survey area.
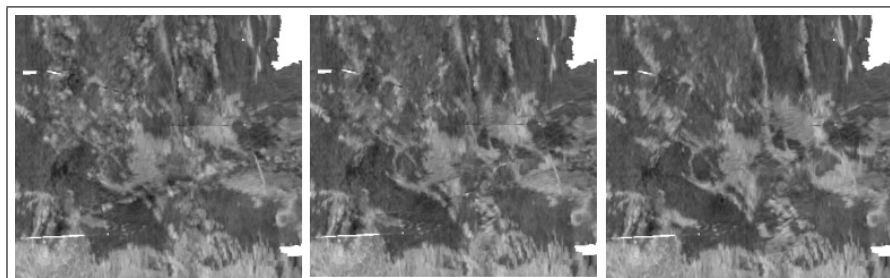
Figure 4.21: Comparison of mosaics generated with different mosaicing methods in *FMGT*. From left to right: full-blend, no nadir 1, no nadir 2.

In Tab. 4.4 the applied correction settings for the final mosaic generation in *FMGT* are summarized.

Parameter	Setting
Source data type	Time series
Tx/Rx power gain correction	on
Beam-pattern correction	on
AVG correction / AVG window size	adaptive/30
(Anti-Aliasing	on)
(Despeckle	on)
Mosaic	no nadir if possible 2

Table 4.4: Correction settings for backscatter processing in *FMGT*.

4.5.2.2 Statistics and Angular Range Analysis

The statistics and the ARA result are calculated with a resolution of 400 m. Various ARA settings were applied like in *CARIS* and the results are compared: Without beam pattern correction, with beam pattern correction of homogeneous area outside of the investigation area, and with beam pattern correction with ground-truthing at SO213-14, SO213-15, and SO213-17. The results are presented in App B, Tab. B.8 and are further discussed in Section 5.3.3 and Section 5.3.4.

The attribute layer, which represents the grain size as a surface, was exported as geotiff and imported in *ArcGIS* for chart generation. They are depicted in Appendix A (Fig. A.9 to A.13) with different settings. The surfaces were automatically created by interpolation of the individual patch results in overlapping areas in *FMGT*.

4.6 Visualization of the results in *Fledermaus*

For interpretation of the results of the backscatter analysis, all processing results (mosaics and ARA analysis) were imported into *Fledermaus*, the central visualization application of the software package.

The mosaics created in *CARIS* and *FMGT* were exported as geotiffs and draped to the bathymetry in *Fledermaus*. This representation is helpful for analysis of the backscatter values in correspondence to the depth variations throughout the area.

The ARA results were exported as ASCII file containing reference coordinates and the grain size information for each patch. The confidence interval was additionally exported from *CARIS*. They were also loaded in *Fledermaus* and saved as SD file. The dots representing the grain size for one patch were colored according to the grain size. The grain size indicators of the *CARIS* results were sized according to the confidence level. The better (i.e., lower) the confidence level, the larger the representing sphere in *Fledermaus*. The scene file with the corresponding SD files is saved on the accompanying CD, together with an executable file of *iView4D*, which is a free software to view *Fledermaus* scene files. Fig. 4.22 shows some screen shots of the *Fledermaus* file.
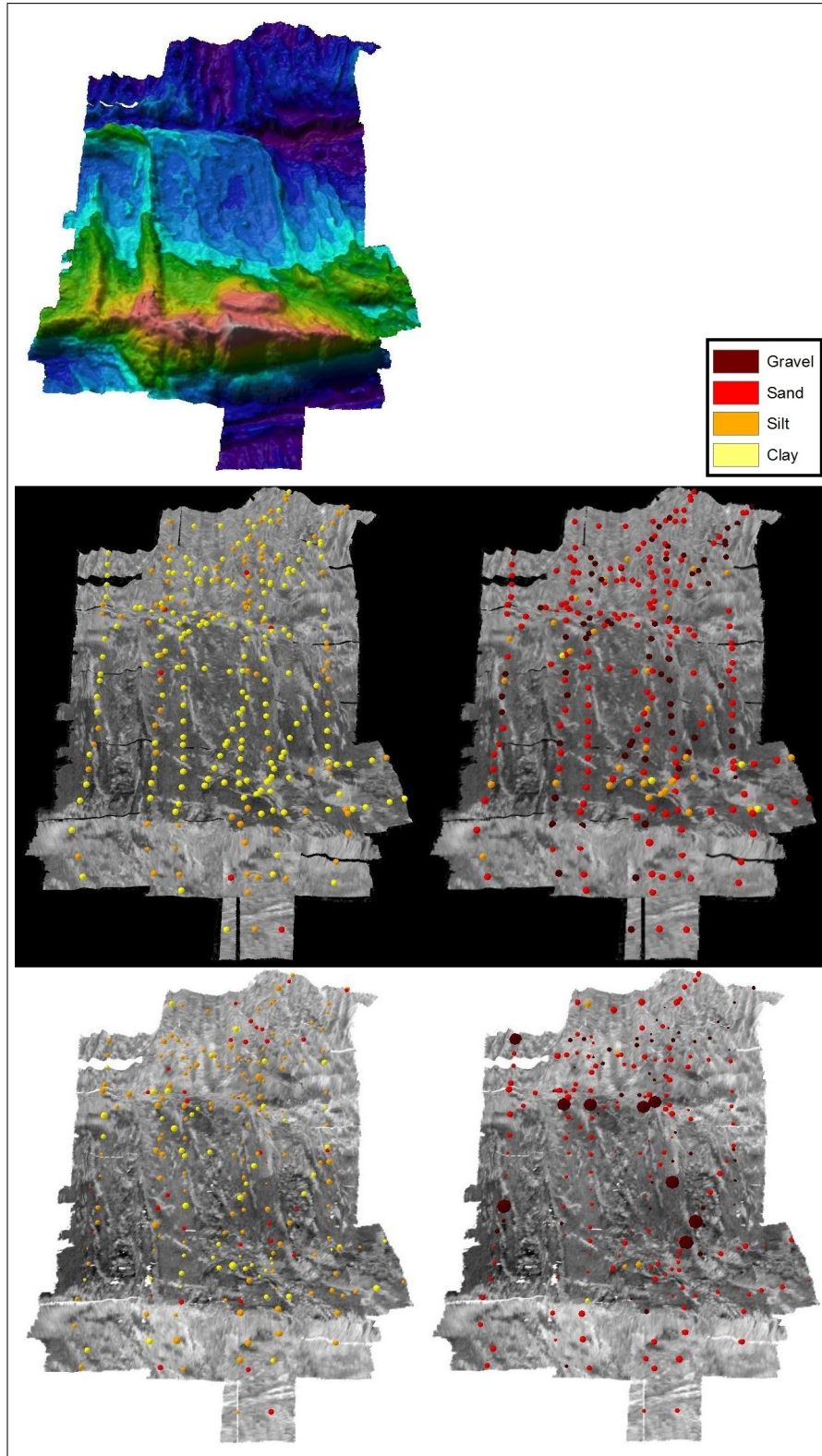
Figure 4.22: Screenshots of the visualized data in *Fledermaus*: digital terrain model of the seafloor (top), mosaic and ARA results computed by *FMGT* with no beam pattern correction (middle left), mosaic and ARA results computed in *FMGT* with ground-truthing at station SO213-15 (middle right), mosaic and ARA results computed in *CARIS* with no beam pattern correction (bottom left) and mosaic and ARA results computed in *CARIS* with ground-truthing at station SO213-15 (bottom right).

Chapter 5

Geocoder – Discussion

This chapter discusses the results of backscatter processing and ARA sediment classification obtained using Geocoder in *CARIS HIPS and SIPS* and *FMGeocoder Toolbox*. The different processing steps (backscatter correction, mosaicing, and ARA) are examined and compared, before both software products are compared with each other. Lastly, the usage of Geocoder for investigation of deep-sea data is evaluated.

5.1   Backscatter processing

Generally, the corrections applied to the backscatter data are both very similar in *CARIS* and *FMGT*. In *CARIS* there are fewer hidden corrections, which permits a larger choice of possible specifications and therefore a better understanding of the processing steps than in *FMGT*.

Examining the angular responses more closely, one problem could be observed in both software products. It seems that the removal of topographic effects from the backscatter data is not applied to full success as some artifacts caused by the bathymetry are still visible in the data in both software packages. The topographic correction is part of the radiometric corrections. Geocoder calculates the effective incident angle "[...] from the scalar product of the beam vector (from the footprint on the seafloor to the transducer) and the normal to the bathymetric surface at the boresight of the footprint, which is the projection of the principle axis of the beam on the seafloor." (Fonseca et al., 2007a). In both software products this correction is hidden and cannot be switched off by the user for comparing data with and without appliance of that correction. Fig. 5.1 (top left) shows the ground-truthing location SO213-17, a cross-section along one swath of profile 14 through the bathymetry (top right), and the corresponding angular response in *CARIS* (bottom left) and *FMGT* (bottom right). The angular responses visualized by the different software look very similar. Comparing the marine topography with the angular response curves, it is obvious that when the seafloor is oriented towards the echosounder beam, large backscatter values are shown in the angular response graphs. The two most apparent are highlighted by blues circles. When the slope is facing away from the transducer, the corrected angular response shows very low values.
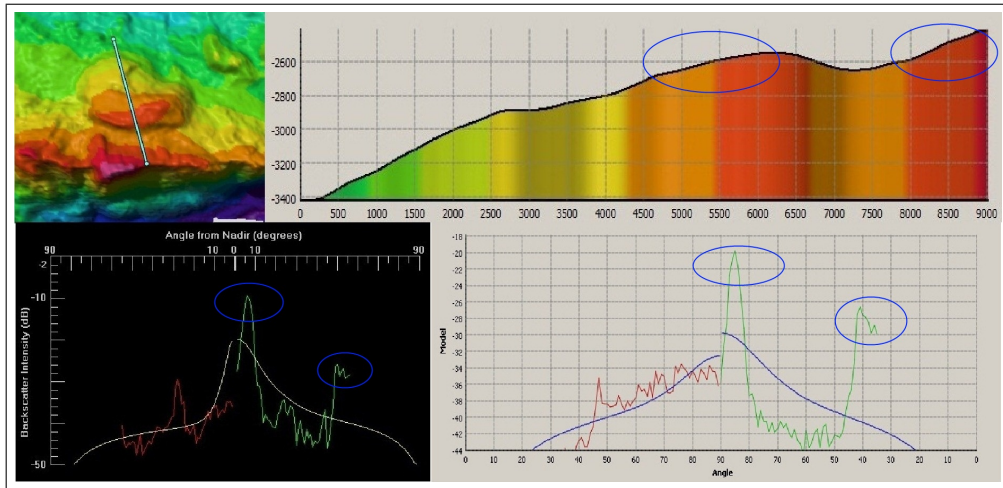
Figure 5.1: Visualization of remaining bathymetric artifacts in the angular responses. The turquoise line indicates the location of a median ping of a patch (top left) and a profile showing the bathymetry of the highlighted ping (top right). Angular response of the corresponding patch in *CARIS* (bottom left) and *FMGT* (bottom right). Blue circles indicate locations, where the seafloor slope is oriented towards the echosounder beam.

Another problem was noted regarding the beam pattern correction in conjunction with the characteristics of the survey area. It was not possible to create a beam pattern file in a homogeneous area with the appropriate extent like recommended in CARIS (2012a). Large water depths result in a broad swath coverage in across-track direction (about 12 km). It is hardly possible to find suitable data sections in such regions with strong morphological variations and furthermore, it cannot be assumed that the sediment type does not change across the swath due to its large extent. This complicates the search for a suited region for beam pattern file generation. Nevertheless, a beam pattern file was created in an area which seemed the most suitable and was applied to the data for comparison of the resulting mosaics. *FMGT* allows to create a beam pattern file over different raw data files, so that the chosen area is about twice as large as the one in *CARIS*. However, applying a beam pattern correction did not have a large influence on the appearance of the resulting mosaic in either software product.
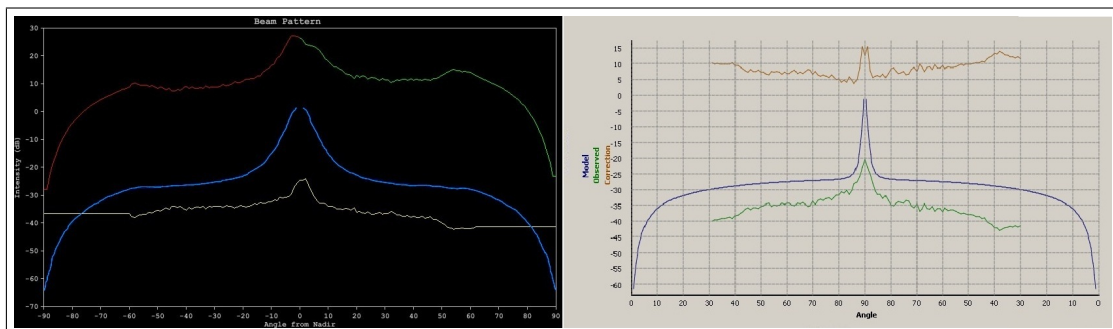
Figure 5.2: Beam patterns of an area outside the investigation area in *CARIS* (left) and *FMGeocoder Toolbox* (right). The blue curves show the modeled angular response, the lowest represents the observed angular response, and the graph on the top shows the resulting correction.

When a beam pattern file is created, the measured angular response of a defined area is compared to a modeled response. Assuming that the topographic correction does not work properly, this has a large influence on the angular response and therefore on the beam pattern correction as local topographic artifacts are considered as systematic hardware or sediment erroneous occurrences. When comparing the observed, modeled, and corrected angular responses generated in *CARIS* (Fig. 5.2, left) and *FMGT*(Fig. 5.2, right), they look similar. The observed angular responses show hardly bathymetric effects, so that the area seems relatively suited for this purpose. In *CARIS* the peak of the corrected response is more developed in horizontal direction, extending over an angular range of 40°, whereas the peak in *FMGT* spans over a range of only 10°. This wider facet regime in *CARIS*, indicates that the selected area is automatically classified as coarser sediment with stronger roughness than in *FMGT*.

5.2 Mosaicing

Both software packages offer mosaicing methods, where weights are applied to the backscatter values according to their position on the swath. In *CARIS* these weights can be viewed as mosaic layer. Fig. 5.3 depicts the weight layers of the mosaics created with the full blend (left) and auto-seam method (right). The scale ranges between 0 (white) and 1 (black). When inspecting the mosaicing weights, they do not correspond to the explanation in CARIS (2012a), where it is said that the weights of nadir beams are assigned with lower weights like the outer beams.
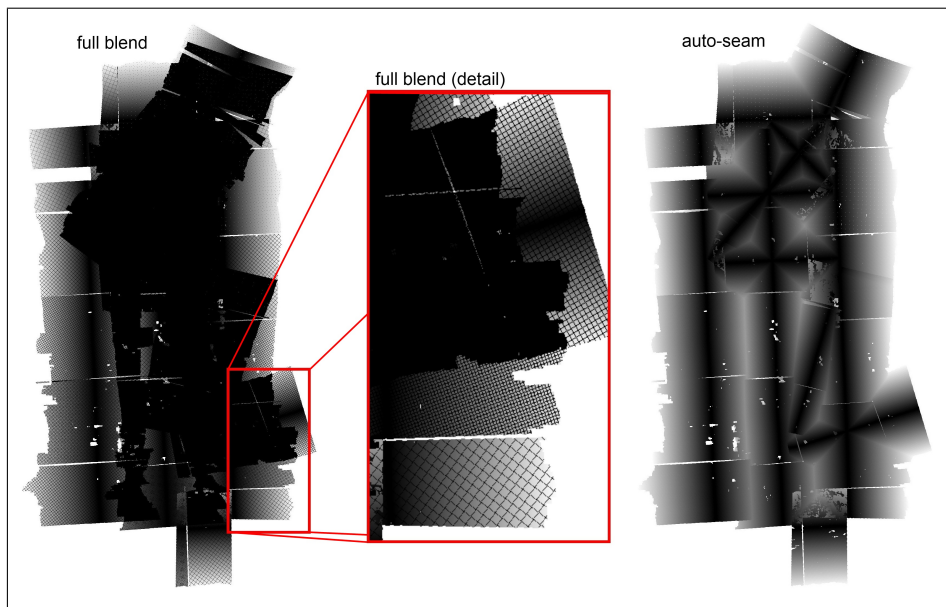
Figure 5.3: Weight distribution of backscatter values for mosaic creation in *CARIS* with the full blend (left) and auto-seam method (right). In the detail view (middle) a part of the full blend mosaic is enlarged to illustrate the systematic artifacts. Large weights (up to 1) are colored black and low weights (down to 0) in white.

Furthermore, it appears that the weights in overlapping areas are summed when the full blend algorithm is used. This is visible in the upper part of the detail view (Fig. 5.3, middle). As a result, the values of profiles in the middle of the area are completely taken for mosaicing like indicated in Fig. 5.4 (left). Moreover, systematic artifacts can be observed in the weight display of the full blend method for areas without overlap. These artifacts may also occur allover the investigation area but cannot be seen due to the summation of weights. They are not visible in the mosaic at the same locations, but in overlapping areas (App. A, Fig. A.4) where backscattered values of different profiles overlap. Considering these observations, it seems that the full blend algorithm in *CARIS* is not working properly.
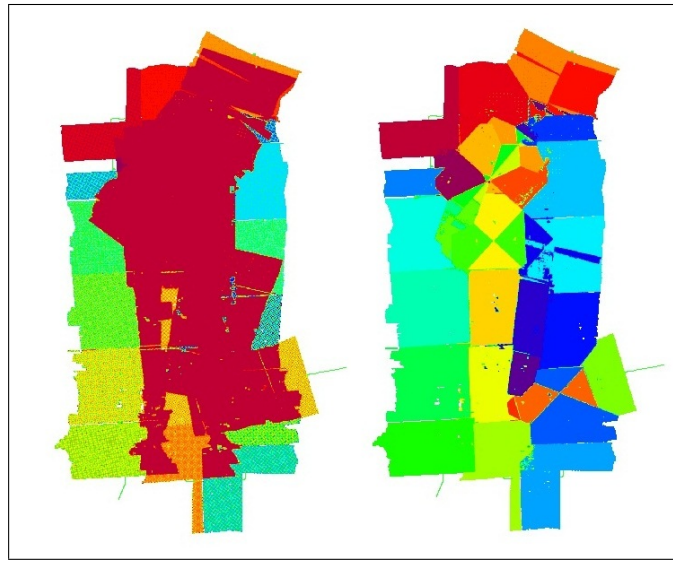
Figure 5.4: Contributing files of mosaics created with the full blend method (left) and the auto-seam method (right) in *CARIS*.

The weight distribution scheme implemented on the investigated data by the auto-seam method in *CARIS* (Fig. 5.3, right) seems more appropriate. Even though the nadir values have the largest weights as well, the calculation appears more consistent. The method does not interpolate between overlapping pixel values, but uses the one with the largest weight for mosaicing. Therefore, strong seam-effects are visible in areas where a larger number of profiles overlap (App A, Fig. A.5). This seam-effects are enforced by the fact that a lot of different smaller parts of files contribute to the mosaic in the northern region of the study area.

When examining the mosaics generated with different interpolation methods in *FMGeocoder Toolbox* (App. A, Fig. A.6 to A.8), the full blend method, which interpolates the pixels without the usage of a weight factor, shows more nadir artifacts in the southern region of the investigation area than in the mosaics compiled with the "no nadir if possible" algorithms. These two methods avoid nadir values if other backscatter information is available during interpolation to reduce nadir artifacts. Nadir artifacts are only visible in the resulting mosaics were no overlap with different data was available (south west of investigation area) and hence have to be used for mosaicing. Comparing the mosaics created with differ-

ent methods, the "no nadir if possible 2" algorithm shows the best result for the southern area of the study area, whereas all mosaics show similar seam-effects across methods in the northern survey area .
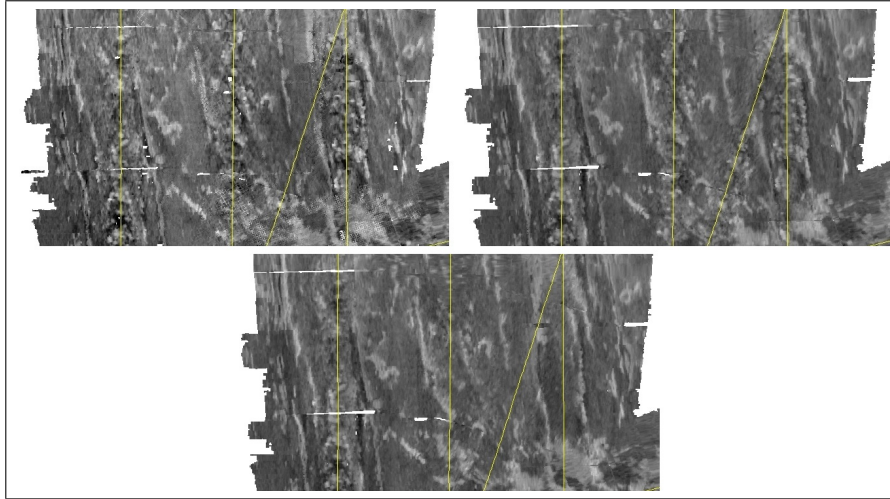
Figure 5.5: Sections of mosaics created in *CARIS* with the full blend algorithm (top left), in *FMGT* with the full blend algorithm (top right), and in *FMGT* with "no nadir if possible 2" (bottom). Yellow lines indicate the ship track.

Comparing the mosaic results obtained by *CARIS* and *FMGT* (Fig. 5.5), the "no nadir if possible 2" in *FMGT* algorithm creates the most homogeneous image of the southern investigation area. Avoidance of nadir values seems to work fine in both "no nadir if possible" algorithms, which is not the case in *CARIS*.

It can be concluded, that all mosaicing methods have problems when a larger number of profiles overlap in different directions like in the north of the study area. There is no algorithm which resolves this problem completely, but a method using a weighted interpolation scheme seems to be the most appropriate (e.g., "no nadir if possible" in *FMGT*).

5.3 ARA

This section discusses the ARA results of Geocoder in *CARIS* and *FMGT*. At first, the expected sediment type distribution for the investigation area is contemplated to allow an evaluation of the returned automatic classifications. Then the crucial parameter of the patch size is examined, before the ARA results with different settings in *CARIS* and *FMGT* are compared. For this comparison two different approaches are adopted: First, the classification results of each patch covering a sediment sampling location are contrasted with the actual grain size measurements (Section 5.3.3). As each of the three sediment sampling locations was recorded by two to four profiles, at least two independent computations for each location are available for evaluation. Afterwards, the areal results are examined (Section 5.3.4) before a conclusion of the computed sediment classifications is drawn.

5.3.1 Expected sediment type distribution of the study area

Before the ARA estimation of sediment types in *CARIS* and *FMGT* can be evaluated, the grain size distribution throughout the survey area needs to be examined. The northern part of the dataset is characterized by large water depths down to 4,800 m. This is below the carbonate compensation depth (CCD) which is generally found in depths between 4,200 m and 4,500 m throughout the Pacific (Pinet, 2006). In this region the sample SO213-14 was recovered in a water depth of 4,050 m. The collected sediment consists of very fine sediment (clay to silt) and manganese nodules, which leads to the assumption that the CCD in this area lies above 4,050 m as organic material is dissolved and the dominant sediment is pelagic clay. Due to the low accumulation rate of clay ($<$1 cm/1,000 years), the evolution of manganese nodules is possible. The recovered manganese nodules have a diameter of 2 – 3 cm. Concerning their size, they can be classified as pebble gravel (-6 $< \phi_{manganese\ nodules} <$ -2) based on the sediment classification scale according to Wentworth (1922). For the computation of sediment classes by *CARIS* and *FMGT* this poses a problem as the grain size scale of both software products covers only the ϕ–range of -1 to 9, which therefore does not include the magnitude of the manganese nodules. The density of manganese nodules at SO213-14 is relatively high, but it cannot be assumed that they cover the seafloor entirely, and no underlying seabed is "visible" for the acoustic signal. This is difficult for the modeling of the angular response because two very different sediment types contribute to the returning angular response. It can be supposed that the acoustic influence of manganese nodules spreads throughout the northern investigation area, where the water depth is larger than 4,000 m.

The intermediate part of the study area can be demarcated by a medium water depth (about 3,600 m) and a relatively homogeneous marine topography. The sediment sample SO213-15 was recovered in this section on a morphological elevation in the north in a water depth of 3,246 m. The measured grain size is coarse silt to very fine sand. The predominant sediment is calcareous ooze, which was expected, as this area lies above the CCD. Calcareous ooze has a larger grain size than pelagic clay and a higher sedimentation rate (few centimeter/1,000 years), which prohibits the evolution of manganese nodules. Similar sediments can be expected throughout the intermediate investigation area.

The southern part of the investigation area is characterized by the Guafo Ridge. Station SO213-17 was recovered at a morphological elevation at the northern slope of this seafloor feature in 2,561 m water depth. The sampled grain size is similar to station SO213-15, but with a slightly larger portion of sandy material, resulting in the recovery of very fine to fine sand. At this location calcareous ooze is also the predominant sediment.

In conclusion, a clayey seabed covered by manganese nodules dominates the northern part of the survey area. The intermediate and southern part seem quite similar in terms of grain size distribution. Therefore a differentiation between the northern part and the shallower areas in the south can be expected from a correct ARA result.

5.3.2 Patch size

The patch size is a very crucial parameter for the ARA as the angular responses of one patch are averaged before they are analyzed by the ARA. Therefore, the requirement that only one sediment type should be dominant per patch is a very important condition for obtaining correct ARA results. In Fonseca et al. (2007a) squared patches are used in a shallow-water environment. This is not practical in deep-water environments as this would result in patches covering huge areas. With increasing patch size the probability of fulfilling the condition of only one predominant sediment type is decreasing. In case of different sediment types per patch, both would contribute to the averaged angular response, which results in a wrong classification.

In *FMGT* the patch size is set to 30 pings in along-track direction and cannot be changed by the user. In *CARIS* this parameter can be specified before the analysis. The width of a patch is defined as half a swath in both software products. In App. B, Tab. B.2 the results of the ARA with different patch sizes are presented. A patch length of 150 pings leads to squared patches, which is not very practical for this dataset as the data files have a recording length of 30 minutes and therefore about 150 pings. Hence, each patch would consist of one whole data file, covering a huge area of the seafloor. Another reason which argues against large patch sizes is, that the files do not correspond to the profile acquisition times. One file can contain data of different profiles. When large patch sizes are chosen, it is more likely that patches are created containing backscatter information of different profiles which should be avoided.

Regarding the classification results with varying patch sizes (App. B, Tab. B.2), all samples are classified smaller in grain size than determined by the laser particle sizer. The results of the computation with patch sizes of 10 pings show the most appropriate grain size estimations with three out of nine correct classified samples (with a deviation of $\pm 1\ \phi$). It can be also observed, that the confidence levels increase (lower probability) when the patch size decreases. Thus, the patch size is set to 10 pings when the data is analyzed for comparison with other results obtained by *CARIS* with changing settings. This way, the probability that areas with less depth variation are averaged together with areas with strong variation is decreased, which should yield better grain size estimations. When the ARA results of *CARIS* and *FMGT* are compared, a patch size of 30 pings is used for a better comparability.

5.3.3 Comparison of ARA results at sediment sampling locations

For the comparison of the ARA results the unsupervised (without ground-truthing during beam pattern correction) and supervised classifications (with ground-truthing during beam pattern correction) are dealt with separately.

69

5.3.3.1 Unsupervised classification

Even though applying a beam pattern correction does not have a large influence on the visual appearance of the compiled mosaic, it has a strong effect on the results of the sediment type estimation by the ARA. Therefore, the data is first analyzed without applying a beam pattern correction before this correction (without ground-truthing) is applied and the analysis repeated.

Without beam pattern correction:

In *CARIS*, the data (without beam pattern correction) is analyzed twice: once applying the Jackson model and then applying the Biot theory. The obtained results are quite similar (App. B, Tab. B.4). The estimated sediment types by the Biot theory are the same or one type greater as when the Jackson model is used (except for SO213-17 profile 14). The confidence levels show similar magnitudes. Overall, three samples are estimated correctly by the Biot theory and only one sample is estimated correct using the Jackson model. Allowing a deviation of one sediment type ($\pm 1\ \phi$), both methods obtain three correct classifications. Fig. 5.6 shows the sediment analysis graph for the same stack of pings computed with the Jackson model (left) and the Biot theory (right). The observed angular responses are colored red and green and the modeled response is presented in yellow. In the left example the patch is classified as medium silt, and in the right as coarse silt. The modeled backscatter curves are nearly identical.
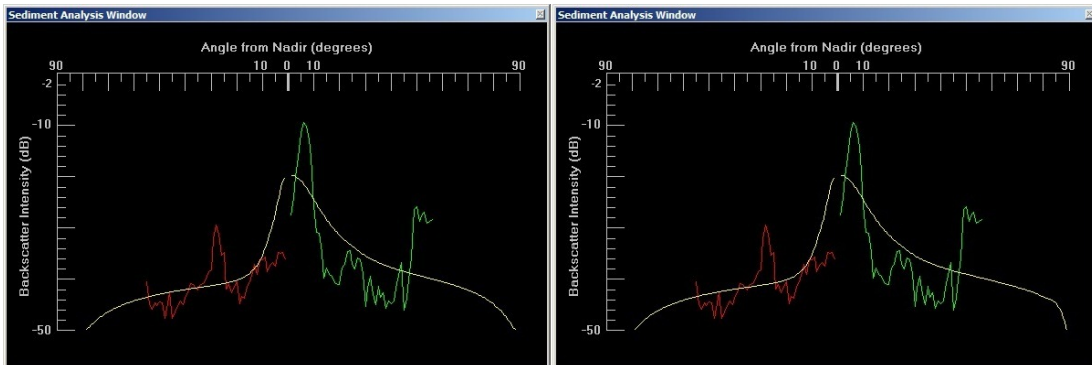
Figure 5.6: Sediment analysis graphs after sediment classification using the Jackson model (left) and the Biot theory (right) for one stacking patch (SO213-17 Profile 14). The recorded and corrected angular responses are shown in green (starboard) and red (port side). The modeled backscatter is presented in yellow.

The Biot theory returns three different sediment classes for the nine samples, classifying over half of the samples as coarse silt. Furthermore, the Biot theory shows problems in calculation and presentation (the automatic analyzing for all patches simultaneously does not work and the colored dot representation of the patch results does not show up). Therefore the Jackson model gives a more reliable impression.

Tab. 5.1 lists the results for the unsupervised sediment classification in *CARIS* (30 pings) and *FMGT* without beam pattern correction. The classification by *FMGT* (two correct estimations with $\pm 1\ \phi$) for SO213-15 is slightly better than in *CARIS* (one correct estimation with $\pm 1\ \phi$) but site SO213-17 is determined as

clay independently in each profile in *FMGT*, which is not correct. Also for SO213-14 two samples were estimated as clay, so that all together five of nine samples are classified as clay in *FMGT*. Therefore both returned results are not satisfying.

Station	Grain size	Profile	*CARIS*	*FMGT*
SO213-14	gravel/	3	coarse silt (1.1)	medium silt
	clay	4	very fine sand (0.8)	coarse silt
		11	very fine sand (0.9)	clay
		12	coarse silt (1.0)	clay
SO213-15	very fine sand/	1	clay (0.4)	medium silt
	coarse silt	11	medium silt (0.6)	coarse silt
SO213-17	fine sand/	2	medium silt (0.9)	clay
	very fine sand	3	medium silt (1.4)	clay
		14	clay (1.6)	clay

Table 5.1: Results of unsupervised sediment classification in *CARIS* and *FMGT*. The data was not corrected for beam pattern and the patch size was set to 30 pings.

In Appendix C the observed angular responses and the modeled response ("No beam pattern correction") from the inverse modeling (Jackson model) are depicted for each patch (30 pings) covering one of the three ground-truthing locations. Afterwards, the grain size was changed to the measured grain size. The model curve adjusts automatically and is also shown in these figures ("Expected model response") as well as all values for the model parameters. Furthermore, the location of the depicted swath is indicated in a digital terrain model and a cross-section of the bathymetry is shown. In comparison, the corrected angular responses look very similar in both software products but both contain marine topographic artifacts. The modeled curves show a better fit to the observed curves in all examples than the adjusted curves according to the true grain size.

With beam pattern correction:

Afterwards, the beam pattern file generated outside of the survey area is applied to the dataset and the ARA is repeated. The results are given in Tab. 5.2 for *CARIS* and *FMGT*. The ARA in *CARIS* determines gravel as dominant grain size for all samples except for SO213-17 profile 14, whereas the ARA in *FMGT* returns four correct estimated sediment types. When allowing one phi deviation, five correct estimations are obtained. These results are clearly more realistic.

Fig. 5.7 shows the angular responses without beam pattern correction (left) and with beam pattern correction (right) in *CARIS* (top) and *FMGT* (bottom) for location SO213-15 profile 1. The measured grain size for the portside is very fine sand to coarse silt. Without beam pattern correction this location is estimated as coarse silt by *CARIS* and as medium silt by *FMGT*. After beam pattern correction these results change to an estimate of gravel in *CARIS* and in *FMGT* to very fine sand. Hence a correct result is changed for the worse in *CARIS*, whereas it is improved in *FMGT* when a beam pattern correction without ground-truthing is applied. This observation is equally valid for the other investigated locations.

Station	Grain size	Profile	*CARIS*	*FMGT*
SO213-14	gravel/	3	gravel (1.6)	very fine sand
	clay	4	gravel (1.2)	medium silt
		11	-	coarse silt / very coarse sand
		12	gravel (0.7)	gravel
SO213-15	very fine sand/	1	gravel (0.7)	very fine sand
	coarse silt	11	gravel (0.8)	coarse sand
SO213-17	fine sand/	2	gravel (3.4)	very fine sand
	very fine sand	3	gravel (1.0)	very fine sand
		14	fine sand (1.9)	coarse silt

Table 5.2: Results of unsupervised sediment classification in *CARIS* and *FMGT*. The data was corrected for beam pattern and the patch size was set to 30 pings.

The observed and modeled angular responses for all nine investigation sites are depicted in Appendix C labeled "With beam pattern correction". The angular responses before and after beam pattern correction show differences in both software products. Before beam pattern correction the angular responses look similar in *CARIS* and *FMGT*, whereas afterwards they differ more strongly. Inspecting the angular responses before and after beam pattern appliance (Fig. 5.7 or Appendix C) together with the applied beam pattern correction (Fig. 5.2), the amplification of the backscatter response across the swath during beam pattern correction in both software programs is visible. The corrected angular response in *CARIS* even reaches values of above 0 dB in the nadir region. The influence of the wider near nadir angular extent of the beam pattern file in *CARIS* is visible in the resulting angular response. The nadir peak in the beam pattern file of *FMGT* covers a smaller angular range and is therefore not that strongly affecting the resulting angular response.
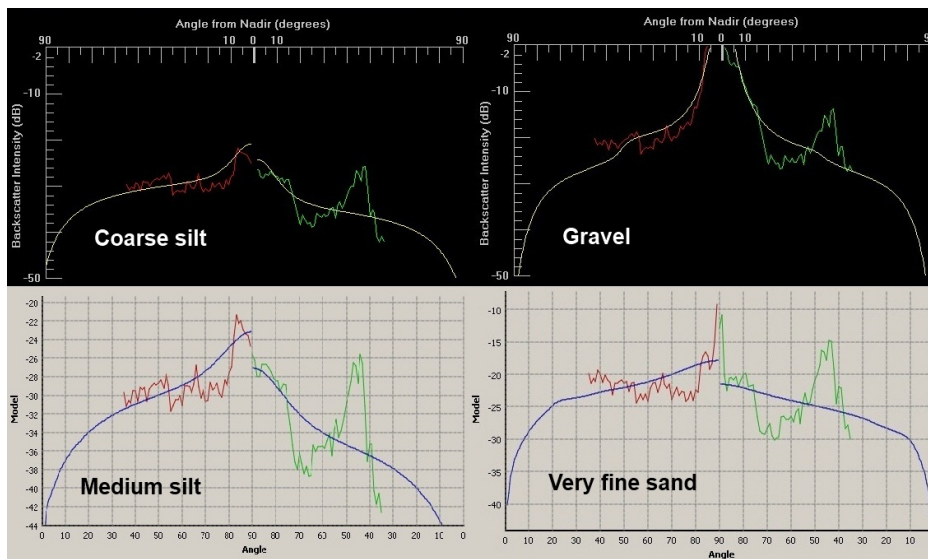

Figure 5.7: Comparison of angular response without beam pattern correction (left) and with beam pattern correction (right) for patch SO213-15 profile 1. The upper graphs were computed in *CARIS* and the bottom graphs in *FMGT*.

The reason for this strong disagreement of the ARA results between the software products may lie in the classification during creation of the beam pattern correction. The observed angular response is modeled by the software under estimation of a specific sediment type. If the assumed sediment type is incorrect, a wrong beam pattern correction is applied to the entire dataset which has a falsifying influence on the following analysis steps. The larger angular extent of the nadir region of *CARIS* indicates the classification of a more coarser sediment leading to a rougher seafloor than in *FMGT*. Regarding the obtained results, the automatic estimation of this particular selected area seems better in *FMGT* than in *CARIS*.

5.3.3.2 Ground-truthing

The ground-truthing possibility in *CARIS* and *FMGT* is given in connection with the beam pattern correction. A beam pattern file of each sediment sampling location is generated, where the sediment type is specified according to the grain size measurement. For this, the profile with the lowest variation of bathymetry covering the investigated location is taken. The across-track depth range of each patch covering a sampling location is listed in Tab. 5.3. The chosen profiles for beam pattern file generation with ground-truthing are underlined.

Station	Profile	Depth variation swath	Depth variation patch
SO213-14	3	450 m	300 m
	4	450 m	450 m
	11	400 m	250 m
	<u>12</u>	400 m	200 m
SO213-15	<u>1</u>	400 m	200 m
	11	550 m	250 m
SO213-17	<u>2</u>	350 m	250 m
	3	800 m	500 m
	14	900 m	300 m

Table 5.3: Depth range variation in across-track direction of each patch covering one of the sampling locations. The underlined profiles indicate which data was used for beam pattern file generation with ground-truthing.

The ARA results obtained by **CARIS** (Jackson model) when applying one of the sites for ground-truthing are listed in App. B, Tab. B.6. The estimated grain sizes do not correspond to the measurements by the laser particle sizer and their confidence levels are worse than when no beam pattern was applied. Using SO213-14 as ground-truthing location, the computed sediment type is gravel for all of the nine examples. For SO213-15 as ground-truthing location, the resulting sediment types are gravel for SO213-14 and medium sand for SO213-15 and SO213-17. This is not very far from reality as it differentiates between the gravel-sized manganese nodules at SO213-14 and the sand to silt sediment at the other locations. The results of SO213-17 as ground-truthing location return gravel for six of the nine samples. In conclusion of this examination, SO213-15 as ground-truthing location seems the be the best choice out of these three in *CARIS*.

Comparing these result with the result of the unsupervised classification, it can be observed that a larger number of correct results are obtained when SO213-15 is used for ground-truthing (6 of 9 with $\pm 1\ \phi$) even though the variation of classes is limited as two different sediment types are mainly returned. When no beam pattern is used (patch size of 10 ping), only three ($\pm 1\ \phi$) correct estimates are returned in comparison. As the variation of the sediment classes is larger and the confidence levels are lower (larger probability) in the unsupervised ARA, the decision on which setting returns the better results is not easily made.

When using the Biot theory (App. B, Tab. B.7) the results are similar as when the Jackson model is used. Nearly all samples are classified as gravel when station SO213-14 or SO213-17 is used for ground-truthing. The best results are obtained with SO213-15 for ground-truthing. The same observation as in the unsupervised classification is made when comparing the results of the Jackson model with the Biot theory for SO213-15 as ground-truthing location: The estimated sediment types returned by the Biot theory are the same or are larger by one sediment class than when the Jackson model is used. Regarding the confidence levels, their values are often given as -1.0 for the Biot theory. This is specified as very good result in the software but it does not seem reliable because, when the confidence level is declared as -1.0, the sediment analysis graph cannot display the modeled angular response. Furthermore, this value represents a vector length and a negative magnitude is therefore implausible. Additionally, it was found out that when the confidence level is declared as 0.0 for a particular patch, this is regarded as "estimate" in the analysis tab of *CARIS*, and therefore a very good estimation for -1.0 does not seem reasonable. Overall, this comparison agrees with the previous observation that the ARA applying the Jackson model seems more robust than the implementation of the Biot theory.

The results of the ARA in **FMGT** are listed in App. B, Tab. B.8. When using SO213-14 as ground-truthing location in *FMGT*, six of the nine samples are classified as gravel, which is similar to the result of *CARIS* and not very trustworthy. Applying SO213-17, no correct classification is returned, whereas the outcome of SO213-15 as ground-truthing location correctly estimates six sediment types (if gravel is assumed for SO213-14). When allowing a deviation of one sediment class, seven correct results were obtained. This corresponds to the evaluation of the ARA results by *CARIS* that station SO213-15 is the best suited ground-truthing location. In *FMGT* the outcome of the ARA with ground-truthing at SO213-15 are slightly better (6 of 9 correct estimations with $\pm 1\ \phi$) than with appliance of a beam pattern without a specified sediment type (5 of 9 with $\pm 1\ \phi$), and even clearly better than when no beam pattern is applied (2 of 9 with $\pm 1\ \phi$).

In Tab. 5.4 the number of correctly estimated sediments type are listed with allowance of a deviation of $\pm 1\ \phi$. The quantity of correct estimations is similar in both software products for the same setting. It can be concluded that applying ground-truthing information yields better results than an unsupervised classification. When station SO213-15 is used for ground-truthing the largest number of correct sediment classification results is obtained. However, when the classifications of *CARIS* are examined more closely, the low variation of returned sediment classes leads to a careful acceptance of the corresponding results.

	Unsupervised classification		Supervised classification		
Software	no bp	bp	gt SO213-14	gt SO213-15	gt SO213-17
CARIS	3/9 (10) & 1/9 (30)	4/9	4/9	6/9	3/9
FMGT	2/9	5/9	3/9	6/9	2/9

Table 5.4: Quantity of correctly estimated sediment types with a deviation of $\pm 1 \phi$ when no beam pattern was applied (no bp), a beam pattern without ground-truthing was applied (bp), and when each of the sediment sampling locations was used for ground-truthing (gt). The quantity of correct results of *CARIS* without beam pattern correction are listed with a patch size of 10 and 30. The other values refer to patch sized of 30 pings.

5.3.4 Comparison of areal ARA results

FMGT provides the possibility to view the ARA results as surface (Fig. 5.8 and App. A, Fig. A.9 to A.13). This resulting surface representation is very clear and user-friendly as the viewer gets a good impression of the grain size distribution throughout the area. It is generated by interpolation of the individual patch results into a regular raster. Overlapping values are interpolated, which results in a mixture of samples of different quality. Furthermore, a distinction between areas where a lot of data is available and areas where only one profile was recorded is not possible. Therefore a representation of the ARA results by indicators colored according to the sediment type per patch seems better suited for the evaluation of the ARA classifications of this data. In surveys where the data acquisition is accomplished systematically (resulting in a homogeneous data distribution) this interpolated surface representation for the results might be suited better.
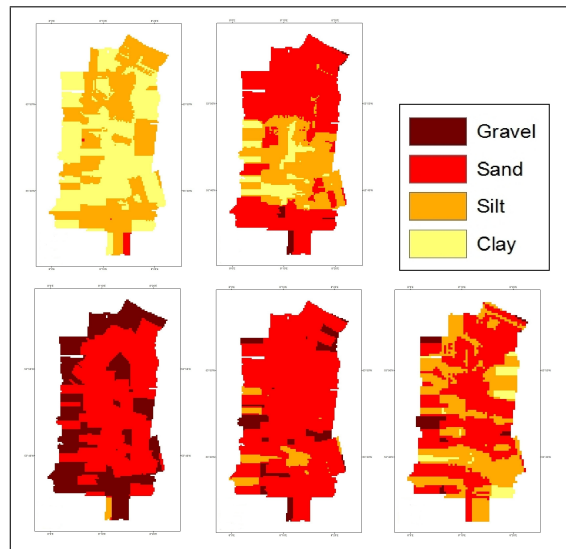
Figure 5.8: ARA results of *FMGT* with different settings. From top left to bottom right: no beam pattern correction, beam pattern correction with reference patch of homogeneous area outside of the investigation area, beam pattern correction with ground-truthing at SO213-14, beam pattern correction with ground-truthing at SO213-15, and beam pattern correction at SO213-17. (Mercator projection, standard parallel: 39° S) See App. A, Fig. A.9 to A.13 for charts in larger scale.

To compare the areal results of the ARA in *CARIS* to the ARA in *FMGT*, a visualization in *Fledermaus* is used (Fig. 5.9). When no beam pattern is applied in *CARIS* the investigation area is classified as a mixture of clay, silt and sand. In *FMGT* clay is more predominant when using the same settings. When a beam pattern is applied, the whole area is classified as gravel in *CARIS*, whereas the ARA in *FMGT* returns sandy sediments for the northern and southern part and silty or clayey sediments for the intermediate region. Applying SO213-14 for ground-truthing, *CARIS* obtains gravel as predominant sediment class with some sandy influence. Also the ARA of *FMGT* returns a mixture of sand and gravel, but the sandy part is larger than in *CARIS*. When SO213-15 is used for ground-truthing, sand, along with some gravel, is returned as predominant sediment in *CARIS*. The ARA of *FMGT* estimates mostly sandy sediments mixed with some gravel and silt. Applying SO213-17 as ground-truthing location the *CARIS* returns a mixture of gravel (mostly in the north and south) and sand, and *FMGT* a heterogeneous distribution of all sediment types.

Comparing the areal results to the expected sediment distribution, the best result is obtained in *CARIS* when SO213-17 is used for ground-truthing as the north and very south of the survey area are estimated as gravel and the intermediate region as sand. This evaluation of the areal results stands in contrast to the assessment based on the patch comparison, where the classification with the same setting only yields 3 out of 9 correct results.

When examining the areal results of *FMGT* more closely, two classifications coincide best with the expected distribution. When a beam pattern correction without ground-truthing is applied, the estimation of the relative grain size distribution differentiates between coarser sediment in the north and very south and finer-grained material in the intermediate investigation area. This corresponds to the expected assumption, even though the absolute grain sizes are estimated to be smaller (sand and silt-to-clay). When SO213-14 is used for ground-truthing, the ARA in *FMGT* returns correct grain sizes (gravel and sand) but their distribution is not as clearly defined as when a beam pattern correction without ground-truthing is applied. The assessment of the result applying a beam pattern correction (without ground-truthing) as one of the best results in *FMGT* corresponds to the evaluation based on the patch results at the sediment sampling locations. The classification with SO213-14 as ground-truthing was evaluated as a weaker estimation when comparing the results at the sediment sampling locations as only 3 of 9 (with a deviation of $\pm 1\,\phi$) samples were classified correctly.

The results of *CARIS* and *FMGT* differ significantly from each other, which was already observed during investigation of the patch results for the ground-truthing locations. The evaluation of the classification results with diverse settings differs between the two assessment approaches (location-based and areal). These differences can be attributed to local erroneous estimations which can strongly influence the comparison at few chosen locations. In the areal inspection they are not that distinct and their effect on an evaluation is reduced. The reliability of a location-beased observation can be increased by using a larger quantity of locations with known sediment type.
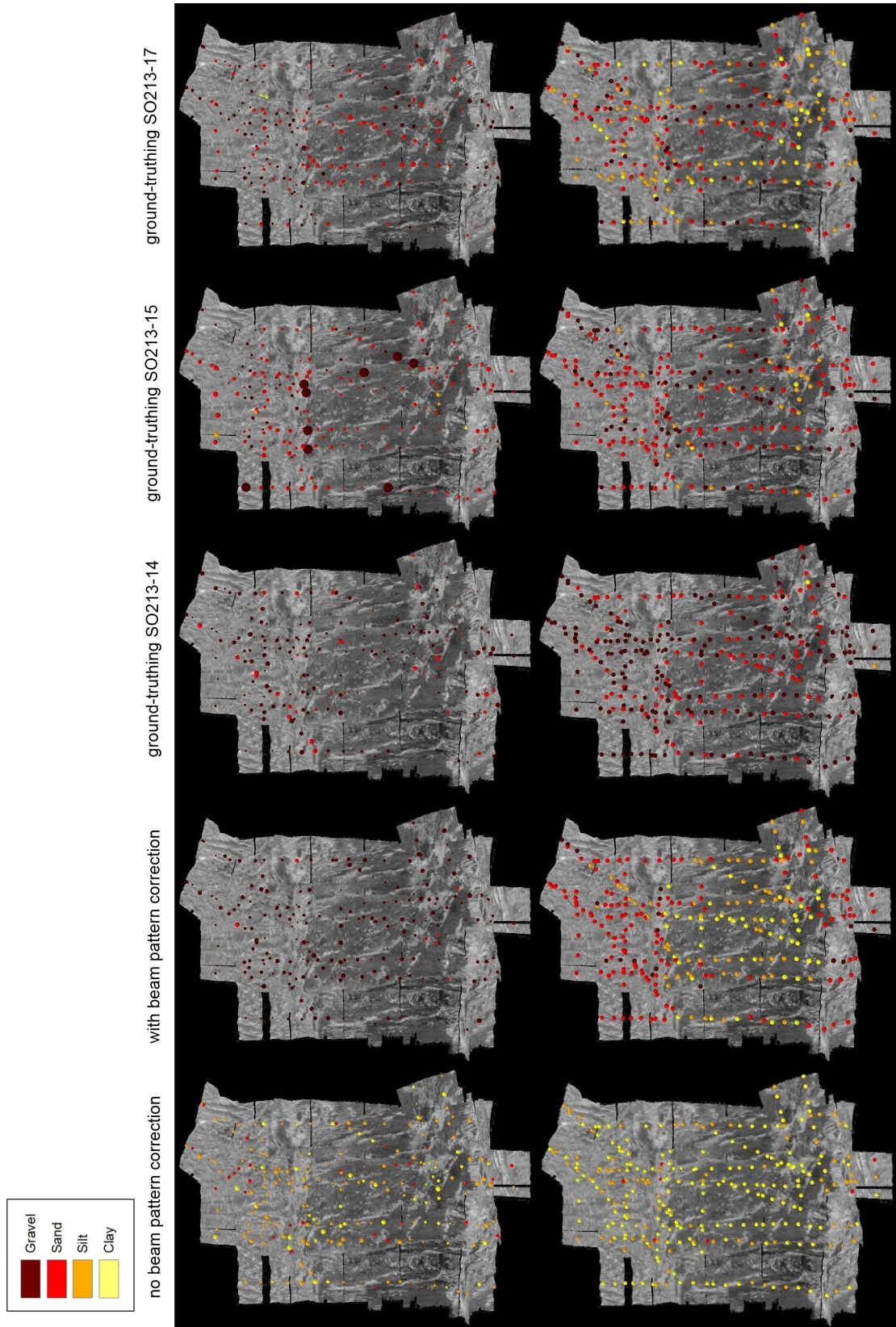
Figure 5.9: ARA results of *CARIS* (top) and *FMGT* (bottom) with different settings for beam pattern correction visualized in *Fledermaus*.

5.3.5 ARA – Conclusion

Comparing the measured sediment grain sizes to the results of the ARA in *CARIS* and *FMGT* of the corresponding patch sizes (Section 5.3.3), the sediment sampling location of SO213-15 is estimated more often correctly than SO213-14 or SO213-17. It also has the lowest confidence levels (largest probability) in *CARIS*, and furthermore, the ARA returns better results when SO213-15 is used as ground-truthing location than one of the other two locations.

To analyze the reason for better results at SO213-15 the local bathymetry of the sediment sampling locations is further inspected. Fig. 5.10 shows overviews and bathymetric cross-sections of the patches at the investigated locations used for ground-truthing. White markers indicate the sampling sites. Even though the swath at SO213-15 (profile 1) has a quite large depth variation of 400 m to 500 m, the variation along each patch in across-track direction is relatively homogeneous. The largest depth change occurs in the nadir region. The cross-section of SO213-17 looks quite similar, but the depth range is larger and the analyzed patch covers a downslope, which results in a heterogeneous angular response. The cross-section of SO213-14 shows depth variations at a smaller scale in horizontal direction and a large depth range across the swath of 800 m to 900 m. Beyond that the sediment is covered with manganese nodules, which leads to a combination of the angular response by different sediment types that cannot clearly be assigned by the ARA.
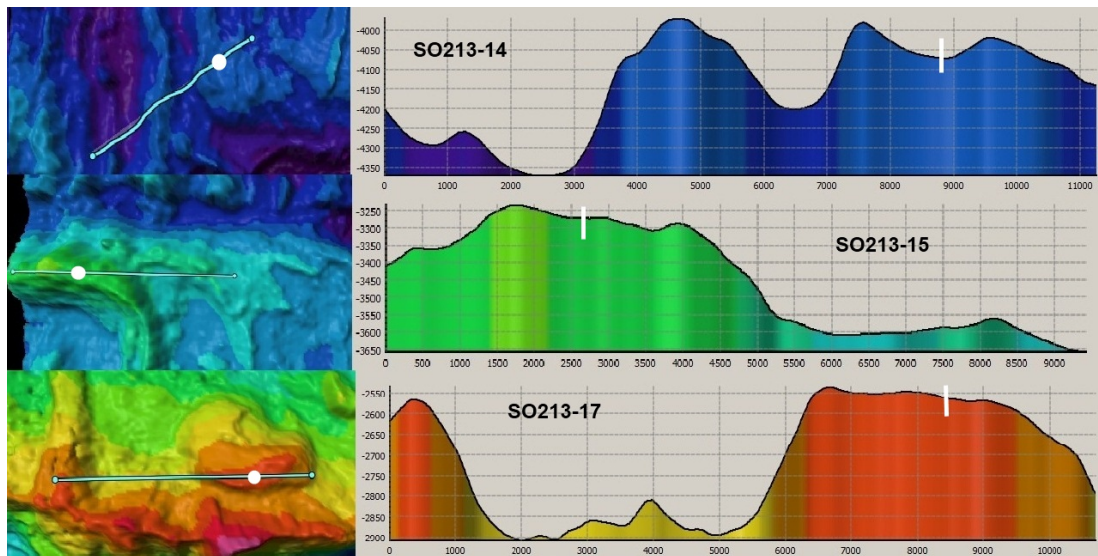

Figure 5.10: Marine topography at ground-truthing locations. The turquoise line shows the location of an average swath of the corresponding patch. A bathymetric cross-section at each location is shown on the right. The white dots (left) and lines (right) indicate the sediment sampling location.

In conclusion, it can be stated that the bathymetric variation plays an important role for the sediment classification. Due to the imperfect topographic correction, the angular responses are falsified and in areas with strong depth variations, estimates of sediment types are unreliable. At the most homogeneous location of SO213-15 the unsupervised classification and the ground-truthing works best.

5.4 Comparison of Geocoder in *CARIS HIPS and SIPS* and *Fledermaus*

The main focus of both software products is quite different. *CARIS HIPS and SIPS* is intended for processing and mapping of different geodata (SBES, MBES, SSS, Lidar) whereas *Fledemaus* has its main focus on data visualization. It is not designed for as many geodata sources as *CARIS*, which can import over 40 different industrial formats. The Geocoder software by Dr. L. Fonseca was implemented into both software packages a few years ago. As the same software tool was implemented, no large differences in the main algorithm are expected. But due to the differing focuses, slight differences in readable formats and result representation are recognizable. The most important differences are listed in Tab. 5.5 and are further outlined in the following.

CARIS offers a larger variety of import formats (Tab. 5.5), whereas the readable backscatter formats are the same in both software packages (beam average, beam time series, sidescan time series). *FMGT* has its main focus on multibeam backscatter processing and analysis, but sidescan data can also be loaded. *CARIS* in contrary already had tools for handling sidescan data before Geocoder implementation. It offers special sidescan routines, which are not available in *FMGT*.

Both software products have the same Geocoder **corrections** built in. The default settings are slightly different, but the main distinction is that in *CARIS* a smaller number of corrections are hidden, which allows a stronger involvement and a better understanding of the processing steps. By using the intermediate step of GeoBaR creation in *CARIS*, different tiles for the same line can be created with various correction settings for comparison, without the influence of interpolation of overlapping areas caused by mosaicing. In *FMGT* processing is done automatically during mosaic creation. To generate mosaics with different correction settings, the flags of the first processing steps (coverage, adjusting, filtering) need to be deleted before re-computing a mosaic. *FMGT* is designed for fast backscatter processing on a regular base where no large changes in the settings are necessary, whereas the backscatter processing in *CARIS* permits a stronger involvement by the user.

In Geocoder by Dr. L. Fonseca a weighted interpolation is used for **mosaic** blending, where the nadir and outer beams are assigned with lower values than the mid-range beams. The implementation of this blending algorithm did not fully succeed in *CARIS* (Sec. 5.2) but is accomplished in *FMGT*. *FMGT* displays more mosaic statistics if required by the user. *CARIS* and *FMGT* offer different methods to improve the visual appearance of mosaics. In *FMGT* the range of the color palette can be adjusted to the range of the data values (histogram stretching). In *CARIS* the visual improvement of a mosaic is done using two sliders: one for the brightness and one for the contrast. This approach makes it harder to repeat a distinctive setting for another mosaic. *FMGT* offers a larger variety of mosaic export formats than *CARIS* (Tab. 5.5).

Both software solutions use the Jackson model for the **ARA** but *CARIS* additionally offers the Biot theory for modeling the angular response. Beyond that,

	Product	*CARIS HIPS and SIPS*	*Fledermaus (FMGeocoder Toolbox)*
	Version	7.1.1	7.3.1
	Import formats	Over 40 formats	GSF, XTF, GSF/XTF Pair, GSF/S7K Pair, Kongsberg (*.all)
Backscatter processing	Backscatter format	Beam average, beam time series, time series (sidescan)	Beam average, beam time series, time series (sidescan)
	Backscatter corrections (user settings possible)	Auto gain, auto TVG, anti-aliasing, beam pattern, AVG, despeckle	Tx/rx correction, AVG, beam pattern
Mosaicing	Mosaic blending algorithm	Overwrite, shine through, underlay, auto-seam (pixel chosen by weight), full blend (weighted interpolation)	Blend (not weighted), weighted methods: no nadir if possible 1, no nadir if possible 2
	Mosaic statistic	Statistic stored in layers: contributor, intensity, original intensity, weights, bounding polygon	Statistic surfaces: mean, median, minimum, maximum, mode, skewness, kurtosis, variance, m3, m4, quadrille range, num. indep. samples, num. samples, grazing angle, num. samples, 10th percentile, 25th percentile, 75th percentile, 95th percentile
	Mosaic export layers	Contributor, intensity, original intensity, weights	Intensity & statistics (see mosaic statistic)
	Mosaic export formats	TIFF, GeoTIFF, ascii	GeoTIFF, surface (z, xyz, ArcView grid (.asc), binary heights (.bin), GMT grid (.grd), floating point, Fledermaus format (.sd)
	Improvement of mosaic appearance	Changes in brightness and contrast	Histogram stretching
ARA	Acoustic model	Jackson model or Biot theory	Jackson model
	Patch size	Can be set by the user (> 5 pings)	30 pings
	ARA result presentation	Patch based	Surface based and patch based
	ARA export formats	Ascii file (patch based)	Surface: GeoTIFF, surface, ArcGIS format, SD / patch: ascii ARA, point ARA Object (.sd)

Table 5.5: Comparison of possible settings and data formats in *CARIS HIPS and SIPS* and *FMGeocoder Toolbox*.

the sediment grain size table can be edited and the patch size can be specified by the user, whereas its size is fixed to 30 consecutive pings in *FMGT*. In contrast, *FMGT* also offers, besides the regular patch representation, a surface presentation of the ARA results. Furthermore, the export possibilities in *FMGT* for the ARA results are more numerous than in *CARIS*.

In conclusion, *FMGT* has a stronger "black box" character. The user does not have as many possibilities to interfere during data processing and analysis as in *CARIS*. But *CARIS* also has a lot of hidden computation. Neither software manual explains the methods and algorithm precisely. But in comparison, *CARIS* provides the user with more information for an evaluation of the results (e.g., images of mosaic weight distribution, confidence levels assigned to the ARA results, or implementation of the intermediate processing step of GeoBaR generation). The advantage of *FMGT* in contrast lies in a more robust computation routine and a larger variety of export formats which allows more possibilities of result representation.

Even though Geocoder has been implemented in *CARIS HIPS & SIPS* and *Fledermaus* a few years ago, it is continuously improved (Hatzky et al., 2011). Some problems which need to be fixed are obvious, for example the export of ARA results in ArcView format does not work in *FMGT*. There are also possible settings given that do not have a function and will be removed in the next version (IVS3D Fledermaus, 2011). The latest two versions of *FMGT* crashed when loading Kongsberg raw files and the automatic sediment analysis in *CARIS* does not work for the Biot theory and some angular response graphs could not be viewed for the Jackson model. But when comparing both software applications today with their stages one year ago, large improvements are noticeable.

Another important circumstance that needs to be taken into account regards the extent of the imported raw data files into *CARIS*. For backscatter processing, it is desired to investigate only straight recorded profiles and no data in between where the ship changes direction. In *CARIS* the data between profiles was deleted in the Swath Editor during depth measurement processing. It was noticed that GeoBaRs cannot be created from data files where the first pings are missing. This does not apply to data files, where the last pings were deleted. Therefore, the relevant files were split according to the start and end time of the profiles. Before loading the data in *FMGT*, all raw files were split to remove the ship movements. It would have also been possible to remove undesired data segments after loading. The most simple approach would be to align the file extents to the profiles during data acquisition by stop and start recording according to the profiles.

A further problem occurred when pings were deleted in the middle of a file in *CARIS*: when patches were generated for the ARA, these missing pings were ignored for patch creation, but the start or end of a patch was not adjusted to the data gap and instead always consisted of the given ping number. As a result, a patch could inherit data of different profiles. Therefore, it is recommended that the data is split before importing in *CARIS* so that the ARA results are not corrupted by incorrect stacking.

5.5 Evaluation of the usage of Geocoder for the backscatter data of SO213-1

Geocoder is mainly used for mosaicing and remote sediment classifications of shallow-water environments and shows good results for such areas (Fonseca et al., 2009; Llewellyn, 2006). Deep-water surveys in contrast cover larger areas per swath, have a lower ping rate (data acquisition rate), and a smaller swath angle, as the slant-range of the outer beams is very long and is subject of attenuation in water. These differences create complications in processing and analyzing of deep-water data in Geocoder. Furthermore, the area under investigation shows a strong variation in marine topography due to its location in a tectonically active environment. Therefore the regular Geocoder settings developed for shallow-water environments cannot be applied to the deep-water data of SO213-1 without constraints.

The corrections applied to the multibeam data in the Geocoder implementation in *CARIS* and especially *FMGT* cannot be greatly interfered with by the user. The characteristics of deep-water data did not play a larger role when the corrections were applied, as they are mainly focusing on mapping and gain recalculation. The only correction which has to be examined more closely is the specification of the AVG window size parameter. A smaller value was chosen (30 instead of 300) so that the averaging over a larger quantity of pings was prevented. This seemed reasonable due to the strong morphological variation in the data and their insufficient compensation.

The resolution of intensity pixel values is much better in across-track direction than in along-track direction for the investigated data, which is visible in the resulting mosaics. Furthermore, the mosaics show seam-effects in the northern part of the survey area where a larger number of profiles overlap. The seam-artifacts are not caused primarily by the deep-water acquisition geometry but are amplified by the locally strong changing bathymetry and therefore small scaled backscatter pattern. On the contrary, areas with no overlap (i.e., south-western part) show nadir artifacts as there is no data of a further profile available for interpolation, which is not due to the deep-water environment.

The properties of a deep-water environment are especially crucial for the ARA. The ARA resolution is defined by the patch size and is therefore linked to the swath width. Due to the acquisition geometry in deep-water environments the ARA resolution is very low compared to shallow water surveys. A very important requirement for a robust grain size classification is that there should be only one sediment type per patch. The larger the patches, the greater the possibility of containing different sediment types. In shallow-water studies an approximate length of 30 consecutive pings is used, resulting in squared patches (Fonseca et al., 2009). As stated earlier, squared patches are not practical for the data used in this thesis. When using a patch length of 30 pings for the data of SO213-1, the resulting patch has an average patch size of 2.3 x 6.2 km². As the possibility of covering different sediment types in one patch is very high in deep-water environments, the risk of falsified ARA results is high.

Sediments do not consist of equally sized particles as they are usually a mixture of sediments of different sizes. Thus, angular responses are usually a mixture of different contributors anyway. The described differentiation of sediment classes becomes important when sharp sediment boundaries occur like the boundary between the area covered by manganese nodules and the silt-to-sandy section in the investigation area. In deep-water environments the possibility is high that such boundaries are not clearly detectable.

In literature a solution for the problem of varying sediment types within a patch (sediment boundaries) is discussed. It is proposed to cluster areas with similar angular responses and therefore the same sediment type. For each cluster (or acoustic themes) an average angular response is calculated instead over half a swath and used for the ARA. To identify such clusters a computed mosaic is used. But in mosaics the angular response in normalized by applying an AVG correction. As a result, similar sediment types can be mapped with different backscatter values in a mosaic or different sediment types can be mapped with similar values as observed by Fonseca et al. (2009). In Fonseca et al. (2007b) an attempt was made to use an automatic clustering algorithm (unsupervised k-means clustering algorithm). Furthermore it is tested to combine mosaicing and the ARA. The research to improve these techniques is on-going (Fonseca et al., 2007b). The clustering approach is not yet implemented into *CARIS* and *FMGT* but would be very promising especially for the remote sediment estimation in deep-water environments, where the chance of not resolving sediment boundaries properly is very high due to the large swath width. This would also give a possibility to improve the ARA resolution of deep-water surveys.

The ARA analyzes the backscatter strength variation according to different grazing angles. The swath aperture angle of a deep-water area is smaller in comparison to shallow-water surveys. This limitation of grazing angle reduces the angular resolution and has a negative impact on the ARA results.

Considering the imperfect suited characteristics of the survey area for the processing and analysis by Geocoder, the final results are better than probably expected. In IVS3D Fledermaus (2011) it is stated that the ARA does hardly work for deep-water environments. Nevertheless, two third of the samples were estimated correctly in the end. But for this overall result the chosen methods and settings are very important and need to be examined carefully.

In conclusion, Geocoder can be used for backscatter processing, mosaicing and analysis of data acquired in deep-water environments. A patch test in a homogeneous area with grain size determination (ground-truthing) is highly recommended. To obtain a homogeneous mosaic, parallel profiles with strong overlap (over 50 %) should be recorded. To obtain a reliable estimation of the sediment type by the ARA the survey area should not include very strong bathymetric variations.

Chapter 6

Backscatter Analysis

In this chapter the angle-invariant backscatter data is examined more closely. At first, an attempt is made to explain the evolution of the geomorphological features as they influence the acoustic response of the seafloor. Then the variations in mosaicked backscatter are described and a conclusion on the sediment type is derived from the angle-invariant backscatter. Furthermore, the source of high backscatter strengths of topographic slopes is discussed.

6.1 Geological description of the investigation area
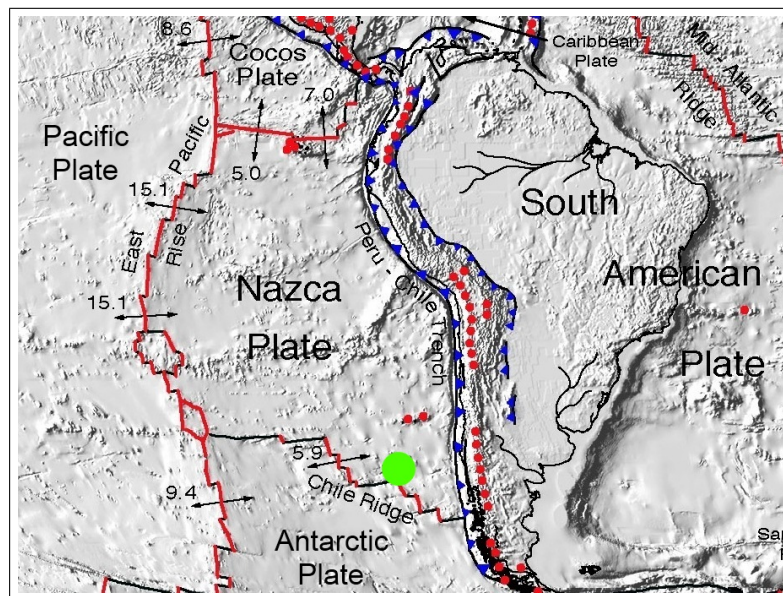
Figure 6.1: Tectonic environment of the investigation area. The arrows and numbers indicate the local spreading direction and its rate in cm/year. The location of the survey area is marked in green. (NASA, 2002)

The area of investigation is situated in a tectonically active environment with the Chile Rise as the dominant tectonic feature. The Chile Rise depicts the boundary of the Nazca and the Antarctic Plate (Fig. 6.1). It is a fast spreading ridge with an average spreading rate of 6 cm/year (Bahlburg et al., 2012). The Valdivia

Fracture Zone shifts the spreading center of the Chile Rise about 650 km to the east. At the transform fault of this fracture zone dextral[8] movement takes place. The area of investigation is located north of the eastern part of the Chile Rise and to the east of the southern continuation of it (Fig. 6.2).
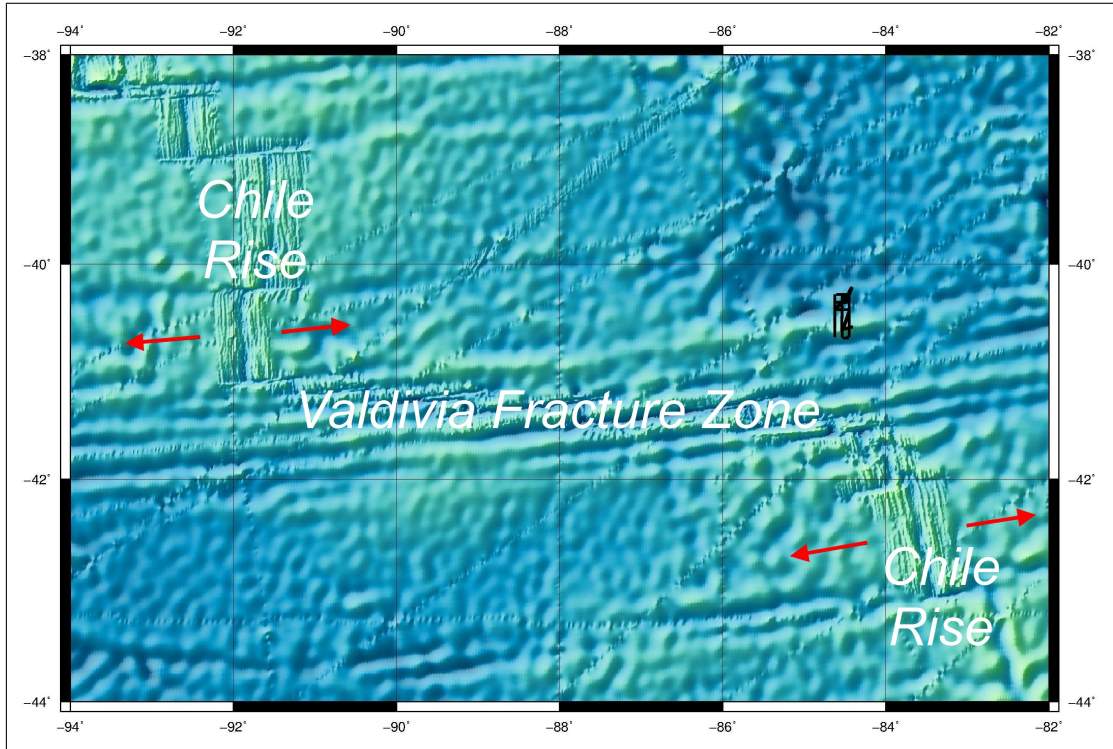

Figure 6.2: Geomorphological environment of the investigation area (profiles are depicted as black lines). The spreading directions of the Chile Rise are indicated by red arrows. The bathymetric source data is GEBCO_08 (30 arc-seconds). As the data originates from different sources, variations in accuracy are noticeable. The high resolution data of ship soundings for example can be recognized in this chart. (Mercator projection, standard parallel: 41° S)

The geomorphological structure of the investigation area can be ascribed to the influence of the Chile Rise and the corresponding transform fault of the Valdivia Fracture Zone. The spreading center of the ridge runs in north-south direction. As the plates move apart, new crust material ascends and welds as new crust to the edges of the older. This is not a continuous process but is subject to variations, and therefore the amount of ascending material varies with time. As a result, linear seafloor features (lobes or abyssal hill fabric) are developed that are oriented in north-south direction parallel to the spreading ridge. Such structures are visible in the intermediate depth region of the study area (Fig. 6.3). They can also be found in the northern part, but there they are overlain by folding caused by spreading of the western part of the Chile Rise.

In the very south of the survey area (south of the Guafo Ridge) similar seafloor characteristics as in the north are noticeable: the water depth reaches values of more than 4,000 m, and lobes (created during formation of the crust) are overlain by folds.

---

[8]The northern plate moves to the east, the southern plate moves to the west.

The intermediate area (including the Guafo Ridge) shows different characteristics than the north and very south, as its morphology is not affected by folding and its water depth generally does not exceed 4,000 m. The boundaries between these three differentiated areas are depicted by faults in the seafloor topography, which are highlighted in 6.3 with black lines. As the intermediate area shows smaller water depths, it can be assumed that it was moved upwards. This seems reasonable as vertical movements can usually be observed at transform faults close to the spreading axis as a result of upwards ascending crust material. The material underneath a fast spreading ridge is evenly distributed along its axis (Standish et al., 2010). Even though the spreading center is located somewhat to the south of the investigation area, hot material located underneath the survey area may have caused the vertical movement. This assumption is corroborated by the seamount at the southern slope of the Guafo Ridge. This feature might be a volcanic origin, as its caldera can be recognized in the bathymetric data. Its presence underpins the thesis of past volcanic activity in this area.
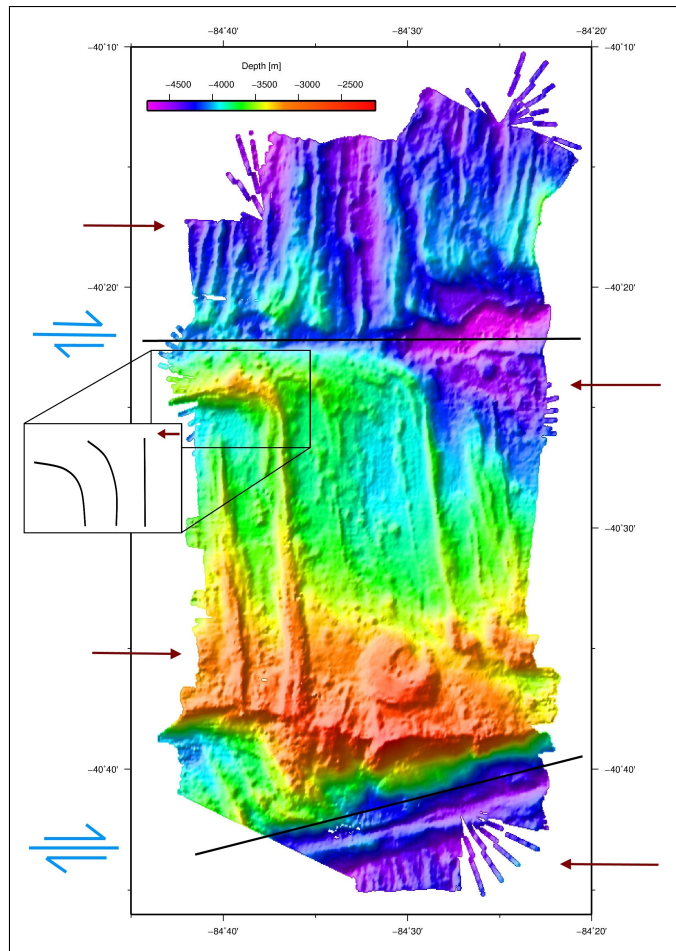

Figure 6.3: Survey area with depicted tectonic forces (red arrows) as source for geomorphological evolution of that area. The boundaries between areas of different forces are presented as black lines.

When examining the seafloor structures more closely, it can be assumed that different directed forces are active in the area of investigation (Fig. 6.3). In the northern area which is characterized by folding, the force is oriented from west to east, caused by the spreading at the western Chile Rise. In the northwest

of the intermediate part, eastwards distractions of north-south oriented lobes are observable and are generated by a force from east to west (inlet in Fig. 6.3). This direction of force is opposite to the direction of the northern area. The boundary between these areas of different influences is depicted by the northern fault. The similar distraction of lobes can be recognized in the southeastern part of the intermediate area. But there, the direction of distortion is oriented in the opposite direction, induced by a western force. As the southern fault indicates a boundary between different tectonic movements, an eastern force can be assumed to be predominant in the very southern part of the survey area. These sudden changes in direction of active forces are probably not realistic in such a small area. The above described forces can also be understood as relative forces resulting of different velocities into the same direction of the outlined parts of the investigation area. That would mean that the northern part has the largest, the intermediate area a medium, and the southern part the lowest velocity in eastern direction.

6.2   Description of angle-invariant backscatter data

When examining the angle-invariant backscatter data in the mosaic created in *FMGeocoder Toolbox*, three different areas can broadly be separated according to their backscatter strength (Fig. 6.4): the northern (A) and southern (C) parts show high backscatter values whereas the intermediate region (B) generally shows lower values.

The strong reflections in **area A** correspond to the bathymetric deep-water area with depths of more than 4,000 m and strong fissured relief. These folds are oriented in north-south direction and have an average height of 100 m compared to their surrounding and a width of 500 m to 1,000 m. The average backscatter value in this area is about -19 dB. The backscatter values are relative values as the system was not calibrated. For a further investigation of the backscatter representation of smaller seafloor features (indicated in Fig. 6.4) the mosaic was draped on a DTM in *Fledermaus* and perspective views of them were created (Fig. 6.5). In area A some local regions with lower backscatter values (ld1, ld2, and ld3) are noticeable. They are generally oriented in north-south direction and coincide with the linear depressions between the folds. The backscatter responses at their bottoms are lower (-27 dB) than of the adjacent flanks (-20 dB) as visible in Fig. 6.5-a,b,c. The fault (f1), which demarcates the bathymetric deeper and intermediate area, is visible in the angle-invariant data due to its relatively low backscatter values of around -30 dB (Fig. 6.5-d). The water depth of the eastern part of the fault lies around 4,700 m and the width of the fault is around 2 km to 3 km. At its bottom, low backscatter values of -30 dB can be observed. Continuing towards the west, the depth decreases to around 4,100 m. Furthermore, a knoll (k) can be recognized in the intensity data of that area, which has a height of 200 m and a width of 2 km. Its top shows lower reflectivity (-30 dB) than its flanks (-10 dB) as visible in Fig. 6.5-d. The high intensity area A extends further south of the fault along the slope into the intermediate-depth area.

Area B is characterized by lower backscatter strengths of around -35 dB. Here, the mosaic shows local heights of intensity oriented mainly in north-south direc-
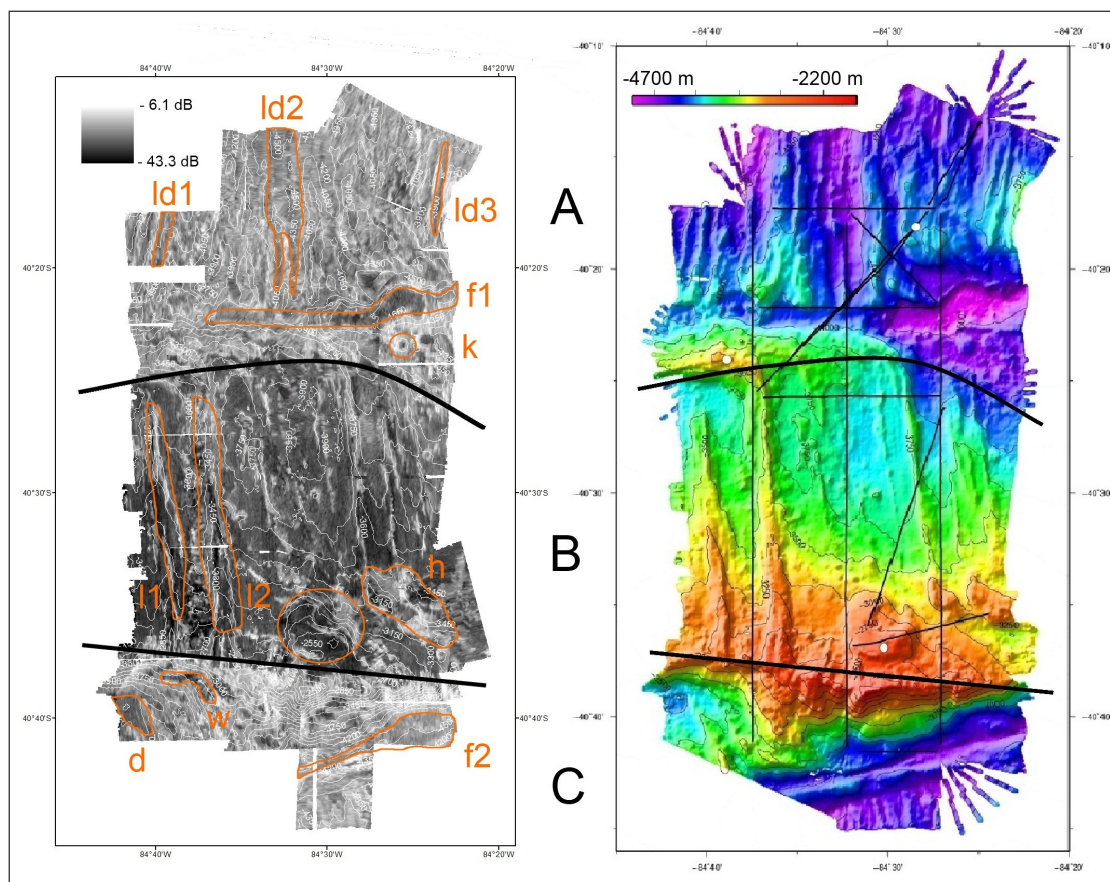
Figure 6.4: Comparison of backscatter responses and bathymetry of the survey area. Mosaic created with the "no nadir if possible 2" method in *FMGT* with 150 m contour intervals (left) and chart of seafloor topography (right). View App. A, Fig. A.14 for a larger scale of the mosaic with contour intervals. (Mercator projection, standard parallel: 39° S)

tion (l1, l2) (Fig. 6.5-e). They correspond to lobes with an average height of 200 m and a width of 2,000 m. They can be found throughout area B and stand out due to the relatively high backscatter response (-17 dB). The backscatter intensities of some of their crests are lower (-32 dB). The hills in the southeastern part of B (h) are visible in the mosaic as an irregular pattern of higher backscatter values (Fig. 6.5-f). These seafloor structures have a combined average height of 400 m relatively to their surrounding and a width of 4 km. The caldera of the seamount (g) on the northern slope of the Guafo Ridge is visible in the angle-invariant data due to its strong seafloor response (Fig. 6.5-f). The southern boundary of B coincides with the linear peak of the Guafo Ridge.

The southernmost **area C** shows strong backscatter values around -20 dB. It corresponds to the southern scarp of the Guafo Ridge and the adjacent fault (f2) in the south of the ridge in large water depths. Along the strong intensity response of the scarp, some darker patches (w) with lower backscatter intensities can be noticed (Fig. 6.5-g). They deviate perpendicular to the gradient of the scarp. In the southwestern corner of the dataset a depression of 800 m (d) is characterized by lower backscatter values (-30 dB) compared to its surrounding (-18 dB) (Fig. 6.5-g). At the foot of the southern fault (f2) a mixture of lower (-23 dB) and much stronger (-6 dB) intensity values are found (Fig. 6.5-h).
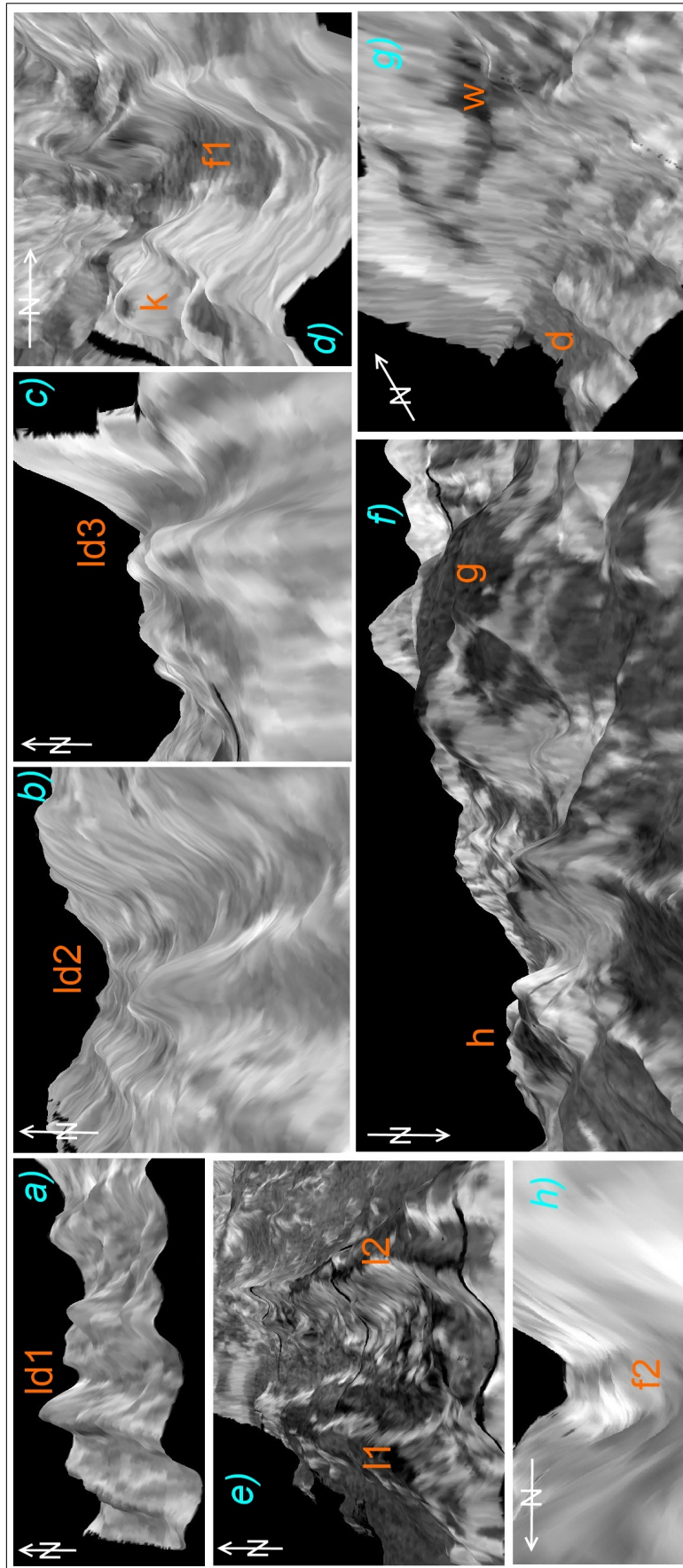
Figure 6.5: Perspective views of seafloor features visible in the backscatter data with a vertical exaggeration (VE) of 6. The arrows indicate North.

Regarding the comparison between backscatter and bathymetric data, it can be stated that the seafloor topography influences the intensity. For a further examination, cross-sections of the bathymetry are compared with the backscatter values (Fig. 6.6). The upper cross-section runs from the north to the south through the entire survey area, the middle example depicts a cross-section from east to west of area A, and the last cross-section is located in area B in east-western direction. The corresponding backscatter values are visible in the cross-section graphs as well as on top of each cross-section.
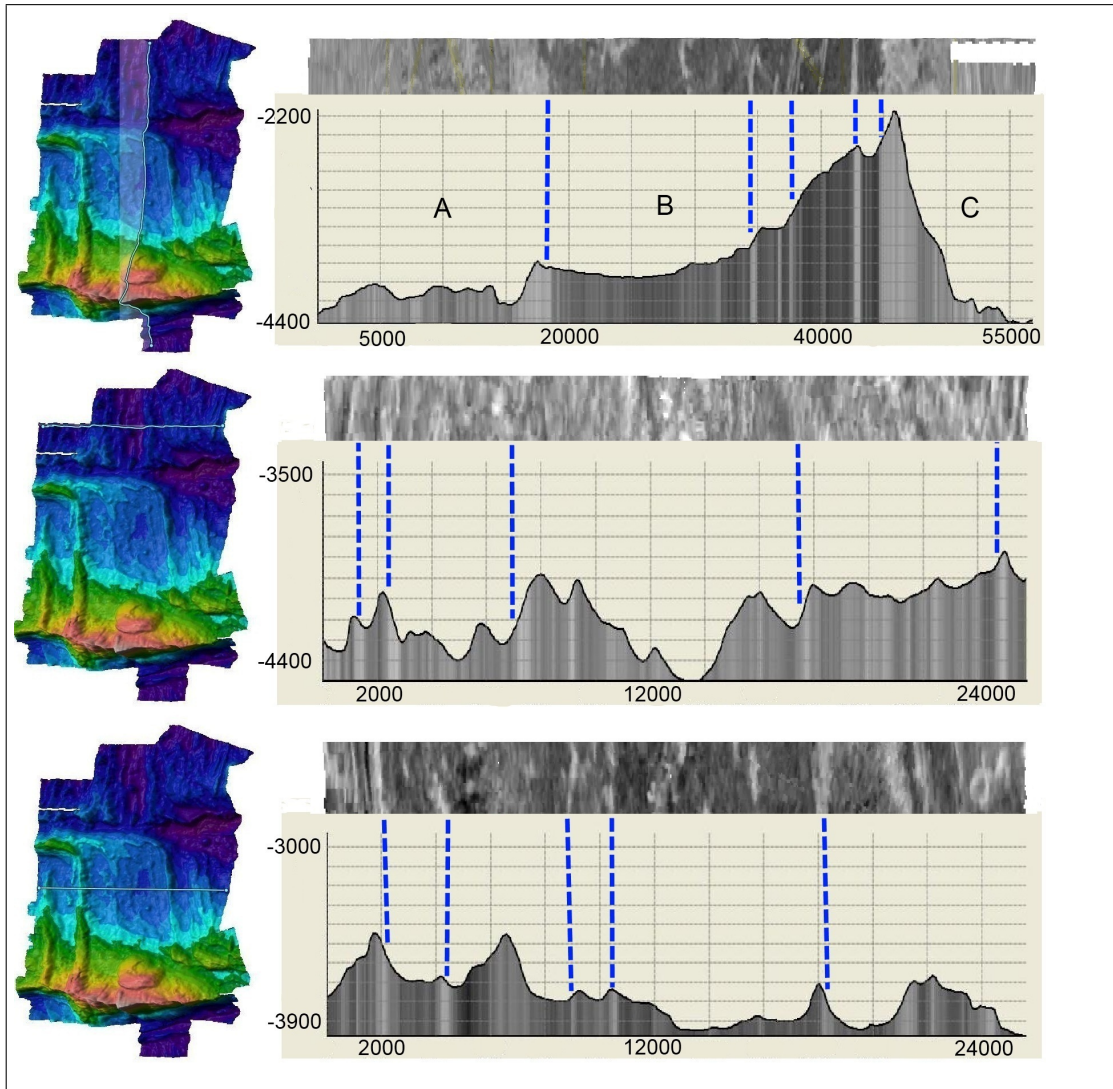
Figure 6.6: Bathymetric cross-sections of the investigation area with corresponding backscatter strengths.

In the upper cross-section it can be seen that the strong backscatter values in C correspond the strong scarp of the Guafo Ridge, which was already noticed before. The slope of the southern scarp is more than 20° in average (2,000 depth meters fall in 5,000 m distance). At the northern scarp of the ridge the slope is gentler with 5° to 10°. The acquired backscattered intensity is much lower in that area.

The boundary between area A and B is apparent in the upper cross-section. The decrease in scattered intensity occurs in correspondence with a decrease of small-scale height variations in B. This is also recognizable when comparing cross-sections through area A (Fig. 6.6, middle) and B (Fig. 6.6, bottom). The seafloor topography of A shows more small-scaled variations and is therefore rougher than area B.

It can be concluded that backscatter values can be correlated with the marine topography: slopes generally larger than 13° can be recognized in the mosaic as areas of strong backscatter response. Even slopes of small horizontal dimensions (300 m) are distinctly visible in the mosaic. This way, flat and homogeneous structures are visible by their relative lower backscatter response in areas with a high backscatter return, whereas in low backscatter regions, features are depicted by the high backscatter response of their slopes.

6.3 Influences on backscatter responses

Generally, there are different reasons for variation in intensity responses of the seafloor in MBES backscatter data. They can be linked to seafloor roughness by features (e.g., ripples) or to seabed sediment structures and their physical properties (Medialdea et al., 2008). Backscattered responses are also influenced by instrumental parameters like the local angle of incidence of the beam at the seafloor, signal absorption, or sudden changes in seafloor topography (Lurton, 2010). The variation of sediment grain size is the main contributor to variations in backscatter strength. Generally, the backscatter intensities increase with grain size (De Moustier et al., 1991; IHO, 2005), so that softer sediments like clay show smaller backscatter strengths than when coarser sediments with low water content are predominant. The seafloor response can be further influenced by local factors as gas outflow or occurrence of benthic fauna (Medialdea et al., 2008).

The survey area is characterized by strong variations in bathymetry. As this has an influence on the backscattered intensity, first, the more homogeneous areas are compared for a conclusion on the sediment distribution throughout the investigation area (Section 6.3.1), before the influence of seafloor topography and directionality of ensonification are investigated (Section 6.3.2).

6.3.1 Conclusion on grain size distribution based on backscatter measurements

For a probable conclusion on sediment type distribution, the local backscatter intensities were inspected more closely. The angular responses could not be used due to the influence of seafloor topography on the angular responses.

Examining morphologically relatively flat areas of the dataset, it can be recognized that local variations in backscatter strength are present. To link backscatter strengths to grain sizes, the sediment sampling locations are examined

more closely. They are situated on mounds or valleys, and their backscatter response is comparatively low to their surrounding (Fig. 6.7).
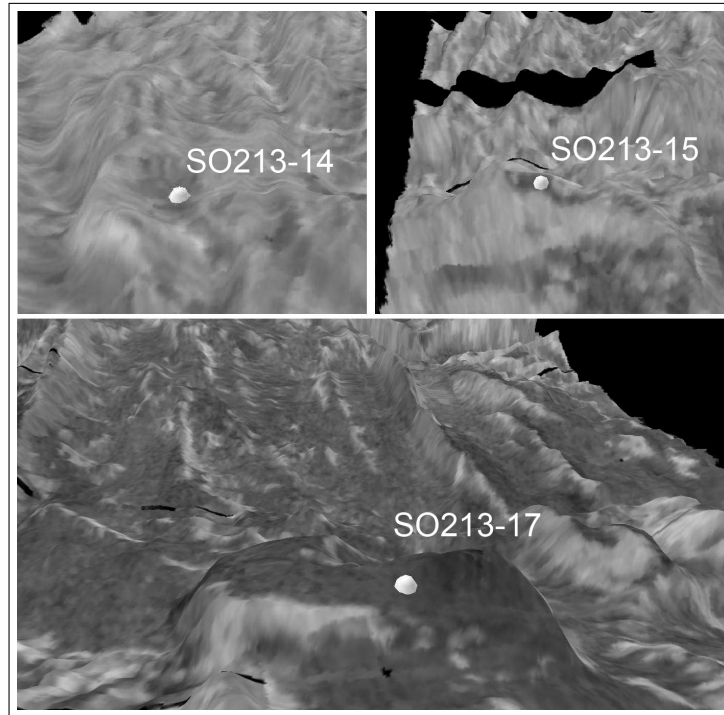

Figure 6.7: Perspective view of sediment sampling locations in *Fledermaus* (VE = 6). The line of sight is oriented towards north for all images.

The backscatter values at these stations differ slightly (Tab. 6.1). Station SO213-14 shows the highest backscatter response (-27 dB), which is probably caused by the nodule abundance. A nodule-bearing seafloor results in higher seafloor roughness and therefore yields a higher backscatter response than sandy or silty seabed (Scanlon et al., 1992). At the other two sites calcareous ooze was determined as predominant sediment with a grain size in the order of fine sand to coarse silt. Such finer sediment has a lower roughness and the acoustic impulse penetrates deeper into the seabed where it is stronger attenuated. Therefore, the acquired backscatter values are lower (-33 dB and -34 dB) than at SO213-14, which corresponds to the general assumption that coarser sediments show stronger backscatter intensities.

Station	Sediment type	Backscatter strength
SO213-14	gravel/clay	-27 dB
SO213-15	very fine sand/coarse silt	-33 dB
SO213-17	fine sand/very fine sand	-34 dB

Table 6.1: Backscatter strengths of sediment sampling locations.

In Fig. 6.8 the Parasound echograms at the sampling locations are depicted. During the acquisition of these echograms, the ship's speed was reduced until the sampling location was reached. Therefore the mayor part of the data shows the ensonification of one particular seafloor sector.

The echogram of SO213-14 shows the strongest reflection and smallest seabed penetration of the signal in comparison to the other locations. This corresponds to the observation of highest backscatter response compared to the other stations and can be explained by the presence of manganese nodules. The hardest reflector is not found at the surface, which may be due to side effects. Side effects occur if the horizontal resolution of the Parasound system is lower than the dimension of seafloor features. As a result, a larger number of seafloor features are ensonified simultaneously and their responses are overlain in the echogram. This effect can also be observed above the surface of SO213-14, where a weak and wavy sediment layer of a neighboring topographic elevation can be distinguished.
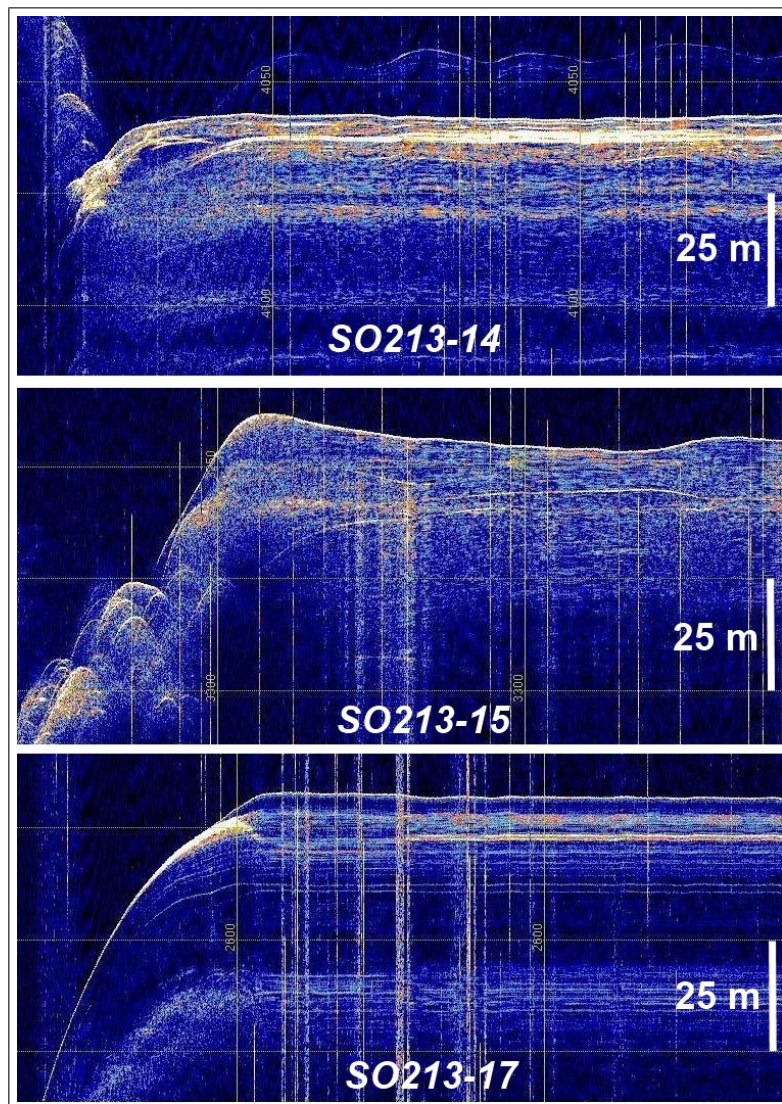
Figure 6.8: Parasound echograms of sediment sampling locations. Refer to App. B, Fig. B.3 for a larger representation.

At SO213-15 and SO213-17 the penetration of the signal into the seafloor is greater (about 20 m) than at SO213-14 (about 10 m). Site SO213-17 shows stratified sediment layers, whereas at SO213-15 the different layers are not recognizable and side effects can be observed. SO213-15 shows a hard surface reflector, whereas the upper sediment layer at SO213-17 implicates a greater water content

due to its transparent appearance in the echogram. A higher water content in the seabed surface results in a lower impedance contrast at the water-sediment boundary and therefore a weaker backscattering signal. This higher water content may be the reason why the backscatter value at SO213-17 is lower than at SO213-15 even though the grain size is larger.

Parasound data was collected during backscatter and bathymetric data acquisition along the profiles. However, the data could not be used for further information on sediment distribution throughout the area due to side effects caused by strong topography variations. The sub-bottom profiler has a larger beam angle (4°) than the EM 120 (2°) and therefore a lower horizontal resolution. This way, adjacent seafloor features influence the collected data which is visible as side effect in the echogram like pointed out before.

The remote detection and investigation of manganese nodules by sonar systems is of large interesting for a future resource exploitation. Yet, problems in detection arise as manganese nodules vary strongly in sizes and seafloor coverage and therefore make a prediction of their general backscatter response difficult. Nodule-bearing seafloor generally yields a higher backscatter response (Scanlon et al., 1992). Different backscatter surveys with towed sidescan sonars with various frequencies discovered that it is possible to estimate the percentage of seafloor covered by nodules when a frequency of 30 kHz and higher is used. Conclusions on the nodule size are possible using a frequency of 9 kHz and to lesser extent at 15 kHz (Weydert, 1990). The mapping of nodules is crucial at low frequencies, as the visibility of nodules depends on the contrast to the surrounding sediment and therefore on the frequency. As the wavelength of the EM 120 (about 16 cm) is larger than the size of the nodules (few centimeters), they should not be visible in the backscatter data (Mitchell, 1993). However, the nodules in the investigation area show a large density and are therefore combined into larger acoustic targets which also can be detected in low-frequency data (Chakraborty et al., 2004; Scanlon et al., 1992).

The obtained values for nodule-bearing seabed (-27 dB) and silt-to-sandy sediments (-33 dB) can be applied throughout the survey area (for flat seafloor topography) to determine the boundary of nodule abundance. When inspecting the linear depressions in the folded part in the north of the dataset (area A), they show similar backscatter values (ld1: -26 dB, ld2: -27 dB, ld3: -25 dB) as at SO213-14. Therefore a similar density of manganese nodule as at SO213-17 can be assumed at these locations. Furthermore, as the backscatter values generally do not decrease below -30 dB in area A, it can be concluded that manganese nodules spread all over this part. This assumption is further strengthened by the presence of large water depths (below 4,000 m) which are greater than the assumed CCD. The only exception regarding the higher backscatter level is the fault (f1), which is displayed in the angle-invariant data with a value of -31 dB for its deeper part in the east. This backscatter response is considerably lower than the average of that part, but higher than at SO213-15 and SO214-17. A possible explanation for this local decrease in intensity could be that the manganese abundance is lower in this fault than in the other part of that area.
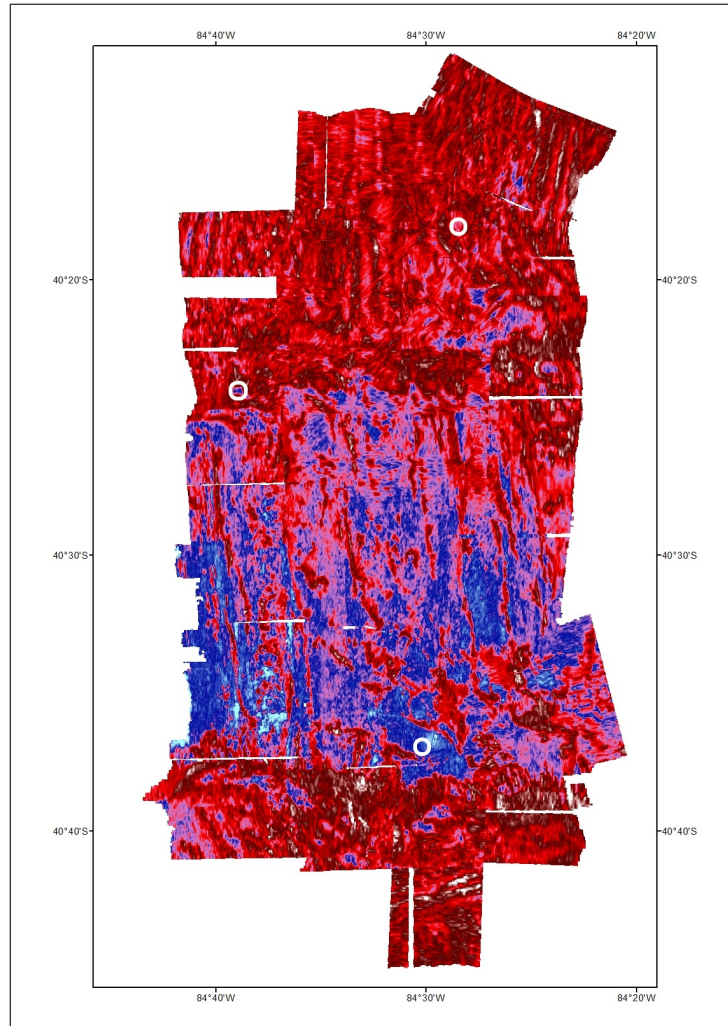
Figure 6.9: Mosaic generated in *FMGT* showing angle-invariant data with a different color palette than gray scale to enhance backscatter strength variations. The color palette ranges from dark red (high backscatter strengths) to light blue (low backscatter strengths). The sediment sampling locations are marked by white circles. (Mercator projection, standard parallel: 39° S) [App. A, Fig. A.15]

Area B is characterized by average backscatter values between -35 dB and -29 dB. Higher intensities can be correlated to topographic variations, which is further analyzed in Sec. 6.3.2. When investigating the distribution of low backscatter strength throughout that region, it can be observed that the intensity of the backscattered signal decreases towards the peak of the Guafo Ridge (Fig. 6.9). This would initially indicate a decrease in grain size towards the south (De Falco et al., 2010). This assumption does not correlate with the measured grain sizes at the ground-truthing locations SO213-15 and SO213-17. Different explanations are possible for this contradiction: First, the measured grain sizes do not represent the overall sediment distribution (i.e., the coarser grain size at SO213-17 is just a local variation). Second, it could be possible that the seabed in the south has a greater water content in the upper sediment layer and therefore lower backscatter intensities. As the second possibility corresponds with the observation made in conjunction with the Parasound data, this seems to be the more presumable explanation.

The locally increased water content in the upper sediment layer might be explained by currents. In the area of investigation the currents generally flow from the south towards the north with a distraction by the Coriolis force in western direction. A southern seafloor current might be diffracted by the morphological elevation of the Guafo Ridge. Parts of the current could ascend with the Guafo Ridge and result in turbulences on the northern side of the ridge. The current's speed is presumably correlated to the distance to the ridge. As the current decreases in speed, carried sediment particles are accumulated. This might explain the concluded sediment distribution as coarser material is precipitated further south and finer material in the north in conjunction with the decrease in the current's speed.

Area C is characterized by high backscatter responses (about -20 dB). The presence of manganese nodules can be excluded as possible cause for the high backscatter response because the water depth lies above the CCD. As the southern slope of the Guafo Ridge is very steep, sediments cannot accumulate easily and slides are enforced. Basement outcrops in this part are very likely and would explain the high backscatter response as a result of a high impedance contrast. In Fig. 6.5-g part of the southern scarp is depicted. Local backscatter minima can be distinguished, which might be caused by the erosion of sediments and dismantling of the scarp resulting in sedimentary wedges (w) with low backscatter response. The assumption of basement outcrop as source for high backscatter strengths is corroborated when examining the data recorded by the individual profiles for the southern scarp. High backscatter intensities were collected by each profile and are independent of the recording direction. An instrumental cause can therefore be neglected.

As the EM 120 was not calibrated, absolute backscatter values were not determined, and can therefore not directly be matched with other backscatter measurements of different investigations. However, the relative values between two sediment types can be compared to examples in literature: The difference in average backscatter intensities between area C (basement) and area B (sandy sediment) lies around 15 dB. Similar observations were made by Keeton et al. (1996) (13 kHz) where a backscatter contrast of 10 dB was reported between this two facies for uncalibrated data.

6.3.2 Influence of seafloor topography on backscatter responses

As the backscatter data was corrected for topographic influences during Geocoder processing (Fonseca et al., 2007a), backscatter variations in the data should only be due to changes in sediment properties. This is not the case, as patches with very high backscatter values can be observed in nadir regions. This indicates an incorrect AVG correction which normalizes the backscatter response along the swath.

Furthermore, slopes of topographic features throughout the survey area are depicted in the angle-invariant data by high values, which was already stated earlier. This becomes obvious when inspecting the slopes throughout the survey area in conjunction with the backscatter data (Fig. 6.10). It can be observed that slopes steeper than about 13° result in strong acoustic responses. This accounts mainly for area B which has a lower mean angular response and therefore local high backscatter returns are better recognizable than in area A or C. This for example refers to the north-south oriented lobes in both depictions in Fig. 6.10. Some other features like the seamount on the northern slope of the Guafo Ridge are not that easily recognizable in the backscatter mosaic (Fig. 6.10, left) as in the chart with the slope representation. (Fig. 6.10, right)
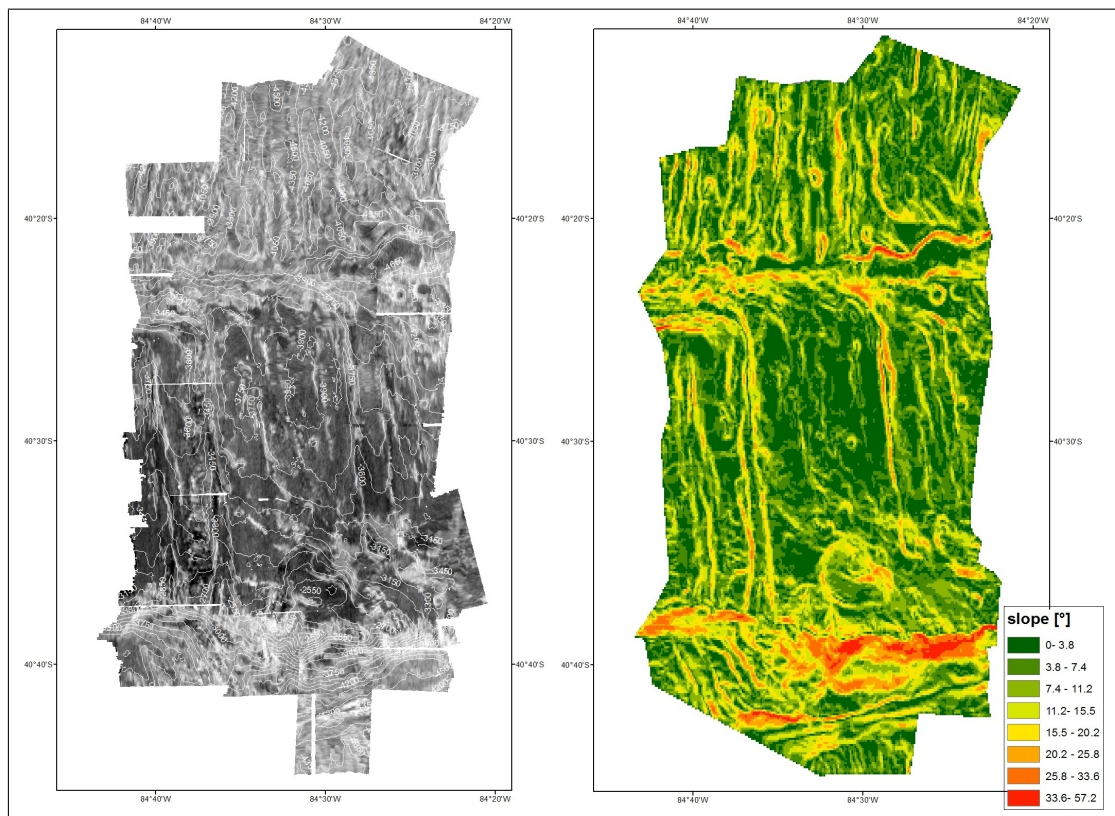
Figure 6.10: Mosaic of angle-invariant backscatter data (left) and slope of survey area computed in *ArcGIS 10* (right). (Mercator projection, standard parallel: 39° S) [Refer to App. A, Fig. A.16 for an enlarged image of the slope representation.]

The comparison of backscatter intensities and slope indicates that the overall strong backscatter response of area A cannot be caused by seafloor slopes. This is a further argument which pinpoints the theory of nodule abundance in that region. The same accounts for the southern scarp of the Guafo Ridge, where the high backscatter strength cannot be correlated satisfyingly to topographic variations and therefore strengthens the assumption of basement outcrops.

Seafloor topography also influences the sediment distribution, as sediments do not accumulate as much on steep slopes as in flat areas. Furthermore, slopes enhance sediment slides. As a result, the sediment cover at slopes would be thinner than in geomorphological flat areas and even basement outcrops may occur

like at the southern scarp of the Guafo Ridge. The acoustic signal penetrates the sediments (depending on the frequency and sediment type) and could reach the underlying basement (or a buried horizon) when the sediment cover is low (Keeton et al., 1996). Both situations (basement outcrops and minor sediment cover) would result in comparably higher backscatter responses. The sediment coverage is estimated to amount to approximately 50 m (personal comment by Prof. Dr. Ralf Tiedemann) in the survey area. As the penetration depth of the echosounder signal can be constituted to a multiple of the signal wavelength, the penetration depth would not exceed 2 m for the EM 120 (Beyer et al., 2005). In conclusion, the penetration of the acoustic signal down to a deeper horizon of rock is not likely for smaller and gentler seafloor features. Therefore, the cause for stronger backscatter values at slopes must be due to another cause than local changes of sediment distribution on slopes.

As the backscatter data was corrected for topography during processing, all variations in intensity should be related to varying sediment types. Yet, the removal of topographic influences was not applied to full success (Chapter 5). For further demarcation of the source of high backscatter intensities at topographic slopes, the backscatter data of each profile was investigated separately to compare the acoustic intensity recorded for a specific seafloor feature from different angles.

As an example, in Fig. 6.11 the backscatter data of profile 2 is depicted. In the cross-section it is clearly visible that slopes which are oriented towards the sonar and are therefore hit by a larger incidence angle are represented by higher backscatter values than slopes facing in the opposite direction.
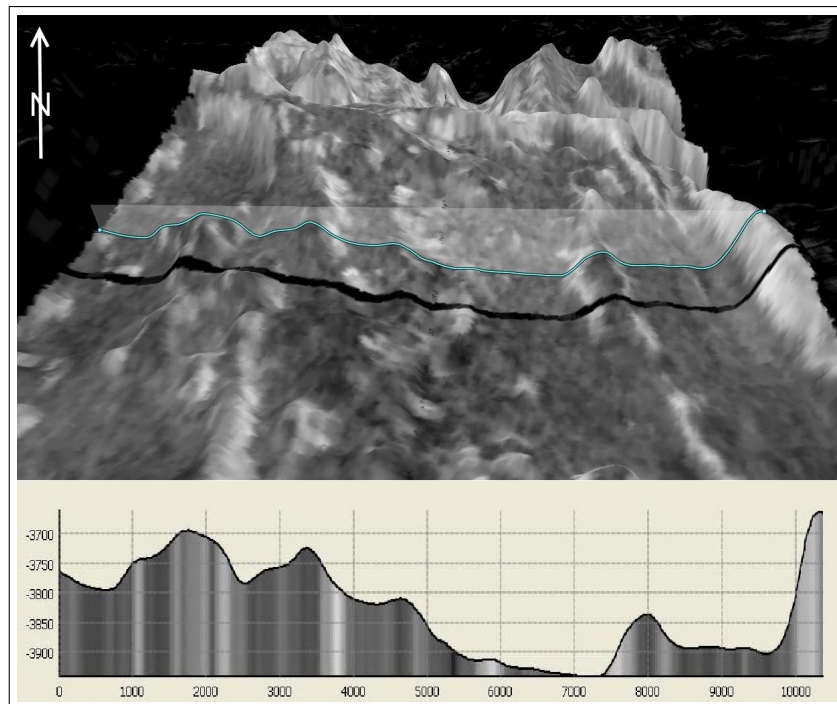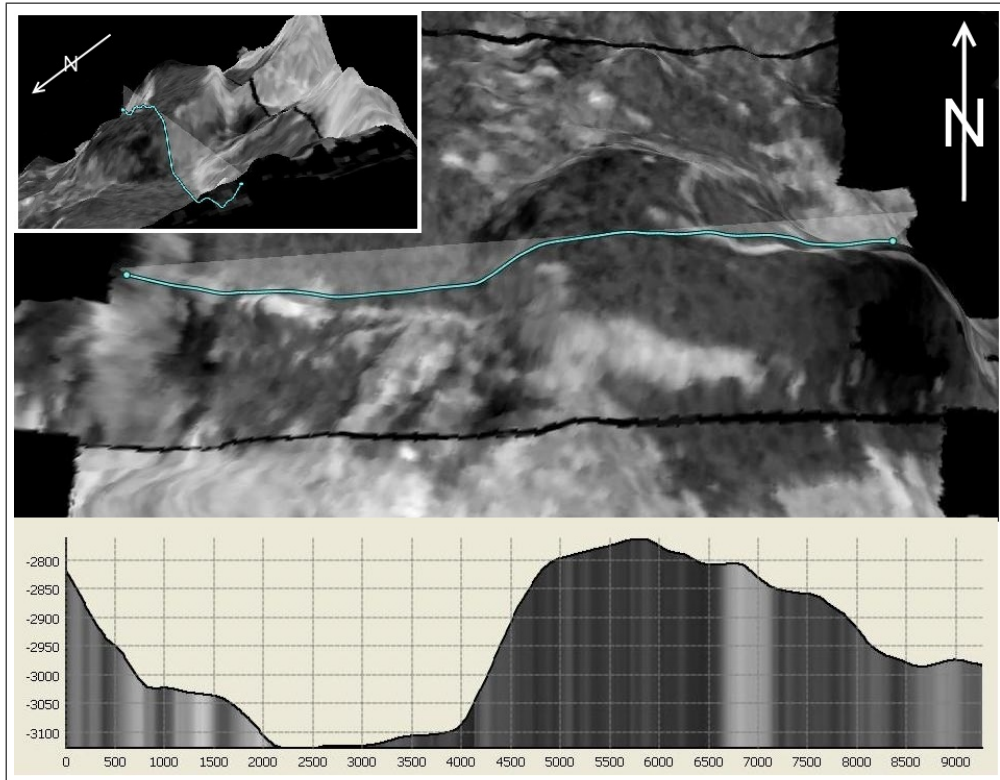

Figure 6.11: Perspective view of backscatter data of profile 2 (top) combined with seafloor topography with corresponding cross-section perpendicular to the travel direction (bottom) generated in *Fledermaus* (VE = 6). The cross-section graph is colored according to the backscatter values and its location is depicted in the overview by a turquoise line.

In Fig. 6.12 in contrast the southern part of profile 2 is shown. It can be observed that the backscatter values of the cross-section in the area of the seamount do not correspond to the previous assumption at first. In a slightly rotated view of the seafloor feature and the cross-section location (inlet in Fig. 6.12) it can be recognized that a slope in direction of travel is present. This circumstance results in a lower backscatter response than actually expected. In conclusion, both presented examples indicate an erroneous computation of the actual slope in Geocoder in across- and along-track direction.

Figure 6.12: Perspective views of backscatter data of profile 2 combined with seafloor topography (top) and corresponding cross-section perpendicular to travel direction (bottom) of the seamount at the northern scarp of the Guafo Ridge in *Fledermaus* (VE = 6). The cross-section graph is colored according to the backscatter values and its location is depicted in the overview by a turquoise line.

In addition, the presentation of a north-south oriented lobe in area B recorded by different profiles in diverse directions is compared. In Fig. 6.13 the data of profile 2 (Fig. 6.13-a), 3 (Fig. 6.13-b), and 6 (Fig. 6.13-c) for one lobe is depicted. Profile 2 was recorded in north-south direction, profile 3 in south-north direction, and profile 6 in east-west direction. When the recording direction is parallel to the elongation of the feature, its slope is facing towards the sonar and therefore its extent is clearly recognizable in the backscatter data like in profile 2 for its western slope. The topographic extent of the lobe in the angle-invariant data differs in the three datasets, as in profile 2 only the slope depicts high backscatter values, whereas in the other two profiles the strong acoustic response expands over a larger extent.
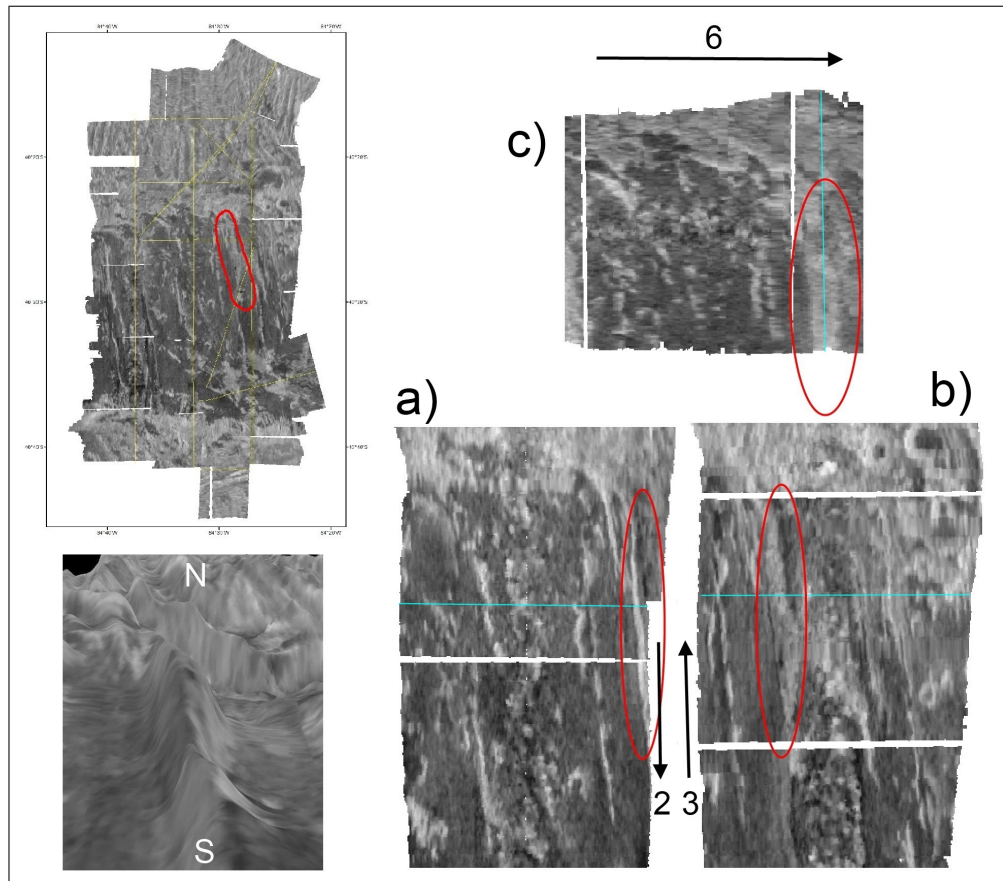
Figure 6.13: Backscatter data of different profiles visualizing a north-south oriented lobe in area B. Its location is marked in the overview map (top left) and a perspective view is depicted (bottom left). Each profile where this feature was recorded is shown: profile 2 (a), profile 3 (b), and profile 6 (c). The directions of recording are indicated by arrows and the locations of the cross-sections depicted in Fig. 6.14 are indicated by turquoise lines.

As it is shown in Fig. 6.13-c, the lobe is distinguishable in profile 6, which was recorded perpendicular to the structure orientation. In Fig. 6.14 cross-sections through the bathymetry are presented. The graphs are color-coded by corresponding backscatter strengths. In this figure, it can be observed that even though no slope is exposed towards the sonar system in profile 6, the acoustic response of the lobe is higher than of the surrounding environment (Fig. 6.14-c).

This example shows that the enhancement of topographic features in the backscatter data does not only occur if the slope is facing towards the echosounder in across- or along-track direction. The cause for the high backscatter response of the lobe in profile 6 could not clearly be distinguished. It was shown that the computation of the actual slope and therefore a complete removal of the topography influence was not accomplished successfully during processing. As this circumstance can be excluded as source for this example (as no slope is present), a possible influence of local changes in sediment can be assumed. This might be a lower sediment coverage or a stronger seafloor roughness caused by small-scales seafloor features (e.g., ripples), which are smaller than the resolution of the sonar.
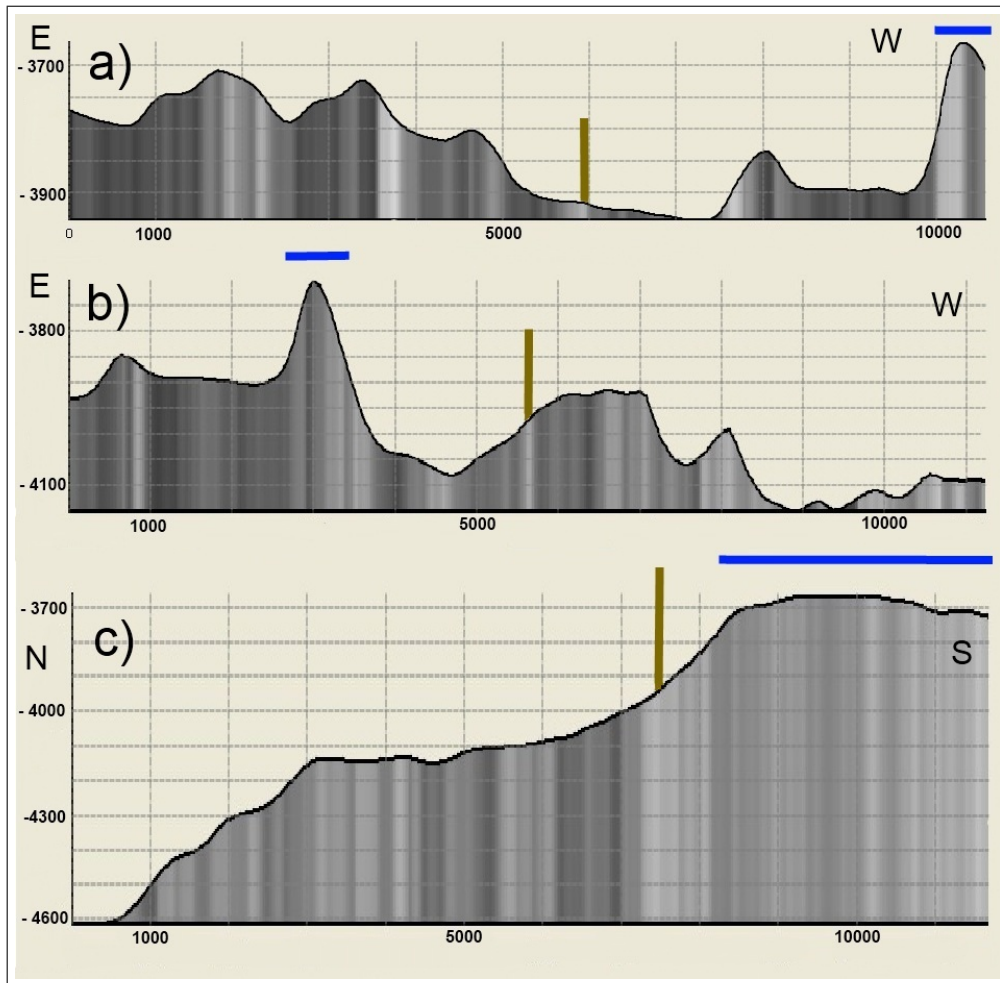
Figure 6.14: Cross-sections through bathymetry (perpendicular to recording direction) and backscatter data are depicted for a lobe of area B with data of profile 2 (a), 3 (b), and 6 (c). The location of the investigated lobe is marked blue in all three cross-sections and green lines indicate the nadir position. The locations of these cross-sections according to the acquisition profiles are depicted in Fig. 6.13.

In conclusion, the angle-invariant data is strongly affected by topography caused by different sources: An incomplete removal of its influence, topography related variations in sediment distribution, and possible small scaled seafloor features. Nevertheless, three different types of seabed could be determined and even small-scaled changes in grain size distribution could be detected. This backscatter analysis shows that the simultaneous analysis of different data sources (i.e., back-scatter data, sediment samples, and sub-bottom profiler echograms) is essential for an detailed analysis of the seafloor characteristics.

Chapter 7

Conclusions

The objectives of this thesis were two-fold: on the one hand, the Geocoder implementation in *CARIS HIPS and SIPS* and *Fledermaus* was examined for multibeam echosounder (MBES) backscatter processing and automatic sediment classification of data acquired in a deep-sea environment. On the other hand, the obtained angle-invariant multibeam backscatter data was investigated for its potential to allow conclusions on the sediment type distribution in the survey area.

The applied corrections showed satisfying results in both software products in general, but the removal of topographic influences did not fully succeed in neither software. The mosaicing algorithm in *CARIS* showed problems with removal of nadir artifacts, whereas computed mosaics in *FMGeocoder Toolset* depicted more homogeneous results regarding the nadir region of the dataset. Both applications showed seam-effects in areas with a larger amount of overlapping profiles.

The automatic sediment classification by an ARA with inverse modeling is not trivial as sediment structures often consist of complex compositions of different particle like pore water, organic material, and probably gas. Acoustic models cannot account for all physical processes. Deep-water environments complicate the patch based ARA due to the large swath width and the comparably low-frequency signal, which penetrates into the upper sediment layers. The higher seabed penetration results in larger influences of underlying sediment heterogeneities. Furthermore, it was observed that the seafloor topography influenced the ARA results, as its effect was not completely removed from the angular responses. However, some of the obtained results of the ARA correspond to the estimated sediment distribution, even though the dataset was not perfectly suited for an ARA. Ground-truthing showed to be very important for a more secure ARA and for the evaluation of its results.

The obtained angle-invariant data was used for an estimate of the sediment type distribution throughout the investigation area. A high abundance of manganese nodules could be assumed for the northern part of the study area, whereas the intermediate part is covered by silt-to-sandy sediments. At the very southern part of the dataset (at the southern scarp of the Guafo Ridge) basement outcrops could be established. Even though topographic artifacts were visible in the data, an estimate of sediment distribution was possible. The combination of different datasets (i.e., backscatter data, sediment samples, sub-bottom profiler echograms) proved to be essential for a precise seabed analysis.

A MBES backscatter analysis is a powerful tool which can be employed for investigation and estimation of sediment type distribution, particularly as accurate bathymetric measurements are co-registered. Information of the seafloor morphology proved to be essential for backscatter investigations as it has a strong influence on the acoustic response of the seabed. Besides this, ground-truthing showed to be very important to correlate acquired backscatter strengths with sediment grain sizes for an extrapolation throughout the survey area. As only surface samples were recovered, a further investigation of the influence of underlying sediment layers could not be considered. This should be taken into account when systems with low frequencies are used as they have a large penetration depth and the heterogeneities of the underlying layers can influence the acoustic seabed response.

Further improvements in data processing in Geocoder are necessary for a more unambiguous backscatter analysis. Especially a more detailed analysis of the source of remaining topographic artifacts in the data would be of large interest. More research and further investigations are desirable to advance the applicability for acoustic models for diverse echosounder formats and seafloor environments.

The implementation of Geocoder in commercial software makes it accessible to a larger user community. This increases the probability of software improvements as it is used for a larger variety of different datasets in diverse environments. Weak points in the software are therefore more likely to be discovered. More detailed software manuals and description would be very useful for a better understanding of the software computations and algorithms.

In conclusion, Geocoder is a promising processing and analysis tool for backscatter data and can also be employed for datasets acquired in deep-water environments. Although improvements are necessary for a better removal of topographic effects, a more homogeneous mosaic computation, and a more secure automatic sediment classification. A new ARA approach that includes clustering of areas with similar angular responses seems promising for an improvement of sediment classification especially for deep-sea environments. Its implementation into Geocoder would constitute an advancement towards a more reliable automatic sediment classification of MBES backscatter data.

Bibliography

Albertz, J. (2007): *Einführung in die Fernerkundung.* 3. Aufl., Wissenschaftliche Buchgesellschaft, Darmstadt.

Anderson , R., Anderson, S. (2012): *Geomorphology – The mechanics and chemistry of landscapes.* 1st Edition, Cambridge University Press, Cambridge.

Bahlburg, H., Breitkreuz, Ch. (2012): *Grundlagen der Geologie.* 4. Aufl., Spektrum-Verlag, Berlin Heidelberg.

Bauer, M. (2002): *Vermessung und Ortung mit Satelliten: GPS und andere satellitengestützte Navigationssysteme.* 5. Aufl., Wichmann Verlag.

Beyer, A., Chakraborty, B., Schenke, H.W. (2005): *Seafloor classification of the mound and channel provinces of the Porcupine Seabight: An application of the multibeam agular backscatter data.* International Journal of Earth Science (Geologische Rundschau), 96(1).

Biot, M. A. (1956): *Theory of propagation of elastic waves in a fluid-saturated porous solid. I. Low-frequency range.* The Journal of the Acoustical Society of America, 28(2), pp. 168-178.

Biot, M. A., (1962): *Generalized theory of acoustic propagation in porous dissipative media.* The Journal of the Acoustic Society of America, 34(5), pp. 1254-1264.

Blondel, P. and Murton, B.J. (1997): *Handbook of seafloor sonar imagery.* 1st Edition, John Wiley and Sons, Praxis Publishing, Chichester.

Blondel, P. (2009): *The handbook of sidescan sonar.* 1st Edition, Springer, Berlin Heidelberg New York.

CARIS (2012a): *CARIS HIPS & SIPS 7.1 users guide.*

CARIS (2012b): *CARIS HIPS & SIPS editors.*

Cervenka, P.S., de Moustier, C. (1993): *Sidescan Sonar image processing techniques.* IEEE Journal of Oceanic Engineering, 18(2), pp. 108-122.

Chakraborty, B., Kodagali, V. (2004): *Characterizing Indian Ocean manganese nodule-bearing seafloor using multi-beam angular backscatter.* Geo-Marine Letters, Volume 24, Number 1, pp. 8-13.

Clark, J. (2005): *Die faszinierende Welt der Kartographie.* Salamander Books Limited, London.

De Falco, G., Tonielli, R., Di Martino, G., Innangi, S., Simeone, S., Parnum, I. (2010): *Relationship between multibeam backscatter, sediment grain size and Posidonia oeanica seagrass distribution.* Continental Shelf Research, 30, pp. 1941-1950.

De Moustier, C., Alexandrou, D. (1991): *Angular dependence of 12-kHz seafloor acoustic backscatter.* Journal of the Acoustical Society of America, 90(1), pp. 522-531.

De Smith, M., Goodchild, M., Longley, P. (2009): *Geospatial Analysis: A comprehensive guide to principles, techniques and software tools.* 3rd Edition, Metador, Great Britain.

Chaves, P.S. (1986): *Processing techniques for digital sonar images from GLORIA.* Photogrammetric Engineering and Remote Sensing, 52(8), pp. 1133-1145.

Fonseca, L., Mayer, L., Orange, D., Discoll, N. (2002): *The high-frequency backscattering angular response of gassy sediments: Model/data comparison from the Eal River Margin, California.* Journal of the Acoustical Society of America, 111(6), pp. 2621-2631.

Fonseca, L., Calder, B. (2005): *Geocoder: An efficient backscatter map constructor.* Proceedings of the U.S. Hydrographic Conference 2005, San Diego, CA, USA.

Fonseca, L., Mayer, L. (2007a): *Remote estimation of surficial seafloor properties through the application angular range analysis to multibeam sonar data.* Marine Geophysical Researches, pp. 119-126.

Fonseca, L., Calder, B. (2007b): *Clustering acoustic backscatter in the angular response space.* Proceedings of the U.S. Hydrographic Conference 2007, Norfolk (VA), USA.

Fonseca, L., Brown, C., Calder, B., Mayer, L., Rzhanov, Y.: *Angular range analysis of acoustic themes from Stanton Banks Ireland: A link between visual interpretation and multibeam angular signatures.* Applied Acoustics (70), pp. 1298-1304.

Halbach P., Friedrich G., Stackelberg, U. (1988): *The manganese nodule belt of the Pacific Ocean.* Ferdinand Enke Verlag, Stuttgart.

Hamilton, E. (1974): *Prediction of deep-sea sediment properties: State-of-the-art.* Deep-Sea Sediments, Physical and Mechanical Properties, Plenum Press, pp. 1-43, New York.

Hammerstad, E., Pohner,F., Parthoit, F., Bennet, J. (1991): *Field testing of a new deep water multibeam echo sounder.* Proceedings IEEE, 2, pp. 743-749.

Hastie, T., Tibshiranim R., Friedman, J.H. (2001): *The elements of statistical learning.* Springer-Verlag.

Ivankin, A.N. (1998): *A unified approach to volume and roughness scattering.* Journal of the Acoustic Society of America, 103(2), pp. 827-837.

IVS3D Fledermaus (2011): *Fledermaus reference manual.* Version 7.

Jackson, D., Winebrenner, D., Ishimaru, I. (1986): *Application of the composite roughness model to high-frequency bottom backscattering.* Journal of the Acoustic Society of America, 79(5), pp. 1410-1422.

Jackson, D., Ivakin, A.N. (1998): *Scattering from elastic sea beds: First-order theory.* Journal of the Acoustic Society of America, 103(1), pp. 336-345.

Jackson, D., Richardson, M.D. (2007): *High-frequency seafloor acoustics.* 1st Edition, Springer, New York.

Jahne, B. (2005): *Digitale Bildverarbeitung.* 6. Aufl., Springer, Heidelberg.

Keeton, J.A., Searle, R. (1996): *Analysis of Simrad EM12 multibeam bathymetry and acoustic backscatter data for seafloor mapping, exemplified at the Mid-Atlantic Ridge at 45° N.* Marine Geophysical Researches, 18, pp. 663-688.

Kelletat, D. (1999): *Physische Geographie der Meere und Küsten: Eine Einführung.* 2. Aufl., Teubner, Stuttgart.

Kemp, K. (2008): *Encyclopedia of geographic information science.* SAGE Publications, Inc.

Kennett, J. (1992): *Marine Geology.* Prentice-Hall, New York.

Kongsberg (1999): *EM 120 product description.*

Kongsberg (2006): *Seatex MRU user's manual.*

Krumbein, W.C. (1934): *Size frequency distribution of sediments.* J. Sediment. Petrol. 4, pp. 65-77.

Leick, A. (2004): *GPS satellite surveying.* 3rd Edition, John Wiley & Sons, New Jersey.

Luhmann, T. (2003): *Nahbereichsphotogrammetrie.* 2. Aufl., Wichmann, Heidelberg.

Lurton, X. (2010): *An introduction to underwater acoustics - principles and application.* 2nd Edition, Springer, Berlin Heidelberg.

Malinverno, A., Edwards, M., Ryan, B. (1990): *Processing of SeaMARC swath sonar data.* IEEE Journal of Oceanic Engineering, Vol. 15(1), pp. 14-23.

MARUM (2011): *Manual Beckman Coulter Laser Particle Sizer LS 200 & LS 13320.*

Masetti, G., Sacile, G., Trucco, A. (2011): *Remote characterization of seafloor adjacent to shipwrecks using mosaicking and analysis of backscatter response.* Italian Journal of Remote Sensing, 43 (2), pp. 77-92.

Medialdea, T., Somaza, L., León, R., Farrán, M., Ercilla, G., Maestro, A., Casas, D., Llave, E., Hernández-Molina, F.J., Fernández-Puga, M.C., Alonso, B. (2008): *Multibeam backscatter as a tool for sea-floor characterization and identification of oil spills in the Galicia Bank.* Elsevier, Marine Geology, 249 (1-2), pp. 93-107.

Mulhearn, P.J. (2000): *Modeling acoustic backscatter from near-normal incidence echosounders - sensitivity analysis of the Jackson model.*

Miller, C.L., La Flamme, R.A. (1958): *The digital terrain model - theory and applications.* Photogrammetric Engineering, 24, pp. 433-442.

Mitchell, N.C. (1993): *Comment on the mapping of iron-manganese nodule fields using reconnaissance sonars such as GLORIA.* Geo-Marine Letters, 13 (4), pp. 244-147.

Mourad,P. D., Jackson, D.R. (1989): *High frequency sonar equation model for bottom backscatter and forward loss.* Processings of OCEANS '89, IEEE, New York, pp. 1168-1175.

Mullace, D. (2010): *FMGeocoder Webinar.*

Pierce, A.D. (1989): *Acoustics: An introduction to its physical principles and applications.* The Acoustical Society of America.

Pinet, P.R. (2006): *Invitation to oceanography.* 4th Edition, Jones and Bartlett, Sudbury (USA).

Press, F., Siever R. (2008): *Allgemeine Geologie.* 5. Auflage, Springer-Verlag, Berlin Heidelberg.

Rzhanov, Y., Linnett L., Forbes, R. (2000): *Underwater video mosaicing for seabed mapping.* Proceedings of the IEEE conference on image processing, vol. 1, pp. 224-227.

Rzhanov, Y., Huff, L., Cutter, G.R. (2002): *Seafloor video mapping: Modeling algorithms, appartus.* Proceedings IEEE International Conference on IMage Processing (ICIP02), Rochester, New York.

Sandwell, D.T., Smith, W.H.F (1997): *Marine gravity from Geosat and ERS-1 altimetry.* Journal of Geophysical Research, 102, pp. 10039-10054.

Scanlon, K.M., Masson, D.G. (1992): *Fe-Mn nodule field indicated by GLORIA, north of the Puerto Rico Trench.* Geo-Marine Letters, 12(4), pp. 208-213.

Schenke, H.-W. (1992): *GPS und Fächersonarmessung mit Hydrosweep auf FS Polarstern.* ZfV, 117. Jahrgang, Heft 8/9, pp. 599-615.

Spektrum Akademischer Verlag [Hrsg.] (2002): *Lexikon der Geowissenschaften.* CD-ROM-Version, Heidelberg.

Standish, J.J., Kenneth, W.W (2010): *Young off-axis volcanism along the ultraslow-spreading Southwest Indian Ridge.* Nature Geoscience , Vol. 3, pp. 286-292.

Stockhausen, J.H. (1963): *Scattering from the volume of an inhomogeneous half-space.* Rep. No. 63/9, Naval Research Establishment, Canada.

Tarnuck, E., Lutgens F. (2009): *Allgemeine Geologie.* 9. Auf., Pearsom Studium, München.

Beuck, G. (2006): *Wer war Alexander Behm?* Treene-Spiegel, Nr. 368.

University of Washington - Applied Physics Laboratory (1994): *APL-UW High-frequency ocean environmental acoustic models handbook.* Technical Report APL-UW TR 9407.

Wille, P.C. (2005): *Sound Images of the Ocean (in research and monitoring).* Springer, Berlin.

Williams, K.L. (2001): *An effective density fluid model for acoustic propagation in sediments derived from Biot theory.* Journal of the Acoustic Society of America, 110(5), pp. 2276-2281.

Wentworth, C.K. (1922): *A scale of grade and class terms for clastic sediments.* The Journal of Geology Vol. 30 No.5, pp. 377-392.

Weydert, M.M.P. (1990): *Measurements of the acoustic backscatter of selected areas of the deep seafloor and some implications for the assessment of manganese nodule resources.* Journal of the Acoustic Society of America, 88(1), pp. 350-366.

Internet sources:

Amolo, R.C. (2010): *Habitat mapping and identifying suitable habitat redfish rocks pilot marine reserve, Port Orford, Oregon.* Master Thesis, Oregon State University. http://ir.library.oregonstate.edu/xmlui/bitstream/handle/1957/18825/AmoloRizallerC2010.pdf (accessed May 2012).

Atlas Hydrographic GmbH (2012): *Parasound P70 – Short product description.* http://www.atlashydro.atlas-elektronik.com/en/products/sub-bottom-profiler (accessed April 2012).

Bellevue College: Marine Sediments. http://scidiv.bellevuecollege.edu/gj/Ocean101-Ch05.pdf (accessed March 2012).

Bundesanstalt für Geowissenschaften und Rohstoffe (2009): *Benutzerhandbuch FS Sonne.* http://www.bgr.de/fs_sonne/pdf/handbuch.pdf (accessed March 2012).

Bundesanstalt für Geowissenschaften und Rohstoffe (2012): *Sonne homepage.* www.bgr.de/fs_sonne (accessed March 2012).

Briney, A. (2008): *An overview of remote sensing.* geography.about.com/od/geographictechnology/a/remotesensing.htm About.com Geography homepage, (accessed July 2012).

Bibliography

CCOM/JHC – Center for Coastal and Ocean Mapping Joint Hydrographic Center (2012): *Homepage of CCOM/JHC – Geocoder.* `ccom.unh.edu/theme/data-processing/geocoder` (accessed July 2012).

GEBCO – General Bathymetric Chart of the Oceans (2012): *GEBCO Homepage.* `www.gebco.net` (accessed July 2012).

Hammerstad, E. (2000): *EM Technical Note - Backscattering and seabed image reflectivity.* `http://www.km.kongsberg.com/ks/web/nokbg0397.nsf/AllWeb/226C1AFA658B1343C1256D4E002EC764/` (accessed April 2012).

Hatzky, J., Collins, C., Wong, K. (2011): *Improved geocoder integration for HIPS and SIPS software.* `www.caris.com/downloads/featuredArticles/ImprovedGeocoderIntegrationForHIPSandSIPSSoftware_SeaTechnology(September2011).pdf` Sea Technology (June 2011), (accessed July 2012).

Hewitt, A., Salisbury, R., Wilson, J. (2010): *Using multibeam echosounder backscatter to characterize seafloor features.* `www.fugro.com/downloads/corporate/articles/Using_Multibeam_Echosounder_Backscatter_to_Characterize_Seafloor_Feature.pdf` Sea Technology (September 2010), (accessed July 2012).

International Hydrographic Organization: *Manual on hydrography. Publication M-13. Chapter 4: Seafloor classification and feature detection.* `www.fig.net/commission4/iho/M-13_Chapter_4.pdf` (accessed July 2012).

Kongsberg (2000): *Product description EM 120 multibeam echo sounder.* `www.satlab.hawaii.edu/sunset0/proj/philx/flament_december_07/documentation/MultiBeam-EM120/Product%20Description%20%28Rev%20E%29.pdf` (accessed August 2011).

Kongsberg (2005): *EM120 - 12 kHz multibeam echo sounder.* Brochure. `http://www.kongsberg-simrad.de/pdf/faecherlot_em120_eng_broch.pdf` (accessed March 2012).

Llewellyn, K. (2006): *Master Thesis: Corrections for beam pattern residuals in backscatter imagery from the Kongsberg-Simrad EM300 multibeam echosounder.* `http://www.omg.unb.ca/omg/papers/Kristian_MEng_Final.pdf` (accessed May 2012).

MacDonald, A., Collins, C. (2008): *Taking Geocoder to Work.* Shallow Survey 2008. `http://www.caris.com/downloads/brochures/CARIS%20SIPS%20and%20Geocoder.pdf` (accessed April 2012).

MacDonald, A., Collins, C. (2009): *Advancements in area-based imagery processing.* `www.thsoa.org/hy09/0514P_06.pdf` (accessed July 2012).

Mayer, L., Fonseca, L., Kraft, B., Weber, T. (2007): *Remote identification of seafloor properties in denied areas.* Center for Coastal and Ocean Mapping Annual rept., Durham (NH). `http://auvac.org/uploads/configuration_spec_sheets/UDEL%20UNH%20AUV.pdf` (accessed May 2012).

NOAA (2012): *ETOPO1 Global relief.* www.ngdc.noaa.gov/mgg/global/etopo1sources.html (accessed July 2012).

NASA (2002): *Digital Tectonic Activity Map.* http://denali.gsfc.nasa.gov/dtam/dtam/ (accessed April 2012).

Theberge, A. (1989): *Sounding pole to sea beam.* http://www.photolib.noaa.gov/cgs/sound.html Survey and Cartography, Volume 5, pp. 334-346. (accessed July 2012).

Tiedemann, R. (2011): *2. Weekly Report SO213-1.* http://www.bgr.de/fs_sonne/aktuelles/wochenberichte.html (accessed August 2011).

Wessel, P. and Smith W.H.F. (2012): *The Generic Mapping Tools (GMT) version 4.5.8 Technical Reference & Cookbook, SOEST/NOAA.* http://gmt.soest.hawaii.edu/ (accessed March 2012).

Acknowledgement

Appendix A

Charts

Figure A.1: MBES data profiles which are analyzed in the backscatter analysis. The number and direction of each profile is indicated. The white dots represent coring locations. (Mercator projection, standard parallel: 40° 28' S)
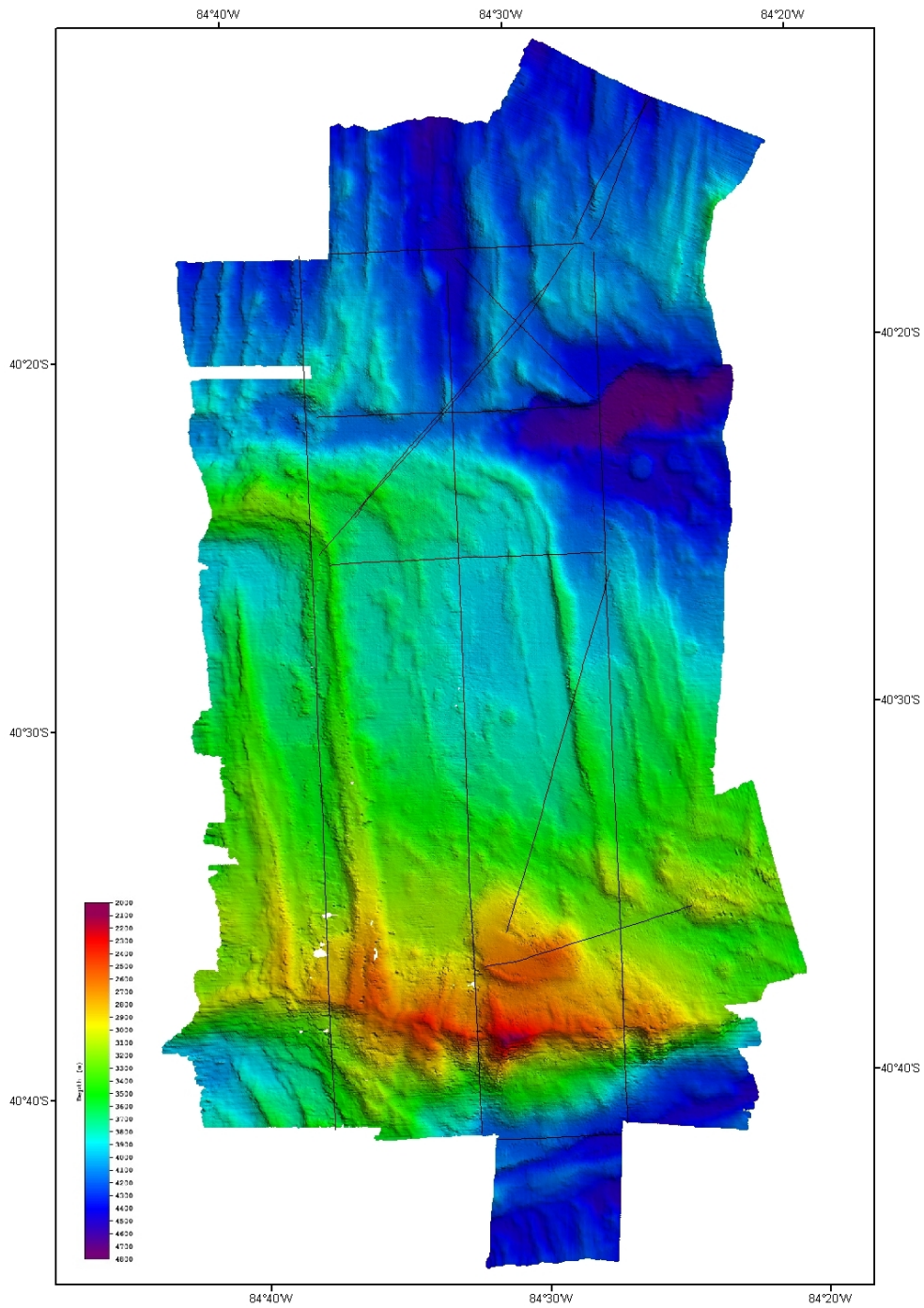
Figure A.2: BASE surface of investigation area created in *CARIS HIPS and SIPS* with a resolution of 30 m. (Mercator projection, standard parallel: 39° S)
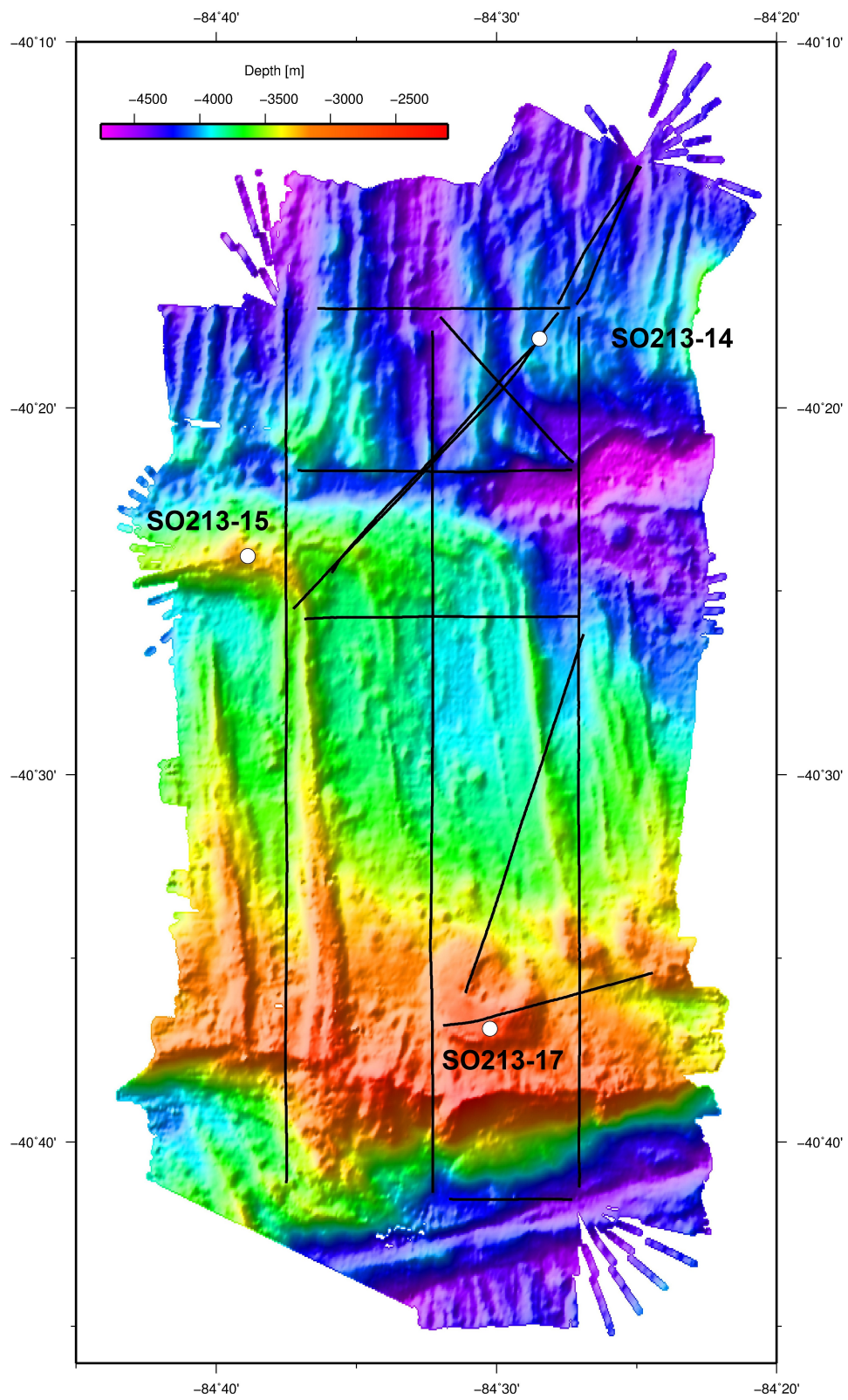
Figure A.3: Area of investigation with location of sediment samples and station numbers. (Mercator projection, standard parallel: 40° 28'S)
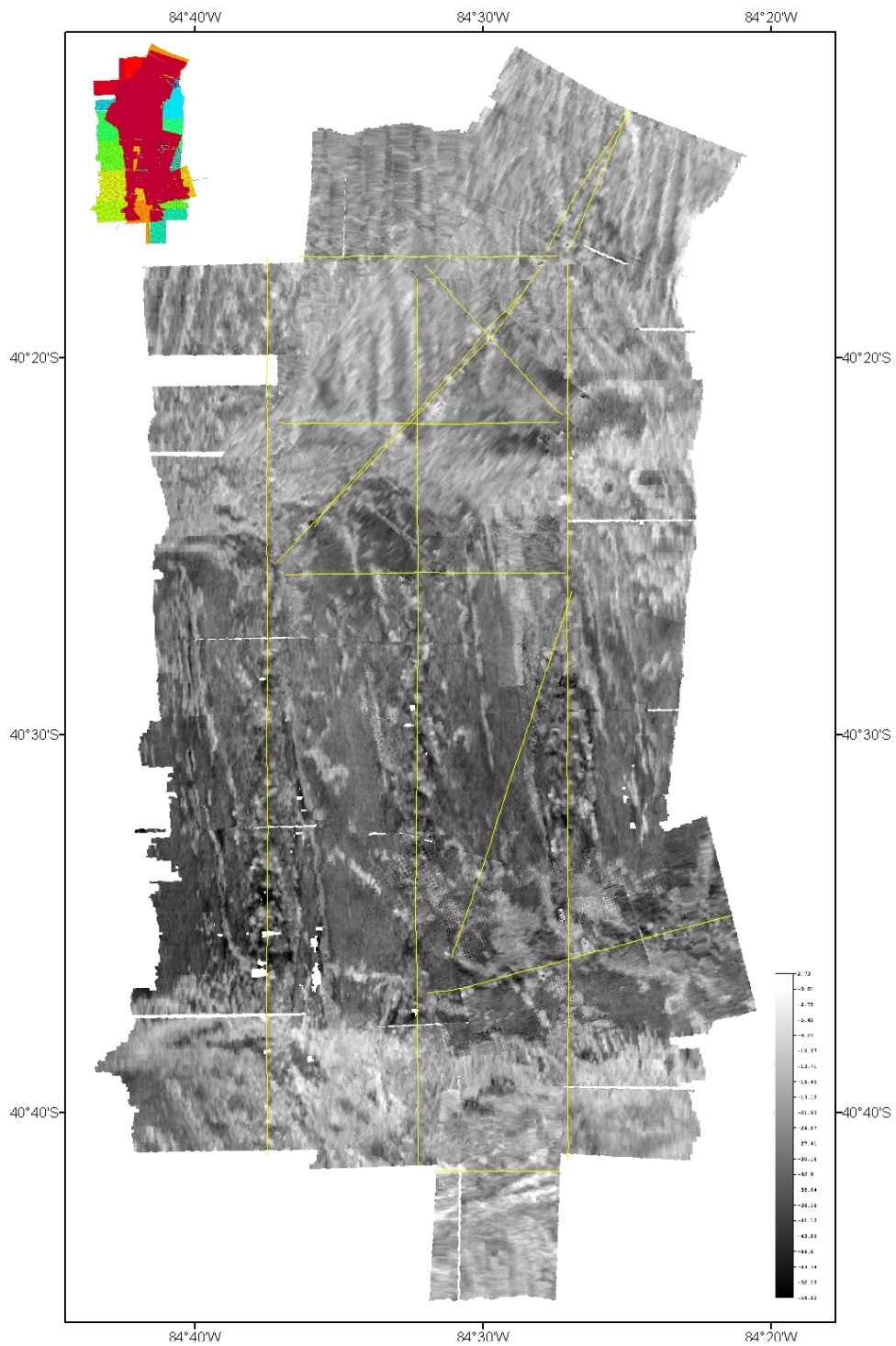
Figure A.4: Mosaic created in *CARIS HIPS and SIPS* with the full blend method. In the top left corner the contributing files are displayed. (Mercator projection, standard parallel: 39° S)
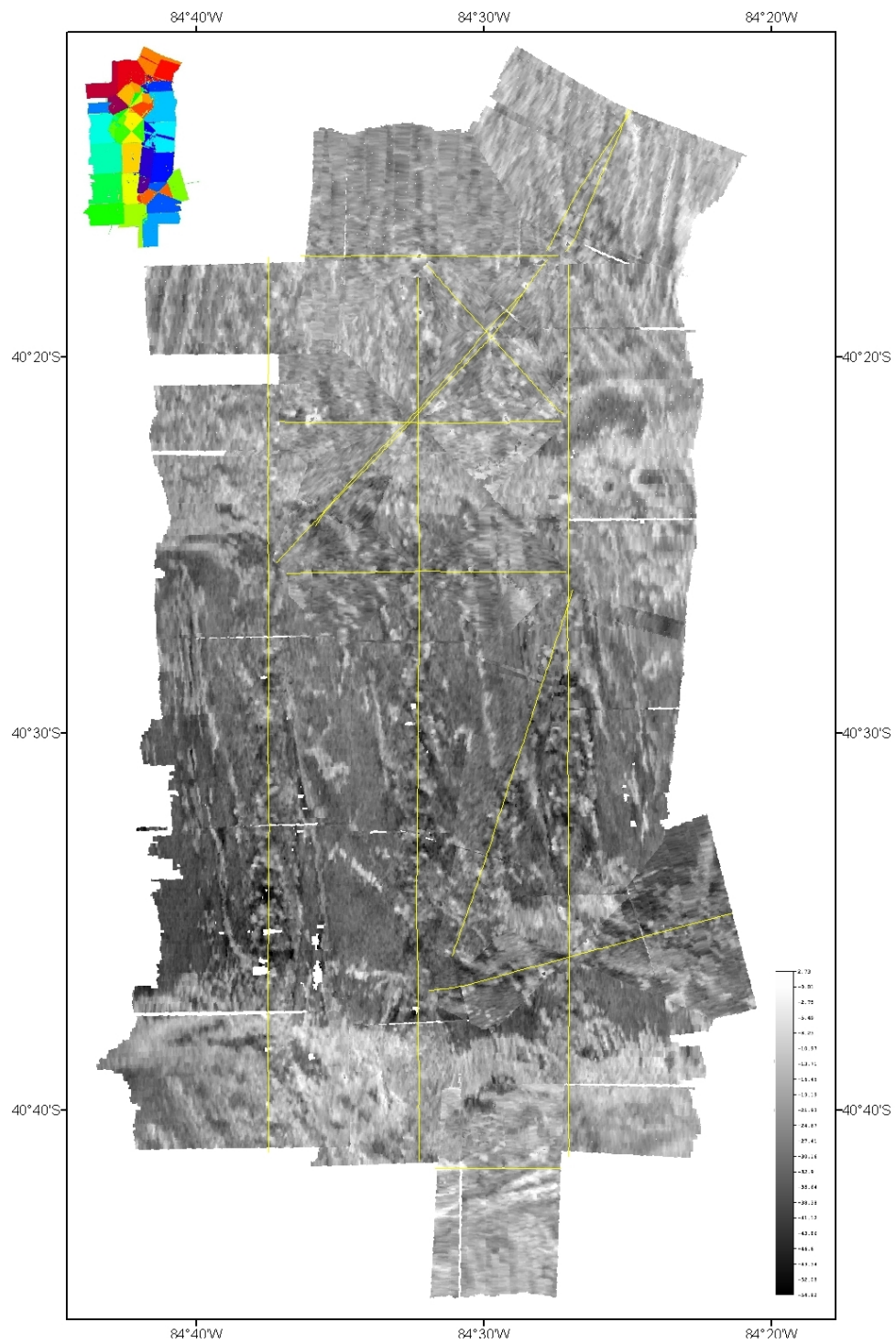
Figure A.5: Mosaic created in *CARIS HIPS and SIPS* with the auto-seam method. In the top left corner the contributing files are displayed. (Mercator projection, standard parallel: 39° S)
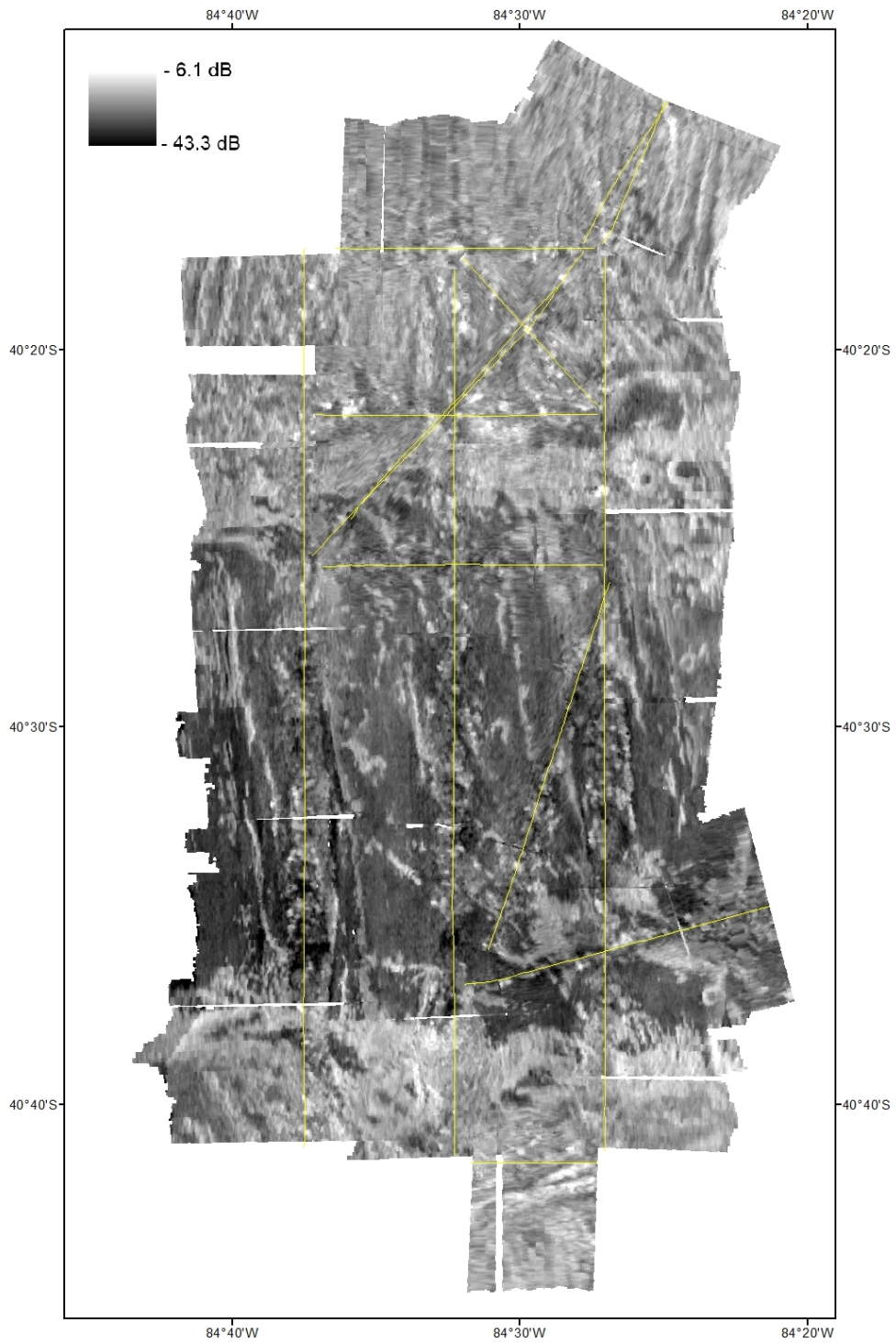
Figure A.6: Mosaic created in *FMGeocoder Toolbox* with the full blend method. (Mercator projection, standard parallel: 39° S)
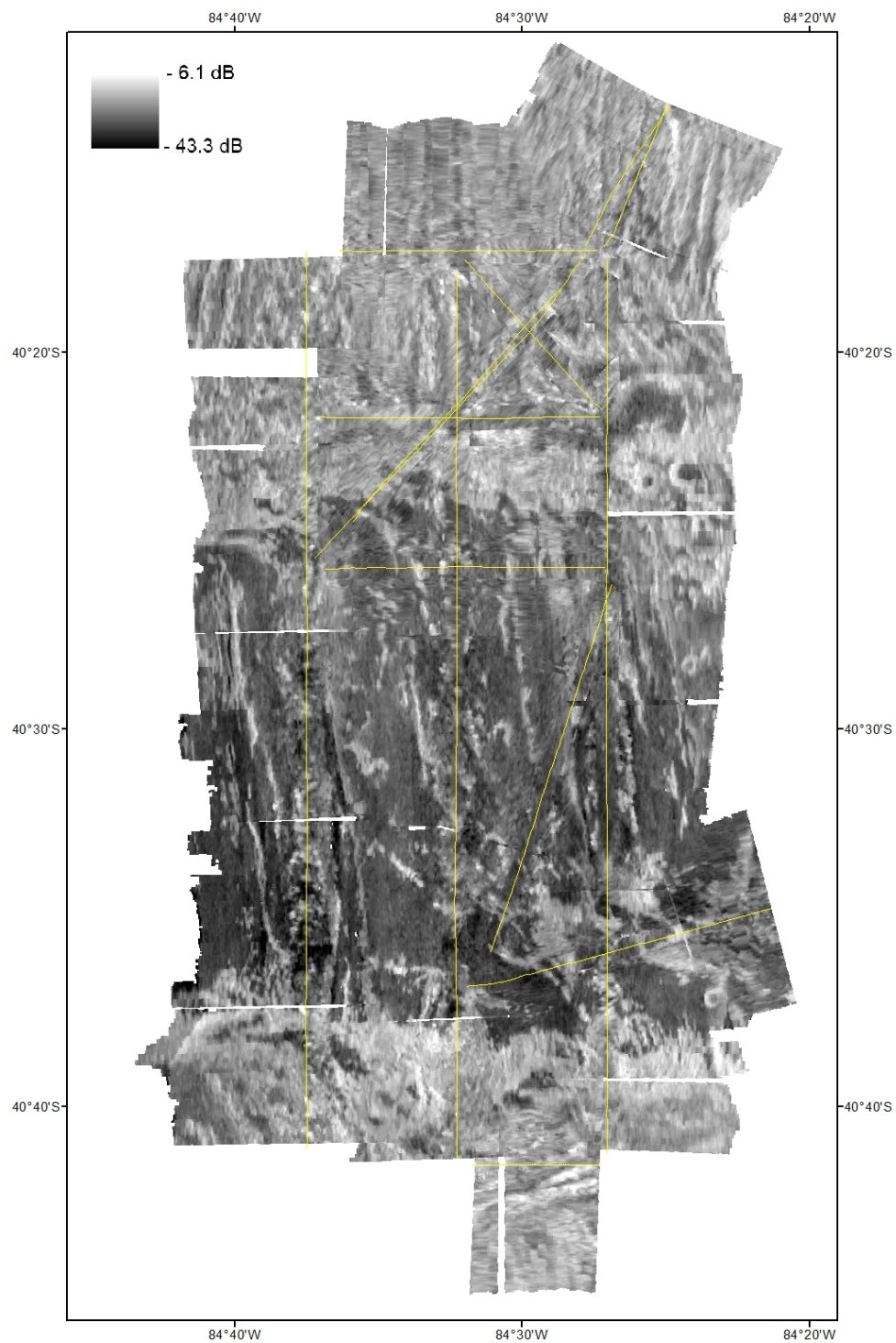
Figure A.7: Mosaic created in *FMGeocoder Toolbox* with the "no nadir if possible 1" method. (Mercator projection, standard parallel: 39° S)
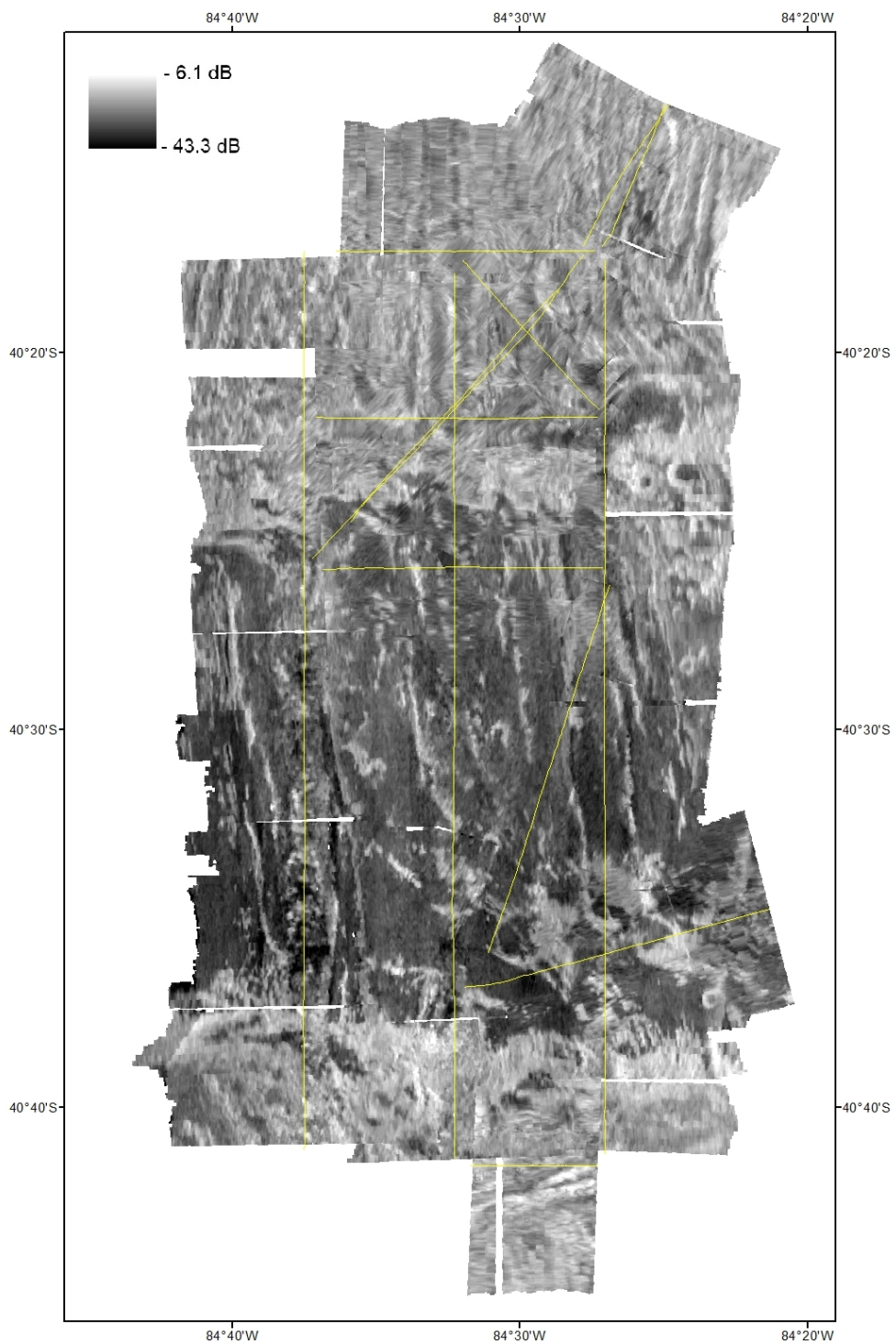
Figure A.8: Mosaic created in *FMGeocoder Toolbox* with the "no nadir if possible 2" method. (Mercator projection, standard parallel: 39° S)
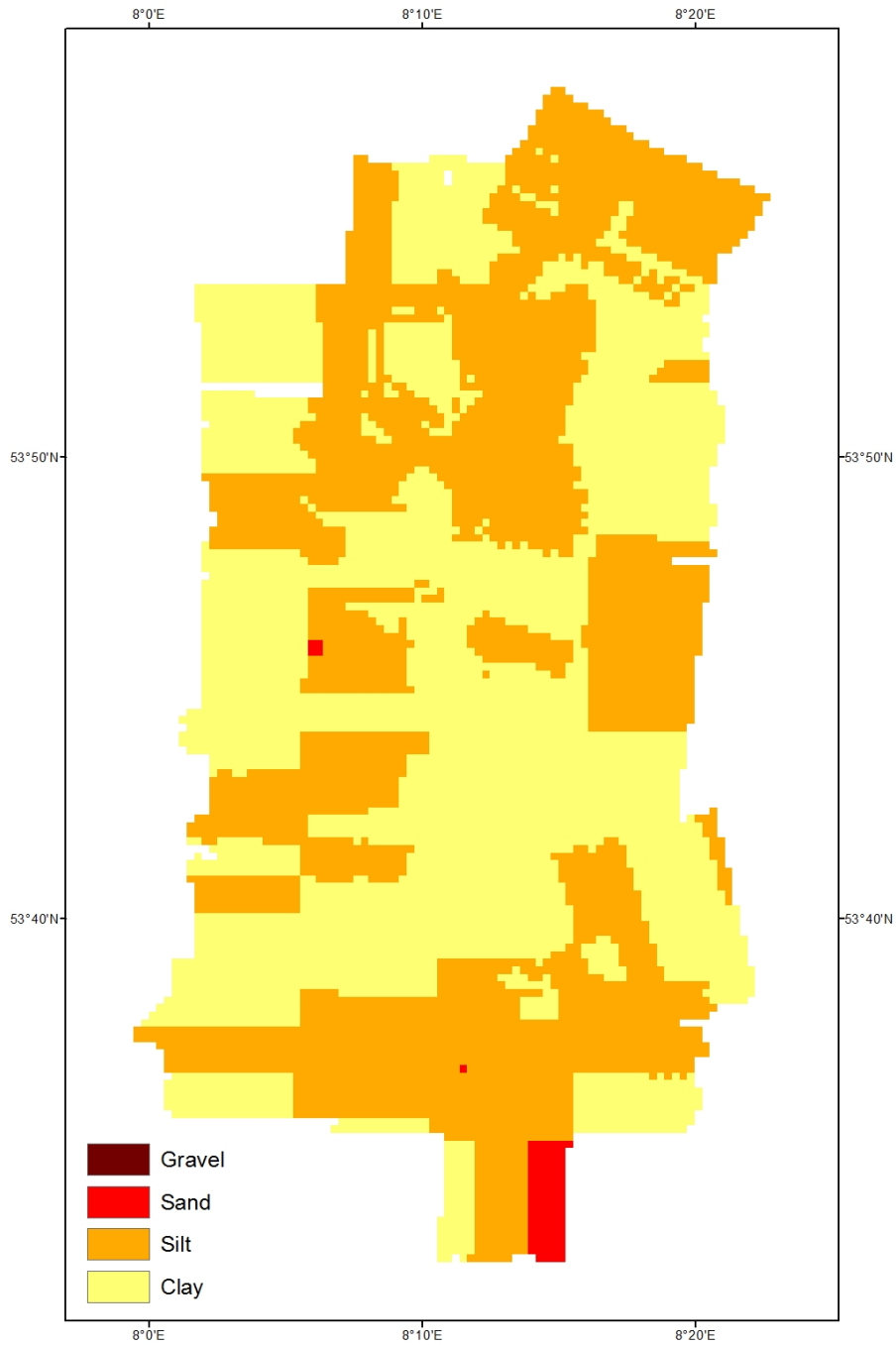
Figure A.9: ARA grain size estimation for the survey area without applying a beam pattern correction. (Mercator projection, standard parallel: 39° S)
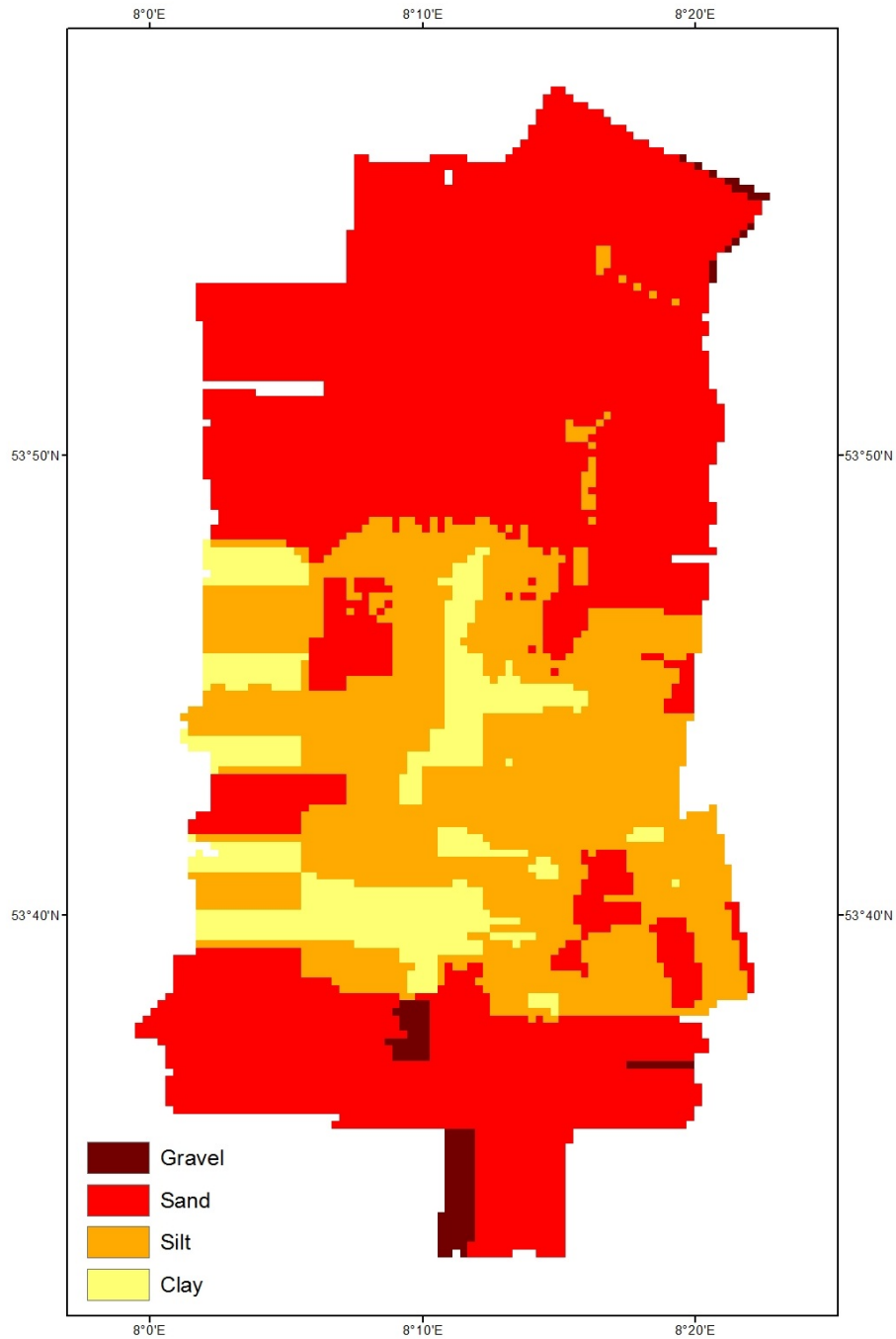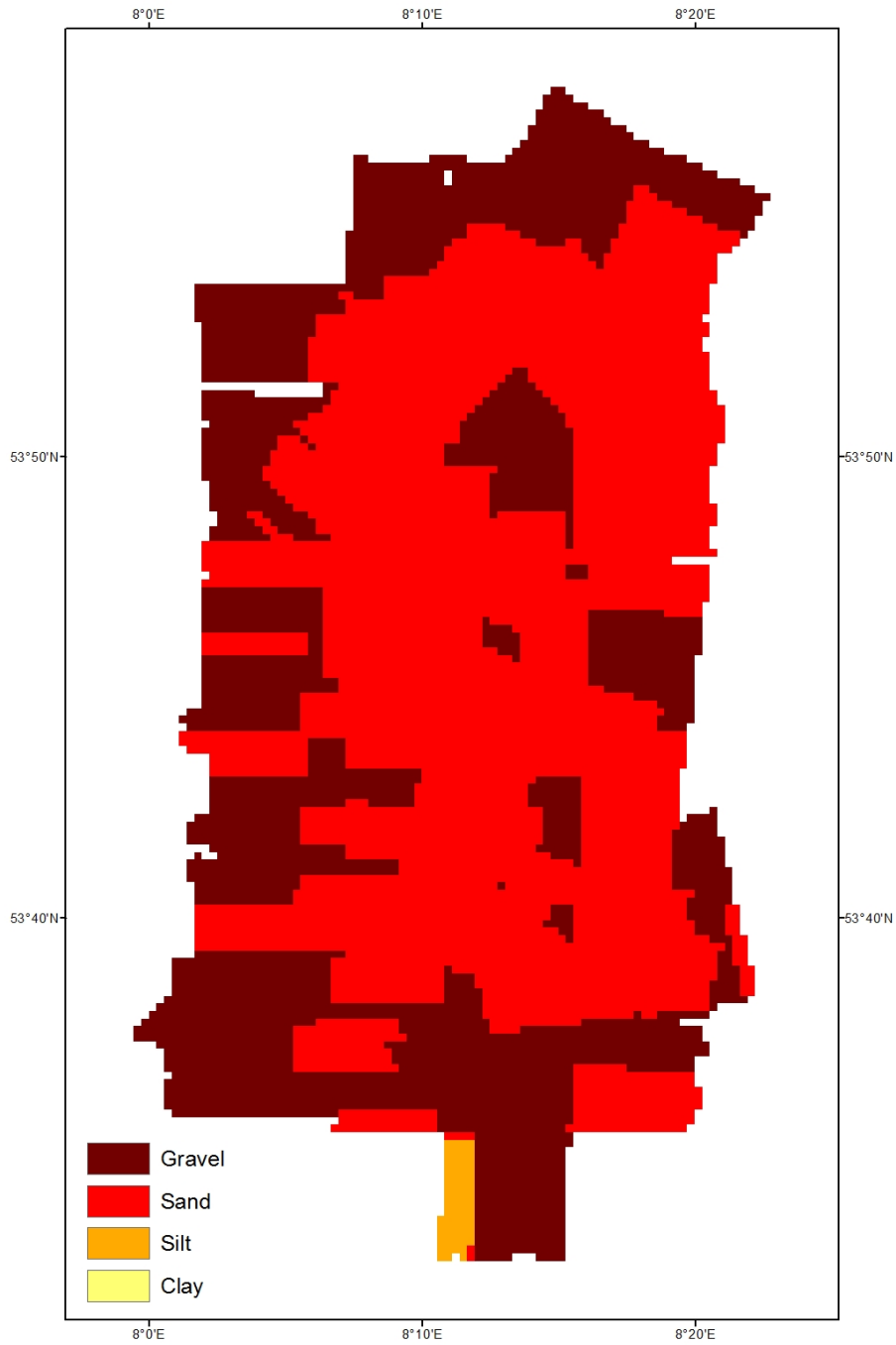
Figure A.10: ARA grain size estimation for the survey area with applied beam pattern correction. The beam pattern file was generated in a homogeneous area outside of the investigation area. (Mercator projection, standard parallel: 39° S)

Figure A.11: ARA grain size estimation for the survey area with applied beam pattern correction. The beam pattern file was generated at sediment sampling location SO213-14. (Mercator projection, standard parallel: 39° S)
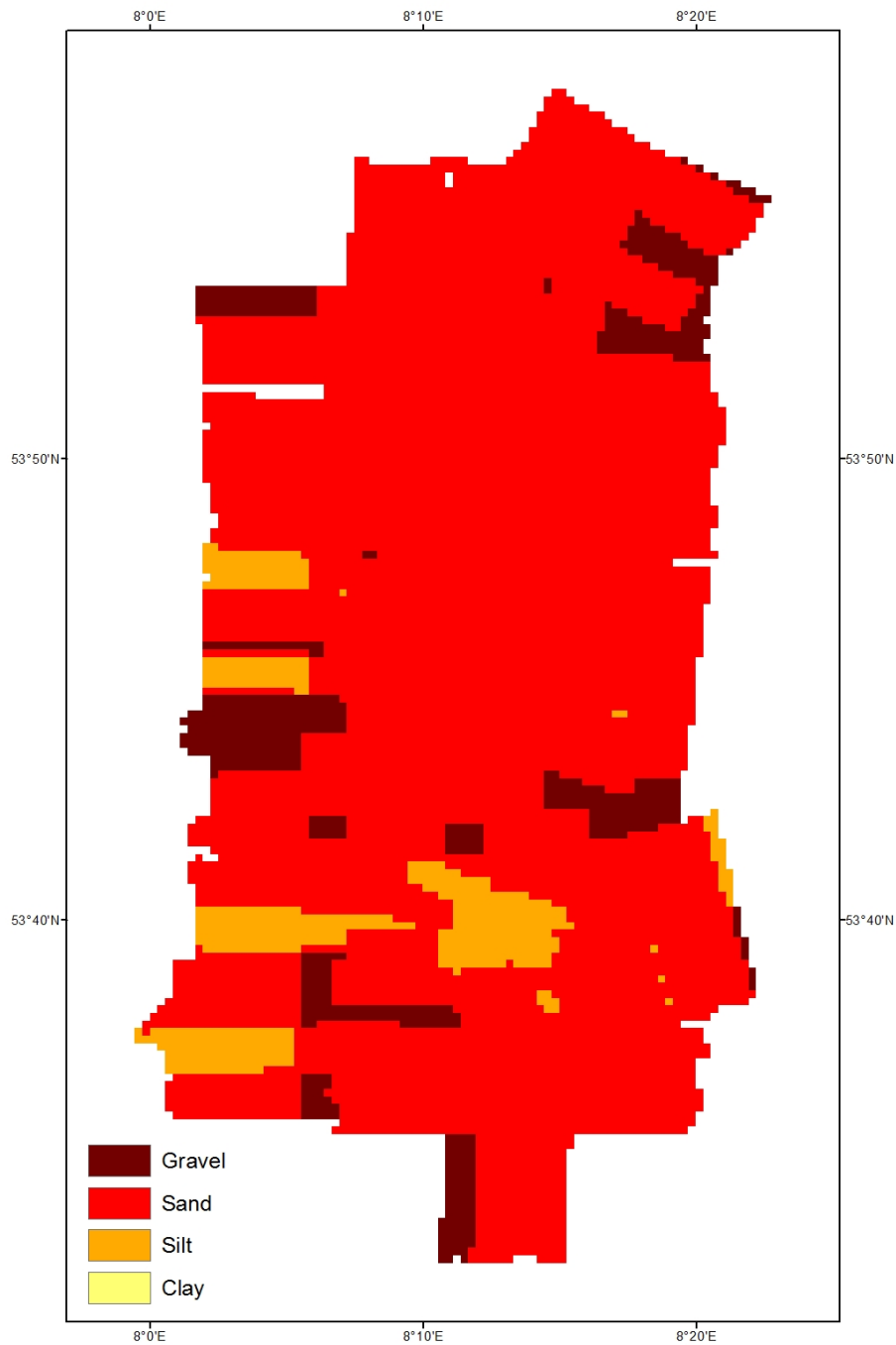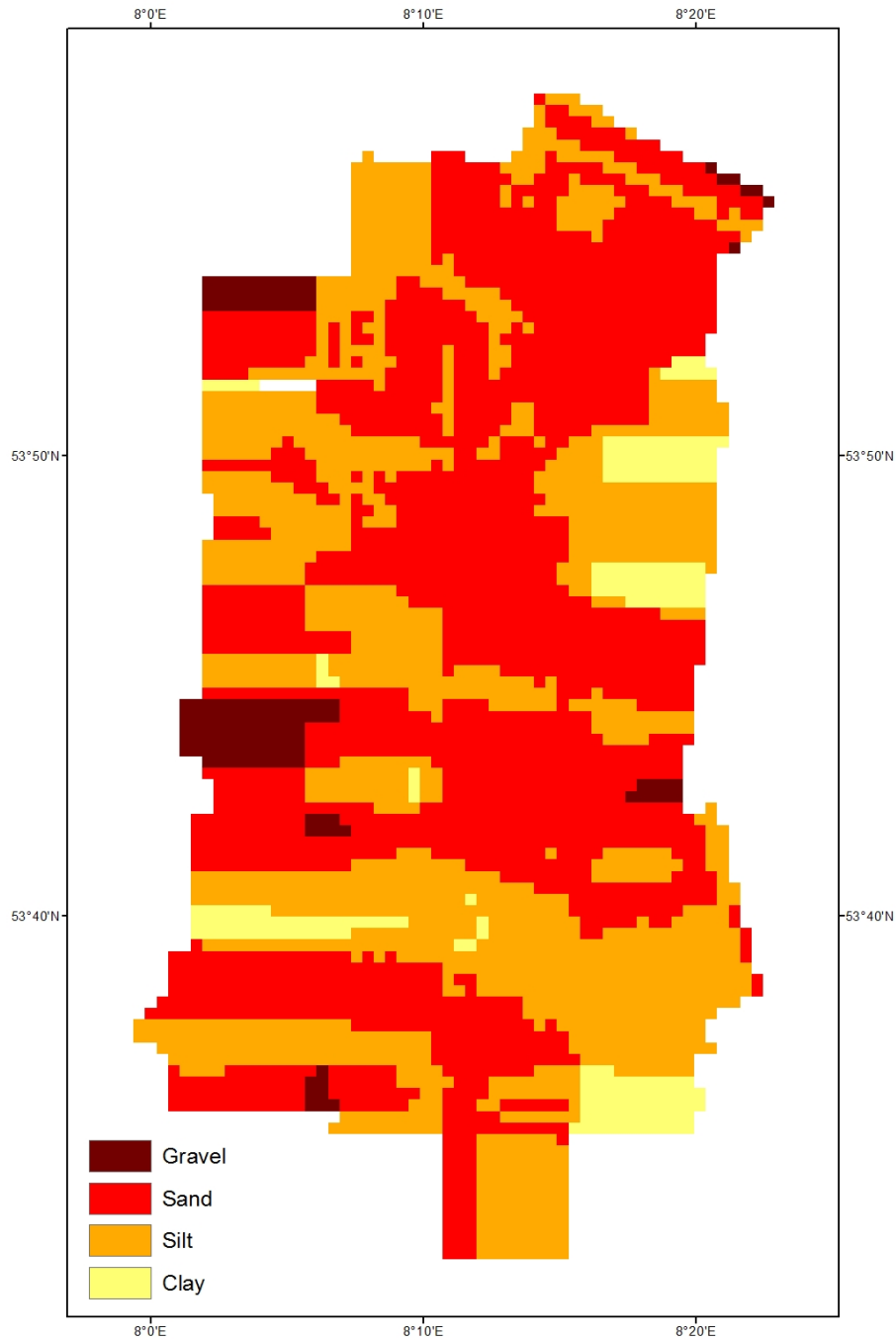
Figure A.12: ARA grain size estimation for the survey area with applied beam pattern correction. The beam pattern file was generated at sediment sampling location SO213-15. (Mercator projection, standard parallel: 39° S)

Figure A.13: ARA grain size estimation for the survey area with applied beam pattern correction. The beam pattern file was generated at sediment sampling location SO213-17. (Mercator projection, standard parallel: 39° S)
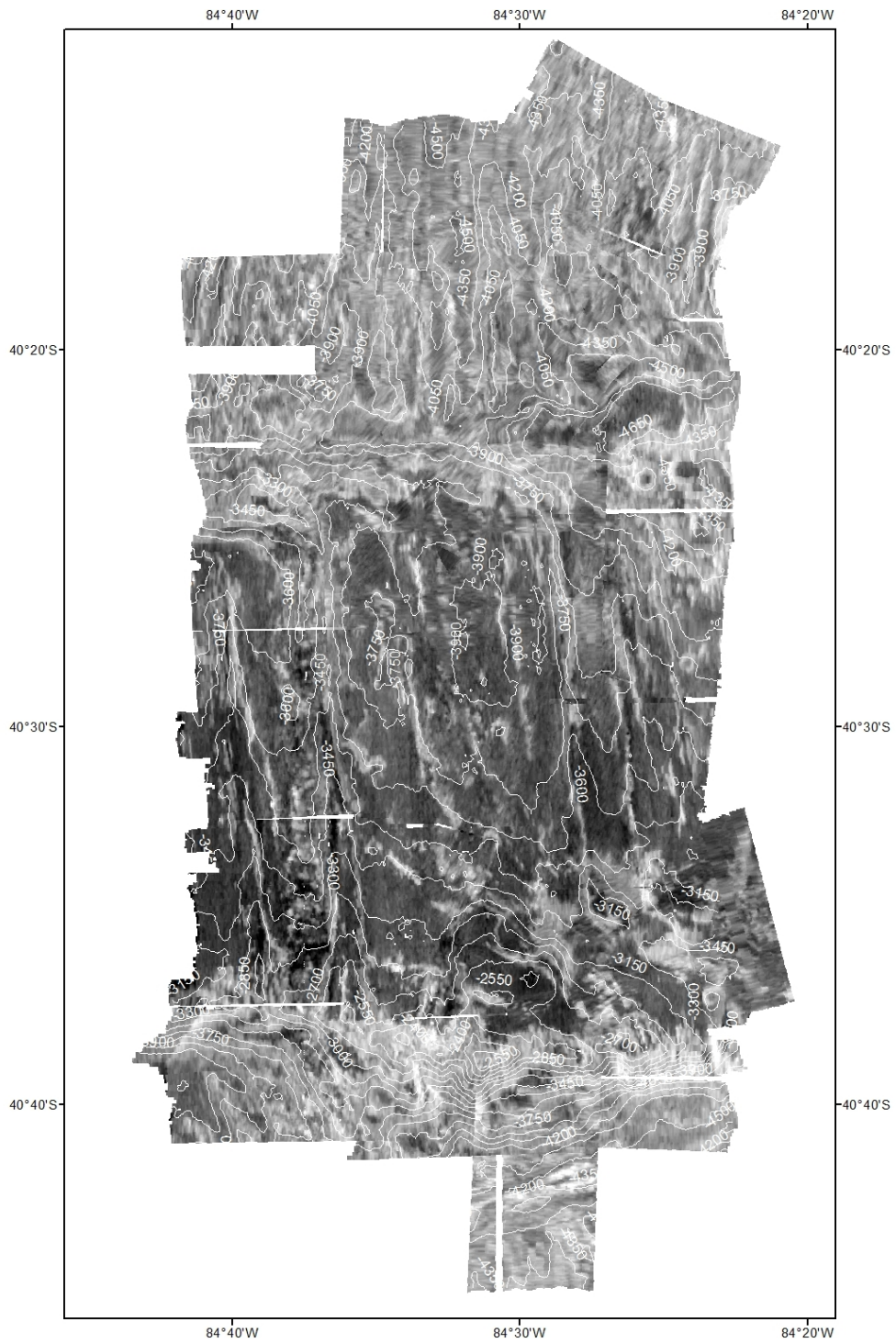
Figure A.14: Mosaic created with the "no nadir if possible 2" method in *FMGT* with 150 m contour interval. (Mercator projection, standard parallel: 39° S)
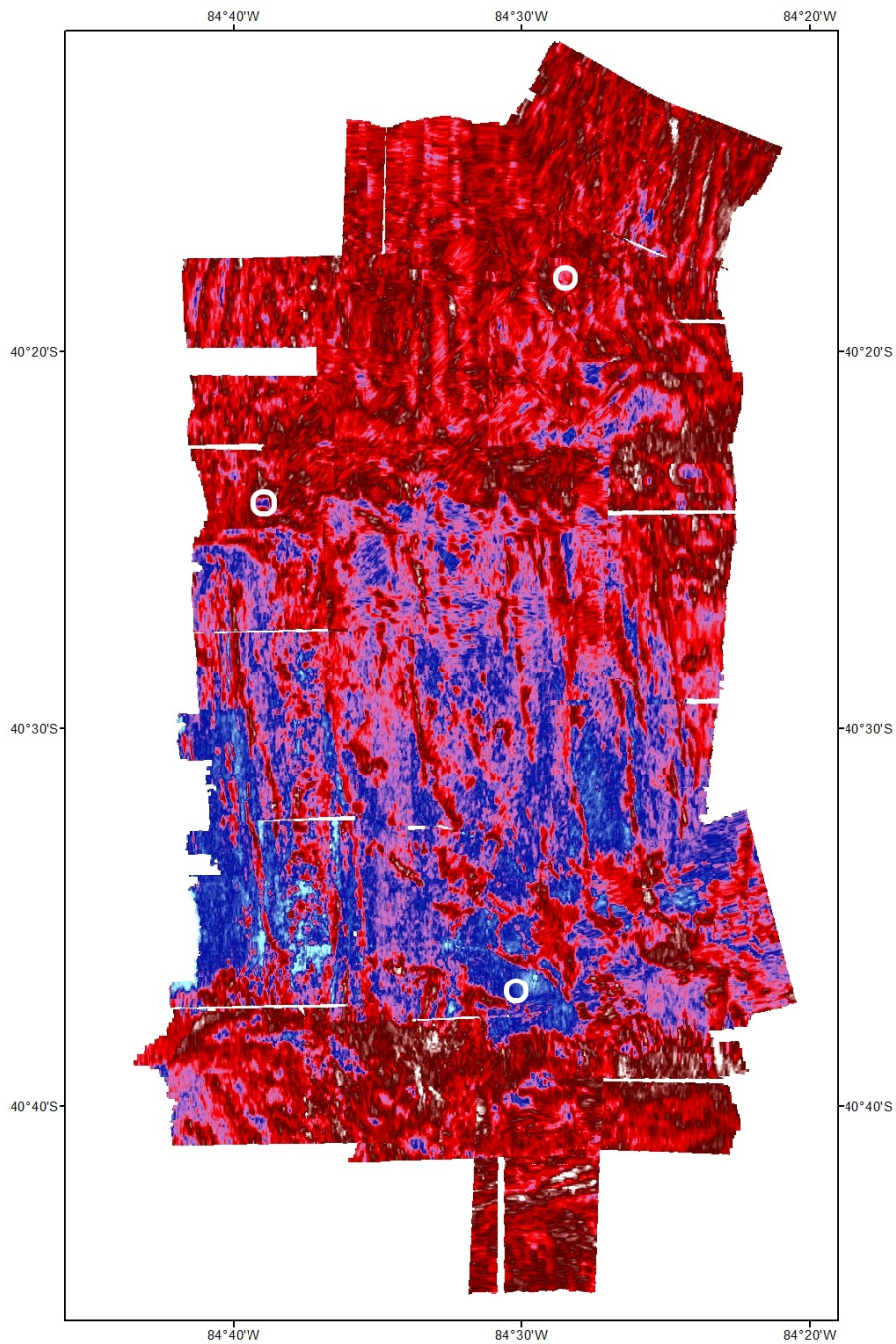
Figure A.15: Mosaic generated in *FMGT* showing angle-invariant data with a different color palette than gray scale. (Mercator projection, standard parallel: 39° S)
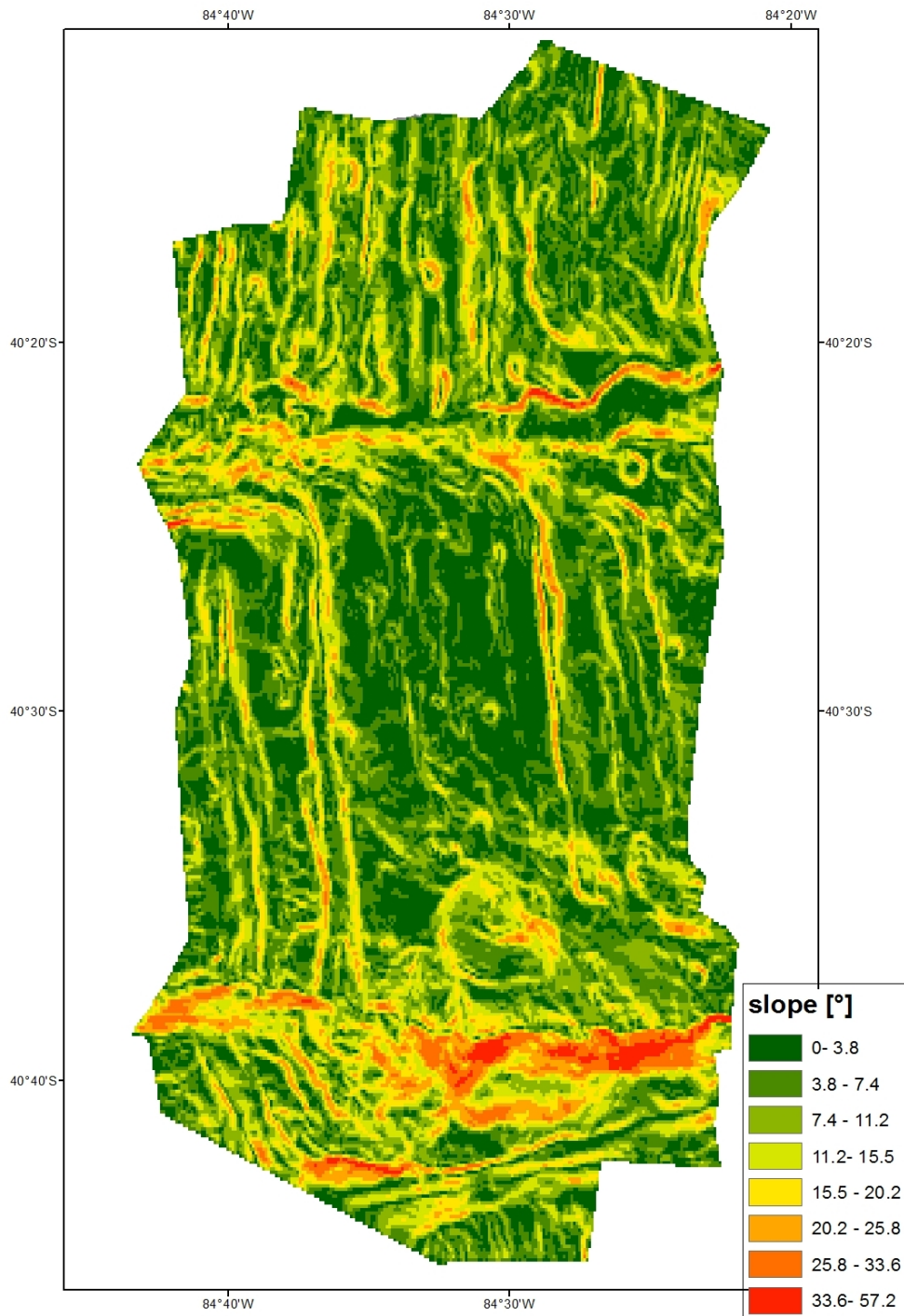
Figure A.16: Representation of geomorphological slopes in the survey area computed in *ArcGIS 10*. (Mercator projection, standard parallel: 39° S)

Appendix B

Auxiliary Information

Profile No.	Start Time	End Time	Length [km]
01	7.1. 08:56:39	7.1. 10:59:11	
	7.1. 11:16:38	7.1. 11:33:21	44.5
02	8.1. 04:05:51	8.1. 06:26:08	44.3
03	8.1. 06:52:48	8.1. 09:14:00	44.5
04	7.1. 11:40:35	7.1. 12:25:19	13.6
05	8.1. 02:41:31	8.1. 03:26:18	13.7
06	8.1. 10:29:32	8.1. 11:14:39	14.0
07	8.1. 06:29:47	8.1. 06:49:28	6.5
08	7.1. 12:26:47	7.1. 12:52:03	7.0
09	7.1. 12:55:44	7.1. 13:22:36	8.0
10	7.1. 19:30:30	7.1. 20:10:57	14.7
11	8.1. 09:19:33	8.1. 10:25:26	19.0
12	8.1. 03:29:41	8.1. 04:01:30	9.7
13	8.1. 11:19:07	8.1. 12:21:11	19.0
14	8.1. 17:36:50	8.1. 18:25:01	15.4

Table B.1: Profile acquisition times (UTC) and lengths.

```
disk loc: 0x2a08, length 5632, opcode: 0x53
EM 3000 Image Datagram # 1, ping number: 359
2011/01/08 11020.03
total pixels: 4397

disk loc: 0x1474, length 3040, opcode: 0x44
Depth Datagram model:   120   2011-01-08, 11020.027  Depth Datagram # 1
Number of depths: 188, ping number     359
Sound velocity: 1497.70
Sampling Rate:    501.0
Trans 1 depth:    -0.03 Trans 2 depth:    4.98
  #    Across / Along / Depth / Depression / Azimuth  /  Range / Ref. (dB) / Quality
   1  -6323.84    35.52  4434.24  35.110      270.22    10328.00   -31.5  -6323.84 4434.24   0x81 (P)
   2  -6257.60    35.52  4435.36  35.400      270.22    10256.00   -32.0  -6257.60 4435.36   0x81 (P)
   3  -6197.12    35.52  4438.40  35.680      270.22    10193.00   -32.5  -6197.12 4438.40   0x82 (P)
   4  -6135.36    35.20  4442.72  35.980      270.23    10129.00   -32.5  -6135.36 4442.72   0x83 (P)
   5  -6069.44    35.20  4445.52  36.290      270.23    10060.00   -33.0  -6069.44 4445.52   0x83 (P)
   6  -6003.84    35.20  4446.24  36.590      270.23     9990.00   -33.5  -6003.84 4446.24   0x84 (P)
   7  -5924.16    34.88  4436.32  36.890      270.23     9897.00   -34.5  -5924.16 4436.32   0x85 (P)
   8  -5844.80    34.56  4427.28  37.200      270.23     9805.00   -35.0  -5844.80 4427.28   0x86 (P)
   9  -5789.44    34.56  4434.56  37.510      270.23     9752.00   -36.0  -5789.44 4434.56   0x86 (P)
  10  -5743.36    32.96  4449.76  37.830      270.22     9715.00   -39.0  -5743.36 4449.76   0x84 (P)
  11  -5683.84    32.96  4457.68  38.170      270.22     9658.00   -38.5  -5683.84 4457.68   0x86 (P)
  12  -5612.48    32.64  4453.12  38.490      270.22     9580.00   -39.5  -5612.48 4453.12   0x87 (P)
  13  -5549.44    32.64  4456.96  38.830      270.22     9517.00   -38.0  -5549.44 4456.96   0x86 (P)
  14  -5484.16    32.32  4458.56  39.170      270.22     9450.00   -38.0  -5484.16 4458.56   0x86 (P)
  15  -5416.96    32.32  4456.24  39.500      270.22     9379.00   -35.5  -5416.96 4456.24   0x84 (P)
  16  -5340.16    32.00  4450.48  39.860      270.22     9295.00   -35.0  -5340.16 4450.48   0x83 (P)
  17  -5267.52    31.68  4445.12  40.210      270.22     9216.00   -34.0  -5267.52 4445.12   0x83 (P)
  18  -5195.52    31.36  4442.48  40.580      270.23     9141.00   -33.5  -5195.52 4442.48   0x83 (P)
  19  -5130.24    31.36  4441.52  40.940      270.23     9074.00   -33.5  -5130.24 4441.52   0x84 (P)
  20  -5063.36    31.04  4441.36  41.310      270.23     9006.00   -33.0  -5063.36 4441.36   0x83 (P)
  21  -4983.68    30.72  4431.12  41.690      270.23     8918.00   -33.0  -4983.68 4431.12   0x82 (P)
  22  -4905.28    30.40  4422.32  42.080      270.23     8832.00   -33.0  -4905.28 4422.32   0x82 (P)
  23  -4834.56    30.40  4417.60  42.460      270.23     8758.00   -33.0  -4834.56 4417.60   0x82 (P)
  24  -4767.68    30.08  4416.48  42.850      270.23     8691.00   -33.5  -4767.68 4416.48   0x83 (P)
  25  -4699.52    29.76  4415.20  43.250      270.23     8624.00   -34.0  -4699.52 4415.20   0x81 (P)
  26  -4628.80    29.76  4413.28  43.670      270.23     8553.00   -33.5  -4628.80 4413.28   0x81 (P)
  27  -4563.20    29.44  4412.08  44.070      270.23     8489.00   -33.5  -4563.20 4412.08   0x82 (P)
  28  -4493.44    29.12  4409.36  44.490      270.23     8420.00   -33.5  -4493.44 4409.36   0x83 (P)
  29  -4430.72    29.12  4413.52  44.920      270.23     8364.00   -33.5  -4430.72 4413.52   0x83 (P)
```

Figure B.1: Section of a Kongsberg raw file (*.all). First the image datagram is listed with 4397 intensity values (time series format). Underneath a part of the depth datagram is visible. For each ping an average intensity value is recorded (beam average format).

```
#!/bin/csh

set FILE=./so213                                                    #Variables
set OUT=./so213.ps
set GRENZEN=-R-84:45/-84:20/-40:48/-40:10
set TB=-200/200
set GRID=-Ba15mf15m/a15mf5mWSNE
set PRJ=-Jm25.5c
set GSC=-I0.09m
set GSR=-I0.04m
set AEQ=-C250
set LAB=-A20f10
set VIEW=-E160/30
set SUN=-A315

gmtset PAPER_MEDIA        = a5+                                     #Changes in GMT default
gmtset PAGE_ORIENTATION       = portrait #portrait / landscape
gmtset X_ORIGIN          = 2.5c    #Rechtswert
gmtset Y_ORIGIN          = -2.0c   #Hochwert
gmtset BASEMAP_TYPE        = plain   #fancy / plain
gmtset DEGREE_FORMAT        = 0
gmtset GRID_CROSS_SIZE= 0

gmtconvert $FILE.xyz -bo -V > $FILE.b
blockmean $FILE.b $GRENZEN $GSC -bi3 -bo -V > $FILE.mean.b
surface $FILE.mean.b -G$FILE.grd $GSR $GRENZEN -T0.35 -bi3 -V
grdmask $FILE.xyz -G$FILE.mask.grd $GRENZEN $GSR -NNaN/0/0 -S0.2k -V
grdmath -V $FILE.grd $FILE.mask.grd ADD = $FILE.3.grd
grdgradient $FILE.3.grd $SUN -M -G$FILE.3.grad.grd -V -Ne0.7
grd2cpt -Crainbow $FILE.3.grd -Z -Chaxby > $FILE.3.cpt
grdimage $FILE.3.grd $GRENZEN -V $PRJ -Y4.5c -C./bathymetrie.3.cpt -I$FILE.3.grad.grd -K >! $OUT
pscoast $PRJ $GRENZEN -Df -G200/200/200 -V -O -K >> $OUT
psbasemap $PRJ $GRENZEN $GRID -V -O -K >> $OUT
psxy ../profile/profil01.xy $PRJ $GRENZEN -W1.5p/black -V -O -K >> $OUT
[···]
psxy ../profile/profil14.xy $PRJ $GRENZEN -W1.5p/black -V -O -K >> $OUT
psxy ./stationen.xy $PRJ $GRENZEN -Sc0.3c -Wblack -Gwhite -V -O -K >> $OUT

#--------------------------------------------------------
#stationen.xy :
#-84.4745167 -40.3018333
#-84.648 -40.4008333
#-84.5038333 -40.5986667
```

Figure B.2: GMT commands for chart generation.

136

Results of Angular Range Analysis

Station	Grain size	Profile	150 pings	60 pings	30 pings	20 pings	10 pings
SO213-14	clay/ gravel	3	-	very fine sand (1.1)	coarse silt (1.1)	clay (0.8)	coarse silt (1.1)
		4	-	very fine sand (1.0)	very fine sand (0.8)	very fine sand (1.2)	coarse silt (0.5)
		11	-	very fine sand (0.8)	very fine sand (0.9)	very fine sand (0.7)	very fine sand (0.7)
		12	coarse silt (1.0)	coarse silt (1.0)	coarse silt (1.0)	coarse silt (0.9)	medium silt (1.2)
SO213-15	very fine sand/ coarse silt	1	very fine silt (0.8)	clay (0.4)	clay (0.4)	medium silt (0.5)	coarse silt (1.1)
		11	coarse silt (1.0)	coarse silt (1.0)	medium silt (0.6)	coarse silt (1.1)	medium silt (0.7)
SO213-17	fine sand/ very fine sand	2	medium silt (0.8)	clay (1.3)	medium silt (0.9)	medium silt (1.0)	coarse silt (1.6)
		3	medium silt (0.7)	medium silt (1.2)	medium silt (1.4)	fine silt (0.8)	clay (2.0)
		14	clay (0.6)	clay (1.3)	clay (1.6)	clay (1.6)	medium silt (1.7)

Table B.2: Results of automatic sediment classification in *CARIS HIPS and SIPS* using the Jackson model with varying patch sizes. The confidence level is given in round brackets (refer to Tab. B.3).

very good	≤ 0.4
good	0.5 - 0.7
fair	0.8 - 0.9
inconclusive	≥ 1

Table B.3: Confidence levels in *CARIS HIPS and SIPS*.

Table B.4: Results of Angular Range Analysis

Station	Grain size	Profile	no bp jackson	no bp biot	bp jackson
SO213-14	gravel/ clay	3	coarse silt (1.1)	coarse silt (1.0)	gravel (1.6)
		4	coarse silt (0.5)	coarse silt (0.8)	gravel (1.2)
		11	very fine sand (0.7)	-	-
		12	medium silt (1.2)	coarse silt (1.2)	gravel (0.7)
SO213-15	very fine sand/ coarse silt	1	coarse silt (1.1)	coarse silt (0.6)	gravel (0.7)
		11	medium silt (0.7)	coarse silt (0.8)	gravel (0.8)
SO213-17	fine sand/ very fine sand	2	coarse silt (1.6)	very fine sand (1.6)	gravel (3.4)
		3	clay (2.0)	clay (2.0)	gravel (1.0)
		14	medium silt (1.7)	clay (1.6)	fine sand (1.9)

Table B.4: Results of automatic sediment classification in *CARIS HIPS and SIPS* with and without applying a beam pattern correction and with different ARA models. The confidence levels are given in brackets (Tab. B.3). The patch size was set to 10 pings. For explanation of abbreviations see Tab. B.5.

no bp	no beam pattern correction was applied
bp	beam pattern correction was applied (bp-file was generated at a homogeneous area outside of investigation area
gt	ground-truthing (beam pattern file was created at sample location and sediment type was defined).

Table B.5: Explanation of abbreviations of Tab. B.4 / B.6 / B.7.

138

				Results of Angular Range Analysis		
Station	Grain size	Profile	no bp	gt SO213-14	gt SO213-15	gt SO213-17
SO213-14	gravel/ clay	3	coarse silt (1.1)	gravel (1.5)	fine sand (0.7)	medium sand (0.9)
		4	very fine sand (0.8)	gravel (0.5)	gravel (1.0)	gravel (1.4)
		11	very fine sand (0.9)	gravel (1.7)	gravel (1.4)	gravel (1.3)
		12	coarse silt (1.0)	gravel (0.9)	gravel (1.2)	gravel (1.3)
SO213-15	very fine sand/ coarse silt	1	clay (0.4)	gravel (0.5)	medium sand (0.5)	gravel (1.3)
		11	medium silt (0.6)	gravel (0.7)	medium sand (0.9)	gravel (1.3)
SO213-17	fine sand/ very fine sand	2	medium silt (0.9)	gravel (3.4)	medium sand (0.9)	gravel (1.6)
		3	medium silt (1.4)	gravel (1.0)	medium sand (1.2)	fine sand (2.0)
		14	clay (1.6)	gravel (2.1)	medium sand (2.1)	very coarse sand (2.1)

Table B.6: Results of sediment classification in *CARIS HIPS and SIPS* with different ground-truthing locations using the Jackson model. The confidence levels are given in brackets (refer to Tab. B.3). The patch size was set to 30 pings for comparison of the results with *FMGT*. For explanation of abbreviations see Tab. B.5.

| | | | Results of Angular Range Analysis | | |
Station	Grain size	Profile	gt SO213-14	gt SO213-15	gt SO213-17
SO213-14	gravel/ clay	3	gravel (-1.0)	medium sand (0.7)	gravel (-1.0)
		4	gravel (-1.0)	gravel (-1.0)	gravel (-1.0)
		11	gravel (-1.0)	gravel (-1.0)	gravel (-1.0)
		12	gravel (-1.0)	gravel (-1.0)	gravel (-1.0)
SO213-15	very fine sand/ coarse silt	1	gravel (0.5)	medium sand (0.6)	gravel (-1.0)
		11	gravel (0.8)	coarse sand (0.9)	gravel (-1.0)
SO213-17	fine sand/ very fine sand	2	gravel (-1.0)	coarse sand (0.9)	gravel (-1.0)
		3	gravel (-1.0)	medium sand (1.2)	fine sand (2.0)
		14	gravel (2.1)	coarse sand (2.1)	gravel (2.2)

Table B.7: Results of sediment classification in *CARIS HIPS and SIPS* with different ground-truthing locations using the Biot theory. The confidence levels are given in brackets (refer to Tab. B.3). The patch size was set to 30 pings. For explanation of abbreviations see Tab. B.5. 5cm

| | | | Results of Angular Range Analysis | | | | |
Station	Grain size	Profile	no beam pattern	with beam pattern	gt SO213-14	gt SO213-15	gt SO213-17
SO213-14	gravel/ clay	3	medium silt	very fine sand	gravel	fine sand	medium sand
		4	coarse silt	medium sand	gravel	medium sand	very fine sand
		11	clay	coarse silt / very coarse sand	medium sand	gravel	fine sand
		12	clay	gravel	medium sand	gravel	coarse silt
SO213-15	very fine sand/ coarse silt	1	medium silt	very fine sand	gravel	very fine sand	medium sand
		11	coarse silt	coarse sand	gravel	fine sand	medium silt
SO213-17	fine sand/ very fine sand	2	clay	very fine sand	gravel	very fine sand	coarse silt
		3	clay	very fine sand	gravel	very fine sand	clay
		14	clay	coarse silt	fine sand	very fine sand	medium silt

Table B.8: Results of sediment classification in *FMGeocoder Toolbox*. Two results for SO213-14 "with beam pattern" are listed, because the station is situated in the nadir area and the results of the adjacent patches differ a lot.
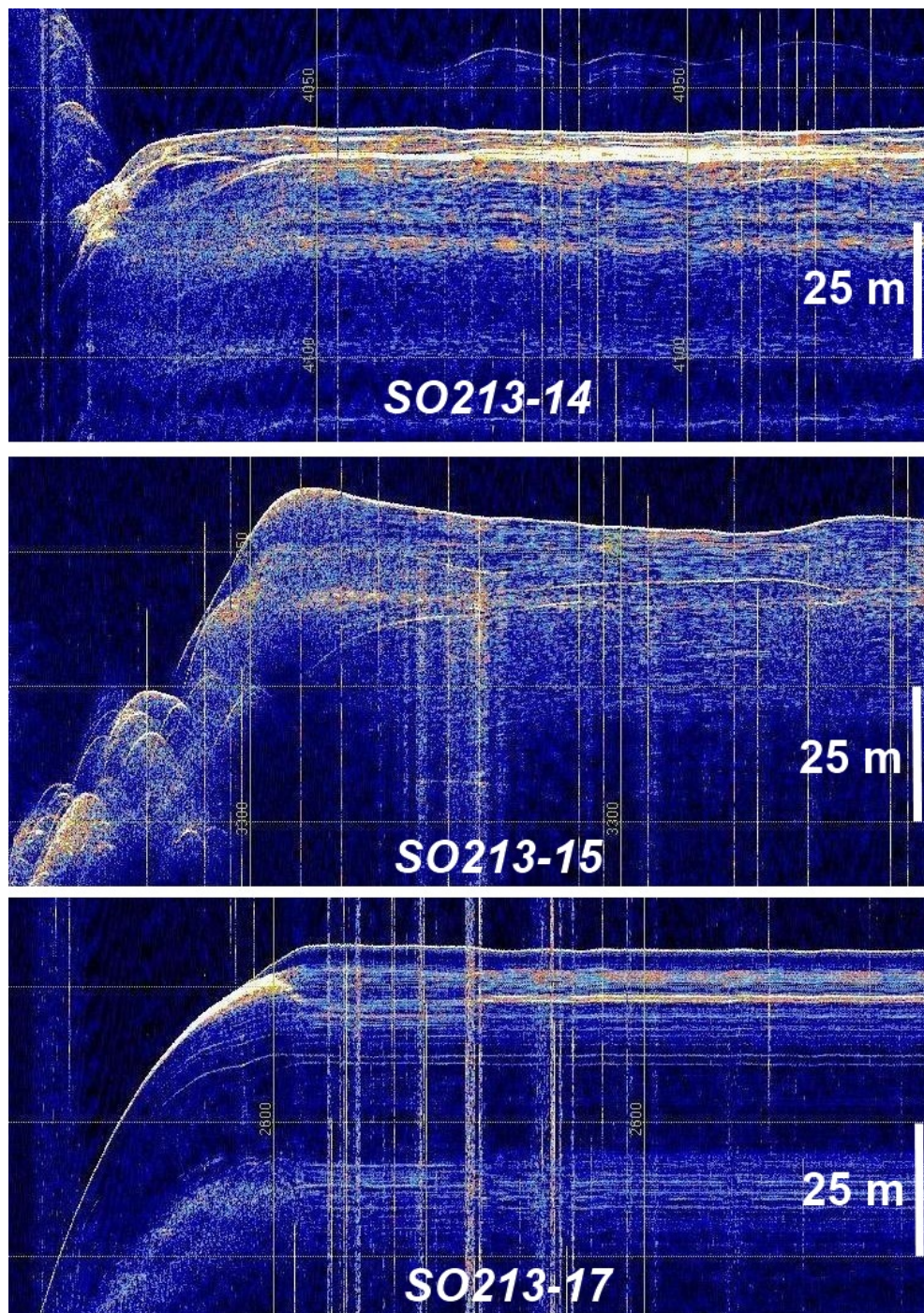
Figure B.3: Parasound profiles of ground-truthing locations.

Appendix C

ARA – Angular response classification
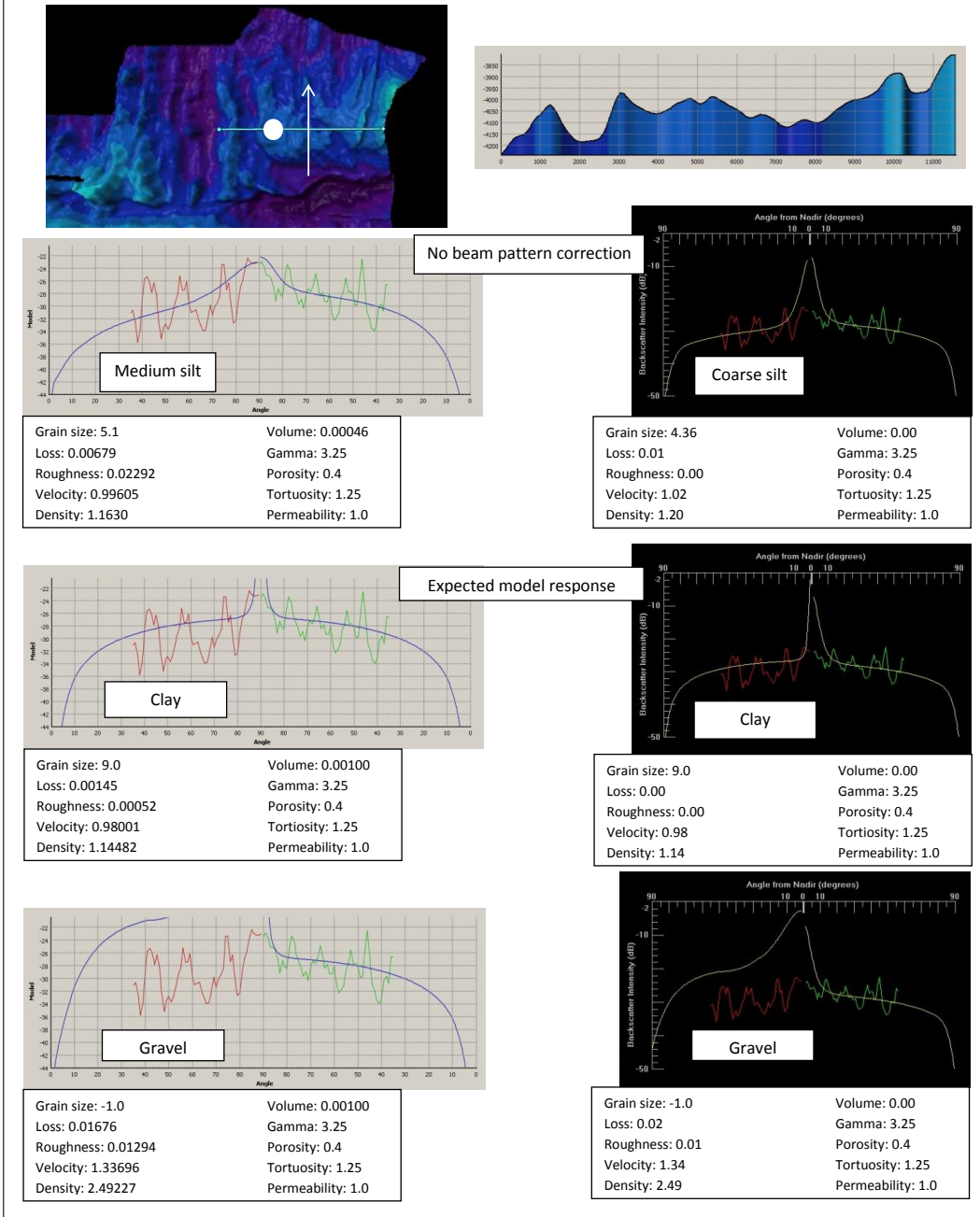
Figure C.1: Observed (green/red) and modeled (blue/yellow) angular response at ground-truthing location SO213-14 recorded by profile 3 generated in *FMGT* (left) and *CARIS* (right). No beam pattern correction was applied to the data ("No beam pattern correction"). The grain size was adjusted to the measured grain size value. The resulting modeled angular responses are shown below ("Expected angular repsonse").
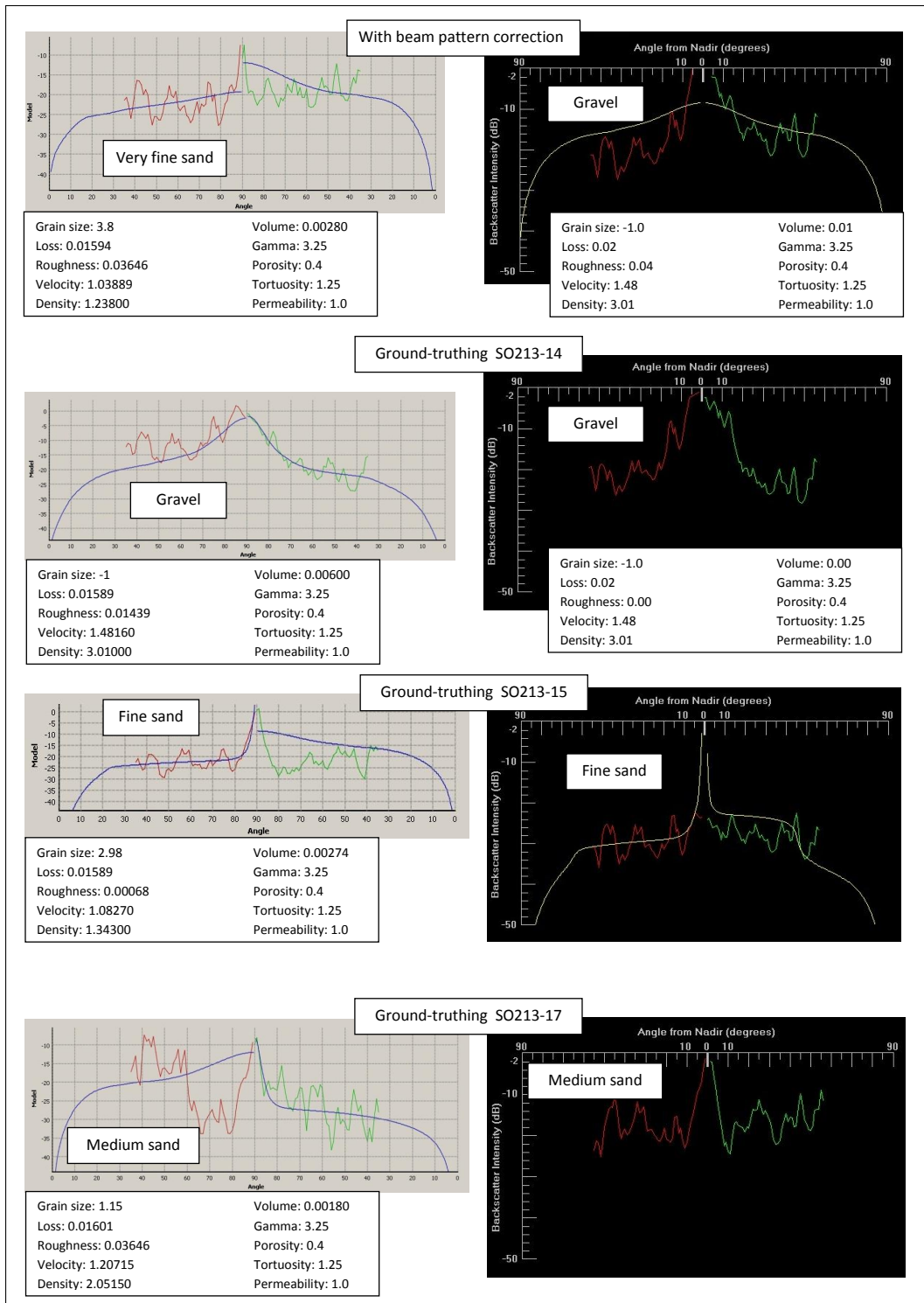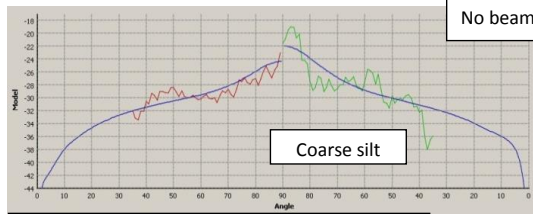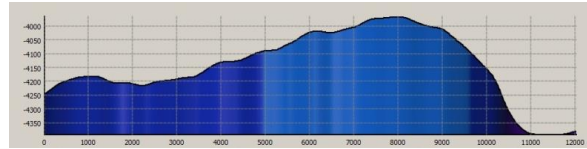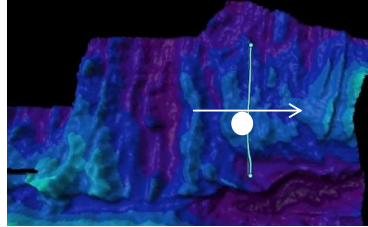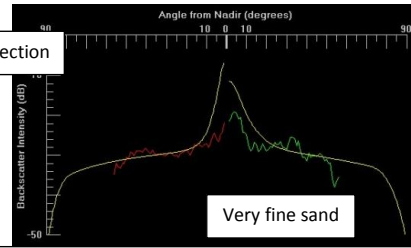
Figure C.2: Observed (green/red) and modeled (blue/yellow) angular response at ground-truthing location SO213-14 recorded by profile 3 generated in *FMGT* (left) and *CARIS* (right). To the data in the upper graph a beam pattern correction with no specification of the sediment type was applied. The data in the second graph from the top was corrected for beam pattern with SO213-14 used for ground-truthing. For the third data the applied beam pattern file was generated at SO213-15 with declaration of the measured sediment type. The bottom graph shows data, which was beam pattern corrected by using SO213-17 as ground-truthing location.

Figure C.3: Observed (green/red) and modeled (blue/yellow) angular response at ground-truthing location SO213-14 recorded by profile 4 generated in *FMGT* (left) and *CARIS* (right). No beam pattern correction was applied to the data ("No beam pattern correction"). The grain size was adjusted to the measured grain size value. The resulting modeled angular responses are shown below ("Expected angular response").
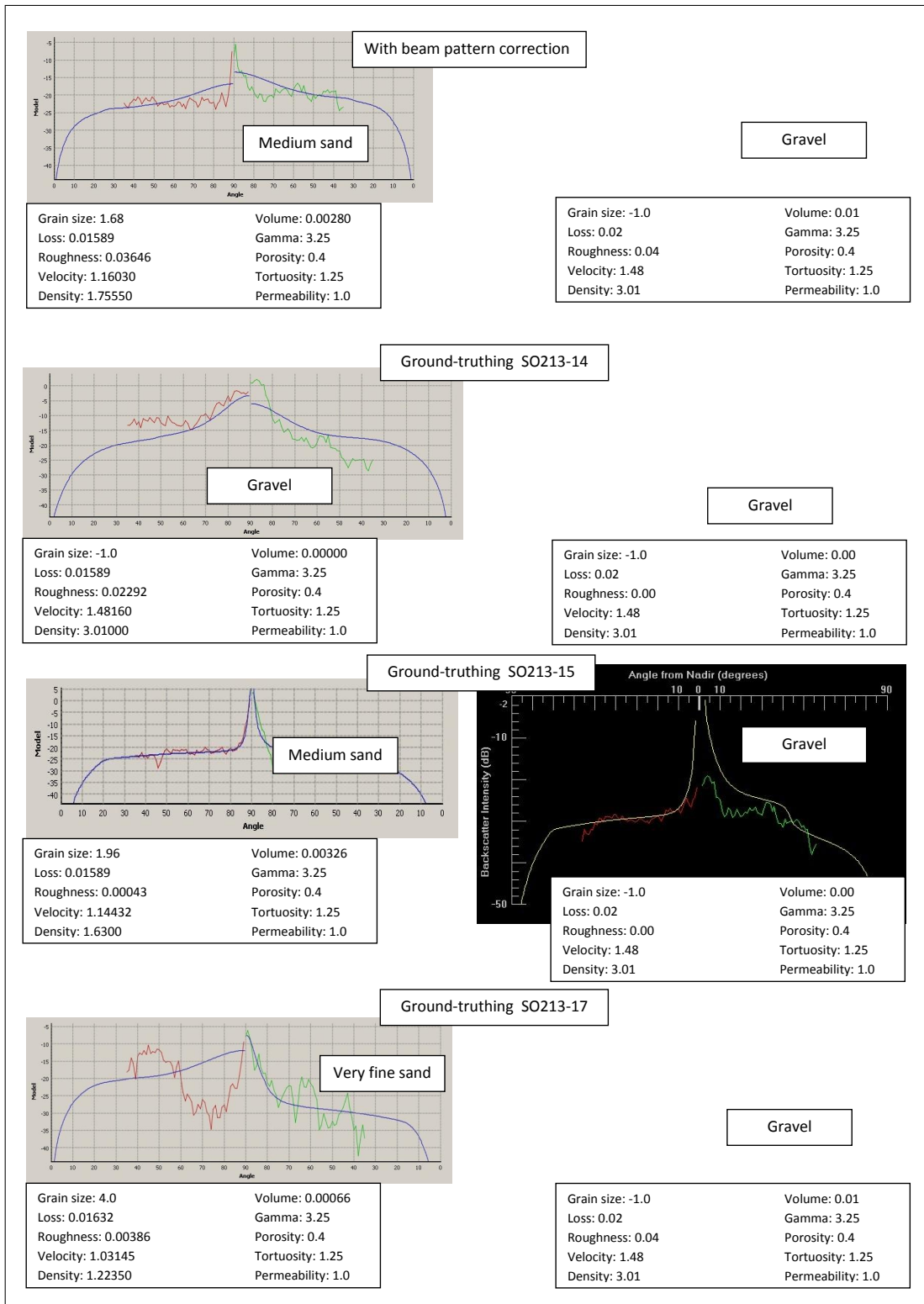
Figure C.4: Observed (green/red) and modeled (blue/yellow) angular response at ground-truthing location SO213-14 recorded by profile 4 generated in *FMGT* (left) and *CARIS* (right). To the data in the upper graph a beam pattern correction with no specification of the sediment type was applied. The data in the second graph from the top was corrected for beam pattern with SO213-14 used for ground-truthing. For the third data the applied beam pattern file was generated at SO213-15 with declaration of the measured sediment type. The bottom graph shows data, which was beam pattern corrected by using SO213-17 as ground-truthing location.
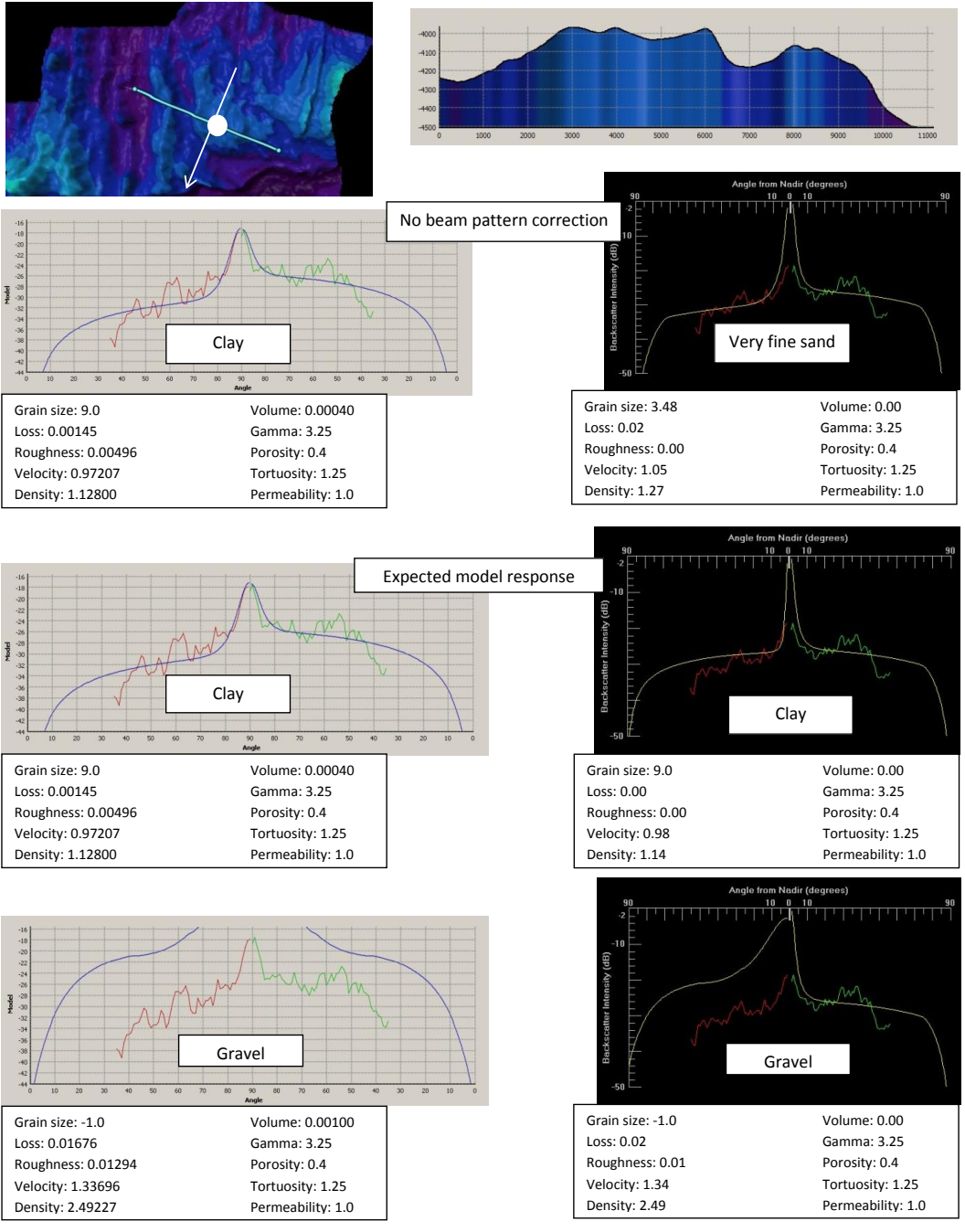
Figure C.5: Observed (green/red) and modeled (blue/yellow) angular response at ground-truthing location SO213-14 recorded by profile 11 generated in *FMGT* (left) and *CARIS* (right). No beam pattern correction was applied to the data ("No beam pattern correction"). The grain size was adjusted to the measured grain size value. The resulting modeled angular responses are shown below ("Expected angular response").
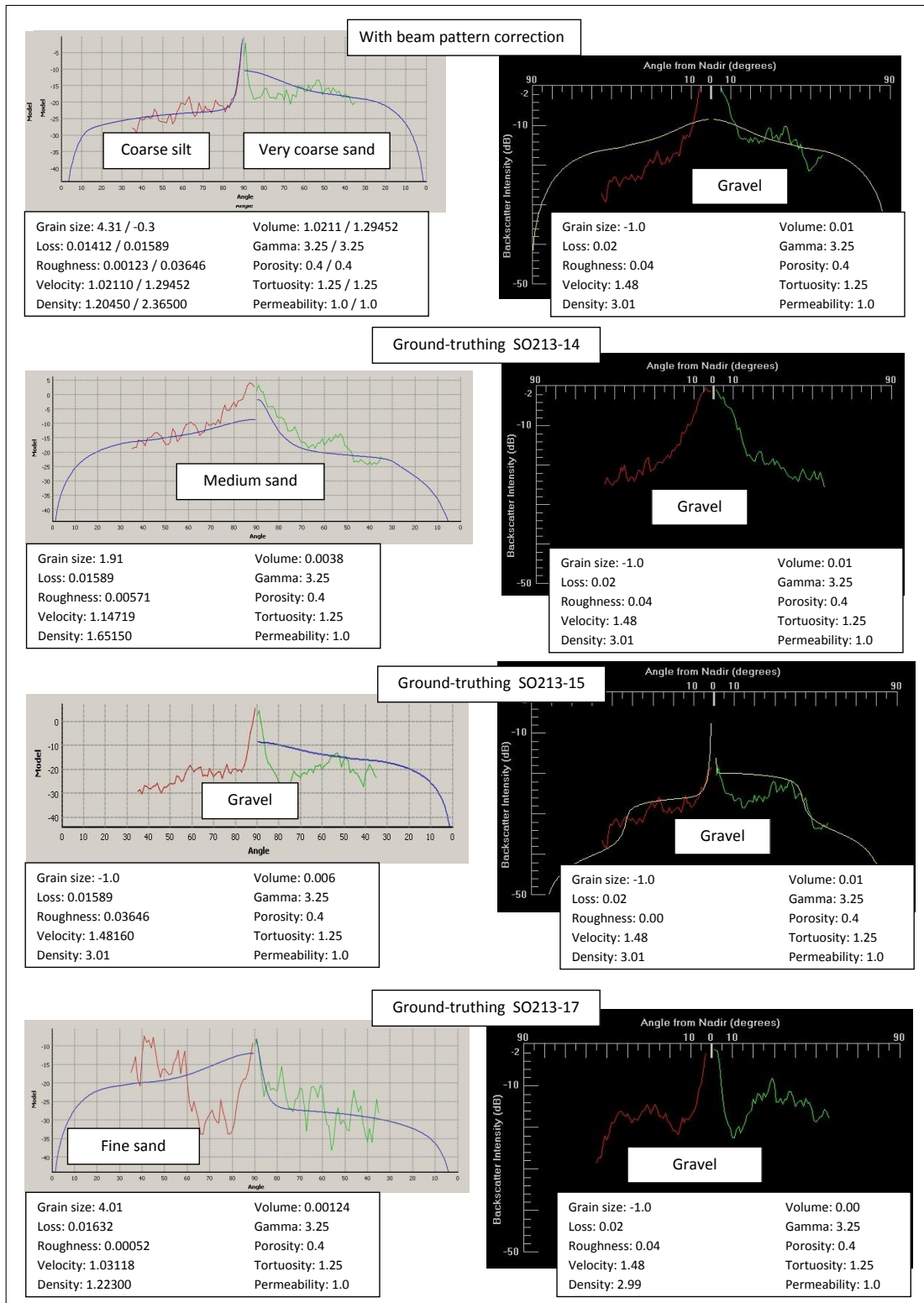
Figure C.6: Observed (green/red) and modeled (blue/yellow) angular response at ground-truthing location SO213-14 recorded by profile 11 generated in *FMGT* (left) and *CARIS* (right). To the data in the upper graph a beam pattern correction with no specification of the sediment type was applied. The data in the second graph from the top was corrected for beam pattern with SO213-14 used for ground-truthing. For the third data the applied beam pattern file was generated at SO213-15 with declaration of the measured sediment type. The bottom graph shows data, which was beam pattern corrected by using SO213-17 as ground-truthing location.
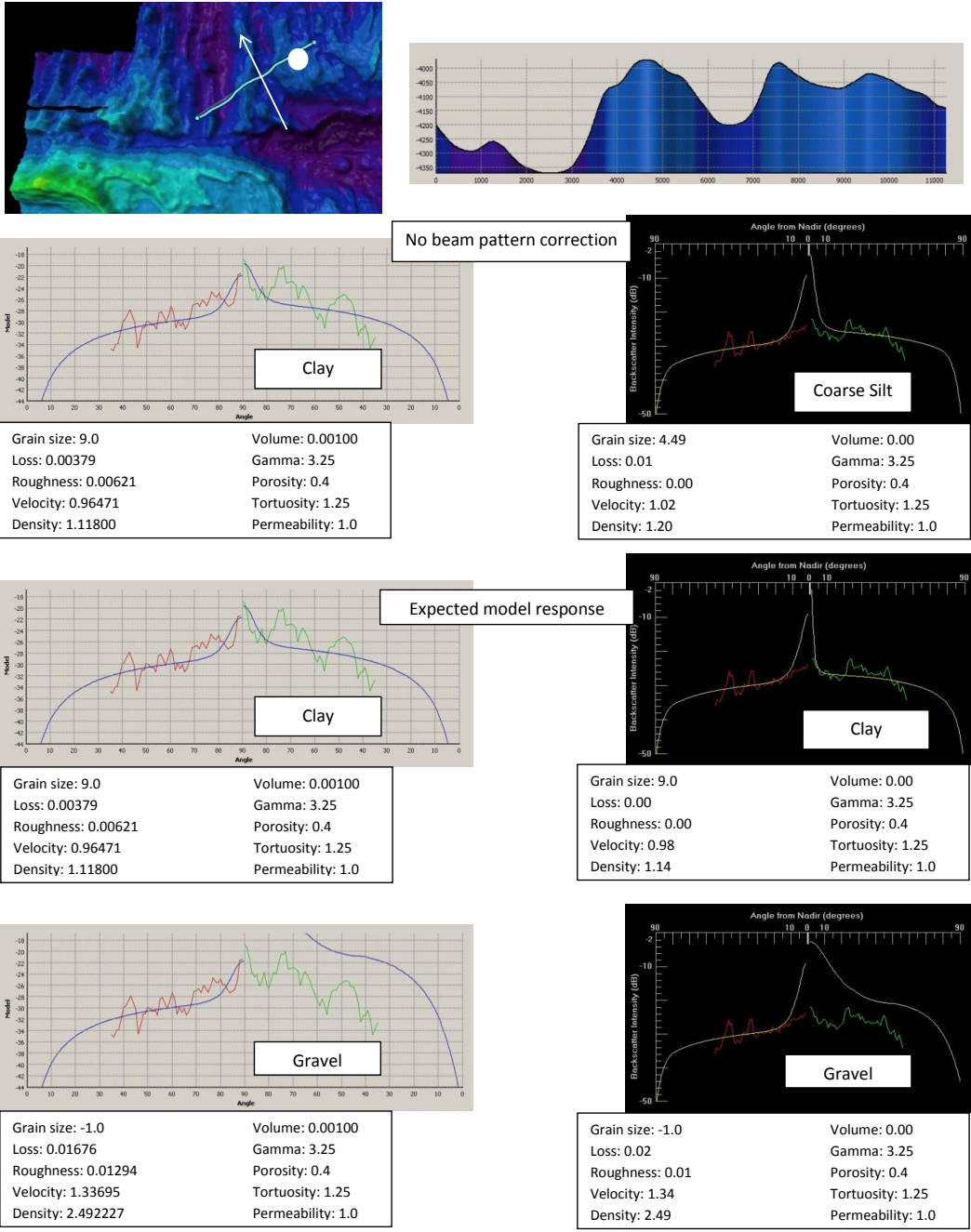
Figure C.7: Observed (green/red) and modeled (blue/yellow) angular response at ground-truthing location SO213-14 recorded by profile 12 generated in *FMGT* (left) and *CARIS* (right). No beam pattern correction was applied to the data ("No beam pattern correction"). The grain size was adjusted to the measured grain size value. The resulting modeled angular responses are shown below ("Expected angular response").
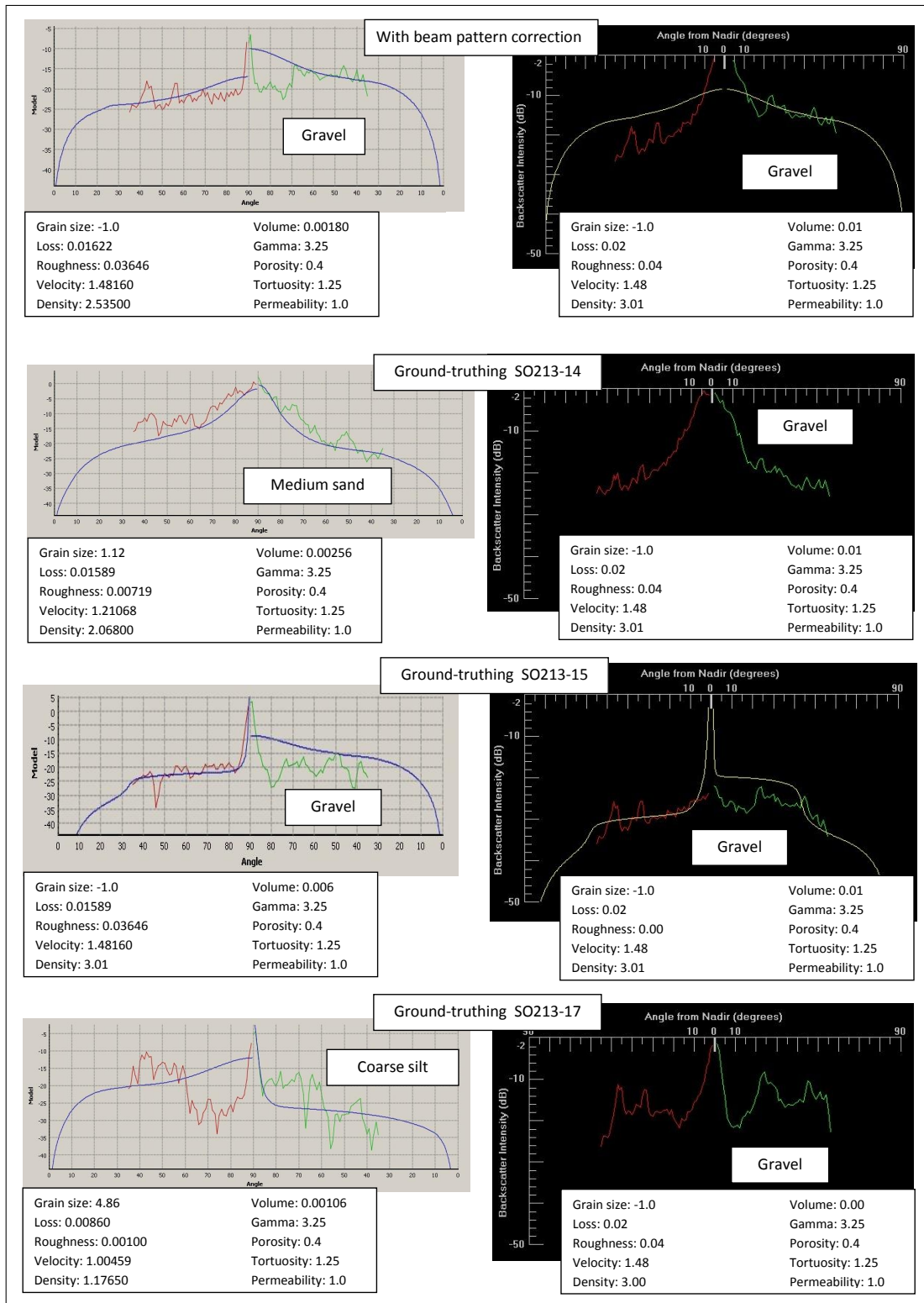
Figure C.8: Observed (green/red) and modeled (blue/yellow) angular response at ground-truthing location SO213-14 recorded by profile 12 generated in *FMGT* (left) and *CARIS* (right). To the data in the upper graph a beam pattern correction with no specification of the sediment type was applied. The data in the second graph from the top was corrected for beam pattern with SO213-14 used for ground-truthing. For the third data the applied beam pattern file was generated at SO213-15 with declaration of the measured sediment type. The bottom graph shows data, which was beam pattern corrected by using SO213-17 as ground-truthing location.
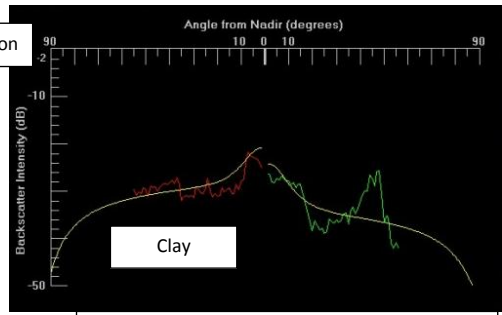
SO213-15 Profile 1 (portside)

No beam pattern correction

Medium silt
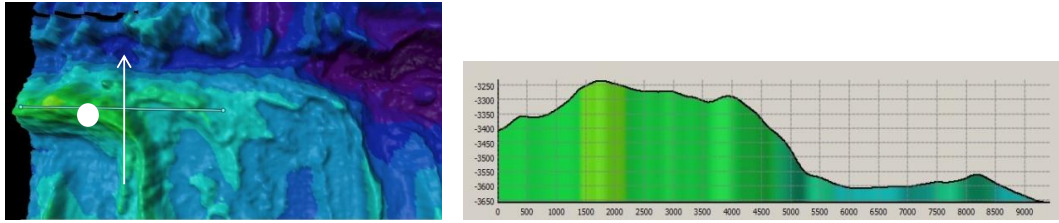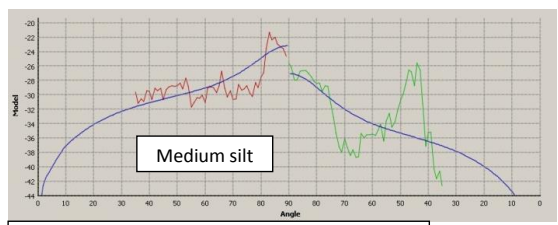
|	
Grain size: 5.19	Volume: 0.00054
Loss: 0.00542	Gamma: 3.25
Roughness: 0.02292	Porosity: 0.4
Velocity: 0.99312	Tortuosity: 1.25
Density: 1.15850	Permeability: 1.0

Clay

Grain size: 8.47	Volume: 0.00
Loss: 0.00	Gamma: 3.25
Roughness: 0.01	Porosity: 0.4
Velocity: 0.98	Tortuosity: 1.25
Density: 1.14	Permeability: 1.0

Expected model response

Very fine sand/ Coarse silt
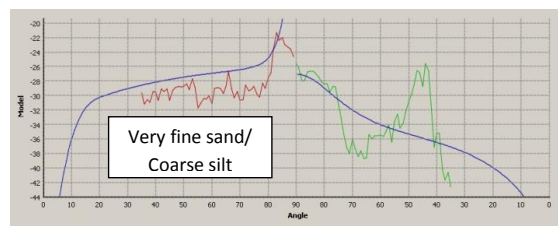
Grain size: 4.0	Volume: 0.00100
Loss: 0.01984	Gamma: 3.25
Roughness: 0.00112	Porosity: 0.4
Velocity: 1.03644	Tortuosity: 1.25
Density: 1.22361	Permeability: 1.0

Very fine sand/ Coarse silt
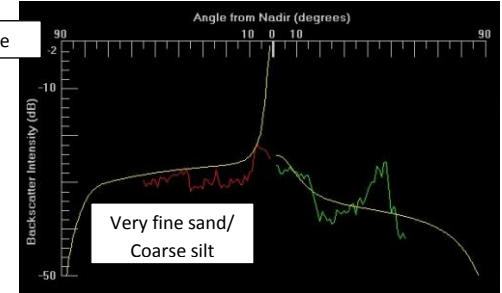
Grain size: 4.0	Volume: 0.00
Loss: 0.02	Gamma: 3.25
Roughness: 0.00	Porosity: 0.4
Velocity: 1.04	Tortuosity: 1.25
Density: 1.22	Permeability: 1.0

Figure C.9: Observed (green/red) and modeled (blue/yellow) angular response at ground-truthing location SO213-15 recorded by profile 1 generated in *FMGT* (left) and *CARIS* (right). No beam pattern correction was applied to the data ("No beam pattern correction"). The grain size was adjusted to the measured grain size value. The resulting modeled angular responses are shown below ("Expected angular response").

Figure C.10: Observed (green/red) and modeled (blue/yellow) angular response at ground-truthing location SO213-15 recorded by profile 1 generated in *FMGT* (left) and *CARIS* (right). To the data in the upper graph a beam pattern correction with no specification of the sediment type was applied. The data in the second graph from the top was corrected for beam pattern with SO213-14 used for ground-truthing. For the third data the applied beam pattern file was generated at SO213-15 with declaration of the measured sediment type. The bottom graph shows data, which was beam pattern corrected by using SO213-17 as ground-truthing location.
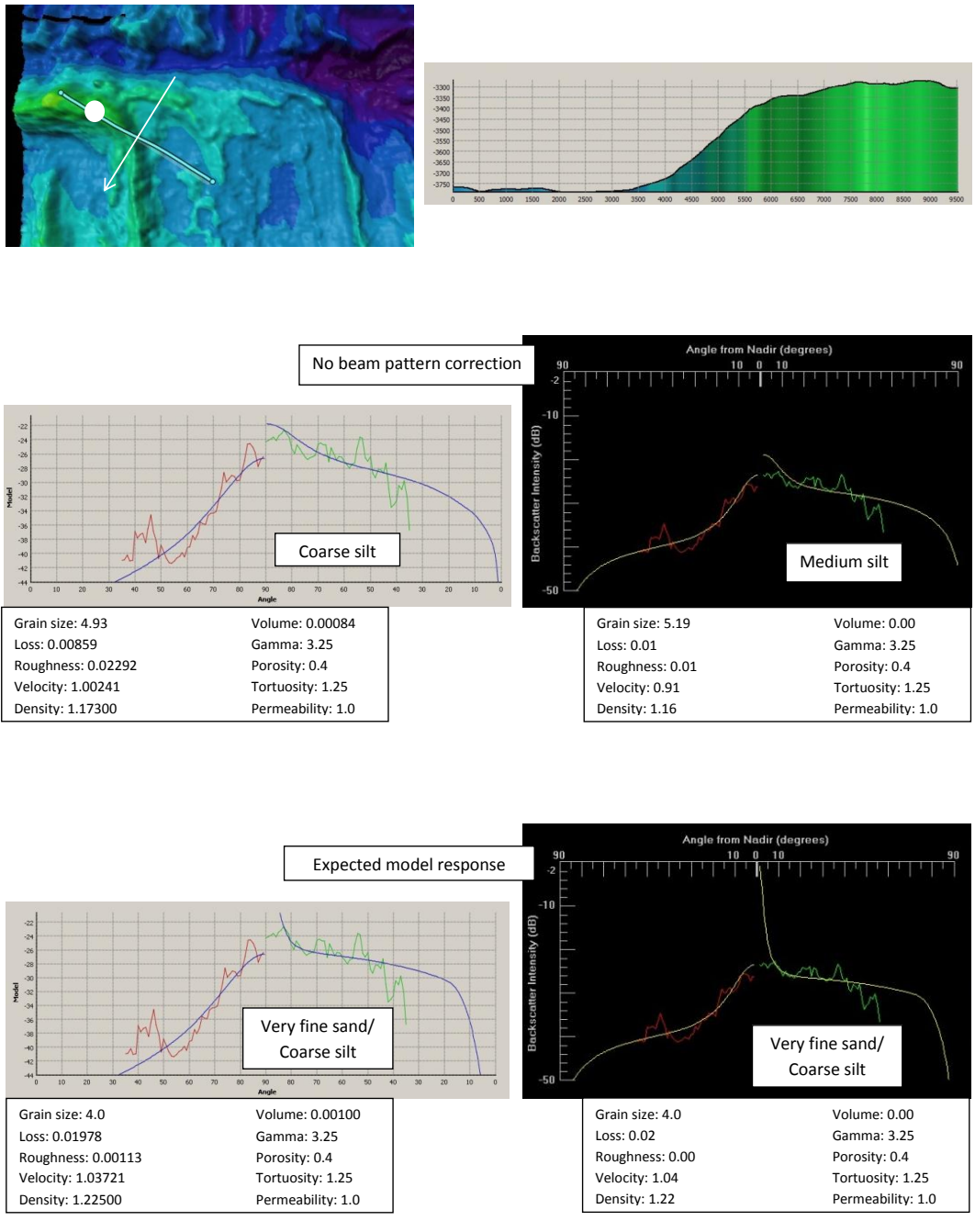
Figure C.11: Observed (green/red) and modeled (blue/yellow) angular response at ground-truthing location SO213-15 recorded by profile 11 generated in *FMGT* (left) and *CARIS* (right). No beam pattern correction was applied to the data ("No beam pattern correction"). The grain size was adjusted to the measured grain size value. The resulting modeled angular responses are shown below ("Expected angular response").
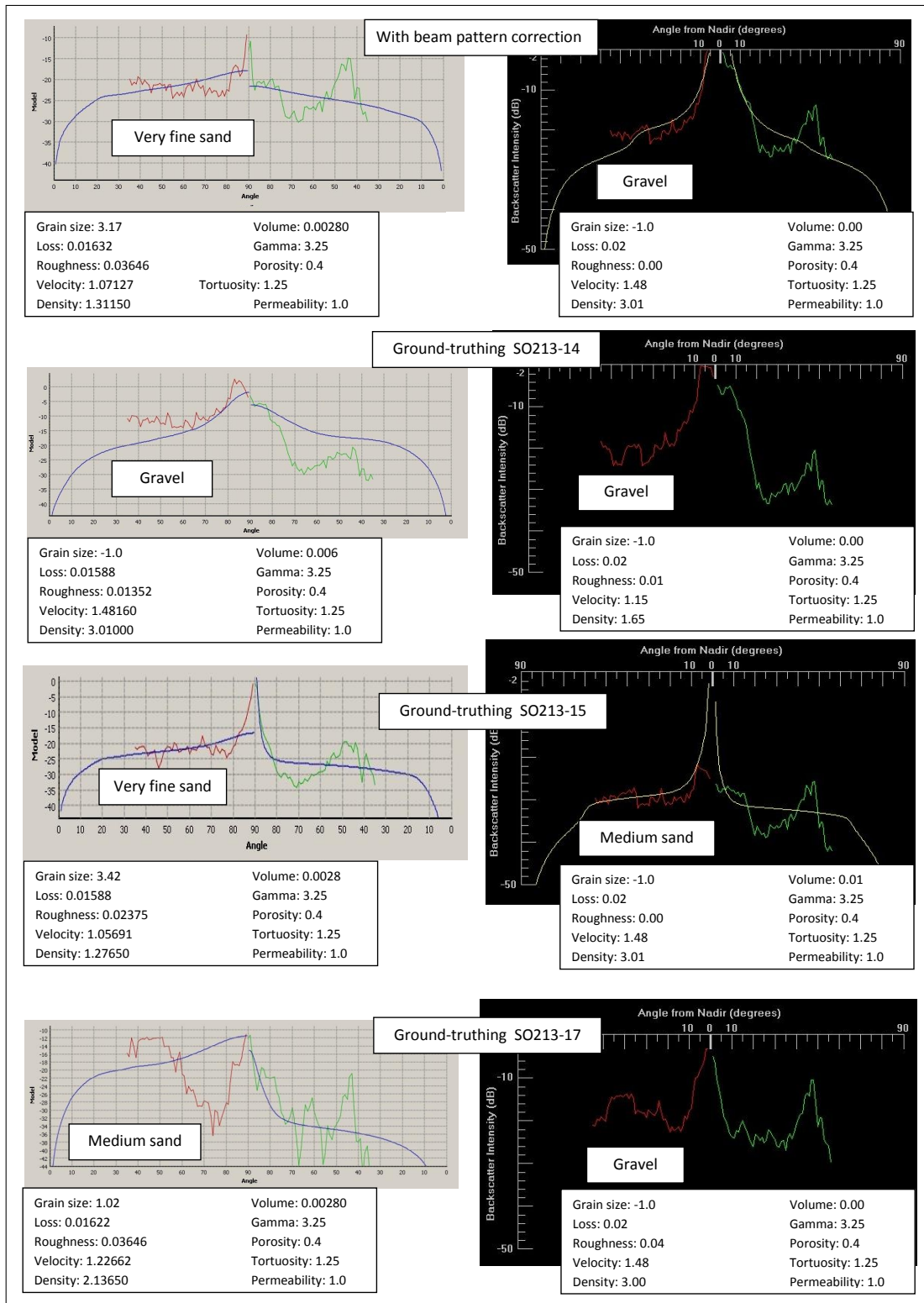
With beam pattern correction

Angle from Nadir (degrees)

Coarse sand

Gravel

Grain size: 0.66	Volume: 0.00280
Loss: 0.01593	Gamma: 3.25
Roughness: 0.03646	Porosity: 0.4
Velocity: 1.24467	Tortuosity: 1.25
Density: 2.20500	Permeability: 1.0

Grain size: -1.0	Volume: 0.00
Loss: 0.02	Gamma: 3.25
Roughness: 0.04	Porosity: 0.4
Velocity: 1.48	Tortuosity: 1.25
Density: 3.01	Permeability: 1.0

Ground-truthing SO213-14

Gravel

Gravel

Grain size: -1.0	Volume: 0.0
Loss: 0.01588	Gamma: 3.25
Roughness: 0.02992	Porosity: 0.4
Velocity: 1.48160	Tortuosity: 1.25
Density: 3.01000	Permeability: 1.0

Grain size: -1.0	Volume: 0.00
Loss: 0.02	Gamma: 3.25
Roughness: 0.01	Porosity: 0.4
Velocity: 1.35	Tortuosity: 1.25
Density: 2.53	Permeability: 1.0

Ground-truthing SO213-15

Fine Sand

Medium sand

Grain size: 2.1	Volume: 0.0028
Loss: 0.01588	Gamma: 3.25
Roughness: 0.03646	Porosity: 0.4
Velocity: 1.13662	Tortuosity: 1.25
Density: 1.57650	Permeability: 1.0

Grain size: 1.10	Volume: 0.00
Loss: 0.02	Gamma: 3.25
Roughness: 0.00	Porosity: 0.4
Velocity: 1.21	Tortuosity: 1.25
Density: 2.08	Permeability: 1.0

Ground-truthing SO213-17

Angle from Nadir (degrees)

Medium silt

Gravel

Grain size: 5.02	Volume: 0.00056
Loss: 0.00679	Gamma: 3.25
Roughness: 0.004442	Porosity: 0.4
Velocity: 0.99926	Tortuosity: 1.25
Density: 1.16800	Permeability: 1.0

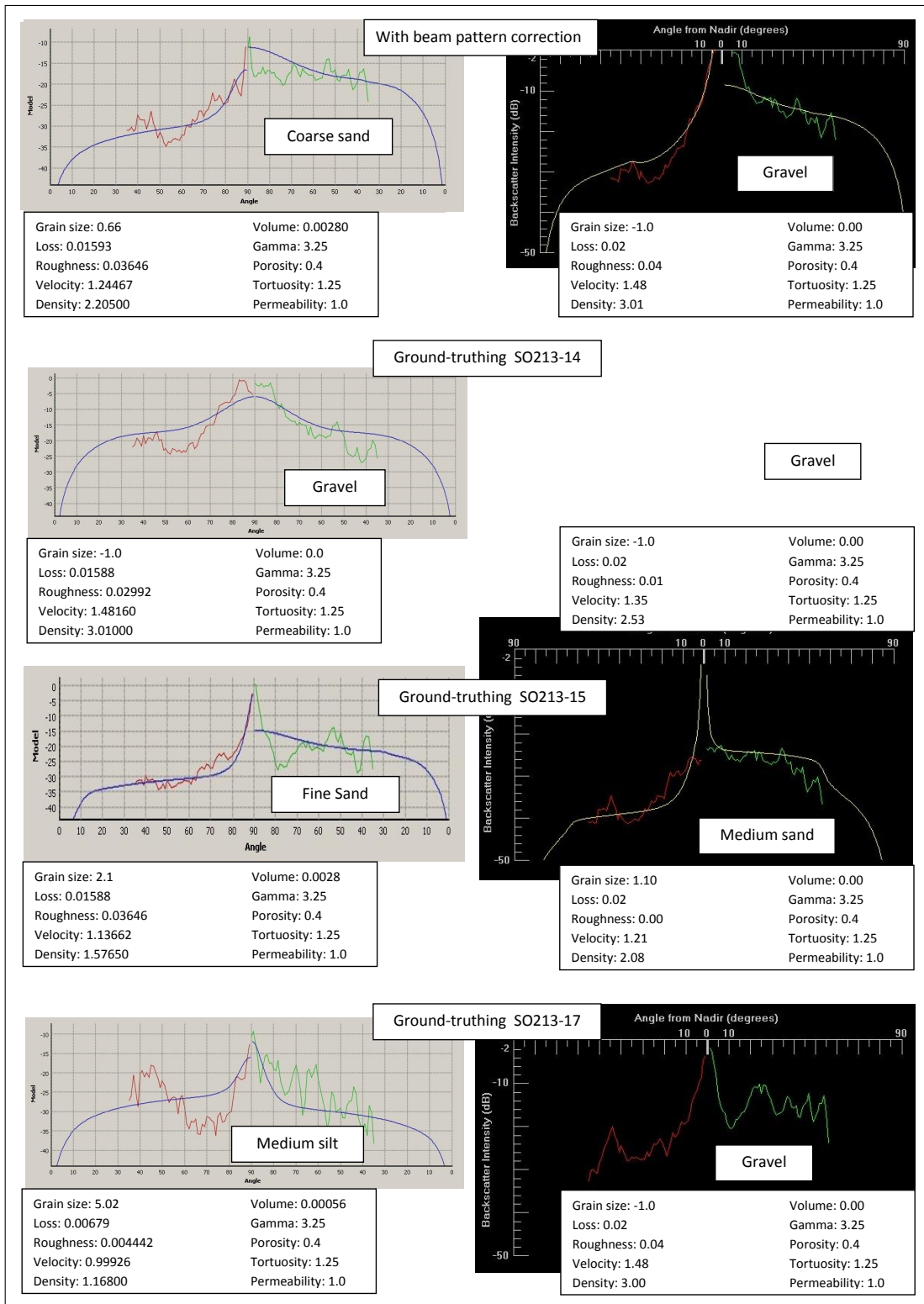| Grain size: -1.0	Volume: 0.00
Loss: 0.02	Gamma: 3.25
Roughness: 0.04	Porosity: 0.4
Velocity: 1.48	Tortuosity: 1.25
Density: 3.00	Permeability: 1.0

Figure C.12: Observed (green/red) and modeled (blue/yellow) angular response at ground-truthing location SO213-15 recorded by profile 11 generated in *FMGT* (left) and *CARIS* (right). To the data in the upper graph a beam pattern correction with no specification of the sediment type was applied. The data in the second graph from the top was corrected for beam pattern with SO213-14 used for ground-truthing. For the third data the applied beam pattern file was generated at SO213-15 with declaration of the measured sediment type. The bottom graph shows data, which was beam pattern corrected by using SO213-17 as ground-truthing location.
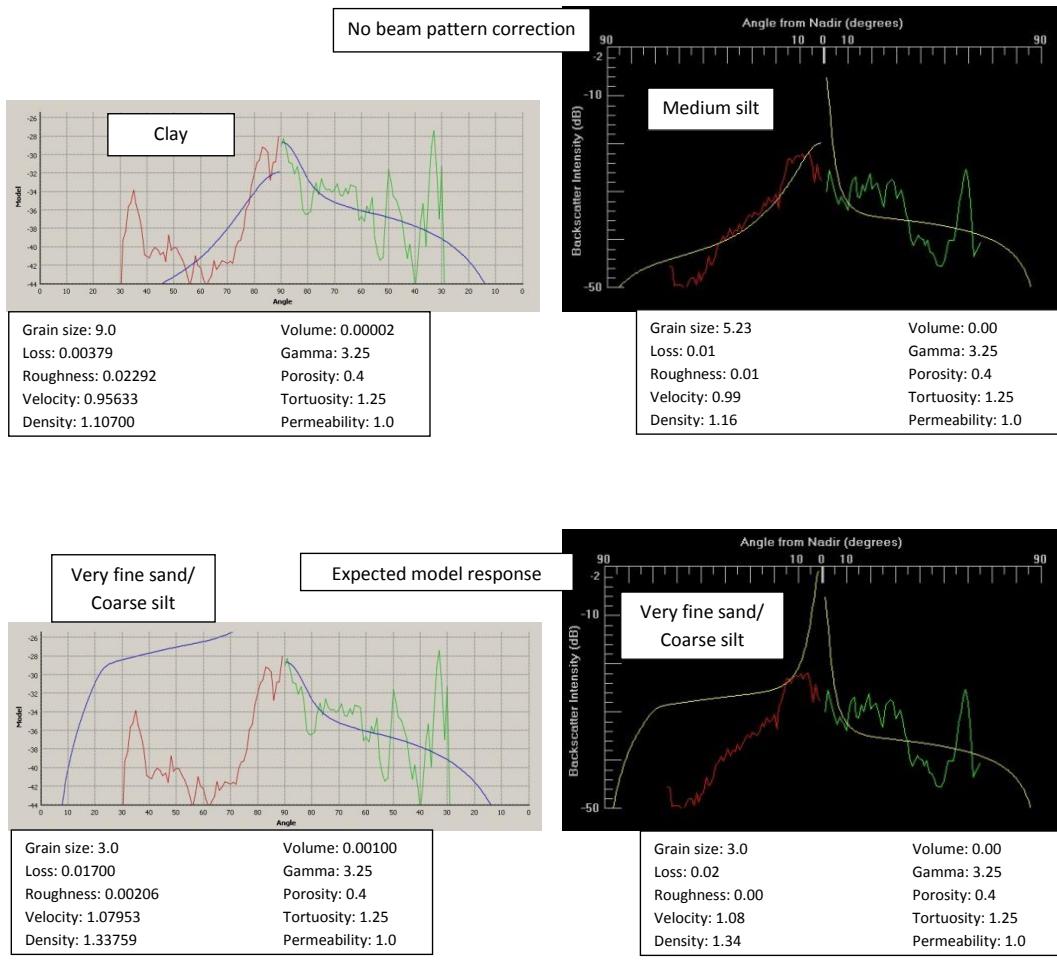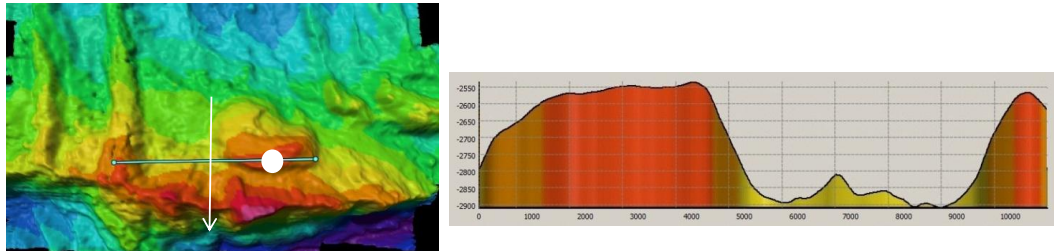
Figure C.13: Observed (green/red) and modeled (blue/yellow) angular response at ground-truthing location SO213-17 recorded by profile 2 generated in *FMGT* (left) and *CARIS* (right). No beam pattern correction was applied to the data ("No beam pattern correction"). The grain size was adjusted to the measured grain size value. The resulting modeled angular responses are shown below ("Expected angular response").
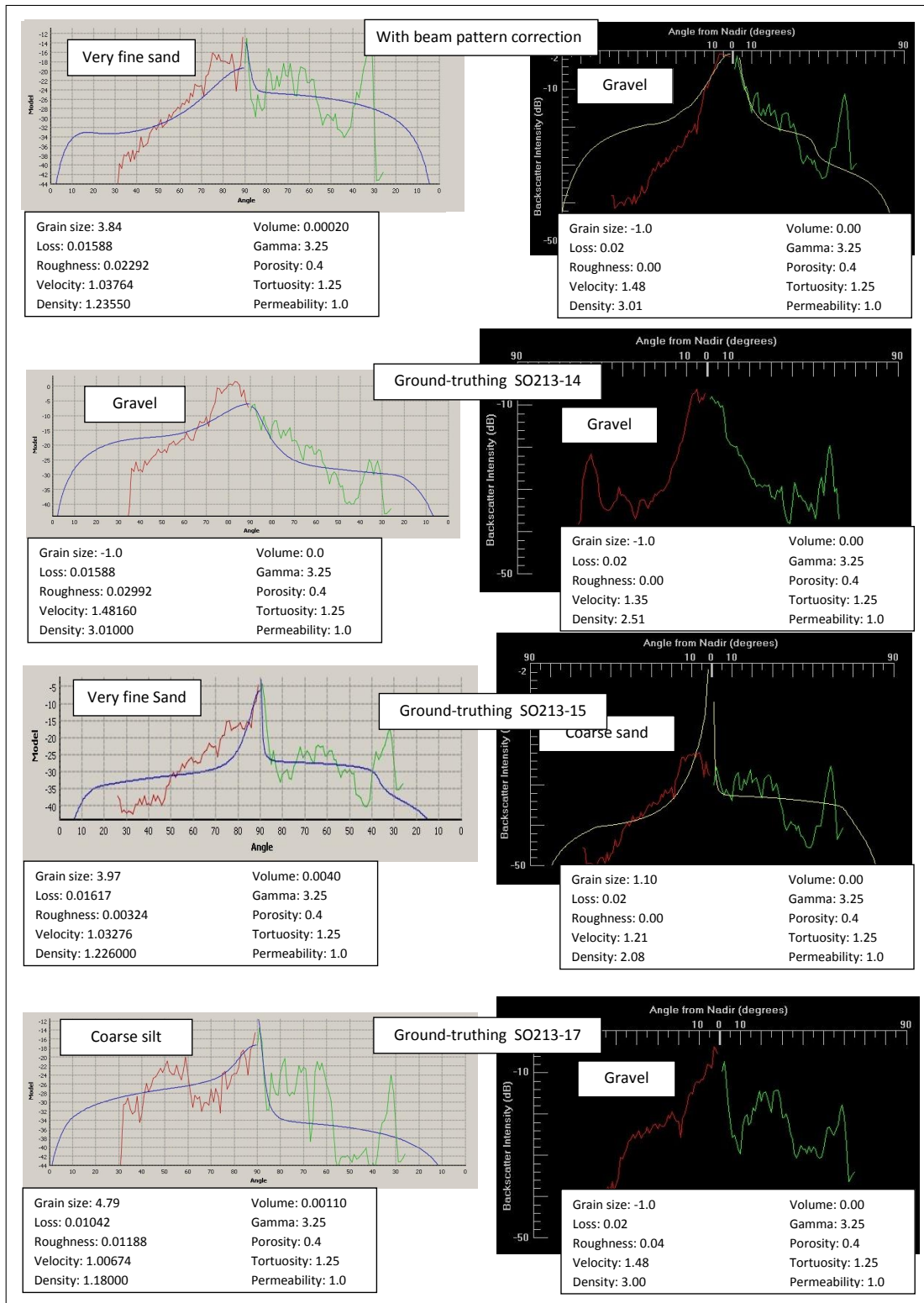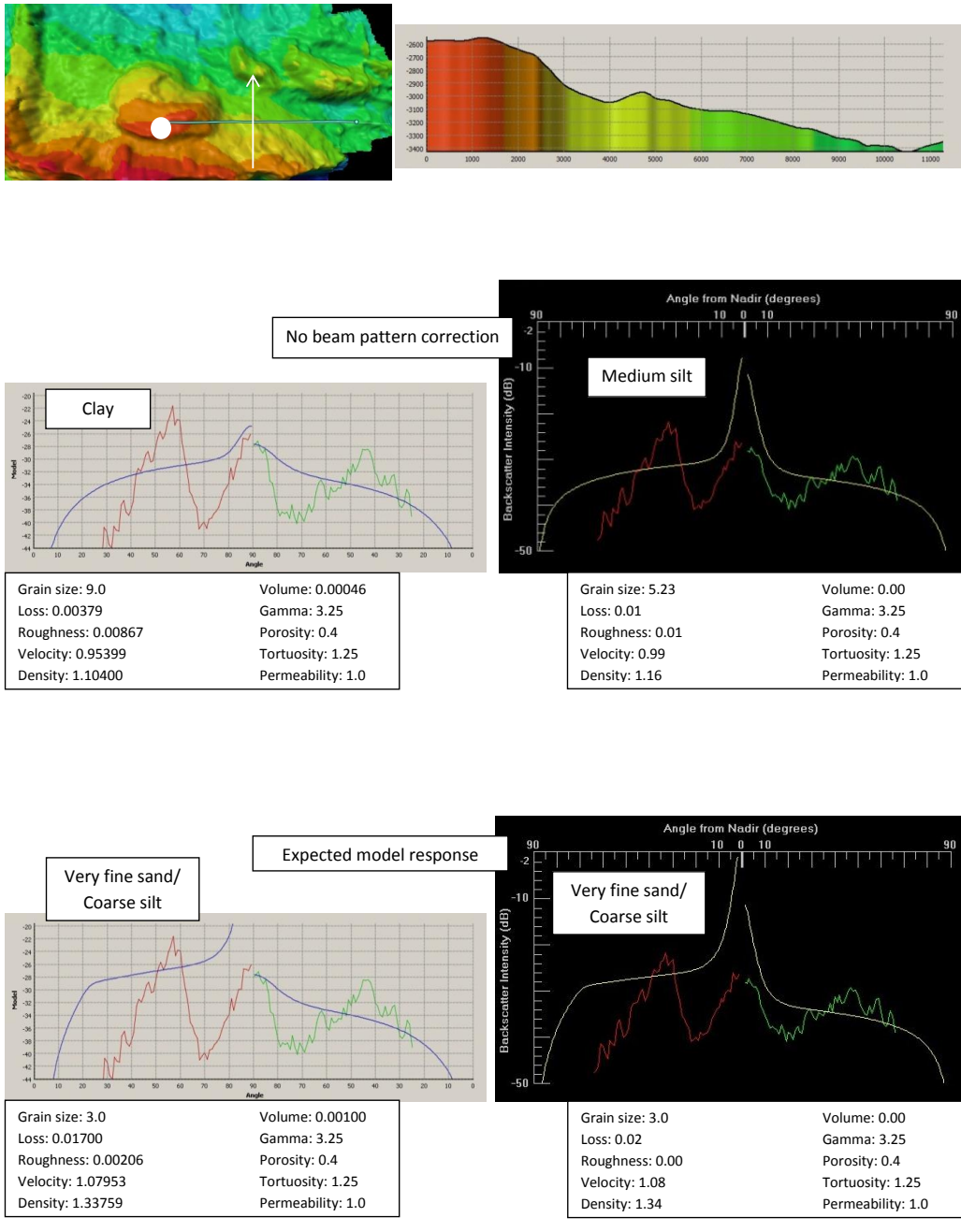
Figure C.14: Observed (green/red) and modeled (blue/yellow) angular response at ground-truthing location SO213-17 recorded by profile 2 generated in *FMGT* (left) and *CARIS* (right). To the data in the upper graph a beam pattern correction with no specification of the sediment type was applied. The data in the second graph from the top was corrected for beam pattern with SO213-14 used for ground-truthing. For the third data the applied beam pattern file was generated at SO213-15 with declaration of the measured sediment type. The bottom graph shows data, which was beam pattern corrected by using SO213-17 as ground-truthing location.
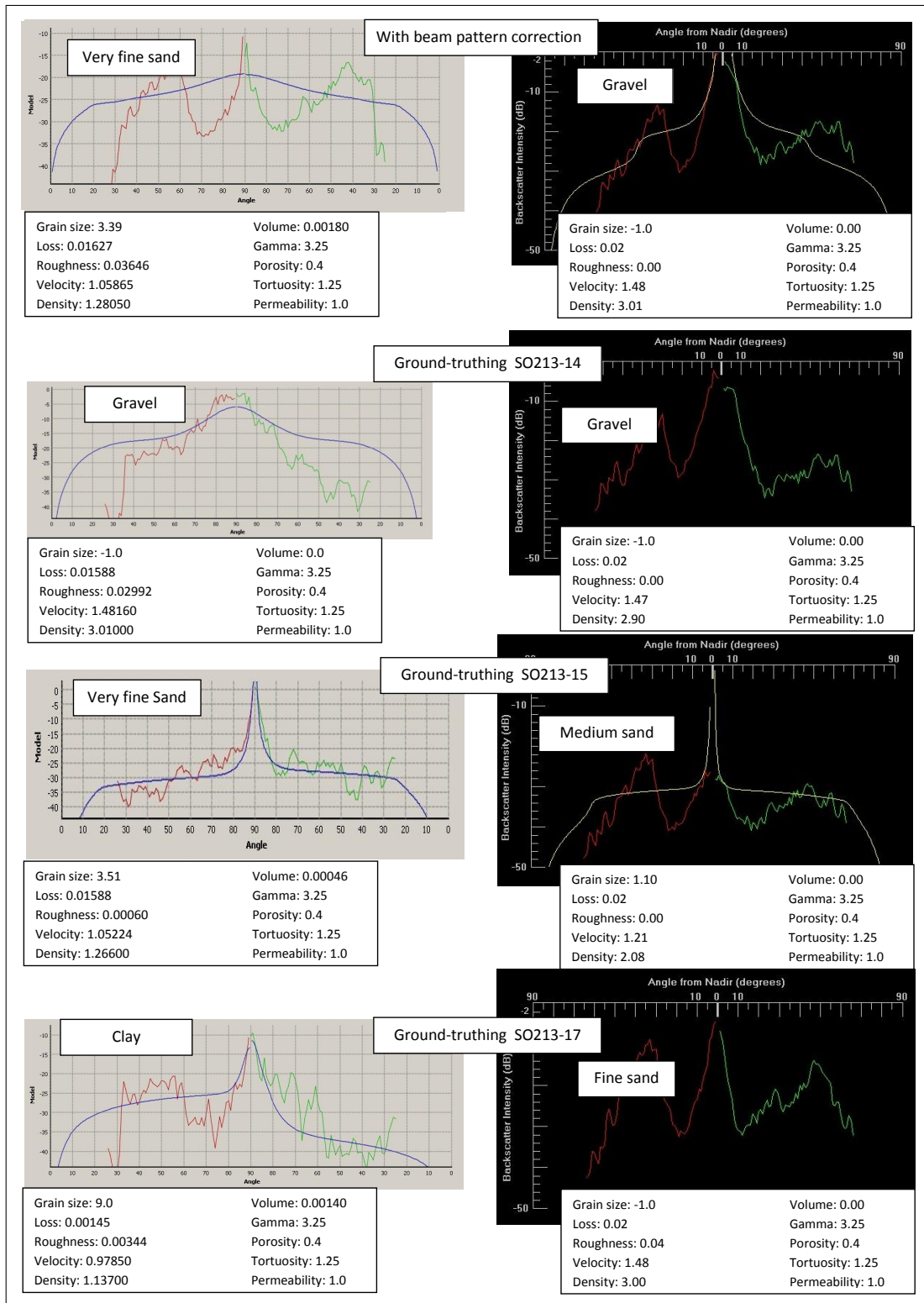
Figure C.15: Observed (green/red) and modeled (blue/yellow) angular response at ground-truthing location SO213-17 recorded by profile 3 generated in *FMGT* (left) and *CARIS* (right). No beam pattern correction was applied to the data ("No beam pattern correction"). The grain size was adjusted to the measured grain size value. The resulting modeled angular responses are shown below ("Expected angular repsonse").

Figure C.16: Observed (green/red) and modeled (blue/yellow) angular response at ground-truthing location SO213-17 recorded by profile 3 generated in *FMGT* (left) and *CARIS* (right). To the data in the upper graph a beam pattern correction with no specification of the sediment type was applied. The data in the second graph from the top was corrected for beam pattern with SO213-14 used for ground-truthing. For the third data the applied beam pattern file was generated at SO213-15 with declaration of the measured sediment type. The bottom graph shows data, which was beam pattern corrected by using SO213-17 as ground-truthing location.
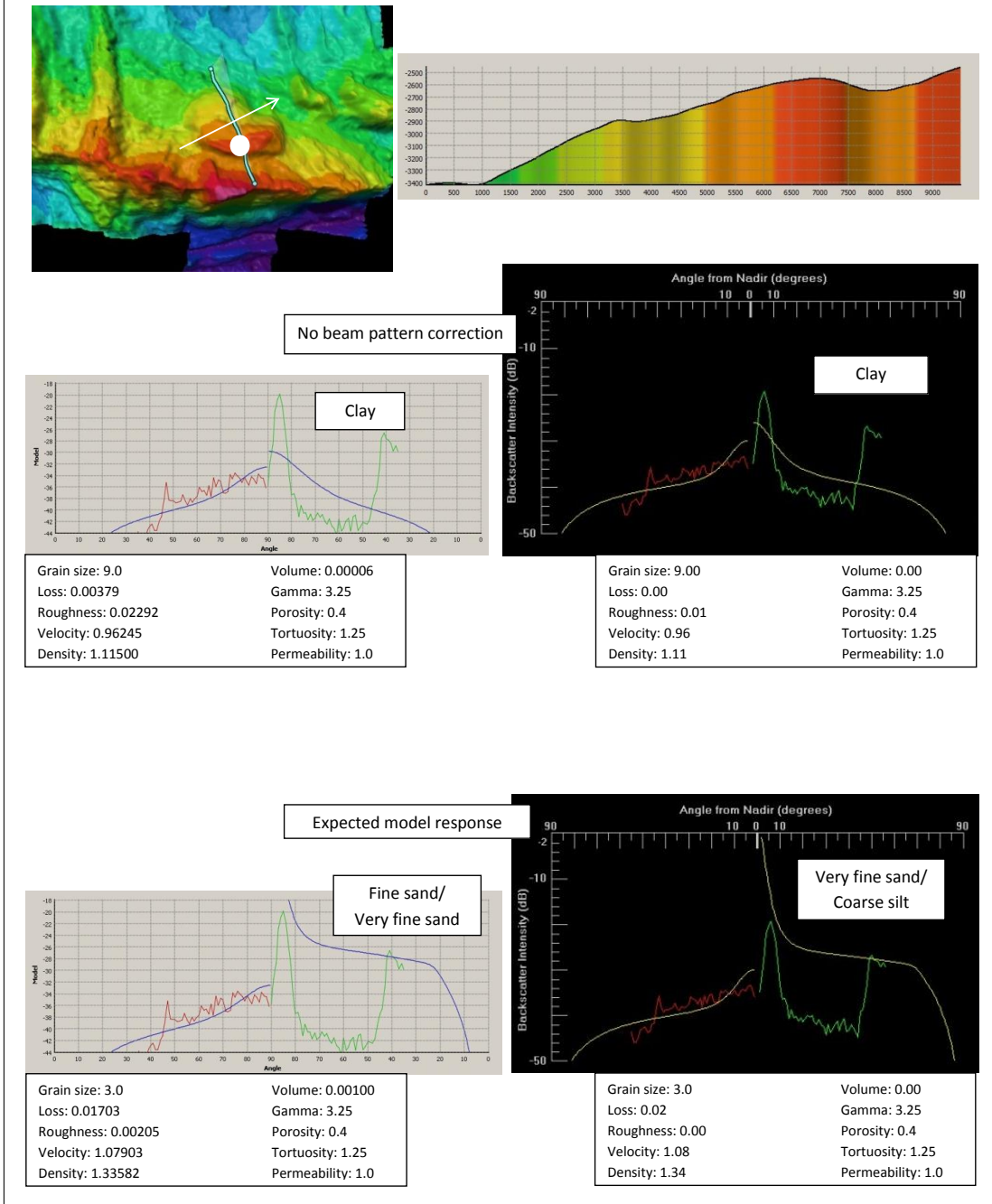
Figure C.17: Observed (green/red) and modeled (blue/yellow) angular response at ground-truthing location SO213-17 recorded by profile 14 generated in *FMGT* (left) and *CARIS* (right). No beam pattern correction was applied to the data ("No beam pattern correction"). The grain size was adjusted to the measured grain size value. The resulting modeled angular responses are shown below ("Expected angular repsonse").
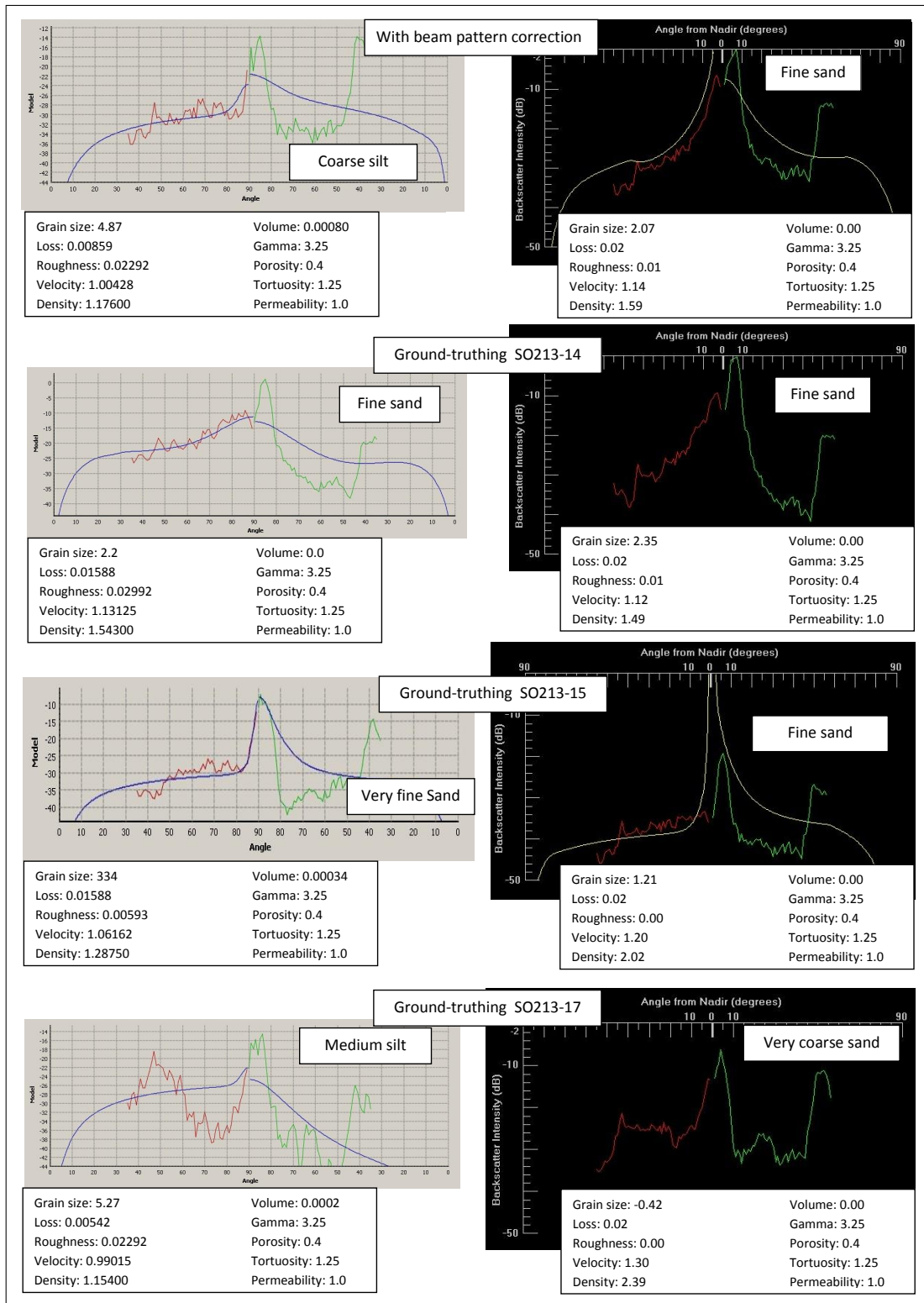
Figure C.18: Observed (green/red) and modeled (blue/yellow) angular response at ground-truthing location SO213-17 recorded by profile 14 generated in *FMGT* (left) and *CARIS* (right). To the data in the upper graph a beam pattern correction with no specification of the sediment type was applied. The data in the second graph from the top was corrected for beam pattern with SO213-14 used for ground-truthing. For the third data the applied beam pattern file was generated at SO213-15 with declaration of the measured sediment type. The bottom graph shows data, which was beam pattern corrected by using SO213-17 as ground-truthing location.

Appendix D

CD Contents

- Master thesis in pdf format

- Figures of the thesis

- *Fledermaus*

  - *iView4D* (executable)
  - SO213-1.scene (*Fledermaus* scene file - can be opend with *iView4D*)
    * Bathymetric surface
    * Mosaics (generated in *FMGT* and *CARIS*)
    * Backscatter data of each profile
    * ARA results (computed in *CARIS* and *FMGT* with different settings)